

Université du Québec
Institut National de la Recherche Scientifique
Centre Énergie, Matériaux et Télécommunications

**GROWTH AND CHARACTERIZATION OF EPITAXIAL THIN FILMS
OF EPSILON FERRITE (ϵ -Fe₂O₃).**

By
Luca Corbellini

Thesis presented to obtain the degree of
Philosophiae doctor (Ph.D.)
In Material Science

Evaluation Jury

Jury president and Internal juror	Emanuele Orgiu INRS, Centre EMT
External juror	John T. Wei Department of Physics University of Toronto
External juror	Oussama Moutanabbir Polytechnique Montreal
Supervisor	Alain Pignolet INRS, Centre EMT
Co-Supervisor	David Ménard Polytechnique Montreal

ACKNOWLEDGMENTS

First of all, I would like to thank my advisor Professor Alain Pignolet and my co-supervisor Professor David Ménard, without whom my work at the Institut National de la Recherche Scientifique, centre Énergie, Matériaux et Télécommunications (INRS-EMT) and at Politechnique Montréal would not have been possible. This work would not have been feasible also without the support from the funding agencies NSERC (Natural Sciences and Engineering Research Council of Canada) and FRQNT (Fonds de Recherche du Québec - Nature et Technologies).

I would like to thank Professor Gianluigi Botton and Dr. Andreas Korinek of McMaster university for the amazing transmission electron microscope (TEM) images they provided.

Then I would like to thank Professor Chaker, Professor Legaré, Professor Ozaki and Professor Ruediger for their availability for scientific discussion and useful suggestions on pulsed laser deposition (PLD), second-harmonic phenomena, TeraHertz time domain spectroscopy (TDS), and Raman microscopy and general material science respectively.

A special thank to Dr. Christian Lacroix of Politechnique Montréal and Dr. Catalin Harnagea of INRS-EMT, for constantly engaging me in meaningful and fruitful discussions and teaching me the “secrets” of the vibrating sample magnetometer (VSM) and of the scanning probe microscope (SPM). I would also acknowledge Dr. Xavier Ropagnol for his help with the time domain spectroscopy (TDS) measurements.

I would like to thank the members of Ferroic-Lab, Ali, Julien, Liliana and Thameur, with whom I shared the most part of my time in Varennes, for their constant help and availability to discuss scientific and everyday life topics.

A special thank to Cristophe Chabanier and Etienne Charette, who always showed great patience in training me first, and then help me with many different instruments and techniques I widely used during my doctorate.

I would like to thank my friends Andrea, Artiom, Daniele, Fabrizio, Gianluca, Luis, Piotr, Raffaello, Riccardo, Riccardo and Yohann, who always brought joy and lightheartedness to every lunch break at INRS.

I am very grateful to my mom, my dad, and my whole family, without the support of whom my experience in Canada would have not been possible, and especially to my better half Pia, who has been a constant source of energy and inspiration for the whole time I had the privilege to share with her.

Finally, I would like to thank the president of the jury Professor Emanuele Orgiu for the extreme kindness and availability, along with the other members of the jury, Professor John T. Wei of University of Toronto and Professor Oussama Moutanabbir of Polytechnique Montreal, for accepting to evaluate my thesis and for their comments and corrections.

ABSTRACT

Epsilon ferrite ($\epsilon\text{-Fe}_2\text{O}_3$) is a metastable phase of iron(III) oxide, intermediate between maghemite ($\gamma\text{-Fe}_2\text{O}_3$) and hematite ($\alpha\text{-Fe}_2\text{O}_3$). $\epsilon\text{-Fe}_2\text{O}_3$ has been investigated essentially because of its magnetic properties, in particular its strong magnetocrystalline anisotropy which results in a gigantic coercive field, as high as 2T for nanoparticles, with a Curie temperature of circa 500 K. Given its crystal structure belonging to the polar space group $Pna2_1$, it should exhibit pyroelectric, and possibly ferroelectric behavior, potentially making it one of the few single phase room temperature multiferroic materials. Moreover, the material anisotropy also results in a natural ferromagnetic resonance (FMR) frequency in the low THz range. This is of particular interest given its potential use in short-range wireless communications (*e.g.* 60GHz Wi-Fi) and ultrafast computer non-volatile memories.

To overcome its metastable nature, stabilization of $\epsilon\text{-Fe}_2\text{O}_3$ has been obtained mainly by synthesizing it by sol-gel as nanoparticles embedded inside a SiO_2 matrix. Recently however, deposition of epitaxial thin films of $\epsilon\text{-Fe}_2\text{O}_3$ was demonstrated, with the growth occurring directly, on SrTiO_3 , as well as, with the use of a buffer layer, on YSZ and Al_2O_3 . The ability of depositing high-quality epitaxial thin films of $\epsilon\text{-Fe}_2\text{O}_3$ is a key feature for their development towards integrated devices.

In this thesis, the growth by Pulsed Laser Deposition of epitaxial thin films of pure and Al substituted $\epsilon\text{-Fe}_2\text{O}_3$ on different single crystal substrates, such as SrTiO_3 , LaAlO_3 , LSAT, and YSZ, is reported, and the influence of the chosen substrate and of the aluminum doping on the structural and functional properties of $\epsilon\text{-Fe}_2\text{O}_3$ is discussed. Detailed structural characterization performed by x-ray diffraction and transmission electron microscopy highlighted the differences resulting from growing epsilon ferrite on the diverse substrates, in particular the formation of twins with orientation depending on the choice of substrate. Magnetic characterization confirmed the high magnetocrystalline anisotropy of our film and revealed the presence of a secondary phase which was identified as the well-known magnetite (Fe_3O_4). Angular analysis of the magnetic properties revealed how their azimuthal dependence reflects the angular geometry of the twins. Aluminum insertion inside the $\epsilon\text{-Fe}_2\text{O}_3$ lattice was also achieved, resulting in the ability to modify the coercive field and the magnetization at saturation by controlling the aluminum substitution into the film. Finally, depositions over vicinal STO and YSZ substrates have been performed to overcome the formation of twins, which might represent a fundamental advance given how some applications, *e.g.* non-volatile memories, require films of materials characterized by a single magnetic easy axis, thus twin-free, in order to be implemented into devices.

Keywords: thin films, epitaxy, pulsed laser deposition, iron oxide, multifunctional oxides, magnetism, ferroelectricity, multiferroic, ferromagnetic resonance.

RÉSUMÉ

L'oxyde ferrique epsilon ($\epsilon\text{-Fe}_2\text{O}_3$) est une phase métastable de l'oxyde de fer(III), intermédiaire entre la maghémite ($\gamma\text{-Fe}_2\text{O}_3$) et l'hématite ($\alpha\text{-Fe}_2\text{O}_3$). $\epsilon\text{-Fe}_2\text{O}_3$ a été étudié essentiellement en raison de ses propriétés magnétiques, en particulier sa forte anisotropie magnétocristalline qui a pour conséquence un champ coercitif gigantesque pouvant atteindre 2T pour les nanoparticules, avec une température de Curie d'environ 500 K. Compte tenu de sa structure cristalline appartenant au groupe d'espaces polaires $Pna2_1$, il doit présenter un comportement pyroélectrique et possiblement ferroélectrique, ce qui en ferait l'un des rares matériaux monophasés multiferroïques à température ambiante. En outre, son anisotropie magnétocristalline géante résulte également en une fréquence de résonance ferromagnétique naturelle (FMR) dans la gamme des bas THz. Ceci est particulièrement intéressant compte tenu de son utilisation potentielle dans les communications sans fil à courte portée (par exemple 60 GHz Wi-Fi) et les mémoires non volatiles ultra-rapides.

Pour surmonter sa nature métastable, la stabilisation de $\epsilon\text{-Fe}_2\text{O}_3$ a été obtenue principalement en le synthétisant par sol-gel en tant que nanoparticules incorporées dans une matrice de SiO_2 . Récemment cependant, le dépôt de couches minces épitaxiales de $\epsilon\text{-Fe}_2\text{O}_3$ a été démontré, soit directement sur SrTiO_3 , soit, avec l'utilisation d'une couche tampon, sur YSZ et Al_2O_3 . La capacité de déposer une couche mince épitaxiée de $\epsilon\text{-Fe}_2\text{O}_3$ de haute qualité est une caractéristique clé pour son application potentielle à des dispositifs intégrés.

Dans ce manuscrit, le dépôt par ablation laser pulsé de couches minces épitaxiales de $\epsilon\text{-Fe}_2\text{O}_3$ pur et dopé avec de l'aluminium sur différents substrats monocristallins, tels que SrTiO_3 , LaAlO_3 , LSAT et YSZ est décrit, et l'influence du substrat choisi et du dopage d'aluminium sur les propriétés structurales et fonctionnelles est discuté. La caractérisation structurale détaillée réalisée par diffraction de rayons X et microscopie électronique à transmission, a mis en évidence les différences résultant de la croissance de $\epsilon\text{-Fe}_2\text{O}_3$ sur les divers substrats, en particulier la formation de macles avec diverses orientations selon le choix du substrat. La caractérisation magnétique a confirmé l'anisotropie magnétocristalline élevée de nos films et a révélé la présence d'une phase secondaire qui a été identifiée comme étant de magnétite (Fe_3O_4). L'analyse angulaire des propriétés magnétiques a révélé comment la présence de macle affecte leur dépendance azimutale. L'insertion d'aluminium dans le réseau $\epsilon\text{-Fe}_2\text{O}_3$ a également été réalisée, ce qui a permis de contrôler le champ coercitif et l'aimantation à saturation en fonction du pourcentage d'aluminium. Enfin, des dépôts sur des substrats STO et YSZ monocristallin avec un « miscut » ont été effectués pour prévenir la formation de macles, ce qui pourrait représenter une avance fondamentale compte tenu de la façon dont les applications, par exemple les mémoires non-volatiles, nécessitent des couches cristallines sans macles pour pouvoir être mises en œuvre dans des dispositifs.

Mots-clés: couches minces, épitaxie, ablation laser pulsé, oxyde de fer, oxydes multifonctionnels, magnétisme, ferroélectricité, multiferroïque, résonance ferromagnétique.

TABLE OF CONTENTS

INTRODUCTION	1
CHAPTER 1 THEORETICAL BACKGROUND.....	11
1.1 STRUCTURE AND PROPERTIES OF EPSILON FERRITE.....	11
1.2 BRIEF DISCUSSION ON MAGNETISM.....	13
1.2.1 <i>Magnetic interactions and classes of magnetic materials.</i>	13
1.2.2 <i>The magnetic hysteresis</i>	16
1.2.3 <i>Ferromagnetic Resonance Frequency.</i>	19
1.3 FERROELECTRICITY AND MULTIFERROICITY.....	21
1.3.1 <i>Phenomenological description of ferroelectricity.</i>	21
1.3.2 <i>Multiferroicity.</i>	23
CHAPTER 2 EXPERIMENTAL TECHNIQUES.....	25
2.1 SYNTHESIS OF EPITAXIAL THIN FILMS OF EPSILON FERRITE BY PULSED LASER DEPOSITION.	26
2.1.1 <i>Fundamentals on pulsed laser deposition.</i>	26
2.1.2 <i>Growth mode at thermodynamic equilibrium.</i>	30
2.1.3 <i>Homoepitaxial growth modes.</i>	37
2.1.4 <i>Pulsed Laser Interval Deposition.</i>	38
2.1.5 <i>Heteroepitaxy.</i>	38
2.1.6 <i>Pulsed Laser Deposition Experimental Setup setup.</i>	42
2.2 CHARACTERIZATION OF EPSILON FERRITE THIN FILMS.....	44
2.2.1 <i>Characterization of the crystal structure via x-ray diffractometry.</i>	44
2.2.2 <i>Transmission Electron Microscopy.</i>	46
2.2.3 <i>Thickness.</i>	47
2.2.4 <i>Macroscopic Magnetic Characterization.</i>	47
2.2.5 <i>Macroscopic Ferroelectric Characterization.</i>	50
2.2.6 <i>Surface topology and microscopic characterization of magnetism and ferroelectricity via scanning probe microscopy (SPM).</i>	52
2.2.7 <i>Direct and indirect measurement of the ferromagnetic resonance spectroscopy.</i>	52
CHAPTER 3 GROWTH OF EPITAXIAL THIN FILMS OF EPSILON FERRITE.....	55
3.1 EPITAXIAL STABILIZATION OF EPSILON FERRITE THIN FILM.	56
3.1.1 <i>Choice of substrates and epitaxial matches.</i>	56
3.1.2 <i>Continuity in the oxygen framework.</i>	60
3.1.3 <i>Thermal expansion coefficient of the utilized substrates.</i>	62
<i>Deposition features and “deposition window”.</i>	62
3.1.4 <i>Effect of temperature and pressure on the growth of ϵ-Fe₂O₃ thin films.</i>	63

3.1.5	<i>Determination of the growth-rate and optimal thickness.....</i>	64
3.2	STRUCTURAL CHARACTERIZATION OF EPSILON FERRITE THIN FILMS.	65
3.2.1	<i>Confirmation of epitaxial growth.....</i>	65
3.2.2	<i>Graphical representation of twins.</i>	73
3.2.3	<i>Mosaicity effects.</i>	74
3.2.4	<i>Rocking curve analysis.</i>	76
3.2.5	<i>Structural characterization via transmission electron microscopy.</i>	78
3.3	CONCLUSIONS.....	82
CHAPTER 4 FUNCTIONAL CHARACTERIZATION OF EPSILON FERRITE THIN FILMS.....		83
4.1	MAGNETIC CHARACTERIZATION OF THE EPSILON FERRITE THIN FILMS.	84
4.1.1	<i>Magnetic hysteresis and temperature dependent measurements.</i>	84
4.1.2	<i>Angle dependent measurements.</i>	95
4.1.3	<i>Microscopic magnetic characterization via magnetic force microscopy.</i>	100
4.2	FERROELECTRIC CHARACTERIZATION OF EPSILON FERRITE THIN FILMS.....	101
4.3	DIRECT AND INDIRECT MEASUREMENT OF THE FERROMAGNETIC RESONANCE FREQUENCY.....	104
4.4	CONCLUSIONS.....	107
CHAPTER 5 GROWTH AND CHARACTERIZATION OF ALUMINUM-SUBSTITUTED EPSILON FERRITE THIN FILMS.....		109
5.1	GROWTH AND STRUCTURAL CHARACTERIZATION OF AL-SUBSTITUTED EPSILON FERRITE THIN FILMS.	110
5.2	THE EFFECT OF ALUMINUM SUBSTITUTION ON THE MAGNETIC PROPERTIES.	112
5.3	THE EFFECT OF ALUMINUM SUBSTITUTION ON THE FERROELECTRIC PROPERTIES.	114
5.4	CONCLUSIONS.....	114
CHAPTER 6 THE DEPOSITION ON MISCUT SUBSTRATES.		115
6.1	GROWTH OF EPSILON FERRITE THIN FILMS ON MISCUT SUBSTRATES.	117
6.2	STRUCTURAL CHARACTERIZATION OF EPSILON FERRITE THIN FILMS ON MISCUT SUBSTRATES.	117
6.3	MAGNETIC CHARACTERIZATION OF EPSILON FERRITE THIN FILMS ON MISCUT SUBSTRATES.	123
6.4	CONCLUSIONS.....	125
CHAPTER 7 GENERAL CONCLUSIONS AND PERSPECTIVES.		127
7.1	GENERAL CONCLUSIONS.....	127
7.2	PERSPECTIVES.....	131
CHAPTER 8 SYNOPSIS IN FRENCH.....		133
BIBLIOGRAPHY.....		159

APPENDIX I	HYSTERESIS LOOPS REVISITED: AN EFFICIENT METHOD TO ANALYZE	
FERROIC MATERIALS.....		169
I.1	SEPARATING THE DIFFERENT CONTRIBUTIONS TO THE MEASURED HYSTERESIS LOOPS	171
I.2	VALIDATION OF THE TECHNIQUE	173
I.3	CONCLUSIONS.....	183

LIST OF FIGURES

Figure 1: (a) hematite, (b) magnetite, (c) maghemite, and (d) wüstite minerals. _____	2
Figure 2: Some of the different applications in which iron oxides are utilized (adapted from ²). _____	3
Figure 3: The structures of the three most investigated iron oxides, (a) hematite, (b) magnetite, and (c) maghemite. _____	4
Figure 4: ϵ - Fe_2O_3 has an intermediate structure, characterized by oxygen octahedra like maghemite, and by alternating oxygen/iron layers like in hematite. _____	5
Figure 5: ϵ - Fe_2O_3 unit cell and configuration of the magnetic moments on the four different iron sites. _____	11
Figure 6: Antiferromagnetic order due to superexchange in magnesium oxide. _____	15
Figure 7: The different kind of magnetic orders – (a) ferromagnetic, (b) antiferromagnetic, and (c) ferrimagnetic order. _____	16
Figure 8: Typical magnetic hysteresis loop and behavior of the moments in the different domains in response to the applied field. _____	17
Figure 9: Fine splitting giving source to the ferromagnetic resonance frequency in materials: on the right, the case of a material with high magnetocrystalline anisotropy is depicted. _____	20
Figure 10: Ferroelectric and paraelectric structure for barium titanate beyond and above the Curie temperature. _____	22
Figure 11: Double well potential representing the movement of the Ti ion during the switch of the polarization in BaTiO_3 . _____	22
Figure 12: The different sets and subsets of the ferro-, pyro-, and piezoelectric materials. _____	23
Figure 13: The three class of ferroic materials, separated by their order parameters M , P and ϵ , and the different coupling possible. In the figure, the two magnetoelectric couplings – i.e. the control of polarization by a magnetic field and of magnetization by an electric field – are shown by the green arrows. _____	24
Figure 14: Typical plasma plume in PLD. _____	27
Figure 15: Film growth modes: (a) Layer by layer - Frank-Van der Merwe. (b) Island - Volmer-Weber. (c) Stranski-Krastanov. (d) Step flow. _____	31
Figure 16: Schematic diagram of atomic processes in the nucleation of three dimensional clusters of deposited film atoms on a substrate surface. _____	32
Figure 17: (a) Pseudomorphic and (b) relaxed growth of a cubic epitaxial film on a slightly mismatched cubic substrate. _____	40
Figure 18: (a) Typical PLD setup and (b) schematic of a PLD chamber. _____	42
Figure 19: Graphical representation of Bragg's law. _____	44
Figure 20: The different angles that can be adjusted with high precision during a XRD measurement. The sample is portrayed in blue. _____	45
Figure 21: (a) schematics of the Vibrating Sample Magnetometer (VSM) and (b) in-plane (left) and out-of-plane (right) configuration of the sample in the VSM. _____	48
Figure 22: Classic Tower-Sawyer circuit to measure ferroelectric hysteresis loops (PE loops) in a ferroelectric sample. _____	50

Figure 23: Schematic representation of the FMR setup used in the course of this thesis. The alternating magnetic field H_{AC} of the cavity is applied parallel to the rod and perpendicular to the static magnetic field H_0 .	53
Figure 24: Free energy per volume versus particle diameter in iron oxide (adapted from 40).	56
Figure 25: Graphical representation of the (111) plane of cubic perovskites (in light blue) and the epitaxial relation with the epsilon ferrite unit cell. To be noted, the orientation of the substrate (bottom left corner) and on the film (middle right).	57
Figure 26: Graphical representation of the (100) plane of YSZ (in pink) and the two epitaxial matches between ϵ - Fe_2O_3 (001) and YSZ (100), (a) “parallel” match and (b) “non-parallel” match. To be noted: the same orientation of the two lattices in the “parallel” case and the presence of a rotation in the “non-parallel” one.	59
Figure 27: Graphical representation of the good match of the oxygen polyhedra framework in the epsilon ferrite grown film and in the underlying (111)-oriented perovskite substrate.	60
Figure 28: Graphical representation of the continuity of the oxygen polyhedra framework in epsilon ferrite grown on (100)-oriented YSZ. The continuity in the case of the “parallel” epitaxial match (a) seems, from the graphical representation, to be better than for the “non-parallel”, although, in both cases, it is not as good as for the case of epsilon ferrite grown on perovskites (111).	61
Figure 29: Optimal deposition temperature and pressure (star), and deposition window (in green) for thin films of epsilon ferrite. The area drawn in yellow depicts the condition for which extra magnetite was grown, while the areas in red are either non accessible with the utilized experimental setup or do not yield to the growth of epitaxial thin films.	64
Figure 30: X-ray diffractogram for (001)-oriented thin films of epsilon ferrite grown on STO (111) (green line), LSAT (111) (red line), LAO (111) (blue line), and YSZ (100) (orange line). The peaks belonging to the film are the one of lower intensity marked in the top diffractogram and labeled with the corresponding index. The peaks belonging to the substrates are the high intensity ones marked with red dots in the two top sections.	66
Figure 31: Diffractogram for a thin film of ϵ - Fe_2O_3 (001) grown on STO (111). In red the peaks belonging to highly constraint magnetite are noted. Note also the secondary peaks arising from the substrate (marked in red).	67
Figure 32: Detail of the 004 peak for thin films of epsilon ferrite grown on different substrates (same color code as Figure 30). Note how the position of the peak does not change with the different substrates.	68
Figure 33: Phi scans for the 013 peak of epsilon ferrite when grown on (111)-oriented perovskites (left) and (100)-oriented YSZ (right), along with the scan of peaks belonging to the substrates, in order to infer the mutual orientation between the films and the substrates.	69
Figure 34: Phi scans for the 013 peak of epsilon ferrite thin films grown on different substrates: from the top left clockwise, on YSZ (100) (orange), STO (111) (green), LAO (111) (blue), and LSAT (111) (red).	70
Figure 35: $\theta/2\theta$ scan around the peaks associated with the (013) and the (132) planes of epsilon ferrite. The two different variants (blue line for the “main” growth orientation, red line for the “interstitial”) for the 132 peak confirm the double epitaxy of epsilon ferrite on YSZ (100).	71

- Figure 36:** Phi scan for the 132 peaks of the main growth domains of epsilon ferrite grown on STO (111) (top – green) and YSZ (100) (bottom – orange) plotted along the phi scan of the 132 peaks of the interstitial domains, along with the separation between them. _____72
- Figure 37:** Graphical representation of the different growth orientations possible on (a) (111)-oriented perovskites, and (b) (100)-oriented YSZ. _____73
- Figure 38:** Graphical representation of mosaicity in one particular growth domain in a crystal. Such mosaicity effect can affect both plane parallel to the surface of the sample and perpendicular to it. In the first case, mosaicity will be studied with rocking curve measurements, in the second with Phi-scans. _____74
- Figure 39:** Dispersion in the angular dependence of the 013 peak for epsilon ferrite films: the experimental data are shown as symbols, while the Gaussian fit is represented by the black line. From the top left clockwise, on YSZ (100) (orange), STO (111) (green), LAO (111) (blue), and LSAT (111) (red). _____75
- Figure 40:** Rocking curve measurements for the 004 peak for epsilon ferrite films: the experimental data are shown as symbols, while the Lorentzian fit is represented by the black line. From the top left clockwise, on YSZ (100) (orange), STO (111) (green), LAO (111) (blue), and LSAT (111) (red). _____77
- Figure 41:** (a) STEM image of a circa 120 nm thick film of epsilon ferrite grown on STO (111), highlighting the formation of twins, denoted by the areas with different contrast, separated by randomly oriented boundaries (as noted by the red lines), (b) detail of the interface between the substrate and the film, showing the really sharp interface between (111)-oriented strontium titanate and epsilon ferrite. Below: (1st from the left) graphical simulation of the interface between STO (111) and epsilon ferrite, portraying the same orientation as STO seen in the TEM image. (2nd from left) top view of the epsilon ferrite twins, with the same orientation kept for the substrate, highlighting (in red) the only detectable orientation, which is magnified in the light blue selected area (3rd from left) which is portrayed next to the simulated ϵ -Fe₂O₃ structure rotated according to the proposed epitaxy relationship (4th from left). _____80
- Figure 42:** (a) STEM image of a circa 100 nm thick film of ϵ -Fe₂O₃ on YSZ (100) highlighting the formation of pillar-like twins, (b) detail of the interface between the substrate and the film, evidencing the formation of ‘bubbles’ of a foreign phase (most likely Fe₃O₄) at the interface. Below: high-magnification of the 4 colored selected areas overlapped with simulated ϵ -Fe₂O₃ structures rotated according to the proposed epitaxy relationships to further prove the existence of different growth domains with different in-plane orientations. If the orientation in the red box, with the b axis pointing out-of-plane is taken as 0°, the unit cells depicted in the other boxes are rotated, respectively by 300° (green), and 120° (light blue) (note that the 2 last unit cells (green) and (light blue) have a 180° rotational symmetry). No match was found for the yellow selection, probably due to the overlap of two different growth domains in the depth of the sample and overlapping in the STEM image. _____81
- Figure 43:** Hysteresis loops recorded in-plane for thin films of epsilon ferrite of various thickness deposited on the four substrates that grant epitaxial growth (same color code as XRD measurements). _____84
- Figure 44:** Estimation of the anisotropy field (the point of intersection of the linearization of the saturation part of the loops recorded in and out-of-plane) for a thin film of epsilon ferrite grown on YSZ (100). _____86

Figure 45: Plot of the dependence of the remanent magnetization M_R (blue dots/line) and under the application of a field of 1000 Oe (red dots/line) versus temperature for an epsilon ferrite thin film. _____	87
Figure 46: The complex plot of magnetization versus temperature of an epsilon ferrite epitaxial film for temperatures spanning 300 to 900 K. _____	88
Figure 47: Plot of the dependence of the magnetization versus temperature measured under an applied field of 1000 Oe, for increasing (red – same curve shown above with different scale) and decreasing (blue) temperature. _____	89
Figure 48: Hysteresis in-plane measured before (left) and after (right) the involuntarily induced phase transition, along with the passage used to estimate the new magnetic moment and the value experimentally measured. _____	90
Figure 49: Practical application of the D-D-SI technique to separate the contributions of the two phases to the measured magnetic moment in an epsilon ferrite thin film deposited on YSZ (100). _____	92
Figure 50: Graph of the magnetization (in SI units) for the epsilon and the magnetite phase in a thin film of epsilon ferrite. _____	93
Figure 51: Hysteresis in plane for two thin films of epsilon ferrite grown on YSZ (100) (orange line) and STO (111) (green line). _____	94
Figure 52: Plot of the angular evolution of the coercive field, relative to 0° , measured for a film of epsilon ferrite grown on STO (111). _____	96
Figure 53: Polar plot of the evolution of the measured M_R versus angle (green diamonds) and of the fitted curve (red line) for a sample of epsilon ferrite grown on STO (111). _____	98
Figure 54: Polar plot of the evolution of the measured M_R versus angle (red dots) and of the fitted curve (blue line) for a sample of epsilon ferrite grown on YSZ (100). _____	99
Figure 55: Topography (left) and magnetic contrast (right) measured for a thin film of epsilon ferrite. _____	100
Figure 56: Schematics of the sample structure for ferroelectric characterization: the epsilon ferrite thin film is depicted in red, while the platinum electrodes are drawn, magnified, in silver. _____	101
Figure 57: Polarization and Current vs cyclic voltage plot for a thin film of epsilon ferrite grown on Nb-STO (111), recorded at a driving frequency of (a) 100 Hz and (b) 2KHz. _____	102
Figure 58: PFM signal as measured (black dots and red line), and without the linear electrostatic response (magenta line), and PFM amplitude and phase (right); the recorded signals hint to the presence of a non-switchable polarization (see the magenta line in the PFM signal). _____	103
Figure 59: Field sweep with frequency set at 24GHz for thin films of aluminum ferrite (top green) and epsilon ferrite (middle red) grow on YSZ (100), along with the signal from the bare substrate (blue bottom). _____	105
Figure 60: Amplitude of a THz pulse transmitted through an epsilon ferrite thin film grow on YSZ (100) (orange line), and through a YSZ (100) bare substrate (red line), showing absorption in the 0.1-0.15 THz (100-150 GHz) range. _____	106
Figure 61: (a) $\theta/2\theta$ scans of (100)-oriented ϵ - Fe_2O_3 , ϵ - $Al_{0.1}Fe_{1.9}O_3$, and $AlFeO_3$ thin film, revealing how all the three materials grow epitaxially on (111)-oriented STO. The line drawn in grey helps visualizing the shift in the position of the (006) peak for the Al-substituted films in comparison to pure ϵ - Fe_2O_3 . (b) Evolution of the lattice parameter “c” with increasing Al concentration “x”. _____	111

Figure 62: (a) In-plane (orange) and out-of-plane (green) hysteresis loop measured for a pure $\epsilon\text{-Fe}_2\text{O}_3$ epitaxial thin film, and (b), In-plane (blue) and out-of-plane (red) hysteresis loop measured for a $\epsilon\text{-Al}_{0.1}\text{Fe}_{1.9}\text{O}_3$ epitaxial thin film, both grown on YSZ (100). In both cases we can infer the high magnetic anisotropy of the two samples. _____112

Figure 63: (a) Dependence of the magnetization (M) on the temperature for a $\epsilon\text{-Al}_{0.1}\text{Fe}_{1.9}\text{O}_3$ thin film grown on YSZ (100), recorded under a field of 1000 Oersted applied in -plane. (b) Evolution of the coercive field H_C and (c) of the magnetization at saturation M_S in function of the aluminum concentration “x”. _____113

Figure 64: The magnetic easy axis that arise due to the different epitaxial matches and twinning in thin films of epsilon ferrite grown on (111)-oriented perovskites (left) and on (100)-oriented YSZ (right). _____115

Figure 65: Graphical representation of a section of a (100)-oriented YSZ substrate with a miscut of circa 15° and terraces $\sim 19 \text{ \AA}$ wide. _____116

Figure 66: STEM picture for 50 nm films of epsilon ferrite grown on (a) STO (111) 5° miscut and (b) on YSZ (100) 5° miscut. As was observed for films grown on regular substrates, growth on STO (111) results in sharper interfaces than growth on YSZ (100). (c) Goniometer scan (2θ) of the films shown in the STEM images, revealing that the films grows along the same (001) direction as when grown on regular substrates. The peaks labeled by pound (#) and asterisk (*) belong respectively to the STO (111) and YSZ (100) substrates. _____118

Figure 67: Goniometer scan of 50 nm thick epsilon ferrite epitaxial thin films grown on STO (111) (left) and YSZ (100) right, with increasing degree of miscut. As it was the case for epsilon ferrite thin films grown on regular substrates, the films are (001)-oriented. _____119

Figure 68: Phi scans of the (013) planes for 50 nm thick films of epsilon ferrite grown on STO (111) (left) and YSZ (100) (right) thin films with increasing miscut ($0^\circ - 5^\circ - 10^\circ - 15^\circ - 20^\circ$). The reduction of the multiplicity of the peaks hints to a reduction of the growth orientations. It has to be noted how higher degrees of miscut (higher than 10°) lead to the formation of new growth orientations, highlighted by red circles, given the novel angular distribution of the peaks that was detected. Finally, the two main peaks detected for thin films grown on YSZ (100) miscut 20° circled in violet belong to the substrate and not the film. _____120

Figure 69: STEM image of the interface between a STO (111) 5° miscut substrate and the epitaxial thin film of epsilon ferrite grown on top of it. Note how one growth domain, which boundaries (blue lines), extends over several step edges of the substrate (violet lines). In the two boxes, magnification of two areas picturing two different twins, overlapped with graphical simulation of the unit cell of epsilon ferrite. _____121

Figure 70: STEM image of the interface between a YSZ (100) 5° miscut substrate and the epitaxial thin film of epsilon ferrite grown on top of it. In the two boxes, magnification of two areas picturing two different twins, overlapped with graphical simulation of the epsilon ferrite unit cell. _____122

Figure 71: Magnetic hysteresis in-plane and out-of-plane measured for two 50 nm thick thin films of epsilon ferrite grown on 5° miscut STO (111) (a) and YSZ (100) (b). _____123

Figure 72: Evolution of the remanent magnetization in thin films of epsilon ferrite grown on STO (111) (a) and YSZ (100) (b) with increasing degree of miscut. The measurements hint to an increase in “global” anisotropy for films grown on substrates with miscut higher than 10° , as shown by the decrease in the number of local maxima and the progression to a 180° symmetry. _____124

Figure 73: (a) la maille cristalline élémentaire de ϵ -Fe₂O₃. Relations d'épitaxie entre ϵ -Fe₂O₃ et (b) la surface (111) des perovskites et, (c) et (d), les deux correspondances pour la surface (100) de YSZ. _____140

Figure 74: Représentation graphique de la continuité du réseau de polyèdres d'oxygène de films d' ϵ -Fe₂O₃ déposés sur (a) des perovskites orientées (111) et (b et c) du YSZ orienté (100). La continuité dans le cas de la relation d'épitaxie "parallèle" YSZ (100) semble, à partir de la représentation graphique, être meilleure que pour la relation d'épitaxie "non parallèle" (c). Il faut noter cependant que la correspondance dans les cas (b) et (c) n'est pas aussi bonne que dans le cas d' ϵ -Fe₂O₃ déposé sur des perovskites orientées (111). _____142

Figure 75: Détail du pic de diffraction 004 pour des films minces de ϵ -Fe₂O₃ déposés sur des substrats différents. À noter: la position du pic ne change pas avec les différents substrats. _____143

Figure 76: (a) Analyse Phi scan pour le pic 013 de ϵ -Fe₂O₃ lorsqu'il est déposé sur des perovskites orientées (111) (à gauche) et sur et sur YSZ (100) (à droite), ainsi que les pics 110 et 221 des substrats pérovskite, et des pics 220 des substrats de YSZ, afin de déterminer l'orientation mutuelle entre les films et les substrats. (b) Les mêmes phi-scans pour les pics 013 de ϵ -Fe₂O₃ sur les différents substrats qui assurent une croissance épitaxiale: de en haut à gauche dans le sens des aiguilles d'une montre, sur STO (111) (vert), YSZ (100) (orange), LSAT (111) (rouge) et LAO (111) (bleu). _____145

Figure 77: (Planche de gauche) Dispersion de la dépendance angulaire du pic 013 pour les films de ϵ -Fe₂O₃: les données expérimentales sont présentées sous forme de symboles discrets, tandis que le fit Gaussien est représenté par la ligne noire continue. En haut à gauche dans le sens des aiguilles d'une montre, dépendance angulaire du pic 013 de ϵ -Fe₂O₃ déposé sur YSZ (100), STO (111), LAO (111) et LSAT (111). (Planche de droite) Mesures « rocking curve » pour le pic 004 des films de ϵ -Fe₂O₃: les données expérimentales sont présentées sous forme de symboles discrets, tandis que l'ajustement de Lorentz est représenté par la ligne continue noire. En haut à gauche dans le sens des aiguilles d'une montre, pic 004 des films de ϵ -Fe₂O₃ déposés sur YSZ (100), STO (111), LAO (111) et LSAT (111). _____147

Figure 78: (a) Image STEM d'un film d'une épaisseur d'environ 125nm de ϵ -Fe₂O₃ sur STO (111) et (b) sur YSZ (100) mettant en évidence la différence de l'épaisseur de la couche tampon - quelques angströms dans le premier cas, plusieurs nanomètres dans le second - et la différence de morphologie des « twins » - désordonnés pour les films déposés sur STO, et en forme de pilier régulier pour les films déposés sur YSZ. _____149

Figure 79: (a) Dépendance de l'aimantation d'une couche mince ϵ -Fe₂O₃ déposée sur YSZ (100) avec le champ magnétique appliqué dans le plan de l'échantillon (symboles bleus) et hors du plan de l'échantillon (symboles verts), montrant l'anisotropie magnétique de ϵ -Fe₂O₃. (b) Graphe de M en fonction de T mesuré sous champ nul (bleu) et sous un faible champ magnétique appliqué de 1000 Oe (rouge), montrant que M ne disparaît pas pour une température supérieure à la température de Curie de ϵ -Fe₂O₃ de 460 K lorsqu'un faible champ magnétique est appliqué, révélant la présence d'une phase 'parasite' correspondant à un matériau magnétique doux ayant un TC plus élevé et ayant été assignée à une petite quantité de Fe₃O₄. (c) Mesure de M-H corrigée où les contributions du substrat et du porte-échantillon expérimentalement mesurées (symboles bleus) et analytiquement déterminées (ligne bleue) ont été soustraites, ainsi que les deux cycles d'hystérésis correspondants à la phase d'oxyde ferrique epsilon

(ϵ - Fe_2O_3 - rouge) et la magnétite (Fe_3O_4 - jaune). (d) Estimation de l'anisotropie magnétique en comparant les cycles d'hystérésis mesurées dans le plan et hors du plan. _____151

LIST OF TABLES

Table 1: Lattice mismatch on the in-plane lattice parameters for the three (111)-oriented cubic perovskites. _____	58
Table 2: Lattice mismatch on the in-plane lattice parameters for the two relation in (100)-oriented YSZ. _____	59
Table 3: Thermal expansion coefficients for the different substrates (in red the ones that grant epitaxial growth). _	62
Table 4: Lattice parameters found for epsilon ferrite epitaxial thin films grown on different substrates, the last two rows describe the different matches granted by YSZ (100), along with the lattice parameters for epsilon ferrite nanoparticles and substrates epitaxial matches. _____	69
Table 5: Values for the standard deviation of the Gaussian fit of the Phi scan of the 013 peaks for films grown on different substrates. _____	75
Table 6: Values of the standard deviation of the Lorentzian fit for the Rocking curve of 004 peaks of epsilon ferrite thin films deposited on different substrates. _____	76
Table 7: calculated width of the terrace for miscut YSZ (100) and STO (111) for increasing degrees of miscut. The 0.05° degrees, which is often the tolerance on regular substrates, is shown for comparison. _____	116
Table 8: Le « mismatch » entre paramètre de maille a et b de ferrite epsilon et les substrats choisis pour obtenir une croissance épitaxiale. Le « mismatch » a été calculée en utilisant $mismatch = (a_{film} - a_{sub})/a_{sub}$. En raison du « match » de réseau inhabituelle, il n'est pas possible de définir le « mismatch » pour le cas YSZ "non parallèle" (ici appelé YSZ 2). _____	140
Table 9: Paramètres de mailles trouvés pour les films minces épitaxiales de ferrite epsilon cultivées sur des substrats différents, ainsi que les paramètres de maille de nanoparticules de ferrite epsilon. _____	144
Table 10: Valeurs de l'écart - type de la forme gaussienne, d'évaluer dans le plan mosaïcité, et en forme de Lorentz, pour le hors-plan, pour le balayage « phi » du pic 013 et du « rocking curve » du pic 004 des couches minces de ferrite epsilon déposé sur différents substrats. _____	148
Table 11: Largeur calculée de la terrasse pour substrats de YSZ (100) et STO (111) pour des degrés croissants de miscut, calculées selon la formule: largeur = paramètre de maille * cos (angle de miscut). Les degrés de 0,05 °, souvent tolérants sur des substrats réguliers, sont présentés à titre onéreux. _____	157

LIST OF EQUATIONS

$M = \chi H.$ (1.1)	13
$H = -2J S_i \bullet S_j,$ (1.2)	14
$E_a = K_1 \sin^2 \theta,$ (1.3)	18
$m = \gamma \hbar S.$ (1.4)	19
$H_z = -\mathbf{m} \bullet \mathbf{B}_0 = -\gamma \hbar B_0 S_x.$ (1.5)	19
$\Delta E = \gamma \hbar B_0.$ (1.6)	19
$\omega_0 = \gamma B_0.$ (1.7)	19
$\omega_0 = \gamma \mu_0 H_a^{1/2}.$ (1.8)	20
$\Delta G = a1r2IC - V + a2r2IC - S - a2r2IS - V + a3r3\Delta GV.$ (2.1)	32
$\Delta GV = -k_B T \Omega \ln PPe = -K T \Omega \ln \xi,$ (2.2)	33
$a1IC - V + a2IC - S \geq a2IS - V.$ (2.3)	33
$r^* = -2(a1IC - V + a2IC - S - a2IS - V)3a3\Delta GV.$ (2.4)	33
$\Delta G^* = 4a1IC - V + a2IC - S - a2IS - V327a3\Delta GV^2.$ (2.5)	34
$JC = \text{Arrival rate of atoms at critical} - \text{size nucleus} \times \text{Concentration of critical nuclei.}$ (2.6)	34
$\exp - \Delta G^* / k_B T.$ (2.7)	34
$IC - V + IC - S \leq IS - V.$ (2.8)	35
$lD = DS\tau,$ (2.9)	37
$DS = va2 \exp - EA / k_B T,$ (2.10)	37
$\text{mismatch} = af - as,$ (2.11)	39
$2d \sin \theta = m\lambda.$ (2.12)	44
$Q = C_{ref} * V_{ref}.$ (2.13)	50
$I = dQ/dt.$ (2.14)	51
$P = QS.$ (2.15)	51
$GV = \mu v + 6\sigma d,$ (3.1)	56
$wt = a \cot \theta.$ (3.2)	116

LIST OF ABBREVIATIONS

AFM, Atomic Force Microscopy

CVD, Chemical Vapor Deposition

D-D-SI, Derivative-Deconvolution-Selective Integration

EELS, Electron Energy Loss Spectroscopy

FE, Ferroelectric

FMR, Ferromagnetic Resonance

FWHM, Full Width at Half Maximum

GFO, Gallium Ferrite

HAADF, High-Angle Annular Dark-Field

LaAlO₃ – LAO, Lanthanum Aluminate

LiNbO₃, Lithium Niobate

LSAT, Lanthanum/Strontium Aluminate/Tantalate

MFM, Magnetic Force Microscopy/Microscope

MgO, Magnetisum Oxide

PFM, Piezoresponse Force Microscopy/Microscope

PLD, Pulsed Laser Deposition

RHEED, Reflection High-Energy Electron Diffraction

SPM, Scanning Probe Microscopy/Microscope

SrTiO₃ – STO, Strontium Titanate

STEM, Scanning Transmission Electron Microscopy/Microscope

STM, Scanning Tunneling Microscopy/Microscope

THz-TDS, TeraHertz Time Domain Spectroscopy

UV, Ultra Violet

VSM, Vibrating Sample Magnetometry/Magnetometer

XRD, X-Ray Diffractometry/Diffractometer

YSZ, Yttrium-Stabilized Zirconia

INTRODUCTION – IRON OXIDES AND EPSILON FERRITE.

Iron oxides are ubiquitous in Nature: they are not only abundantly found in Earth's crust, but also in a very different setting such as the surface of Mars, where they are mostly responsible for the color of the “red” planet^{1,2}. The most abundant iron oxide, hematite (α -Fe₂O₃), is the oldest known among the iron oxides: millennia old writings made with an hematite-based red chalks were found in South Africa in what might constitute of one of the earliest evidences of human behavior³. Hematite can be found in a range of colors, among which one is blood-red, from which takes its name from (in Greek, αἱματίτης *haimatitēs* = blood-red). Given the possibility of smelting it into iron ores, hematite played a pivotal role in human development and evolution, from the Iron Age (12th-7th century BCE) to the industrialization era (due to the use of iron to fabricate steel). Hematite is a weak magnetic material, characterized by a corundum structure (like sapphire, α -Al₂O₃), and it is the most stable between the different iron oxides.

The second most abundant iron oxide, magnetite (Fe₃O₄), is the most magnetic among the minerals found in the Earth crust, thus among the iron oxides: as a mineral, when naturally magnetized, is known as lodestone, which properties were well known by Asian and European, who used it as navigation tool (indicating the direction of the North) to aid themselves in their exploration as early as the eleventh century CE (although similar devices were used for divination a thousand year earlier)⁴. Magnetite is responsible for the magnetic properties of most rocks, and is even formed in different organism that base their orientation on magnetism. It is a black, ferrimagnetic mineral, characterized by an inverse spinel (cubic) structure containing both Fe³⁺ and Fe²⁺ ions.

Maghemite (γ -Fe₂O₃) is a brown-red ferrimagnetic compound, isostructural to magnetite but fully oxidized (therefore not characterized by the presence of Fe²⁺ ions). It is, along hematite, the only stable iron (III) oxide that can be found in nature. Its existence was long unknown to man: it was first synthesized by oxidizing magnetite in the second half of the 19th century⁵, and shortly after occurrence in Nature was also demonstrated. After a certain debate, its name was chosen by composing the one of MAGnetite with HEMAtite, in allusion to its magnetic properties, similar to the ones of magnetite, and its composition (alike hematite, i.e. composed only of fully oxidized iron (III))⁶.

The last stable iron oxide is wüstite (FeO), which is the only iron oxide containing uniquely divalent Fe. It is characterized by a black color and it is an important intermediate element in iron ores reduction.

INTRODUCTION

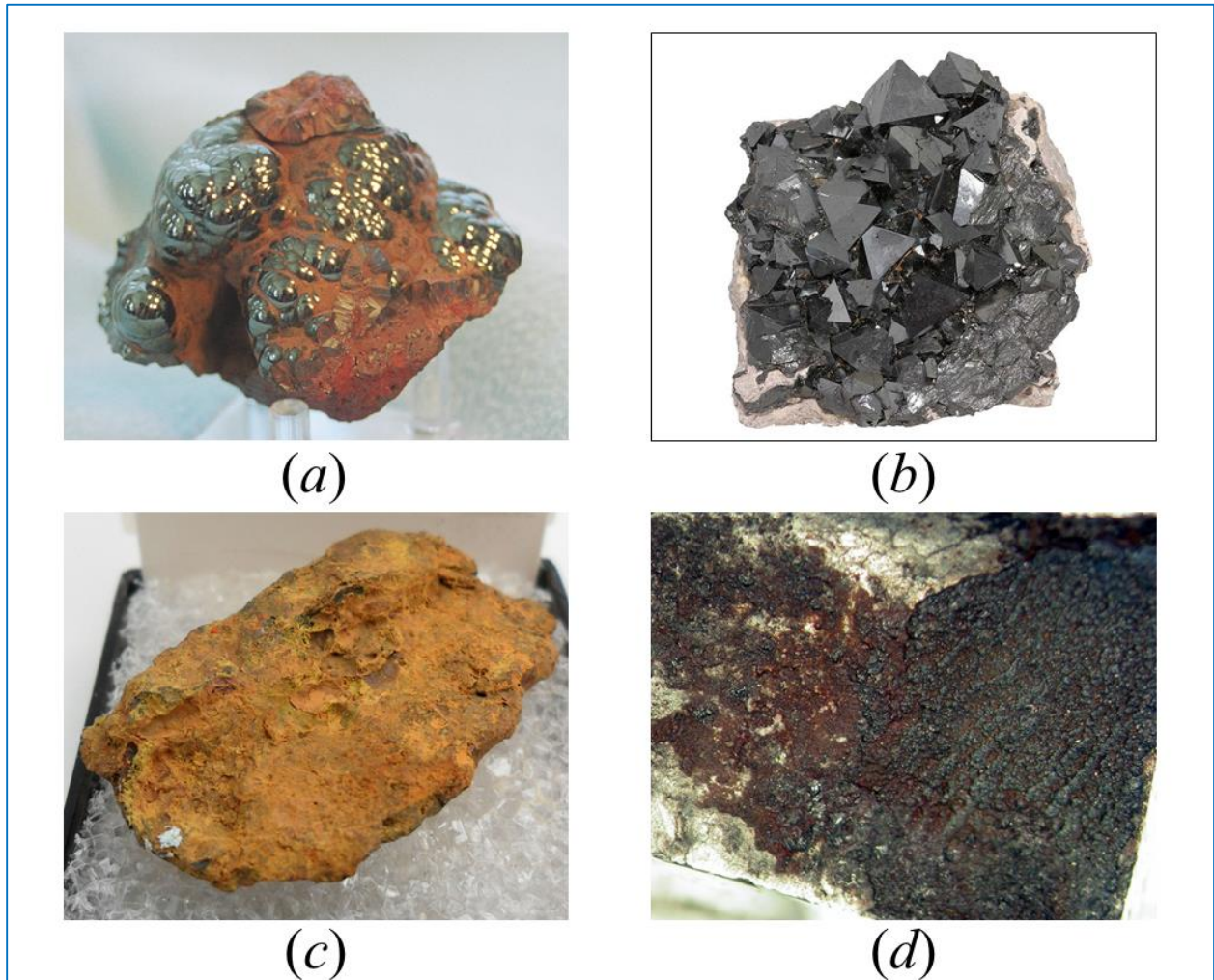


Figure 1: (a) hematite, (b) magnetite, (c) maghemite, and (d) wüstite minerals.

In the recent years iron oxides have attracted renewed interests; along with their abundance and low cost, the ease of obtaining different polymorphs with different oxidation states, and the possibility to access a variety of magnetic and electronic properties, the road towards new applications was opened by the development of new, easy, synthesis routes for nanosized iron oxides. Both chemical and physical approaches to the growth were followed, showing the possibility of achieving high quality nanostructures, along with extreme control on the nanostructures size, via techniques such as chemical precipitation, sol-gel, hydrothermal synthesis, precipitation, chemical vapor deposition, atomic layer deposition, sputtering and pulsed laser deposition⁷.

INTRODUCTION

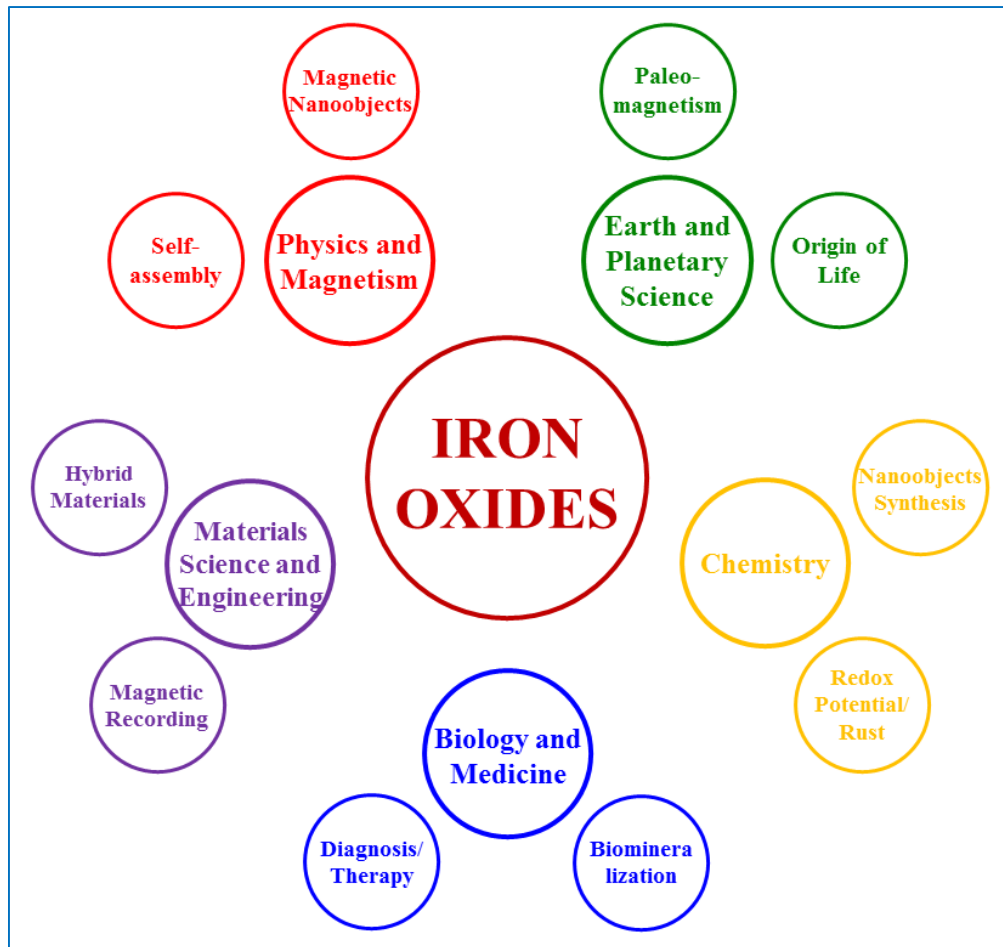


Figure 2: Some of the different applications in which iron oxides are utilized (adapted from ²).

The possibility of displaying different colorations depending on the size of the iron oxides particles, along with their pure hues and high tinting strength, and their extreme stability and resistance to acidic and basic environments, make iron oxides ideally suited for pigments in ceramics and paints¹. Pigments based on hematite, maghemite and magnetite are respectively red, brown, and black. Magnetite-based pigments are also used in magnetic ink in recognition devices, and in metallography for detecting defects in engines¹. All the iron oxides are characterized by an overall environmental safety and stability in water at neutral pH and in physiological conditions, and, especially in their fully oxidized form, they are non-toxic, biodegradable, and biocompatible, making them ideal for applications in various fields of medicine. Last but not least, their intrinsic magnetic properties, *e.g.* the high magnetization at room temperature and high Curie temperature of magnetite and maghemite, is probably what has been exploited the most, making them suitable for many different applications. Moreover, the possibility of synthesizing them as superparamagnetic nanoparticles, thus having no remnant magnetization that could lead to agglomeration

INTRODUCTION

of these particles, constitutes a major advantage given the need of avoiding any sort of cluster to prevent the very dangerous blockage of blood vessels. Hematite, due to its low cost, resistance to corrosion, environmental safety, and n-type semiconductor behavior, has been intensively investigated for applications in gas and chemical sensors^{8,9}, rechargeable lithium ion batteries⁸, as catalyst¹⁰ or photocatalyst¹¹, and for waste-water treatment¹². The use of magnetite and maghemite nanoparticles has received considerable attention in different biomedical applications^{13,14}, given their magnetic properties and the possibility to engineer their large surface area with different functional groups. Iron oxides nanoparticles have proved very efficient for *in vivo* applications, like in magnetic-guided drug delivery^{15,16}, as contrast agent in magnetic resonance imaging (MRI)¹⁷, and for hyperthermia therapy^{18,19}. Functionalized iron oxides nanoparticles also find many application *in vitro*, for example in biosensors²⁰, and for cell separation²¹, displaying high cost-effectiveness ratio, sensitivity and speed. Maghemite also proved to be very efficient for removal of toxic agents, both *ex situ* and *in situ*, such as the water remediation of Cr^{VI}, a byproduct of many industrial processes that can act as a mutagen, carcinogen, and teratogen in mammals²², as well as for the removal of arsenic ions from wastewaters²³. Finally, magnetite and hematite have been and are currently used as catalysts for several industrially important reactions, like in the desulfurization of natural gas, in the synthesis of NH₃ (in the so-called Haber process), and in the high temperature water gas shift reaction^{1,3,24,25}.

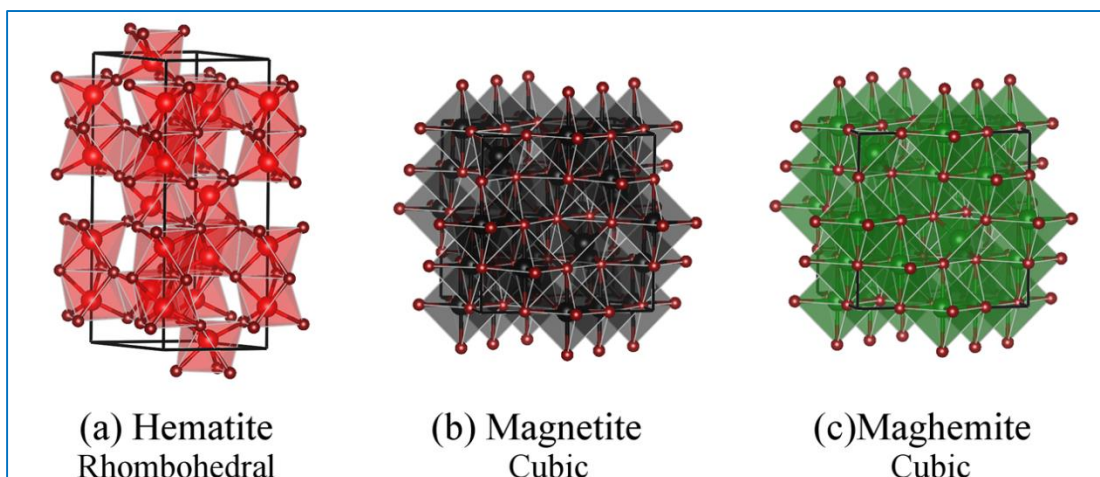


Figure 3: The structures of the three most investigated iron oxides, (a) hematite, (b) magnetite, and (c) maghemite.¹

¹ The graphical representation was obtained with the software VESTA¹⁶², which has been used for every graphical representation of crystal structures in his thesis.

INTRODUCTION

Although it is very rarely found in nature and it is not as easy to synthesize as its isomers, due to its inherent instability in ambient condition (which, however, did not stop Chinese craftsmen to use it as a pigment 1000 years ago²⁶), attention must also be given to epsilon ferrite ($\epsilon\text{-Fe}_2\text{O}_3$), an intermediate phase of maghemite ($\gamma\text{-Fe}_2\text{O}_3$) and hematite ($\alpha\text{-Fe}_2\text{O}_3$) with a complex orthorhombic crystal structure (Figure 4).

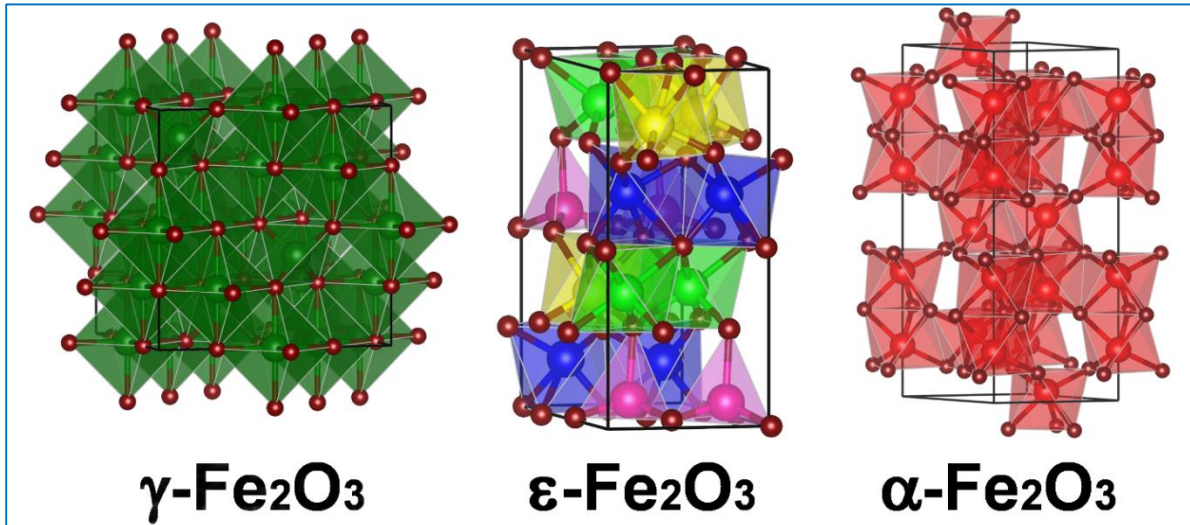


Figure 4: $\epsilon\text{-Fe}_2\text{O}_3$ has an intermediate structure, characterized by oxygen octahedra like maghemite, and by alternating oxygen/iron layers like in hematite.

Epsilon ferrite has first been synthesized in 1934, when Forestier and Guiot-Guillain²⁷ reported an iron(III) oxide different from α - and $\gamma\text{-Fe}_2\text{O}_3$. Then in 1963, Schrader and Buttner²⁸, and almost at the same time Walter-Levy and Quemeneur²⁹, were able to synthesize the material, to measure its X-ray diffraction (XRD) pattern for the first time and named it epsilon ferrite. Phase purity was first obtained by Trautmann and Forestier in 1965³⁰. Complete description of its structure, along with Mossbauer studies of its magnetic properties was reported by Tronc *et al.* in 1998³¹, which renewed the interest towards the material prompting refined reports on its synthesis, structural, and magnetic characterization^{32,33}. The then chosen form of synthesis was mostly nanoparticles embedded in a SiO_2 matrix synthesized by Sol-Gel. The silica matrix proved to be crucial for the stabilization of metastable $\epsilon\text{-Fe}_2\text{O}_3$ through size confinement mechanism. However, it was the first report on the giant coercive field in epsilon ferrite nanoparticles by Ohkoshi *et al* in 2004 which sparked the attention on this iron(III) oxide isomer³⁴. The value found for $H_C \approx 20$ kOe was the highest ever recorded for metal oxide-based material (commercially used hard magnetic materials barium hexaferrite and Co-ferrites are characterized by H_C values of 6.4 and 7.4 kOe, respectively), opening up a new path for metal oxide-based nanomagnet. This discovery prompted even more detailed studies of the magnetic properties of epsilon ferrite nanoparticles, which highlighted a magnetic softening for temperatures $T \sim 100\text{K}$ ³⁵. Along with the renewed interest, came reports on the synthesis of epsilon ferrite

INTRODUCTION

in forms different than nanoparticles, such as nanorods and nanowires^{36–39}. A very important breakthrough was achieved when Ohkoshi *et al.* first showed how the magnetocrystalline anisotropy characterizing epsilon ferrite also results in a natural ferromagnetic resonance (FMR) frequency around 200 GHz, and showed the possibility of metal substitution into epsilon ferrite, thus obtaining $\epsilon\text{-M}_x\text{Fe}_{2-x}\text{O}_3$, in order to tune the FMR frequency⁴⁰. This frequency falls in the so-called millimeter wave range (30–300 GHz), which recently has started to be used in electronic devices for high-speed wireless communication. In various publications, it was shown how it is possible to lower the FMR frequency by substituting iron ions in $\epsilon\text{-Fe}_2\text{O}_3$ with metals characterized by a smaller ionic radius compared to Fe^{3+} , such as Ga^{3+} and Al^{3+} , results in a lowering of the FMR frequency^{41–43}, while substituting with ions having a larger radius like Rh^{3+} results in an the opposite effect, i.e. an increase of the FMR frequency⁴⁴. Indium substitution in nanoparticles has been reported as well, however, while it was shown how it lowers the Curie temperature and the magnetization, no effect on the FMR frequency has been observed⁴⁵. Finally, the last advancement on epsilon ferrite, was to show the possibility of synthesizing it in form different than nano-sized particles. In a recent publication, Carraro *et al.* reported on the growth of a mixture of supported $\epsilon\text{-}$ and $\beta\text{-Fe}_2\text{O}_3$ nanorods on silicon wafers by chemical vapor deposition⁴⁶. These nanostructures proved to not possess the same interesting functional properties as their nanoparticle counterparts; in particular, they exhibit a much lower coercive field, thus much lower magnetic anisotropy and much lower FMR. Moreover, they do not exhibit a completely ordered structure, making them not suitable for applications where such order is needed, like magnetic memories. However, they proved to be very efficient catalyst for hydrogen generation, with production rates as high as $125 \text{ mmol h}^{-1} \text{ m}^{-2}$, significantly superior to the commonly investigated $\alpha\text{-Fe}_2\text{O}_3$ ⁴⁷.

In order to favor integration of $\epsilon\text{-Fe}_2\text{O}_3$ in devices and to take advantage of the magnetic order characterizing the material, the most suitable form would be epitaxial thin films. Recently, growth of epitaxially stabilized epsilon ferrite thin films by pulsed laser deposition (PLD) has been reported by Gich *et al.*, where the phase stabilization was accomplished by taking advantage of the epitaxial strain induced by the single crystal strontium titanate (SrTiO_3) substrate⁴⁸. Growth on substrates other than SrTiO_3 , namely alumina and yttrium stabilized zirconia (YSZ), has also been recently achieved, although not directly on YSZ, but with a 50 nm thick buffer layer of GaFeO_3 (GFO) on top of YSZ used to promote the growth of epsilon ferrite⁴⁹. Besides allowing better integration, epsilon ferrite in the form of thin films, given its polar structure (belonging to space group $Pna2_1$), also elicit the hope to be able to exploit its natural polarization. Although the ferroelectric behavior of single epsilon ferrite films has never been experimentally demonstrated, the presence of reversible spontaneous polarization was recently reported in layered structure of $\text{SrTiO}_3\text{:Nb/AlFeO}_3\text{/SrRuO}_3\text{/}\epsilon\text{-Fe}_2\text{O}_3$ ⁵⁰.

INTRODUCTION

In such a context, my research focuses on expanding the current knowledge on the growth of epitaxial thin films of epsilon ferrite on different single crystal substrates by pulsed laser deposition and on the detailed characterization of their structural and functional properties. Initially, the idea to investigate $\epsilon\text{-Fe}_2\text{O}_3$ was prompted by a publication by Ohkoshi *et al.* who showed that it was possible to induce the precession of the magnetization in epsilon ferrite nanoparticles utilizing an intense electromagnetic pulse of frequency equal to its FMR frequency⁵¹. Along with more fundamental research on the underlying physics of ultrafast demagnetization induced by femtosecond laser pulses⁵²⁻⁵⁸, epsilon-ferrite generated great interest at INRS-EMT given how, besides the expertise of our group Ferroic Lab in the growth and characterization of epitaxial thin film of multifunctional complex oxides a state-of-the-art laboratory for the generation and study of Terahertz radiation was in operation within the Advanced Laser Light Source (ALLS)⁵⁹. $\epsilon\text{-Fe}_2\text{O}_3$, due its natural FMR frequency in the low THz range^{II}, was indeed an ideally suited material for such an investigation.

The ultimate goal of the project was to achieve ultrafast switching of the magnetization by utilizing high intensity asymmetric THz pulses. Such feat would greatly increase the speed of magnetization reversal, which is a key feature in magnetic data storage, not to mention it would also be a switching process triggered remotely without the need of electrodes. In the state of the art recording technology, the magnetization reversal, i.e., the complete inversion of the direction of the magnetization vector \mathbf{M} , occurs on a time scale on the order of the nanosecond, which is much larger than the characteristic precession time of the magnetization - on the order of picoseconds⁶⁰. Having epitaxial thin films rather than nanoparticles, allows to have ordered structure of macroscopic dimensions, and is also very favorable for their eventual integration into consumer electronic devices. The first challenge encountered was to achieve the growth of epitaxial thin films by PLD and to understand the mechanisms behind the stabilization of the $\epsilon\text{-Fe}_2\text{O}_3$ metastable phase. Then, the functional properties of the epsilon ferrite films were characterized to ensure they were showing the same features as the nanoparticles. In early stages of the research we were mainly interested in the high coercive field which is an effect of the high magnetic anisotropy, which in turn is also responsible for the FMR frequency in the low THz range.

The following step was to investigate the dielectric properties of our films, given their non-centrosymmetric crystal structure, in the hope to reveal a switchable polarization, therefore obtaining a novel multiferroic material with a very simple chemical composition and operating at room temperature. Finally, we looked

^{II} The THz range traditionally referring to frequencies between 0.1 and 100 THz.

INTRODUCTION

into the effect of metal substitution in epsilon ferrite, focusing on the effects of aluminum, in order to replicate the studies on metal inclusion in epsilon ferrite nanoparticles.

This thesis will therefore be organized in the following way:

Part I comprises the theoretical background and the description of the experimental techniques utilized in the course of my doctorate. It is divided into two chapters:

Chapter 1: Theoretical background. Chapter 1 will introduce the physics behind the development of my research. First, I will give more details about epsilon ferrite; then I will discuss about the magnetic order, about the ferroelectric order, and conclude introducing the concept of multiferroicity.

Chapter 2: Experimental. This chapter will be divided in two parts: The first will discuss the deposition technique utilized in this work, pulsed laser deposition, both from the theoretical and practical point of view. The second part will review the main characterization methods that have been used through the course of the whole investigation.

Part II will discuss the different experimental results obtained in my research. It will be divided into five chapters:

Chapter 3: Epitaxial stabilization of epsilon ferrite thin films. First, the features of the growth of epitaxial thin films of epsilon ferrite by pulsed laser deposition will be presented, with focus given to the epitaxial match with the various substrates and the different growth mode they promote, and to the PLD growth conditions and their effect on the structure of the film. A detailed analysis of the structural results measured by X-ray diffractometry and scanning transmission electron microscopy will follow, detailing the effect on the different substrates on the structural properties of epsilon ferrite thin films.

Chapter 4: Functional characterization of epsilon ferrite thin films. This chapter will present the characterization of the main functional properties of epitaxial thin films of $\epsilon\text{-Fe}_2\text{O}_3$, namely their magnetic and dielectric properties. Extensive analysis will once more focus on the effect of the different substrates, this time on the magnetic properties.

Chapter 5: Growth and characterization of aluminum-substituted thin films. This section of the thesis will cover the growth of aluminum-substituted epitaxial thin film of epsilon ferrite ($\epsilon\text{-Al}_x\text{Fe}_{2-x}\text{O}_3$), highlighting how, by changing the aluminum concentration in the films, it is possible to control their coercive field and remanent magnetization.

Chapter 6: Deposition of epsilon ferrite on miscut substrates. Lastly, the study of the effect of growth on substrates with high degree of miscut in order to avoid the formation of twins will be presented, focusing

INTRODUCTION

on the effect of the miscut substrates on reducing the number of in-plane growth orientation, resulting in a material characterized by a quasi-uniaxial magnetic anisotropy.

Chapter 7: General conclusions and perspectives. This chapter will serve as general conclusion of the thesis along with the future work needed towards improvement and integration of epsilon ferrite films as well as perspectives on the potential applications of $\epsilon\text{-Fe}_2\text{O}_3$ thin films.

INTRODUCTION

PART I

CHAPTER 1 THEORETICAL BACKGROUND

This first chapter will serve as an overview of the theoretical background of the thesis. Firstly, I will review the main properties of epsilon ferrite, starting from its crystal structure. Then, I will move to a review of the exchange interaction in magnetic materials, the different magnetic orders, and then introducing the concepts of magnetocrystalline anisotropy and its effect on magnetic materials. Lastly, I will conclude with a brief discussion over ferroelectricity and multiferroicity.

1.1 Structure and properties of epsilon ferrite.

Epsilon ferrite is characterized by an orthorhombic crystal structure which belongs to the non-centrosymmetric space group $Pna2_1$ (see Figure 5). Its structure is composed by 16 iron and 24 oxygen ions; the Fe atoms are divided into four different sites. Three of them, namely “A”, “B”, and “C” are

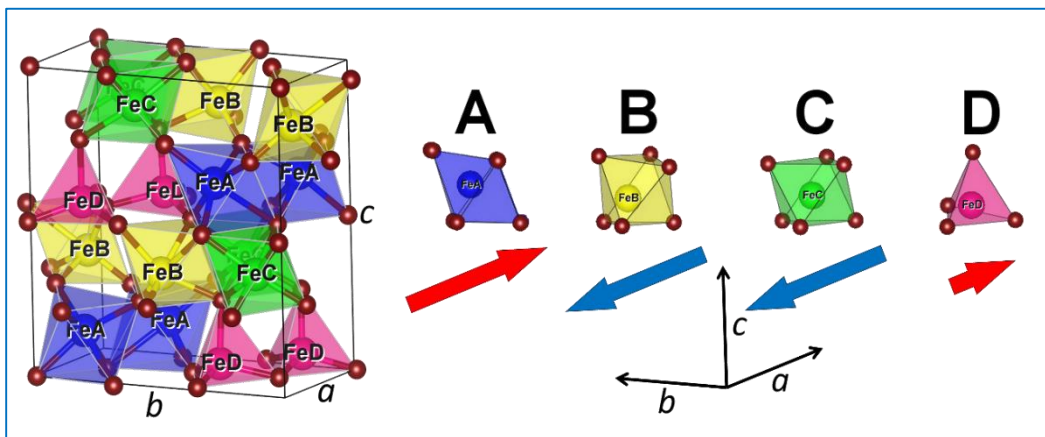


Figure 5: ϵ - Fe_2O_3 unit cell and configuration of the magnetic moments on the four different

Chapter 1

centering regular or distorted oxygen octahedra, while one, “D”, is centering oxygen tetrahedra. When grown as nanoparticles the lattice parameters of epsilon ferrite are $a = 5.095 \text{ \AA}$, $b = 8.789 \text{ \AA}$, and $c = 9.437 \text{ \AA}$.

Epsilon ferrite is a collinear ferrimagnet, with a Curie temperature $T_C \approx 490 \text{ K}$ ⁴³, composed by magnetic moment on the iron ions aligned anti-parallel two by two; the net magnetization is due to smaller magnetic moment on the “D” site (Figure 5)⁴⁰.

Although being characterized by lower magnetization compared to $\gamma\text{-Fe}_2\text{O}_3$ and Fe_3O_4 , $\epsilon\text{-Fe}_2\text{O}_3$ exhibits high magnetocrystalline anisotropy which results in a gigantic room temperature coercive field, as high as $H_C \approx 20 \text{ kOe}$ in nanoparticles^{32,34,43,61,62}. This characteristic makes it a promising candidate for non-volatile memories.

X-ray magnetic circular dichroism showed that the large coercivity of $\epsilon\text{-Fe}_2\text{O}_3$ nanoparticles originates from the presence of a large magnetocrystalline anisotropy⁶³. This large magnetocrystalline anisotropy, induced by the lattice distortions of the Fe^{3+} coordination polyhedra, leads to a strong hybridization between the Fe_{3d} and the O_{2p} orbitals, resulting in a non-zero orbital magnetic moment \mathbf{L} , which, through spin-orbit coupling, defines a magnetic-easy axis. First principle calculations supported the experimental finding, predicting that the magnetic easy axis lies along the crystal \mathbf{a} axis direction⁶⁴. The magnetic anisotropy results also in a natural ferromagnetic resonance (FMR) frequency in the low THz range ($\sim 0.1\text{-}100 \text{ THz}$) at room temperature⁴³, which is of particular interest given its potential use in short-range wireless communications (e.g. 60GHz Wi-Fi)⁴² and ultrafast non-volatile memories⁶⁵.

Being characterized by a non-centrosymmetric crystal structure, belonging to a polar space group, $\epsilon\text{-Fe}_2\text{O}_3$ is also characterized by a spontaneous polarization, which, if proved switchable at room temperature, will make of epsilon ferrite one of the few single phase room temperature multiferroic materials.

1.2 Brief discussion on magnetism.

1.2.1 Magnetic interactions and classes of magnetic materials.

The foundations of magnetic interactions lie in the study of the orbital and spin motions of electrons and their interaction with one another. The main distinction between the different materials is the presence or absence of interaction between the magnetic moments on the different atoms. Most of the materials do not show such interactions and will react weakly to applied fields, whereas the materials which are identified as magnetic, hold a very strong interaction between the moments. In order to introduce the different types of magnetic order, the simplest way is to describe the response of a material when subjected to an applied magnetic field. The first type of order discussed are the ones where the interactions between the magnetic moments on different atoms are ignored: diamagnetism and paramagnetism. The description that will follow will therefore describe the behavior of isolated atoms when exposed to a magnetic field. The complete description of these two phenomena requires treating the application of a magnetic field to an atom as a perturbation of its Hamiltonian \hat{H}_0 (see the books cited in reference for the complete derivation)^{66,67}. However, in case of linear materials such as diamagnetic and paramagnetic materials, the relationship between an applied field \mathbf{H} and the resulting magnetic moment per unit of volume (or magnetization \mathbf{M}) generated on a material, is expressed in term of the dimensionless quantity χ , called magnetic susceptibility, according to the law:

$$\mathbf{M} = \chi \mathbf{H}. \quad (1.1)$$

Diamagnetic materials (all the non-magnetic materials are at least diamagnetic if not paramagnetic, although such effect is often very weak), are characterized by a negative susceptibility χ , and will respond to an external field by generating an opposing magnetization. The diamagnetic interaction arises from the precession of the electron orbits. A diamagnetic material has its electrons all paired so that its atoms possesses only a net orbital moment (\mathbf{L}) and no spin moment (\mathbf{S}) in an applied field. In such case, the moments will have antiparallel alignment with respect to the applied field. The classical theory of diamagnetism was first suggested in 1905 by Paul Langevin and it is based on the Larmor precession of electrons.

Paramagnetism instead is described by a positive susceptibility χ , so that the effect of an external field would be to induce a magnetization parallel to the applied field. Unlike the case of diamagnetism, paramagnetic materials are characterized by atoms with unpaired electrons, thus having a net magnetic

moment. However, due to the non-interaction between the atoms, these moments are randomly organized. Applying an external field will have the effect of aligning all the moments, with higher alignment for more intense fields. In competition with the effect of the applied field, thermal energy will randomize the spins and the magnetic moments, resulting in a temperature dependency of the susceptibility, known as the Curie Law.

As previously stated, the materials which are usually identified as magnetic are characterized by a very strong interaction between the magnetic moments in neighboring ions. In order to evaluate the interaction between atoms, whose total electronic spins are \mathbf{S}_i and \mathbf{S}_j , Werner Heisenberg formulated the following Hamiltonian known as the exchange interaction:

$$H = -2J \mathbf{S}_i \cdot \mathbf{S}_j, \quad (1.2)$$

where J is the exchange constant. Exchange interactions are the fundamental entities that control long range magnetic order. Such interactions are electrostatic interactions, generated due to cost of keeping charges of the same sign close together. Exchange interaction will keep the moment on neighboring atoms aligned, while the sign of the exchange constant J will determine whether they are parallel or anti-parallel.

Different kind of exchange interactions exist. Amongst them, the most important are:

- If the electrons on two neighboring atoms interact through exchange, this is called **direct exchange**. However, such interaction is rare because it depends on the overlap of the magnetic orbitals, which is often insufficient due to their strongly localized nature;
- In many cases, a third atom will act as a mediator between two magnetic ions. In such cases, one refers to **indirect exchange** and, more specifically, to **superexchange**. Such form of interactions extends longer than the short-range exchange thanks to the mediating non-magnetic ion.

Superexchange characterizes many ionic solids, including **oxides** and fluorides. In order to simplify the description, the phenomena will be treated under the assumption that the magnetic moment arises from a single unpaired electron. Thus, in the case depicted in Figure 6 of MnO, there will be a single unpaired electron (in a d orbital), and the two electrons on the oxygen ion (on the p orbital). As shown in Figure 6, the antiferromagnetic alignment is the favorable one, since it would result in a delocalization of the electrons over the Mn-O-Mn bonds though decreasing the kinetic energy of the electron. However, superexchange can also lead to ferromagnetic, depending on the type of orbital (e_g over t_{2g} orbitals), or the angle between the metal (M) orbitals. The favorable configuration is described by the Anderson formulation of the so-called Goodenough-Kanamori rules.

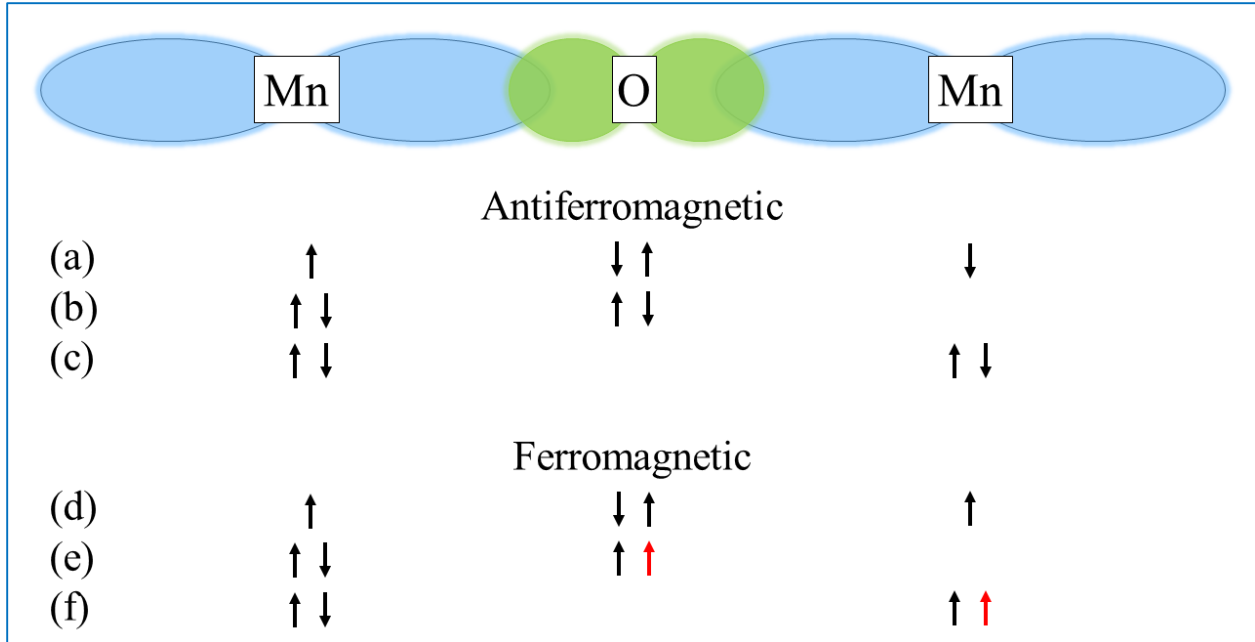


Figure 6: Antiferromagnetic order due to superexchange in magnesium oxide.

After this brief introduction of *superexchange*, the main interaction between magnetic ions in oxides, the different order that can be produced by such interaction will be reviewed. The different orders are, as shown in Figure 7:

- **Ferromagnetism:** where the magnetic moments on neighboring ions lie in parallel alignment;
- **Antiferromagnetism:** where the magnetic moments are in antiparallel alignment. This can also be seen as two equal and alternating parallel sub-lattices with opposite magnetic alignment;
- **Ferrimagnetism:** is the case in which there is an antiparallel alignment, like in antiferromagnetism, but the two sub-lattices are not equal.

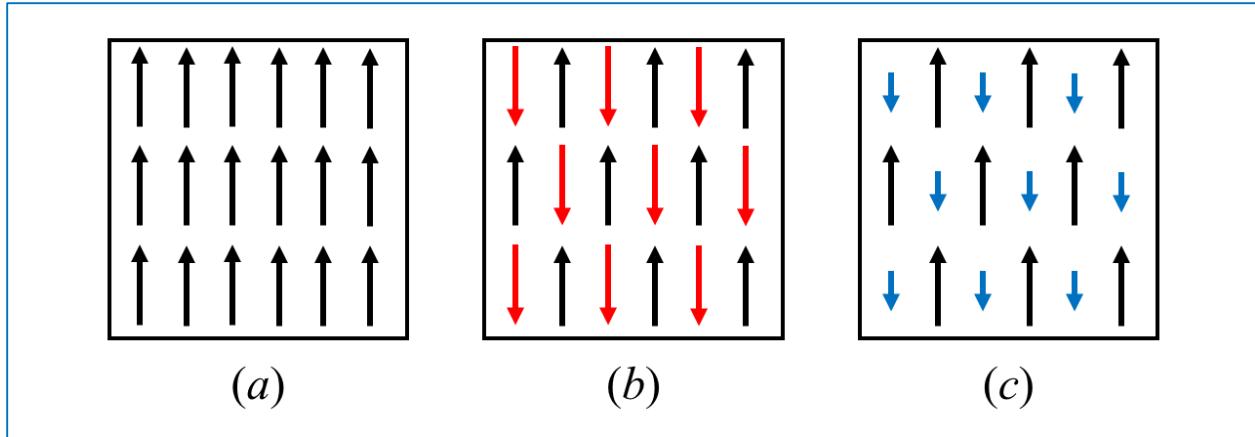


Figure 7: The different kind of magnetic orders – (a) ferromagnetic, (b) antiferromagnetic, and (c) ferrimagnetic order.

Epsilon ferrite is characterized by ferrimagnetic ordering, like was shown in Figure 5, given how the moments are antiparallel two by two, and the lower moment on the “D” sites results in a net magnetic moment. Therefore, like in a ferromagnet, the response of the magnetization \mathbf{M} of epsilon ferrite to an applied magnetic field \mathbf{H} will be described by a hysteresis loop. As it will be shown more in detail later for the specific case of $\epsilon\text{-Fe}_2\text{O}_3$, the specifics of the material will determine the shape of the hysteresis loop, and affect the principal quantities characterizing it.

As in the case of paramagnets under an applied field, thermal agitation will introduce disorder into a magnetic material, weakening the exchange interaction between the neighboring ions. The effect of increased temperature on the order in magnetic materials is described by the Weiss model of ferromagnetism, and will result in a ferromagnetic-to-paramagnetic reversible transition at a critical temperature defined as the Curie temperature T_c . For the full mathematical discussion on the effects of temperature on magnetic order in magnetic materials, and how to derive the dependence of the spontaneous magnetization as a function of the temperature, refer to “Magnetism and Magnetic Materials” by J. M. D. Coey⁶⁷.

1.2.2 The magnetic hysteresis.

As introduced by Lev Landau and Evgenii Lifschitz, a magnetic material (whether is ferro-, antiferro- or ferrimagnetic), in order to minimize its internal energy, unless it is in particular nano-sized structures, will be formed by several magnetic domains, which will be all characterized by the same order, but (rather) randomly aligned between each other. The application of a magnetic field, as shown in Figure 8, will align

the different domains, until they will be all parallel to the applied field, thus reaching the maximum magnetization \mathbf{M} achievable, which will be defined as *magnetization at saturation* (M_S) for that particular material. Switching off the applied field will leave a non-zero magnetization called the *remanent magnetization* (M_R). Finally, the value of the applied field at which there will be reversal of the magnetization \mathbf{M} is defined as the *coercive field* (H_C). These values, along with the effects of the applied field on the different domains and the on the hysteresis loop are shown in Figure 8.

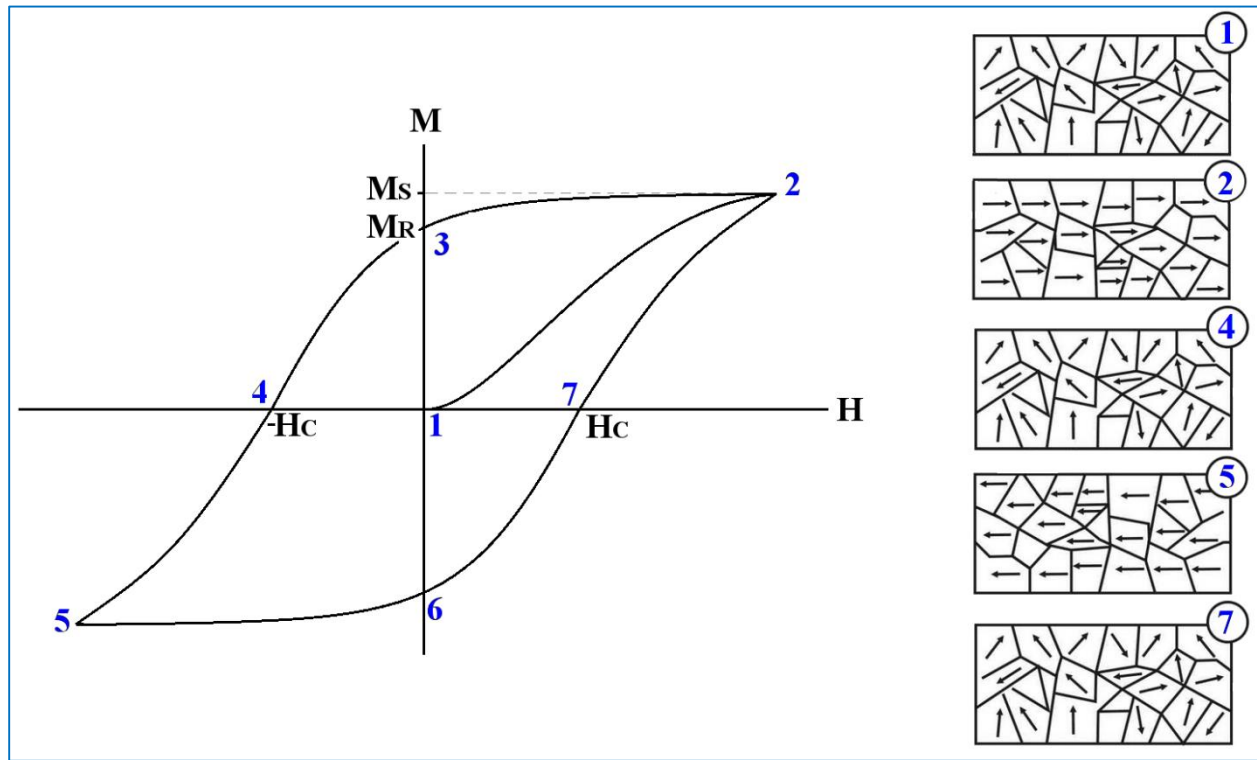


Figure 8: Typical magnetic hysteresis loop and behavior of the moments in the different domains in response to the applied field.

From the shape of the hysteresis loop it will be possible to infer some properties of the analyzed material. *Hard magnetic materials* will be characterized by a wide square loop: after being magnetized they will retain most of their magnetization, therefore $M_R \approx M_S$, and they will require important field in order to achieve magnetization reversal (meaning high values of the coercive field). On the other hand, *soft magnetic materials*, will have a narrow loop, with very small values for both M_R and H_C .

In general, magnetic materials will be characterized based on how easy it is to reverse their magnetization or on how much order they will retain once the applied field is removed. Such characteristics are ruled by magnetic anisotropy. The presence of magnetic anisotropy signifies that the magnetic material will have a

preferential axis along which to align their magnetization. High magnetic anisotropy is a prerequisite of hard magnetic materials, while near-zero anisotropy characterizes soft magnetic materials. The likeliness of the magnetization to align along a certain axis is described by the anisotropy energy density E_a :

$$E_a = K_I \sin^2 \theta, \quad (1.3)$$

where θ is the angle between \mathbf{M} and the anisotropy axis, while K_I represent the anisotropy constant, which depends on the material and its morphologies. In the case of epitaxial thin films of epsilon ferrite, there are two main sources of anisotropy:

- *Shape anisotropy*, which, as the name suggests, is related to the shape of the magnet and the necessity of the magnetic field to minimize its divergence, thus aligning itself along the “longest” dimension. In case of a magnet of arbitrary shape, the shape anisotropy will be represented by a demagnetizing tensor N . However, special cases exist for special geometries. For example, in a thin film, shape anisotropy will make the magnetic field align in-plane.
- *Magnetocrystalline anisotropy*, which is an intrinsic property of a material, and it is related to the symmetry of the crystal. The origin of magnetocrystalline anisotropy lies in spin-orbit coupling and the crystal-field interaction.

As explained in the previous section and in detail in reference ⁶⁴, the large magnetocrystalline anisotropy in epsilon ferrite is induced by the lattice distortions of the iron polyhedra, which leads to a strong hybridization between the Fe_{3d} and the O_{2p} orbitals, resulting in a charge transfer from the oxygen anion to the iron cation. The transferred charges on the Fe_{3d} orbitals generate a non-zero orbital magnetic moment \mathbf{L} which, through spin-orbit coupling, defines the magnetic-easy axis. Such strong anisotropy will result in a “hard” magnetic nature, meaning a square hysteresis loop with high coercive field, and, most interestingly, in a natural ferromagnetic resonance (FMR) frequency in the low THz range (~0.1-100 THz) at room temperature⁴³. Such anisotropy is often defined as “single-ion anisotropy”, where a single-ion contribution due to the electrostatic interaction of the orbitals, in which the magnetic electrons reside, with the crystal-field. Such type of anisotropy differs from the “two-ion anisotropy” where is given by dipole-dipole interaction of neighboring ions.

1.2.3 Ferromagnetic Resonance Frequency.

The high magnetocrystalline anisotropy characterizing epsilon ferrite gives effect to a natural ferromagnetic resonance frequency at circa 190 GHz at room temperature⁴³.

Any magnetic material, when inserted in a uniform field \mathbf{B}_0 , will absorb electromagnetic radiation at a frequency $\nu_0 = \omega_0 / 2\pi$. A simple interpretation of the FMR frequency can be given by thinking about a single ion with a magnetic moment \mathbf{m} into a magnetic field. The moment \mathbf{m} will be linked to its electronic angular momentum $\hbar\mathbf{S}$ through the gyromagnetic ratio γ :

$$\mathbf{m} = \gamma\hbar\mathbf{S}. \quad (1.4)$$

Application of a magnetic field \mathbf{B}_0 will affect the magnetic moment \mathbf{m} through Zeeman interaction, which is represented by the following Hamiltonian, if the field is applied along a given direction “x”:

$$H_Z = -\mathbf{m} \cdot \mathbf{B}_0 = -\gamma\hbar B_0 S_x. \quad (1.5)$$

Solution of this equations will be spaced by integers given the quantization of the electronic angular momentum, with the spacing between two level be equal to:

$$\Delta E = \gamma\hbar B_0. \quad (1.6)$$

Therefore, magnetic transition can be expected for radiation of frequency ω_0 , where the transition $\Delta E = \hbar\omega_0$, hence:

$$\omega_0 = \gamma B_0. \quad (1.7)$$

Note that the quantity just found is nothing but the classical Larmor precession frequency.

Chapter 1

As for the case of epsilon ferrite, the magnetocrystalline anisotropy results in the presence of an in-built field, called the anisotropy field H_a , which will act as the external field, thus the natural (meaning without any applied field) ferromagnetic resonance frequency. Given how the magnetic easy axis lie in the plane of the thin film, the ferromagnetic resonance frequency, according to the Kittel formula, will be:

$$\omega_0 = \gamma \mu_0 H_a^{1/2}. \quad (1.8)$$

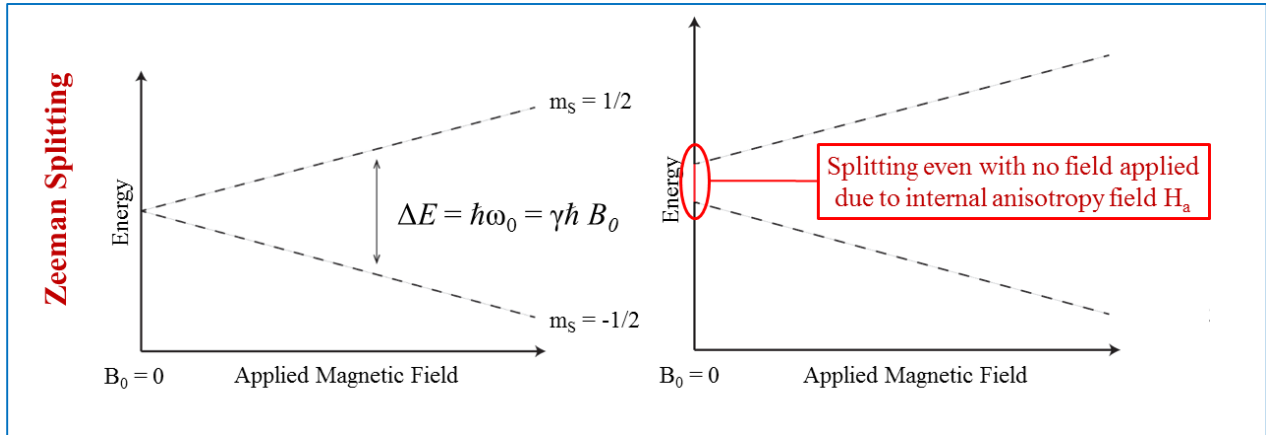


Figure 9: Fine splitting giving source to the ferromagnetic resonance frequency in materials: on the right, the case of a material with high magnetocrystalline anisotropy is depicted.

1.3 Ferroelectricity and Multiferroicity.

As mentioned in the first section of this chapter, besides its unique magnetic properties, epsilon ferrite is also characterized by a polar crystal structure, hence by a spontaneous polarization, which, if proven switchable at room temperature, would make epsilon ferrite one of the few room temperature multiferroic single phase materials.

As was done for ferromagnetism, in the following sections, I will first briefly discuss the concept of ferroelectricity from a phenomenological point of view, then introduce multiferroicity and the fascinating application that can be envisioned while both magnetic and ferroelectric order coexist.

1.3.1 Phenomenological description of ferroelectricity.

Ferroelectricity is a property of a class of materials characterized by a spontaneous electric polarization that can be reversed by applying an electric field. Ferroelectricity was first shown in 1920 in Rochelle salt⁶⁸, and it was named for its analogy to ferromagnetism (which was already known at the time). Thus, the prefix “ferro”, from the Latin word “ferrum” for iron, was used to describe the phenomenon, despite the fact that most ferroelectric materials do not contain iron. However, there are many functional characteristics shared by ferroelectric and ferromagnetic materials: they both are characterized by a hysteretic dependence of the order parameter (namely polarization \mathbf{P} and magnetization \mathbf{M}) to an applied driving field (electric \mathbf{E} or magnetic \mathbf{H}), and they both show a degradation of the order with increasing temperature, up to a critical temperature defined as Curie temperature, where there is a transition from ferroelectric (or ferromagnetic) to paraelectric (or paramagnetic).

However, while in the case of ferromagnetism the Curie temperature indicates the threshold at which the thermal agitation overcomes the exchange interaction, for ferroelectric materials, the Curie temperature corresponds to the phase transition from a non-centrosymmetric structure at low temperature to a centrosymmetric one at high temperature. For example, if we take the case of the widely studied ferroelectric perovskite barium titanate (BaTiO_3), it is characterized by a centrosymmetric cubic structure for $T > T_C$, and a non-centrosymmetric tetragonal structure for $T < T_C$ (see Figure 10) (it has to be noted, for completion, how barium titanate is characterized by two other phase transitions, which however will not be discussed here).

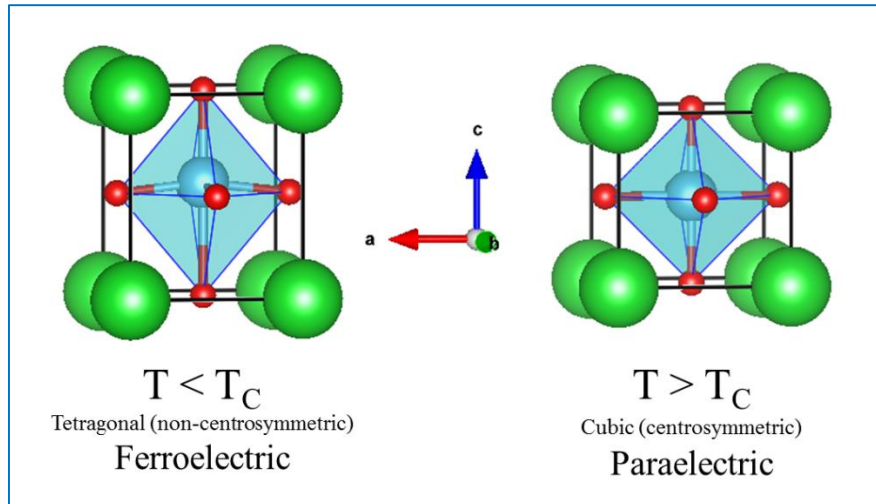


Figure 10: Ferroelectric and paraelectric structure for barium titanate beyond and above the Curie temperature.

In the case depicted in figure, the displacement of the titanium ion generates an electric dipole moment, which, by applying an electric field, can be switched between the two equilibrium states as shown in Figure 11. The energy diagram will be represented by a double-well curve where the two minima corresponds to the two different position of the titanium atoms (and the two states of polarization).

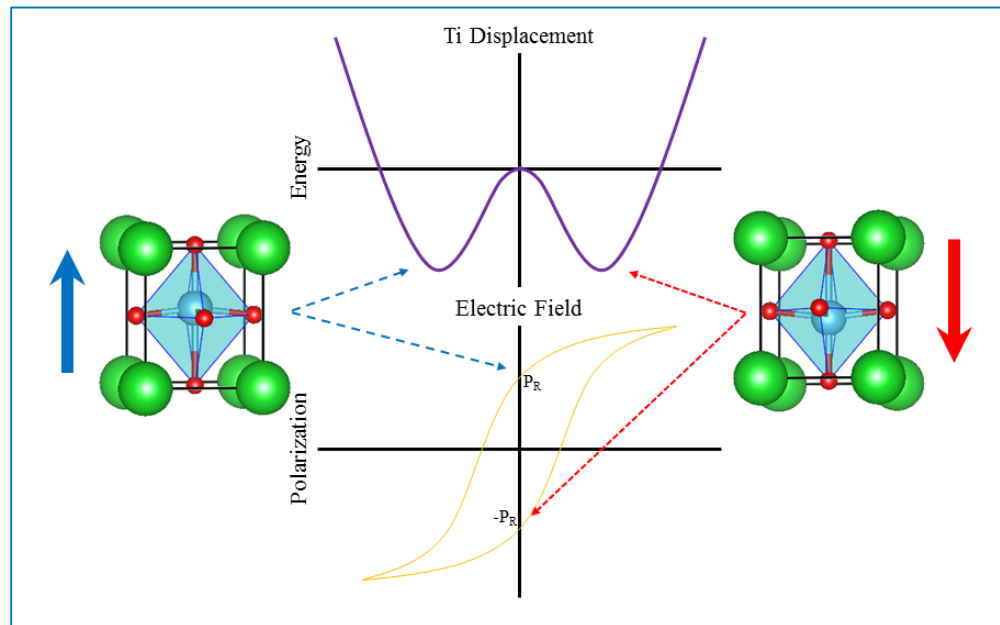


Figure 11: Double well potential representing the movement of the Ti ion during the switch of the polarization in $BaTiO_3$.

The example of barium titanate was utilized to highlight how, in a ferroelectric material, the electric dipole moments are coupled to the structure of the material so that any change of the structure will reflect on the polarization.

The absence of inversion symmetry is a necessary condition for a material to be a ferroelectric. More in detail, ferroelectric materials are a subset of two other sets of dielectric materials, piezoelectric and pyroelectric (see Figure 12). Piezoelectric materials are

characterized by a non-centrosymmetric structure, which however does not hold a spontaneous polarization. Piezoelectric material, however, will produce a voltage when subjected to mechanical stress. Pyroelectric materials instead, are indeed characterized by a spontaneous polarization, but such polarization is non-reversible. However, it will be possible to affect the magnitude of the polarization by applying a temperature gradient. Referring to crystal structures, 230 different space groups exist, divided in 32 crystalline classes. Of these 32 classes, 21 are non-centrosymmetric, with 20 being piezoelectric. Among the piezoelectric ones, 10 are characterized by a spontaneous electric polarization. The materials where such polarization results switchable, are ferroelectric.

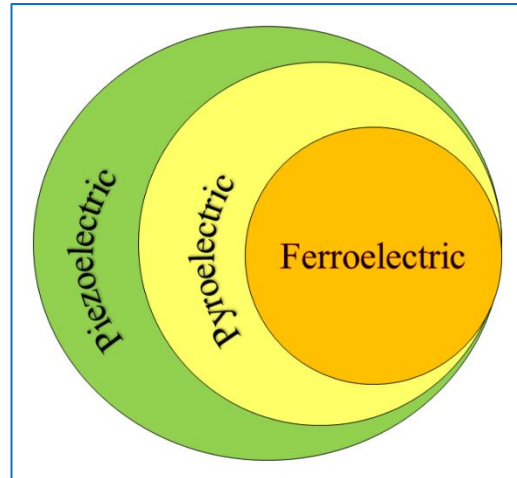


Figure 12: The different sets and subsets of the ferro-, pyro-, and piezoelectric materials.

In such context, epsilon ferrite is characterized by an orthorhombic crystal structure which belongs to the non-centrosymmetric polar space group $Pna2_1$ (see Figure 5), therefore, although such features has not been reported yet for single-phase epsilon ferrite films or nanoparticles, it should exhibit at least pyroelectricity, making it a new member of the family of magneto-electric oxides if not a new room temperature multiferroic.

1.3.2 Multiferroicity.

Ferromagnets and ferroelectrics, along with ferroelastic materials (materials characterized by a hysteretic dependence of their deformation ϵ to an applied stress σ) compose the family of the so-called ferroic materials. Such class of materials, as previously, adopts spontaneous and switchable alignment, and is

characterized by (i) a critical Temperature T_c , at which a phase transition occurs changing the directional symmetry, and (ii) by the existence of domains, which can nucleate, grow, and be switched with an external driving field. In case where one material exhibits more than one primary ferroic order parameter simultaneously, with particular interest towards materials exhibiting both ferroelectricity and ferromagnetism, such material is defined as **multiferroic** (refer to Figure 13 for the different ferroic materials and their possible coupling). Recently there has been an increased interest towards multiferroics given the perspective of a novel generation of devices exploiting both the characteristics of ferromagnetic and ferroelectric materials^{69,70}. To be feasible for technological applications, however, one needs materials characterized by significant magnetization and electric polarization above room temperature (RT) as well as strong coupling between the two orders (**magnetoelectric** effect, represented by the green arrows in Figure 13). This coupling would, for example, might permit to control the magnetization by applying an electric field, removing the need of writing magnetic heads in non-volatile memories. Currently, such properties are rarely found in single phase materials and often such materials exhibit substantial moment for only one of the two orders (see BiFeO_3 , $\text{Bi}_2\text{FeCrO}_6$, Cr_2O_3). The possibility of adding a new, cheap, and relatively non-complex material such as epsilon ferrite to the (rather short) list is a thrilling possibility worth investigating.

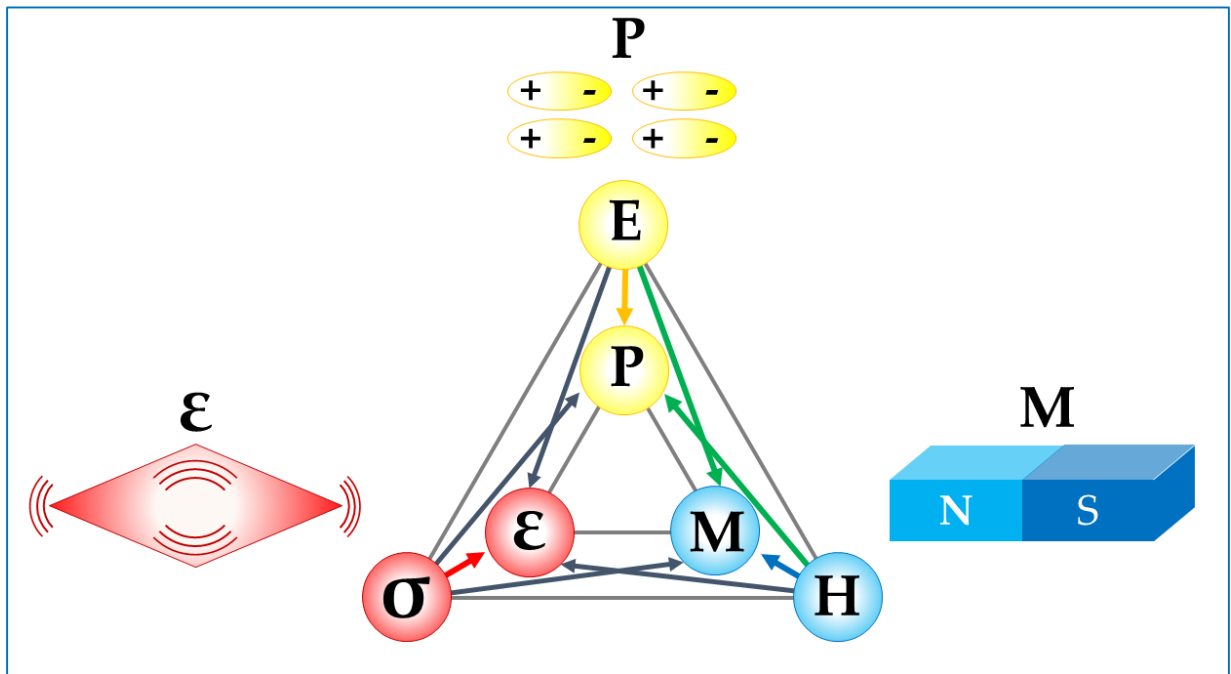


Figure 13: The three class of ferroic materials, separated by their order parameters M , P and ϵ , and the different coupling possible. In the figure, the two magnetoelectric couplings – *i.e.* the control of polarization by a magnetic field and of magnetization by an electric field – are shown by the green arrows.

Chapter 2 EXPERIMENTAL TECHNIQUES

This chapter reviews the synthesis and characterization experimental techniques that have been used in the course of the work for my thesis. Pulsed laser deposition (PLD) was the technique chosen for the growth of epitaxial thin films of ϵ -Fe₂O₃. The choice of PLD is due to its well-known versatility and stoichiometric transfer from the target to the films due to its non-equilibrium nature, as well as the many parameters that can be controlled during the growth and the possibility of growing on many different substrates, all keys to achieve epitaxial stabilization of my films. Structural characterization of the films was mostly performed by x-ray diffractometry (XRD). This non-destructive technique allows to study the growth orientation of the thin films with respect to the substrate and to evaluate the orientation and quality of the grown thin film, which are critical features to study film grown epitaxially, where the structure of the film is highly influenced by the one of the substrate. Local analysis of the microstructure was performed by scanning transmission electron microscopy (STEM), in the group of Professor Gianluigi Botton, (*Department of Material Science and Engineering, McMaster University*). The functional magnetic and ferroelectric properties of the films were characterized macroscopically by vibrating sample magnetometer (VSM), at the laboratory directed by Prof. David Ménard (*Engineering Physics Department of Polytechnique Montréal*) and by a TF analyzer ferroelectric (FE) module, and microscopically by magnetic force microscopy (MFM) and piezoresponse force microscopy (PFM), respectively. The two latter techniques, are modifications of an atomic force microscope (AFM) where a magnetic and a conductive tips are used during the scan. Finally, measurements of the ferromagnetic resonance (FMR) frequencies characterizing the epsilon ferrite phase were conducted directly by ferromagnetic resonance spectroscopy (*Engineering Physics Department of Polytechnique Montréal*) and indirectly via time domain spectroscopy in the group of Prof. Tsuneyuki Ozaki (*INRS-EMT*).

2.1 Synthesis of epitaxial thin films of epsilon ferrite by pulsed laser deposition.

2.1.1 Fundamentals on pulsed laser deposition.

As explained in the introduction, epsilon ferrite is a metastable intermediate phase between hematite (α - Fe_2O_3) and maghemite (γ - Fe_2O_3). Until very recently, stabilization was achieved mostly by growing it by sol-gel as nanoparticles inside a silica matrix, with size confinement acting as the stabilizing factor⁴⁰. However, in order to improve the integrability of epsilon ferrite into devices, synthesis of epsilon ferrite in a more suitable form, like thin films, is required. An alternative route towards stabilization of the epsilon phase was achieved by growing it as supported nanowires on silicon substrates by Chemical Vapor Deposition (CVD). These samples proved to have lower magnetic properties compared to their nanoparticles counterparts, but to be very efficient catalysts for hydrogen generation⁴⁷. To fully take advantage of ϵ - Fe_2O_3 magnetic, and if present, ferroelectric properties, epitaxial thin film are the preferred form of synthesis. Recent reports also showed that it is possible to achieve stabilization by growing ϵ - Fe_2O_3 as thin films via Pulsed Laser Deposition (PLD). The authors of the work reported the possibility of the film to break into different growth domains as the major reason behind stabilization⁴⁸. Such effect is caused by the higher symmetry of the substrate used (strontium titanate) compared to that of epsilon ferrite, and reduces the high surface energy of the (100) surfaces of epsilon ferrite⁴⁸. Moreover, stabilization might also be due to both interface interactions between the surface of the single crystal substrate and the film, and the size confinement induced by epitaxial strain. Both the role of the surface energy of the substrates and of epitaxy will be further discussed in the next chapters.

The history of pulsed laser deposition started, when Smith and Turner⁷¹ showed the possibility of depositing films from materials ablated using a ruby laser. However, strong attention to PLD was attracted in the late 1980s when it was demonstrated that this technique is suitable for fast and reproducible in situ epitaxial high-temperature deposition of superconducting films⁷². The main challenges for growth of high-temperature superconducting oxide thin films were obvious: the compound required that the complex stoichiometry of the target would have been preserved while an oxidizing atmosphere was needed in order to avoid oxygen deficiency. PLD proved to be a technique remarkably competitive in the complex oxide thin-film research as compared to other growth techniques: it was mainly because of the possibility to achieve stoichiometric transfer between the target and the substrate, to have reacting and non-reacting gas atmospheres inside the deposition chamber, and the overall simplicity in the initial setup that promoted it as the technique utilized in the investigation of different oxide compounds. PLD is a so called

physical vapor deposition. In PLD a pulsed laser is focused onto a material: if the energy density of the laser is high enough, part of the material is “vaporized” from the target in a plasma plume (see Figure 14) and it can be deposited as a thin film.

Ablation is carried out under vacuum conditions or reduced ambient atmosphere, since the ablated material cannot reach the substrate under atmospheric pressure. In the case of multicomponent inorganic materials, ablation is usually achieved by using an ultraviolet (UV) laser wavelength with pulse duration of the order of few tenths of nanosecond that is focused on the target and strongly absorbed by a small volume of it. In a typical PLD setup, the pulsed laser beam is focused on the target in order to form a 45° angle with the target surface, so that the plasma arising perpendicularly from it would hit the substrate holder placed exactly in front

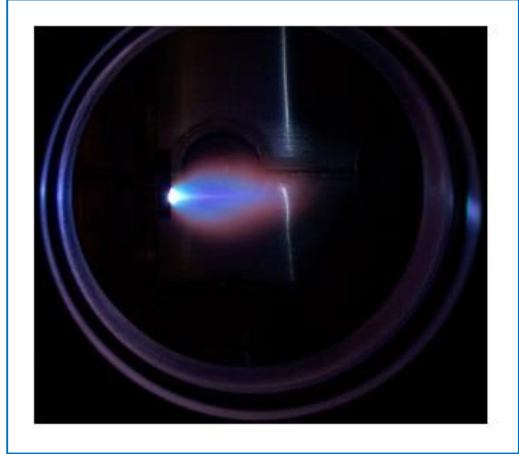


Figure 14: Typical plasma plume in PLD.

of the target. In many setups both the target and the sample are mounted on rotating elements in order to grant a uniform ablation of the ceramic material and a high homogeneity of the deposited film. Moreover, the substrate is either directly mount on a resistive heating plate or its holder is in contact with such heater which temperature can be tuned by a feedback controller through a thermocouple, on a range usually going from room temperature to temperatures of the order of 1000°C .

Ablation is carried out either in vacuum or in a reduce ambient atmosphere: the desired pressure in the chamber is obtained by using a pumping system, which is usually composed by a turbo-molecular pump backed by a mechanical-roughing pump, and tuning a flow of gases (which is often oxygen, but also might be nitrogen, helium or argon) into the chamber.

In spite of the simplicity of the general idea and its realization, processes occurring during ablation and deposition are quite complex.

The deposition process can be separated into several stages:

- Ablation;
- Plasma plume expansion;
- Deposition onto a substrate;
- Nucleation and formation of the film structure.

Chapter 2

The ablation process depends strongly on the properties of the target material and surface quality as well as on characteristic of laser radiation. The laser radiation is absorbed by electronic subsystems and then the energy is transferred to the lattice. In case of oxides, which are mostly natural insulators, free electrons first need to be produced. It occurs as a result of one or several mechanisms: linear absorption, multi-photon absorption, impact avalanche ionization. Depending on the time scale, either the dissociation of material can take place, when a critical free electron density is exceeded through laser-induced breakdown, or energy is transferred from electrons to lattice, so that thermal melting and evaporation occur. The former scheme take place when pulse duration is less than the time constant of energy transfer from electrons to the lattice ($\tau < \tau_{e-ph}$). τ_{e-ph} is typically in the picoseconds range, therefore laser-induced breakdown will occur for femtoseconds and picoseconds pulses. The latter case instead occurs for longer pulses ($\tau > \tau_{e-ph}$), including the nanosecond radiation used in many setups, like the IPEX used at INRS. Thus, gaseous or, more often, partly ionized material (a plasma) is formed and expands from the target. The “evaporation” is very fast, plasma is not thermalized and expansion has ultrasonic character. This plasma can also absorb some part of laser radiation and thus further influence course of the ablation process.

The plume is usually very strongly directed, as can be seen in see Figure 14, which leads to difficult challenges for large area coatings. Individual species in the plasma plume have energies up to 100 eV: this feature of PLD is often utilized to produce crystalline films even at relatively low substrate temperatures. Ambient gas plays a crucial role in the plume expansion process. It can be used to reduce the velocities of plasma species and partly thermalize the plume. Reactive atmosphere can be used to prevent the deficiency of some volatile component: the most common reactive gas used in PLD is oxygen, which helps preventing the formation of oxygen vacancies during the growth of complex oxide films. The most interesting aspect of PLD, that distinguish it from other deposition techniques like sputtering or chemical vapor deposition, is that the particle density in the plasma is high enough to enable chemical reactions between the plasma and the reactive atmosphere, in particular the oxidation of the deposited particles themselves during their course towards the substrate.

In the case of nanosecond laser pulses, not completely evaporated liquid droplets can be desorbed from the target. Loosely attached solid particles can also be dislodged due to stress produced by ablation. These droplets or macro particles deposited on substrate (termed particulates) are one of the major issues of the PLD technique, since they degrade the quality of the fabricated films.

When plume species reach the surface of the substrate, a number of processes take place: depending on their energy, they are adsorbed at the surface or are implanted into the volume of material. Subsequently diffusion and recrystallization processes take place, which are usually stimulated by heating of the substrate. Having particles with too high energies can result in destruction of the already formed film and even

desorption of film material. Depending on process parameters and interaction between substrate and arriving plume species, film formation can occur in different regimes. Generally, due to the high kinetic energy, particles on the surface have enough mobility. Therefore, growth of crystalline films is relatively easy to achieve for PLD processes.

To summarize, the essential characteristics of pulsed laser deposition are:

Advantages:

- Flexibility in choice of material, background atmosphere, etc., due to the fact that the energy source (laser) is located outside of the deposition chamber;
- High energy of plume particles and high degree of ionization thereof that stimulate crystalline film growth;
- Non-equilibrium character of the plume formation, promoting a correct stoichiometry of the deposited material and even deposition of materials non-existent under thermal equilibrium conditions (this is a key feature for deposition of epsilon ferrite).

Disadvantages:

- Large area, uniform coatings are challenging to get, due to strongly directed plasma plume;
- Possibility of high particulates density in the deposited film.

In order to control the surface morphology during the growth of thin films it is necessary to understand the different mechanisms affecting the growth mode. There are two independent processes, nucleation and growth of islands, playing an important role during vapor-phase epitaxial growth. Nucleation causes the formation of surface steps while subsequent growth causes the lateral movements of these steps across the layers. Both these processes are determined by kinetics since they occur far from thermodynamic equilibrium: given how these kinetic effects affect the final quality of the surface morphology, they are extensively studied.

Although I did not have the chance to analyze in depth the growth kinetics, given the impossibility of characterizing the growth *in-situ*, I still think it is interesting to try to come up with a description of such phenomenon. Therefore, in the next section I will first analyze the different growth modes, then the kinetics during growth.

2.1.2 Growth mode at thermodynamic equilibrium.

As explained before, a key to the stabilization of epsilon ferrite and to its growth as thin film is the capability of growing it epitaxially on top of single crystal substrates. The definition of epitaxy according to Merriam Webster is “the growth on a crystalline substrate of a crystalline substance that mimics the orientation of the substrate”. The term epitaxy comes from the Greek roots *epi* (ἐπί), meaning "above", and *taxis* (τάξις), meaning "an ordered manner", which can be translated as "arranging upon". The term was introduced by Royer in 1928, who, thanks to the recent discovery of X-ray diffraction in 1912⁷³, carried out an extensive and systematic study of a wide variety of crystalline growth, examining the effect of the geometry of crystal structure on their relative orientation⁷⁴. According to the nature of the deposited film in comparison with the chosen substrate, the process is defined as homoepitaxy, if the epitaxial film is deposited on a substrate of the same composition and structure, or otherwise it is called heteroepitaxy. In my case we will be talking of heteroepitaxial growth, given how the composition and the lattice of the synthesized material, *i.e.* ϵ -Fe₂O₃, differs from the chosen substrates. Before seeing the experimental detail on the growth of epitaxial thin films of epsilon ferrite, I will give a general overview of the different possible epitaxial growth modes, starting by describing the different growth modes in crystal growth, then to refine the study to the simpler case of homoepitaxy, and finally focusing on heteroepitaxy and the effect of the mismatch in the crystal lattice between a substrate and the film grown on top. In order to study the different growth modes, a thermodynamic approach to crystal growth is followed: the idea is to describe the crystal growth close to equilibrium and to assume that local fluctuations away from it will lead to nucleation. Markov *et al.*⁷³ suggested that it is necessary to have a supersaturated gas phase in order to lead to formation of nuclei, whereas it is the activation energy which determines the formation probability. Nuclei will be formed until a critical density is reached, from that point onwards, the nuclei will grow and crystallization will be in progress.

Now, in considering the general theory of film nucleation and growth and how this can be specifically applied to pulsed laser deposition, it is convenient to separate the discussion into the three conventional modes of film nucleation and growth, as shown in Figure 15:

- Three-dimensional island growth, also known as Volmer-Weber growth mode;
- Two-dimensional full-monolayer growth, also known as layer-by-layer growth or Frank-Van der Merwe growth mode;
- Two-dimensional growth of full monolayer, followed by nucleation and growth of three-dimensional islands, also known as Stranski-Krastanov growth mode.

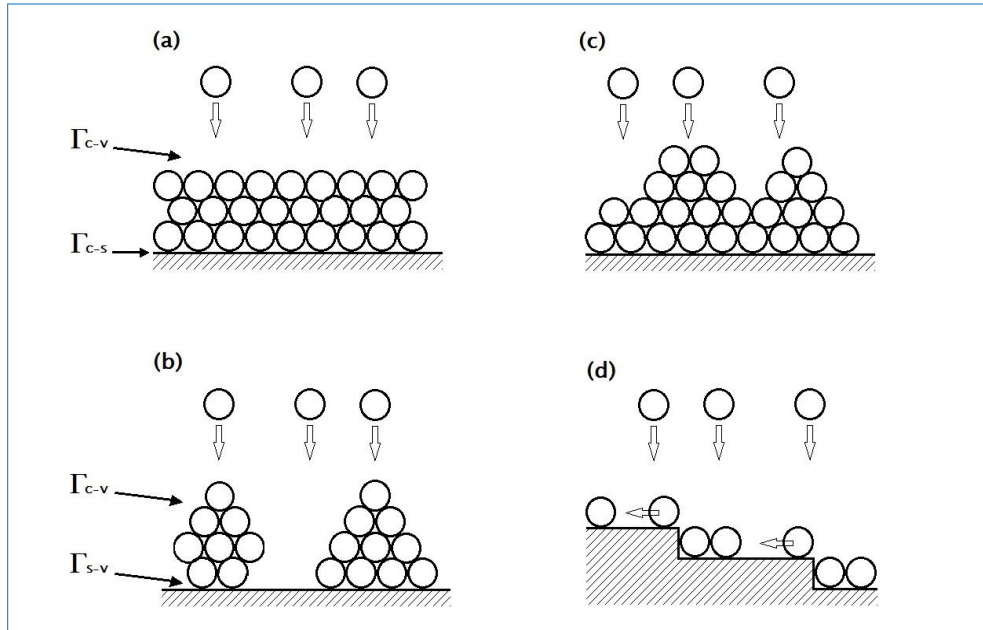


Figure 15: Film growth modes: (a) Layer by layer - Frank-Van der Merwe. (b) Island - Volmer-Weber. (c) Stranski-Krastanov. (d) Step flow.

The conventional theory of film nucleation and growth, as recently reviewed by Greene⁷⁵, states that the selection of one of these growth modes depends on (a) the thermodynamics relating the surface energies of the film and substrate materials and (b) the film-substrate interface energy.

In particular, in order to determine the film morphology, a balance between the free energies on film surface (Γ_{c-v}), substrate surface (Γ_{s-v}), and the interface between film and substrate (Γ_{c-s}) will be used. The subscripts c , s , and v refer to the Cluster, the Substrate and the Vapor, respectively (see Figure 15).

In the following section, the characteristics of the four modes will be summarized examining the possible effects of PLD deposition kinetics on these phenomena.

2.1.2.1 Volmer-Weber nucleation and growth.

The formation of film-atom clusters (also called nucleation) by the vapor deposition of film atoms on a substrate involves several processes, as illustrated in Figure 16. The film atoms arrive either on the bare substrate or on preexisting clusters at a rate which depends on the deposition parameters. These film atoms can subsequently diffuse over the substrate or over the cluster surface. They can encounter other mobile film atoms to form either mobile or stationary clusters, and could attach to preexisting film atom clusters, be re-evaporated from the substrate or cluster or could detach from a cluster and remain on the substrate surface.

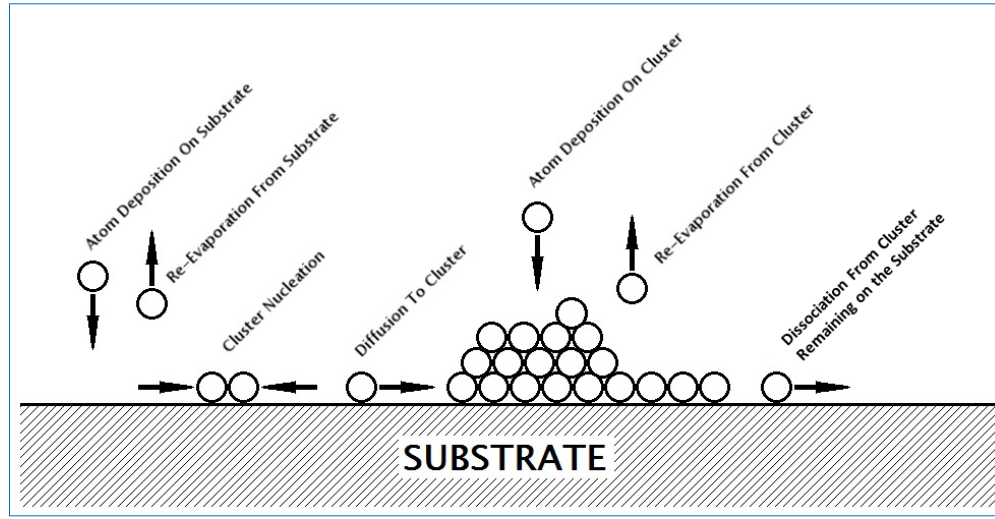


Figure 16: Schematic diagram of atomic processes in the nucleation of three dimensional clusters of deposited film atoms on a substrate surface.

For each cluster, the balance between growth and dissolution processes will be ruled by its total free energy, relative to an ensemble of individual atoms. For a cluster big enough to be treated as a continuum solid, the free energy can be written, using Greene's notation, as:

$$\Delta G = a_1 r^2 \Gamma_{C-V} + a_2 r^2 \Gamma_{C-S} - a_2 r^2 \Gamma_{S-V} + a_3 r^3 \Delta G_V. \quad (2.1)$$

In the equation, r is the cluster's radius, the Γ 's are the interfaces energies that were explained before, ΔG_V is the change in volume free energy on condensation of the cluster and the a 's are constants that depend on the shape of the nuclei.

In order to understand the dynamic of a cluster, we have to look into the derivative of its free energy change (2.1) with respect to number of atoms in the cluster: if it's positive, then the cluster is unstable and clusters of that size will shrink on average; if it's negative, then that cluster is stable and it will grow on average.

Chapter 2

Now let us focus on the volume free energy per unit volume of the cluster G_V which, to a first approximation, can be written as:

$$\Delta G_V = -\frac{k_B T}{\Omega} \ln\left(\frac{P}{P_e}\right) = -\frac{K T}{\Omega} \ln(\xi), \quad (2.2)$$

where p is the pressure of the arriving atoms, p_e is the equilibrium vapor pressure of the film atoms, k_B is Boltzmann's constant, T is the absolute temperature, Ω is the atomic volume of the film atoms and $\xi = P/p_e$ expresses the degree of supersaturation. It is important to note how this expression takes in account only the clusters formed from free condensation, without taking care of exchange of atoms between a cluster and the substrate's surface. This simplification will however not affect substantially the conclusion, that ΔG_V will be negative for a pressure of arriving atoms in excess of the equilibrium vapor pressure and that the volume free energy will become more negative for increased degree of supersaturation.

Since ΔG_V is negative, in order to have three-dimensional cluster growth, an inequality regarding the surface free-energy terms must be satisfied:

$$a_1 \Gamma_{C-V} + a_2 \Gamma_{C-S} \geq a_2 \Gamma_{S-V}. \quad (2.3)$$

If this condition is not satisfied, it will be energetically more favorable for the film to grow as a single and continuous layer on the substrate, leading to Frank-Van der Merwe (layer by layer) growth.

In case of negative volume free energy and net positive surface free energy, the total free energy for cluster formation will increase with atom addition at small nucleus' size, will reach a maximum at a critical nucleus size and will decrease with atom addition for clusters larger than the critical size. At the steady state, the net negative growth rate of clusters smaller than the critical size will be balanced by the negative gradient of clusters number density with respect to the cluster size.

In order to find the radius of a critical-size cluster, we have to set the derivative of the free energy with respect to cluster size to zero, which leads to a critical cluster radius of:

$$r^* = \frac{-2(a_1 \Gamma_{C-V} + a_2 \Gamma_{C-S} - a_2 \Gamma_{S-V})}{3a_3 \Delta G_V}. \quad (2.4)$$

Substituting this critical radius into the expression for the cluster free energy gives us the free-energy barrier for nucleation:

Chapter 2

$$\Delta G^* = \frac{4(a_1\Gamma_{C-V} + a_2\Gamma_{C-S} - a_2\Gamma_{S-V})^3}{27(a_3\Delta G_V)^2}. \quad (2.5)$$

After finding the free-energy barrier for nucleation, we can write the nucleation rate, which, in first approximation is:

$$J_C = \left(\text{Arrival rate of atoms at critical-size nucleus} \right) \times \left(\text{Concentration of critical nuclei} \right). \quad (2.6)$$

It is important to note that the arrival rate of atoms on a critical-size nucleus will be proportional to the surface of the nucleus and to the concentration of mobile atoms on the surface, as well as to the surface diffusion coefficient. The concentration of critical nuclei will indeed be proportional to:

$$\exp\left(\frac{-\Delta G^*}{k_B T}\right). \quad (2.7)$$

This means that, either a decrease in the net surface/interface free energy or an increase in the magnitude of the (negative) volume free energy will produce:

- A decrease in the critical size beyond which a cluster radius will be stable;
- A decrease in the total free-energy barrier for cluster nucleation;
- An increase in the cluster nucleation rate.

Note, however, that one has typically little control over the surface and interface terms in the nucleation equations, for a given film-substrate combination. The only practical parameters that can be easily controlled are the deposition rate and the temperature of the substrate. In particular, increasing the deposition rate or decreasing the temperature of the substrate will also increase the supersaturation of vapor atoms on the surface, leading to a more negative volume free-energy change. A decrease of the temperature of the substrates will, however, also have the effect to reduce the surface diffusion coefficient of the adsorbed vapor atoms. There is therefore a maximum nucleation rate at a certain critical temperature, determined by the competition between an increased supersaturation and a decreased surface diffusion, with a lower nucleation rate both above and below that critical temperature.

In the case of thin film deposition, though, film atoms continue to be added to the system until nucleation occurs: therefore, film formation (in the sense of the quantity of film material deposited on the substrate) does not slow down when the temperature decreases. A decreased temperature can, however, slow down the formation of the right compound or of the right crystal structure: a common example of this phenomenon is the formation of an alternate crystalline structure or the deposition of amorphous phases at low substrate's temperatures.

2.1.2.2 Frank-Van der Merwe nucleation and growth.

If the inequality (2.3) is not satisfied, it could be energetically more favorable for the film to form a complete monolayer followed by more full monolayers than to form three-dimensional clusters on the substrate.

In case of Frank-Van der Merwe growth mode, strong bonding between film and the substrate reduces Γ_{C-V} and the total surface energy, $\Gamma_{C-V} + \Gamma_{C-S}$, of the wetted substrate is lower than the surface energy of the bare substrate Γ_{S-V} giving:

$$\Gamma_{C-V} + \Gamma_{C-S} \leq \Gamma_{S-V}. \quad (2.8)$$

If a film is deposited on a clean surface of the same material, $\Gamma_{C-S} = 0$ and $\Gamma_{C-V} = \Gamma_{S-V}$, and the condition is still satisfied.

In case of heteroepitaxial deposition, full-monolayer nucleation will be promoted by strong film-substrate bonding, low film surface energy and high substrate surface energy. Full-monolayer growth still involves the formation of islands, but these are only one monolayer thick: this case corresponds to a three-dimensional island formation with no barrier to nucleation, since the free-energy change corresponding to a two-dimensional growth of the monolayer island will always be negative. In order to relate the deposition rate and the substrate's temperature to the density of islands, a simple model of the nucleation of two-dimensional island, such as the one from Venables⁷⁶ can be used. In case of free-energy barrier to nucleation, the only thing required for island formation is the encounter of two or more mobile atoms to form a non-mobile cluster: the degree to which true full-monolayer growth will be achieved depends on the density of nucleated clusters. High nucleation density will tend to promote complete filling of monolayers, given that vapor atoms arriving directly on small clusters will be more likely to go to the edges of those clusters before they can encounter other mobile atoms and nucleate a new one-layer thick island.

2.1.2.3 Stranski-Krastanov nucleation and growth.

This mode of growth is a mix of the three-dimensional island growth and the two-dimensional full-monolayer growth. What happens is that the film atoms initially form complete monolayers on the bare substrate, and subsequently nucleate three-dimensional clusters on these layers, typically after 1 to 5 monolayer have grown.

One of the reason that could lead to three-dimensional island growth is the stress due to mismatch in the lattice parameters of the growing films and of the substrate, or more precisely the relaxation of this epitaxial stress while the film becomes thicker. This has been shown in the case of Ge deposition over Si, where the

three-dimensional island nucleation occurs after only 1 or 2 monolayers have been deposited. Strong chemical bonding may also be involved, altering the surface energy of the initial layers.

Whatever drives this particular growth mode, the same factors involved in Frank-Van der Merwe and in Volmer-Weber growth will control the nucleation and growth of the initial layers and of the subsequent islands.

2.1.2.4 Step flow nucleation and growth.

The last growth mode analyzed is the step flow growth mode. Such mode characterizes mainly growth on substrates characterized by miscut, that have surface breaking up into monoatomic steps with low-index terraces and edges (Figure 15d). In case of growth with sufficiently low substrate temperatures or of high flux, which would not allow the adatoms to migrate towards the edges, layer-by-layer or islands nucleation may occur on the vicinal planes (the terraces). However, when the substrate temperature is high enough or the flux is sufficiently low, the mobility of the adatoms can be so high that they will be able to migrate to the step edges and be incorporated in them before having the chance to nucleate. Growth of the epitaxial film will occur by the advancement of steps along the terraces, without requiring nucleation.

2.1.2.5 Effects of substrate surface microstructure.

Thus far the description of the different growth modes has assumed that nucleation occurs at random locations on a perfect surface. Obviously, this does not describe a real experiment, where substrate surface imperfections, such as point defects, atomic steps and dislocations, provide sites where nucleation preferentially occurs. The distribution of low-energy sites will control the nucleation rate and nuclei density at low supersaturations. At sufficiently high supersaturations, however, the homogeneous nucleation rate can surpass the heterogeneous rate, controlled by the distribution of low-energy sites.

2.1.3 Homoepitaxial growth modes.

In case of homoepitaxial growth, the deposited material is identical to the substrate and the exact crystalline structure of the substrate is extended into the growing film. Therefore, complicated effects such a stress induced by mismatch of lattice parameters or of different thermal expansion coefficients, do not play a role. Consequently, only two-dimensional growth mode is expected⁷⁷. This behavior is determined by a number of kinetic parameters, including the surface diffusion coefficient (D_S) of the film atoms, the sticking probability of a film atom arriving at the edge of a terrace and the additional energy barrier (E_S) for film atoms to descend the edge to a lower terrace.

Amongst these kinetic parameters, the diffusion coefficient is the most important one as it describes the average distance an atom can travel on the surface, which is assumed to be atomically flat, before being trapped. This distance is defined as surface diffusion length l_D , given by:

$$l_D = \sqrt{D_S \tau}, \quad (2.9)$$

where τ is the average time before re-evaporation. The surface diffusion coefficient D_S is generally expressed as:

$$D_S = \nu a^2 \exp\left(-\frac{E_A}{k_B T}\right), \quad (2.10)$$

where E_A is the activation energy for diffusion, ν the jump frequency and a the characteristic jump distance. It is critical to underline the importance of temperature in equation (2.10) because it controls the degree of diffusion of the film atoms.

In order to understand the possible 2D growth modes, two diffusion mechanisms have to be considered: first, the diffusion of atoms on a same layer terrace (intra-layer mass transport) and, second, the diffusion of an atom to a lower terrace (inter-layer mass transport). Both processes are regulated by kinetic parameters. A fast intra-layer mass transport will lead to step flow growth, as seen in Figure 16*d*. In this case, l_D is larger than the average terrace width l_T , therefore the film atoms will be able to reach the edges of the substrate end before being trapped. The steps will act as a sink for the deposited atoms diffusing toward the steps preventing nucleation on the terrace: as a result, the step will propagate leading to step flow growth.

If the intra-layer mass transport is not fast enough, nucleation will occur on the terraces. Initially, nuclei will be formed until a saturation density will be reached. After saturation, the probability for film atoms to attach to an existing nucleus will be higher than the probability of a new nucleus to form and islands will start to grow. In this case, the inter-layer mass transport will largely affect the growth mode. Two extreme growth mode can be further distinguished: (i) ideal layer-by-layer and (ii) ideal multilayer growth.

(i) In the ideal layer-by-layer growth, which can be obtained in presence of a steady inter-layer mass transport, atoms deposited on top of a growing island will, first, reach the island's edge and, second, diffuse to the lower step later. In this ideal case, nucleation of a new layer will start after completion of the previous layer. (ii) In case of no or very limited inter-layer mass transport, nucleation will occur on top of islands before these islands have a chance of merging. This will then lead to the growth of multilayer islands. Now, in a real system, the growth mode observed will lie between the two extreme growth modes just described.

2.1.4 Pulsed Laser Interval Deposition.

In order to promote layer-by-layer growth, the so-called pulsed laser interval deposition can be performed. Such technique consists in depositing circa the amount of material necessary to complete a mono-layer, then to turn off the laser to allow the diffusion of the adatoms towards the edge of the terraces. Pulsed laser interval deposition, as it will be shown later, was key in achieving high quality crystallinity films on vicinal substrates, which are substrates characterized by narrow terraces (of width of the order of few tenth of nanometers) due to a miscut of the surface which can be up to 20 degrees.

2.1.5 Heteroepitaxy.

Heteroepitaxy, or the growth of a single-crystalline material on top of a different species, is necessary for the development of a wide series of devices for different applications. The three main motivations behind heteroepitaxial growth are *substrate engineering*, the creation of devices based on *heterojunctions*, and *device integration*. Although *heterojunctions* characterize many different semiconductor devices, like diodes and transistor, this specific topic will not be covered in this thesis. On the other hand, *substrate engineering* is one of the key element for obtaining, through epitaxial stabilization, high quality thin films of the metastable epsilon ferrite, which would be otherwise impossible. Moreover, having a cheap and multifunctional material is of little use unless possibility of its *integration* in consumer electronic devices (thus with common semiconductor as silicon) is demonstrated.

Heteroepitaxial growth of a film usually implies having a substrate having a crystal structure similar to - or at least structurally compatible with - that of the epitaxial film desired. In contrast to the case of

homoepitaxy, the lattice parameters of the substrate, while generally close, are different from those of the desired epitaxial film. In this work, the lattice mismatch between the substrate and the deposited film will be defined as:

$$mismatch = \frac{a_f - a_s}{a_s}, \quad (2.11)^{III}$$

where a_s is the relaxed lattice parameter of the substrate and a_f is the one of the epitaxial film. Usually the mismatch is lower than 10%, and may take either sign depending on whether is compressive ($mismatch > 0$), or tensile ($mismatch < 0$). The degree of lattice mismatch between the substrate and the film has noteworthy effects on epitaxy, the most important being, (i) affecting the growth mode of the film (*e.g.* 3D island and/or layer-by-layer 2D growth), (ii) by influencing the nucleation process, and (iii) inducing structural defects (like misfit dislocations) at the interface region between the substrate and the growing film. These effects are also related to the interfacial energy, thus to the strength of the bonds at the interface between the substrate and the film. In system characterized by low mismatch (usually lower than |1% to 2%|), and for sufficiently thin films, the growth mode will follow a 2D, layer-by-layer mode. For larger mismatch a 3D, island growth mode is generally favored.

Low mismatch and layer-by-layer growth will result in a coherent or pseudomorphic growth of the film, meaning the film will be characterized by the same crystal structure and lattice parameter as the substrate (Figure 17a). With increasing thickness, the amount of strain energy inside the pseudomorphic layer increases; at a certain thickness, called the *critical thickness*, the formation of defects that relax part of the epitaxial strain will become energetically favorable (Figure 17b). For thicknesses higher than the critical thickness, part of the mismatch will therefore be accommodated by misfit dislocations (implying some plastic deformation) and part by elastic strain. The existence of the critical thickness was first predicted in the theoretical study by Frank and van der Merwe⁷⁸, and was subsequently further modeled by others and experimentally detected in various works⁷⁹.

^{III} Other definitions found in literatures are: $mismatch = (a_f - a_s) / a_f$ or $mismatch = (a_s - a_f) / a_f$. All three definition lead to approximately the same absolute values, but there is a difference in sign that must be accounted for when defining the type of strain (compressive or tensile). An alternative (and symmetric) definition is $mismatch = (a_s - a_f) / (a_f + a_s)$.

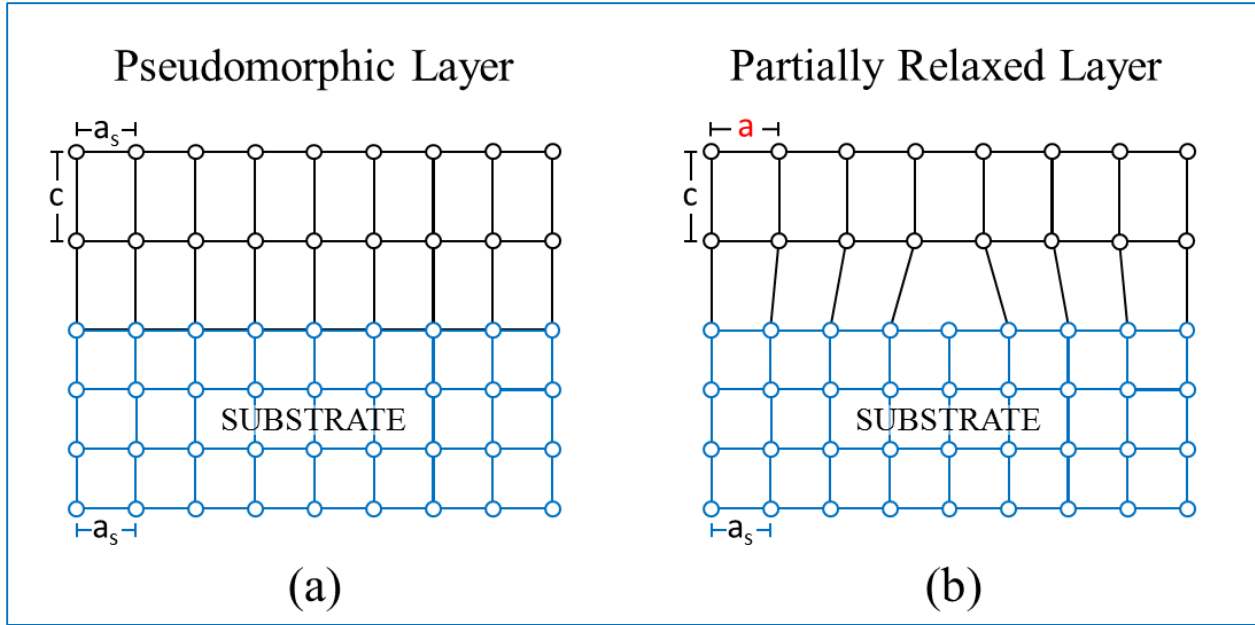


Figure 17: (a) Pseudomorphic and (b) relaxed growth of a cubic epitaxial film on a slightly mismatched cubic substrate.

If we assume, for the sake of simplicity, that both the film and the substrate are cubic, the effect of the epitaxial strain on the pseudomorphic layer is to induce a *tetragonal distortion*, resulting in a out of plane lattice parameter $c > a_f$ (exaggerated in Figure 17). As mentioned earlier, after the critical thickness is reached, the film will partially decrease its strain energy by forming defects. Its in-plane lattice parameter will relax to the unstrained value (for a fully relaxed film) or to an intermediate value (for a partially relaxed film). Different models (Matthews and Blakeslee, Frank and van der Merwe, Matthews and People and Bean) exist to determine the critical thickness: they all consider some energy balance between the gain obtained by the introduction of a particular defect and the cost associated with the formation of this defect. However, for the scope of this thesis, it will suffice knowing that the critical thickness is inversely related to the lattice mismatch and equal to 1-10 nm (for a mismatch in the 1%-10% range)⁸⁰.

Focusing on epsilon ferrite, the picture is more complicated given its complex, non-symmetric crystal structure and the sole existence of $\epsilon\text{-Fe}_2\text{O}_3$ as size-confined nanostructures. The latter feature will make complicated defining a precise lattice strain (in the absence of relaxed single crystals of $\epsilon\text{-Fe}_2\text{O}_3$) thus predicting the growth mode and estimating the critical thickness. The first feature suggests a peculiar epitaxial regime defined as “hard” heteroepitaxy. Hard heteroepitaxy defines the growth of a film on a single crystalline substrate which strongly differs from the film for one or more of the following characteristics: crystal structure, lattice parameters, and/or nature of the chemical bonds⁸¹. As will be explained further in this work, in the case of epsilon ferrite, both the crystal structure and the lattice

Chapter 2

parameters differ from the ones of the chosen substrates (although uncommon epitaxial matches can be and have been identified). On the other hand, however, the nature of the chemical bonds in the epilayer is very similar to the one of the chosen substrates, which is what is believed to promote the epitaxy.

The fundamental problem in hard heteroepitaxy lies in the application of the concept of lattice match. Indeed, for systems characterized by *hard* heteroepitaxy the “classic” criterion of lattice match based on comparison of bulk lattice constants does no longer apply. A new, more relevant to hard heteroepitaxy, definition for lattice mismatch will be: "two lattices are crystallographically matched if the interface translational symmetry could be compatible with the symmetry on both sides of the interface, to within a given precision"⁸². Lattice match in this new context will mean that the two-dimensional interface possesses translational symmetry that is compatible with that of the substrate and that of the film on both sides of the interface. Such compatibility enables local structures of the interface to repeat themselves periodically over large distances. It should be emphasized, however, that the effect of lattice mismatch in hard heteroepitaxy is of secondary importance in comparison to the chemistry of the interface, which will always play the major role as far as epitaxial growth is concerned. Examples of systems characterized by hard epitaxy are CdTe(111)/GaAs(100)⁸³ and CdTe(111)/Al₂O₃⁸⁴.

Now that the fundamentals of nucleation and growth have been explained, and the unusual hard heteroepitaxial regime characterizing epsilon ferrite introduced, the experimental set-ups used in the course of this research will be described.

2.1.6 Pulsed Laser Deposition experimental setup.

The films prepared in the course of this work have been deposited using a pulsed laser deposition (PLD) system located at INRS-EMT like the one shown in Figure 18a. The PLD system, as can be seen in the schematics in Figure 18b, consists of a cylindrical vacuum chamber surrounded by ports which serve as mounts for windows and feedthroughs.

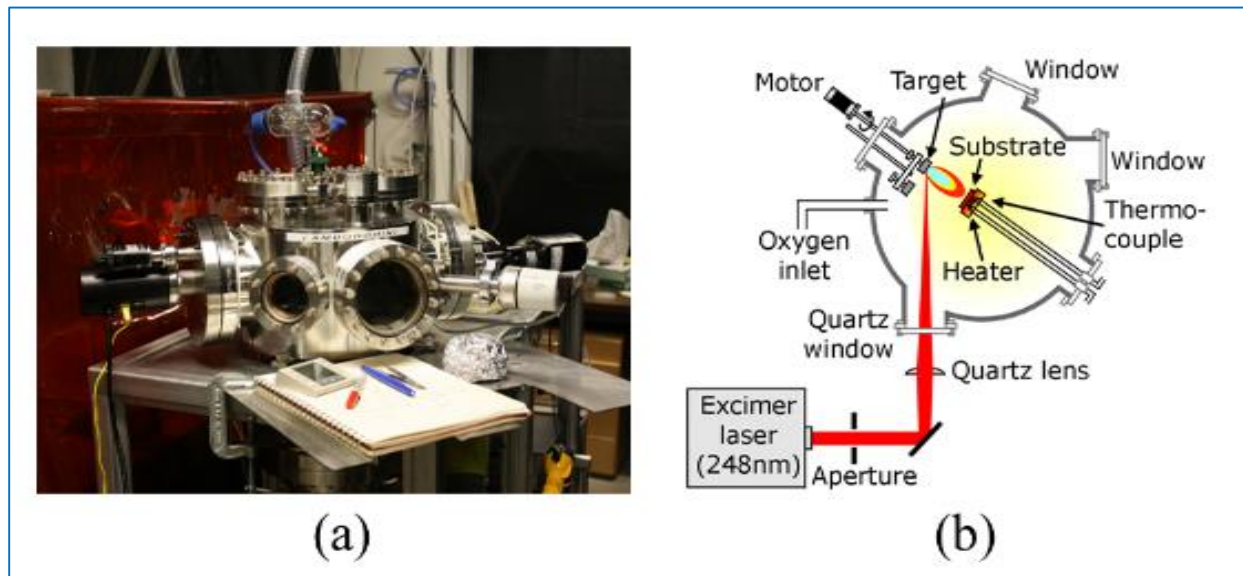


Figure 18: (a) Typical PLD setup and (b) schematic of a PLD chamber.

A pulsed excimer laser (KrF – $\lambda = 248$ nm) was utilized for ablation, with repetition rate tunable between 1 and 50 Hz, pulses duration of approximately 20 ns, and a pulse maximum energy of circa 400 mJ. The beam was then focused onto the target with a system of mirrors and a lens, resulting in a spot size of circa 3 mm^2 . The target was mounted on a rastering system, which allowed rotation and lateral translation of the target in order to obtain a uniform ablation of the target to prevent formation of craters on the target surface. A special target holder which fits up to four interchangeable targets was available for multi-target deposition (however, deposition was also possible from only one target). One or multiple substrates could be installed on the substrate holder, which was rotated during growth to grant a uniform deposition over the whole substrate. The substrates and targets were mounted following a precise geometry, where the laser beam forms an angle of 45° with the target vertical face, while the substrate have to lie in front of the target, in order to be hit completely by the plume. Distance between the target and the substrate could be adjusted between 20 and 5.5 cm, using an endless screw controlled by a knob. The temperature of the substrate could be controlled by utilizing a resistive heater placed behind the substrate holder: the temperature was measured by a k-type thermocouple and regulated by a feedback controller and could reach up to 1000°C .

Chapter 2

However, since the resistive heater is physically separated from the substrate holder, the maximum temperature of the substrate could differ from the measured one by several tenths of degrees (e.g. for our depositions the highest temperature achievable on the substrate being ~ 850 °C). In order to have a correct reading of the temperature of the substrate and of the growing film, a pyrometer was used to monitor the temperature of the substrate/film surface during deposition. Through the controller, it was possible to set programs and change the heating rate (which was usually 20 °C/min), the dwell time, *i.e.* the duration of the segment with constant temperature, which was usually the same for the deposition, and for the cooling. A turbo-molecular pump was installed beneath the chamber, backed by a mechanical pump, which could pump the system down to a pressure in the range of 10^{-6} Torr. By using a set of valves and flowmeters, it was possible to introduce different inert (He, Ar) and reactive (N_2 , O_2) gases into the chamber and to regulate their flow: the gas pressure was controlled by an ion gauge and, additionally, by a convectron gauge, which was designed for more precise measurement in the range used for PLD deposition, namely 10^{-3} -1 Torr.

2.2 Characterization of epsilon ferrite thin films.

2.2.1 Characterization of the crystal structure via x-ray diffractometry.

X-ray diffraction (XRD) is widely used to determine the crystal structure of a material. The technique is based on the fact that the wavelength λ of the X-rays used is of the same order of magnitude (1–100 Å) as the inter-planar spacing d in the crystal investigated, and that when irradiated by a beam of such X-rays, coherent scattering of the atoms in the crystalline lattice causes an interference pattern specific to the crystal structure. By measuring the angles at which the x-rays interfere coherently and their intensities, it is possible to infer the properties of the crystal, such as its orientation, the values of the lattice parameters, and its crystalline quality.

More specifically, coherent interference by the atoms of two adjacent lattice planes will occur when the path length of two X-rays differ by an integer multiple of their wavelength, as expressed by the Bragg's law and portrayed in Figure 19.

$$2d\sin\theta = m\lambda. \quad (2.12)$$

Here d is the spacing between diffracting planes, θ theta is the incident angle, m is any integer, and λ is the wavelength of the beam.

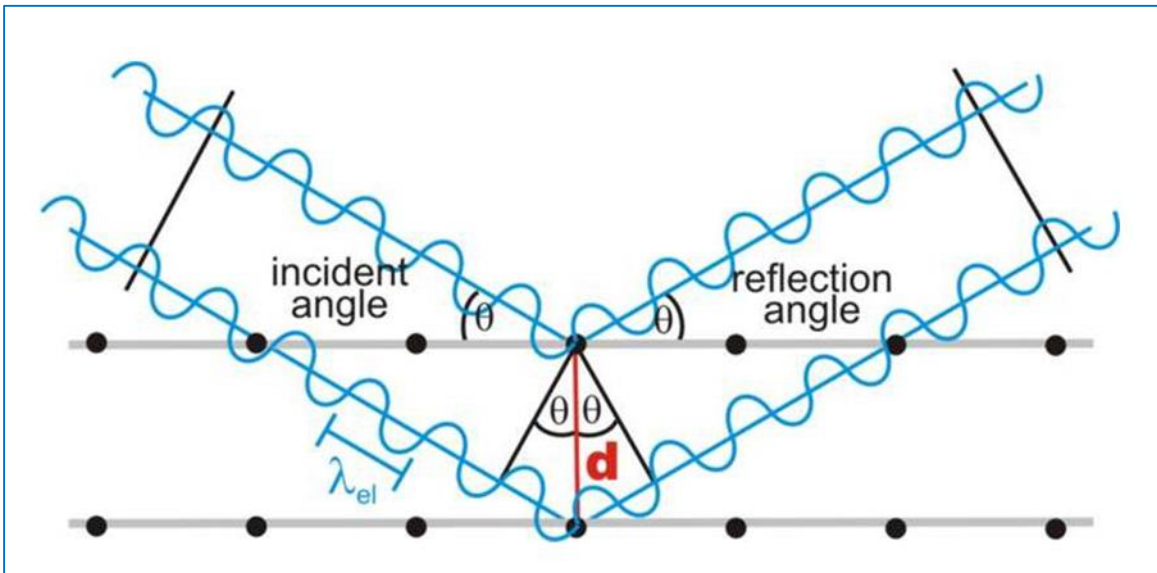


Figure 19: Graphical representation of Bragg's law.

In the course of this work, X-ray diffraction was performed using the $K\alpha$ radiation of copper ($\lambda = 1.5407 \text{ \AA}$) in a PANalytical X'Pert MRD PRO diffractometer. Different kind of measurements were performed, such as classical Bragg-Brentano geometry ($\theta/2\theta$ scan), rocking curve measurements (ω scan), reciprocal space mapping measurements (RSM), and phi (ϕ) scans. To ease the understanding of the different angles scanned during the different measurements, these angles are drawn in Figure 20.

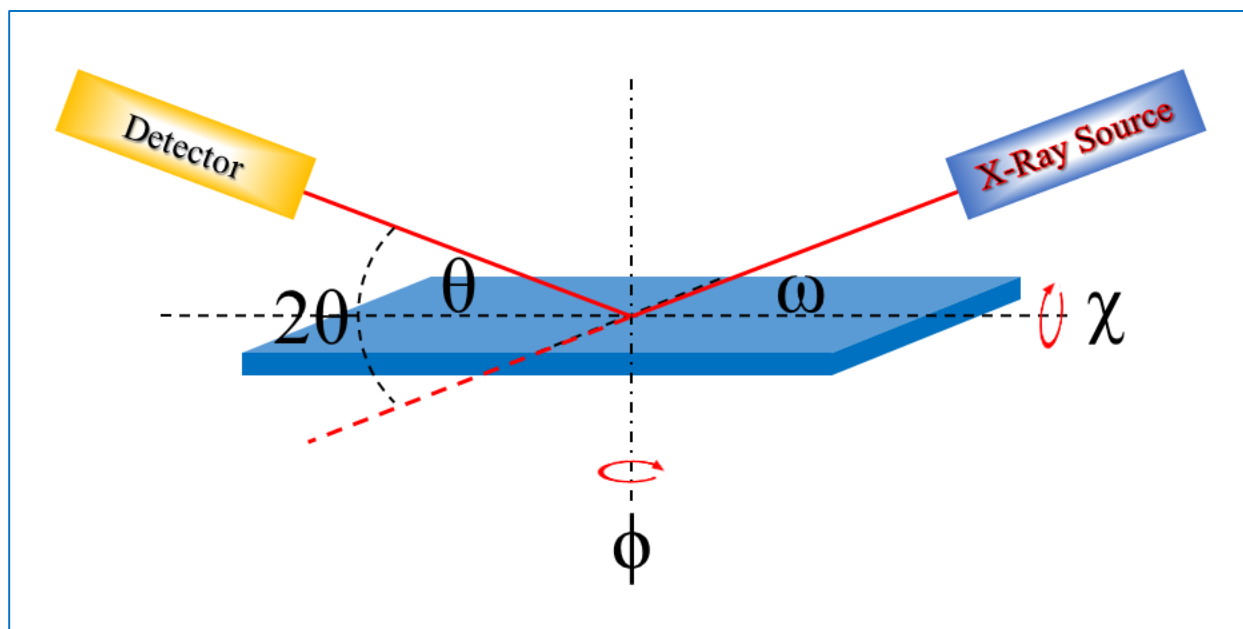


Figure 20: The different angles that can be adjusted with high precision during a XRD measurement. The sample is portrayed in blue.

$\theta/2\theta$ symmetrical (also called goniometer) scans were used to verify the epitaxial growth of (001)-oriented epsilon ferrite films on the different single crystal substrates; as a matter of fact, these kind of measurements, when performed with the sample surface perpendicular to the incidence/diffraction angle bisector ($\chi = 0$), as shown in Figure 20, give information on the out-of-plane lattice parameter. In order to obtain information on the in-plane lattice parameter, the interplanar distance of crystallographic planes non parallel to the surface has to be measured (thus doing a $\theta/2\theta$ scan with an angle $\chi \neq 0$). $\theta/2\theta$ scans will be then characterized by intense peaks, belonging to the different substrates, and smaller ones belonging to the film (such difference in intensity is due to the much higher thickness, of approximately four orders of magnitude, of the substrates used compared to the film thickness). Besides the signal of the substrate arising from diffraction of the main $K\alpha$ line, secondary lines ($K\alpha_2$, $K\beta$, and the L line of the tungsten contamination of the tube) will arise as well; therefore, a nickel filter was used in order to cut these peaks and to obtain cleaner diffractogram.

Rocking curve measurements were performed to estimate the quality of the grown epitaxial films. Such measurements are performed by rocking the sample around diffraction conditions, meaning scanning ω with fixed 2θ values corresponding to the maximum of one of the peak belonging to the film. Rocking curve measurements will result in a peak the full-width at half-maximum of which will provide information on the degree of parallel alignment of the analyzed crystallographic planes. Low values of the full width at half maximum (FWHM) will correspond to crystal with high parallel-alignment of the family of lattice planes investigated, while higher values will be a sign of worse alignment (therefore worse quality of the crystal).

Finally, phi (ϕ) scans provide insights on the symmetry of the crystal structure of the grown epitaxial films, as well as their possible different growth orientations. The latter feature is of particular importance for the analysis of epsilon ferrite thin films, which crystal structure is characterized by lower symmetry compared to the substrates on which is grown, resulting in multiple in-plane growth orientation (also called twins). Moreover, through analysis of the shape in the phi scans peaks, performed by measuring the deviation with the Gauss function used to fit the peaks, it is also possible to infer the degree of lateral mosaicity in the samples.

2.2.2 Transmission Electron Microscopy.

Transmission electron microscopy (TEM) is a microscopy technique where imaging is achieved by transmitting an electron beam through a sample. An image is formed from the interaction of the electrons transmitted through a thin (tenths of nanometer) section of the sample as the beam is transmitted through the specimen. The resolution obtainable with transmission electron microscopes is significantly higher than the one achievable via classic light microscopes, given the smaller de Broglie wavelength of electrons compared to photons. This enables the instrument to capture fine detail, even as small as a single column of atoms, many order of magnitudes smaller than what is resolvable with an optical microscope⁸⁵. Cross-sectional transmission electron microscopy was carried out at the Canadian Centre for Electron Microscopy, at McMaster University. The analyzed samples were prepared with a Focused Ion Beam instrument (Zeiss NVision 40) with multiple milling stages at decreasing incident ion energies down to 5keV, as well as a final polishing step using a Fischione NanoMill Ar-beam milling system operated at liquid nitrogen. This procedure has been shown to minimize damage and oxygen loss even in beam-sensitive samples⁸⁶.

Electron microscopy observations were carried out with an FEI-Titan 80-300 Scanning Transmission Electron Microscope (STEM) equipped with aberration correctors for both the probe and the imaging forming lenses, an energy loss spectrometer (Gatan Quantum model), and an electron beam

monochromator. Imaging with a high-angle annular dark field detector and collection angles providing atomic-number (Z) contrast was used to provide information on the local structural arrangement, including the interface atomic structure and the presence of grain boundaries separating the crystalline grains in the films. Moreover, in order to obtain more information from the Scanning Transmission Electron Microscopy results, multi-slice calculations of high-angle annular dark field (HAADF) images were carried out in different projections corresponding to possible film orientations expected from the X-ray diffraction data.

2.2.3 Thickness.

The thickness of our sample was measured by a profilometer as well as by atomic force microscope (AFM), by taking advantage of the step formed at the edge during growth due to the presence of metal pins to hold the substrate in place. The thickness of different sample was measured, and the total thickness of all the films was then divided by the total number of pulses utilized to grow each sample to determine the growth rate for the epsilon ferrite thin films. Moreover, AFM was also used to determine the roughness and the overall uniformity of the deposited thin film.

2.2.4 Macroscopic Magnetic Characterization.

Magnetic characterization of the epsilon ferrite thin films was performed with an EV9 Vibrating Sample Magnetometer (VSM) made by ADE Technologies (MicroSense, Lowell MA, USA) at Polytechnique Montréal. Magnetic hysteresis loops were recorded for the epsilon ferrite thin films at room temperature with the magnetic field, varying between ± 20000 Oe, applied both parallel (in-plane) and perpendicular (out-of-plane) to the film surface. A schematic of the VSM, along with a representation of the position and orientation of the sample in the magnetic field for the in-plane and out-of-plane configurations is shown in Figure 21.

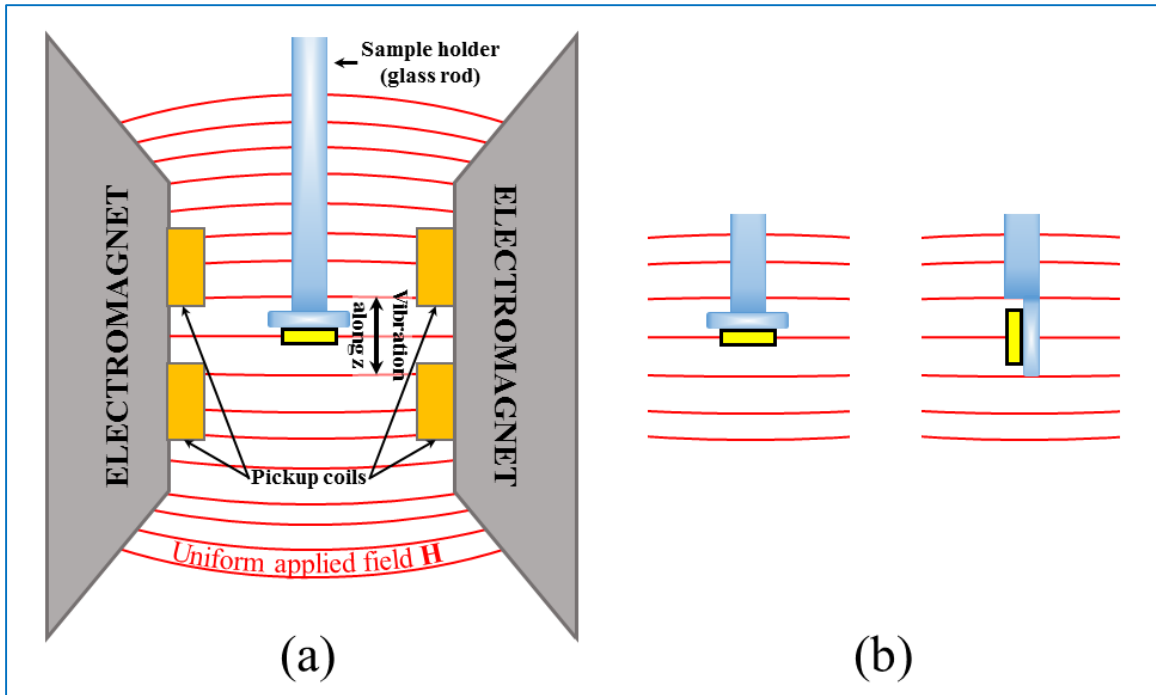


Figure 21: (a) schematics of the Vibrating Sample Magnetometer (VSM) and (b) in-plane (left) and out-of-plane (right) configuration of the sample in the VSM.

In order to obtain solely the film signal, two different approaches were followed: First, the magnetic contributions of the sample holder (glass rod) and of the substrate were measured separately and subtracted from the total signal. Then, a data-analysis technique was developed, consisting in differentiating the measured loop, fitting the various peaks of the 1st derivative by using a summation of Voigt distributions in addition to a constant, deconvoluting the signals originating from the different magnetic phases (which simply correspond to the different peaks), and finally integrating exclusively and independently each Voigt functions⁸⁷. Our technique, which we named D-D-SI, from “Derivative - Deconvolution - Selective Integration” (see ANNEX I for a complete formulation), allows us to discriminate between the various contributions originating from different magnetic phases, and also to eliminate every linear contribution due to the paramagnetic and/or diamagnetic signals arising either from the vibrating rod or/and from the substrate, along with any further linear contribution possibly coming from the film.

Temperature dependent measurement of the remanent magnetization under no field and of the magnetization with an applied magnetic field of 1000 Oe were also performed, in order to determine the

Chapter 2

value of the temperature at which the ferrimagnetic to paramagnetic transition for epsilon ferrite occurs^{IV}. Although, the measurement of the remanent polarization should be sufficient, the application of a small field was found necessary, since it permitted to highlight the presence of a secondary magnetic phase, different from epsilon ferrite, as will be explained later in the thesis. Finally, angle-dependent magnetic properties were obtained by recording in-plane hysteresis loops every 2 or 5 degrees. The in-plane angle dependence of the remanent magnetization M_R was extracted from the measured loops. To analyze the azimuthal dependence of M_R , a simple model which averages the remanence of the different growth variant parallel to the measured axis was utilized⁸⁸. Such model, the complete formulation of which is shown in Appendix II, is based on the assumption that, at zero applied field, the magnetization inside each crystal is uniform and aligned along their magnetic easy axis (a -axis). This assumption is supported by a critical dimension analysis based on the anisotropy field values and the dimensions of our epsilon ferrite crystals obtained from transition electron microscopy allowing us to infer that the crystals are essentially magnetic monodomains^{88,89}. The angular dependence of the normalized remanent magnetization for one specific crystal orientation can thus be modeled by the product of the measured remanent magnetization and of the absolute value of $\cos(\text{angle} + \text{offset})$, where the offset depends on the angular distributions of the different in-plane growth variants (see the next chapter for details).

^{IV} Although, the material being ferrimagnetic, thus its ferrimagnetic to paramagnetic transition temperature being actually defined as the Néel temperature, such a temperature will be referred to as the Curie temperature in agreement with the literature and the common use of the term, in order to indicate the temperature at which the magnetic order disappears.

2.2.5 Macroscopic Ferroelectric Characterization.

Macroscopic ferroelectric loops were recorded with the FE-Module of a TF Analyzer 2000 system by aixACT Systems GmbH (Aachen, Germany). Such setup is based on the classic Tower-Sawyer circuit to measure the polarization (Figure 22). In order to measure the hysteretic behavior of the polarization, the films have to be deposited on conductive substrates, and metal electrodes have to be deposited on its top surface, in order to have a parallel plate capacitor geometry where the ferroelectric material acts as the dielectric (see Figure 22).

In the Tower-Sawyer experiment the driving voltage (which can have sinusoidal or triangular shape) is cycled by the signal generator at high frequency (1 Hz – 2 kHz), and the voltage across the reference capacitor is measured. The charge accumulated on the ferroelectric capacitor is the same as the one over the reference, given that they are in series, resulting in a charge on the ferroelectric equal to:

$$Q = C_{ref} * V_{ref}. \quad (2.13)$$

Here C_{ref} is the capacitance of the reference capacitor (which is of several order of magnitude higher than the capacitance of the ferroelectric sample), and V_{ref} is the voltage measured across the capacitor. With the Tower-Sawyer circuit it was possible to measure the polarization P versus field E by plotting the driving voltage on the x axis and the charge on the y axis.

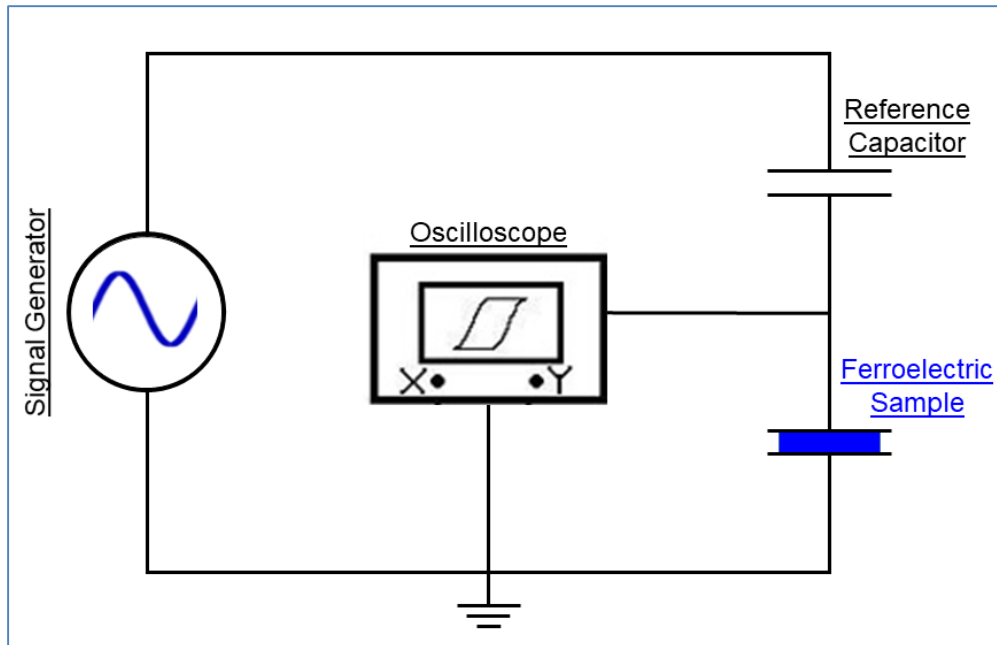


Figure 22: Classic Tower-Sawyer circuit to measure ferroelectric hysteresis loops (PE loops) in a ferroelectric sample.

Chapter 2

In the case of the FE-Module of a TF Analyzer 2000 system, in order to analyze the polarization \mathbf{P} , the physical quantity measured is the switching current $I [A]$ that accompanies the charge transfer induced by even the smallest change in the polarization of the sample:

$$I = dQ/dt. \quad (2.14)$$

By integrating this current in time we will obtain the value of the charge $Q [\mu C]$, which, once divided by the surface area of the electrode $S [cm^2]$, will give us the values for polarization $P [\mu C/cm^2]$.

$$P = Q/S. \quad (2.15)$$

Experimentally, by applying to the electrodes a voltage (thus an electric field across the sample) high enough to switch the polarization, a measurable switching current I will be generated: this current, however, will be highly influenced by any leakage through the ferroelectric that could add to it (phenomenon that is common in oxides and highly troubling for the specific case of epsilon ferrite, as it will be shown later). As shown above, in absence of leakage currents, to obtain the response of the polarization to the applied field, a simple integration of the measured switching current is needed.

2.2.6 Surface topology and microscopic characterization of magnetism and ferroelectricity via scanning probe microscopy (SPM).

Scanning probe microscopy is a term used to describe a group of imaging techniques where pictures of a surface is obtained by scanning it with a physical probe of very small lateral dimension. SPM goes back to 1981, with the first report on scanning tunneling microscope (STM)⁹⁰⁻⁹², an instrument that, by detecting nanoscopic currents tunneling from a conducting material across a very short distance in vacuum, is able to image surfaces with atomic resolution. Since then, other microscopy techniques, based on different interactions, were developed. In particular, the three most interesting to us are atomic force microscopy (AFM), to have an image of the topography of the sample, magnetic force microscopy (MFM) and piezoresponse force microscopy (PFM) to probe magnetism and piezoelectricity at the microscale level.

In all these imaging techniques the samples are scanned with a probe at the end of a cantilever, probe with very small lateral dimensions determining the resolution of the technique: the interactions of the sample with the probe (which is made of different materials depending on the applications) will deflect the probe, this deflection measured and amplified allowing imaging the surface. Thus, the main difference between the various SPM techniques is the kind of interaction between the probe and the sample.

- In AFM, the tip of a semiconducting probe is either attracted or repelled by the sample due to the interactions between atoms as modeled by the Lennard-Jones potential;
- In MFM, a magnetic tip is attracted or repelled by the magnetic moments in the different magnetic domains;
- In PFM, a conducting tip is put in contact with the sample and an alternate current is applied, in order to register the deformation of the sample due to the converse piezoelectric effect (deformation of a material with application of an electric field).

Although not key for my thesis, these three techniques have been used to study the surface topography and the functional properties of my epsilon ferrite films on the micro-scale.

2.2.7 Direct and indirect measurement of the ferromagnetic resonance spectroscopy.

The ferromagnetic resonance frequency was probed with two different techniques: direct measurements were performed at Polytechnique Montréal by utilizing a setup as the one shown in Figure 23. The measurements were conducted using a custom-fabricated cylindrical gold cavity that has its TE₀₁₁ mode at a frequency of 37.6 GHz (cavity loaded). The epsilon ferrite samples were glued on a quartz rod and then placed in the middle of the cavity. The rod was placed so as to be parallel to the AC magnetic field H_{AC} of

the cavity. Microwave generation and detection were performed with a vector network analyzer (VNA) that excites the resonant cavity and measures its complex reflection coefficient R over a frequency range around its resonant frequency. The variation of the amplitude of the reflection coefficient ΔR at the resonant frequency of the cavity depends on the size and magnetic properties of the sample placed in the cavity and is proportional to $\eta\chi''$, where η is a filling factor corresponding to the volume of the magnetic material divided by the volume of the cavity, and χ'' is the imaginary part of the sample magnetic susceptibility⁹³. The proportionality constant is determined by measuring the quality factors of the sole resonant cavity and its coupling hole. For clarity purposes, the quantity $\eta\chi''$ will be called the experimental magnetic susceptibility (χ_{exp}). FMR curves will be presented in terms of χ_{exp} versus the applied static magnetic field H_0 .

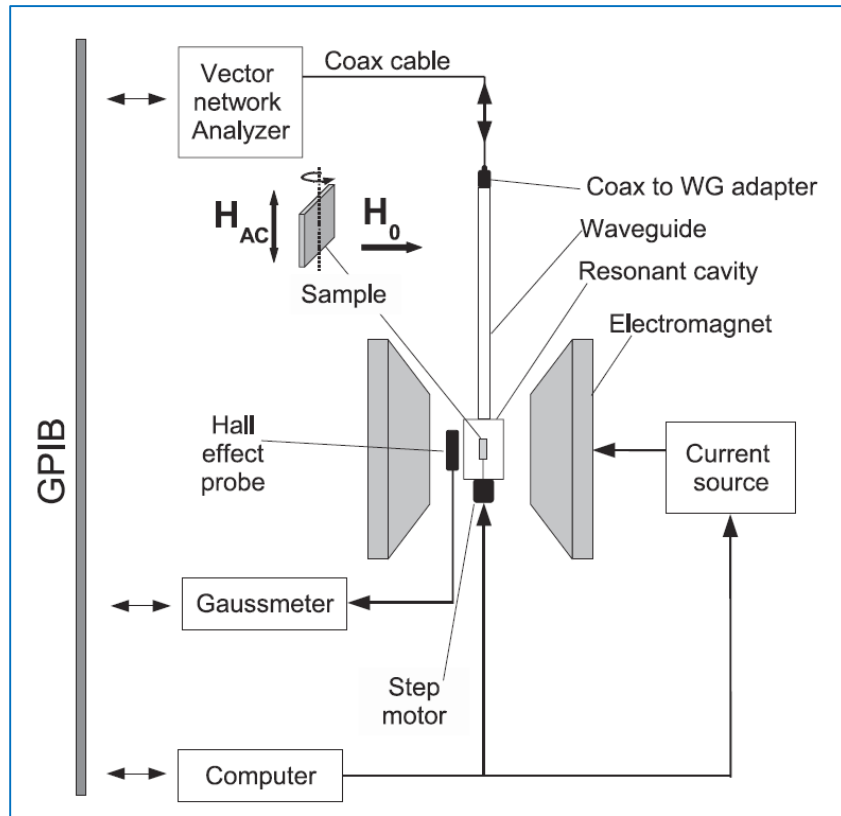


Figure 23: Schematic representation of the FMR setup used in the course of this thesis. The alternating magnetic field H_{AC} of the cavity is applied parallel to the rod and perpendicular to the static magnetic field H_0 .

Terahertz radiations (THz) are electromagnetic waves that sandwiched between the infrared waves and the microwaves. This waves are very specific since it is absorbed by water, drugs, explosives but it is also transparent to clothes, plastic, papers and ceramics⁹⁴⁻⁹⁶. On the other hand, the development of new

Chapter 2

detection technics that allow to detect the field and the phase of the THz waves offers the possibility of making THz time domain spectroscopy (THz-TDS)⁹⁷. THz-TDS is a tool that allow to measure the refractive index, the absorption and the conductivity of a specific material at THz frequencies. During my thesis, THz-TDs was the second technique utilized to probe the ferromagnetic resonance of epsilon ferrite thin films. The samples were probed with short terahertz pulses of frequency ranging between 0.05 and 2 THz. A commercial photoconductive antennas was used for the generation and the detection of the THz waves. Since ϵ -Fe₂O₃ thin films are deposited onto single crystal substrate, the THz waveforms were measured both transmitted through the bare substrate and the substrate with the film deposited on top. Then, by calculating the Fourier transform of the two signals, it was possible to extract the absorption of the sample as a function of the frequency.

PART II

Chapter 3 GROWTH OF EPITAXIAL THIN FILMS OF EPSILON FERRITE

This chapter will describe in detail how it was possible to obtain thin films of the metastable epsilon ferrite by growing them by pulsed laser deposition and utilizing epitaxy and epitaxial strains as the stabilizing mechanism. The main results on the structural characterization of such epitaxial films of the stabilized metastable $\epsilon\text{-Fe}_2\text{O}_3$ phase will be presented.

The first part will list the different substrates on which is possible to achieve epitaxial growth and their lattice match with epsilon ferrite, giving particular attention to the continuity of the oxygen framework between the substrate and the film which is thought to be the key component for stabilization.

Not all the different substrates that were used during the investigation yield epitaxial growth, which will be rationalized in terms of mismatch between their thermal expansion coefficient and that of the epsilon ferrite films.

Then the ideal pulsed laser deposition growth conditions will be presented, and their influence on the structure of the film will be discussed.

The final part of this chapter will present a thorough structural characterization of the PLD-grown film performed by x-ray diffractometry and transmission electron microscopy. The different XRD measurements that were performed in order to study the out-of-plane and in-plane mutual alignment of the substrates and the films will be discussed. The effects of the structure of the different substrates on the properties of the $\epsilon\text{-Fe}_2\text{O}_3$ overlayers will be studied, revealing how the choice of substrate, while it does not modify the out-of-plane properties, changes the in-plane geometry of the film, given the different symmetry of their surface termination.

Finally, high resolution TEM images further revealed the differences in the morphology of the epsilon ferrite films when grown on the different classes of substrates used.

3.1 Epitaxial stabilization of epsilon ferrite thin film.

3.1.1 Choice of substrates and epitaxial matches.

As mentioned in the introduction, ϵ -Fe₂O₃ is a metastable intermediate phase between maghemite (γ -Fe₂O₃) and hematite (α -Fe₂O₃). For many years, the main strategy to achieve phase stabilization was to grow it as nanostructures (mainly as nanoparticles⁴⁰, but later also as nanowires^{36,37}) using size confinement as stabilizing mechanism. As reported by Ohkoshi *et al.*⁴⁰, a range in the nanoparticle diameter d exists where the free energy per volume G/V of epsilon ferrite is the lowest among the three iron(III) oxide polymorphs. The free energy per volume of a nanoparticle can be defined as:

$$G/V = \mu/v + 6\sigma/d, \quad (3.1)$$

where μ is the chemical potential, v is the molar volume, and σ is the surface energy. Equation (3.1) suggests that G depends on the chemical potential when d is very large, whereas the contribution of the surface energy increases as the value of d decreases. Under the assumption that the chemical potentials and the surface energies of the three polymorphs follow the relationships $\mu_\gamma > \mu_\epsilon > \mu_\alpha$ and $\sigma_\gamma < \sigma_\epsilon < \sigma_\alpha$, the curves of G_γ/V , G_ϵ/V , and G_α/V behave as shown in Figure 24.

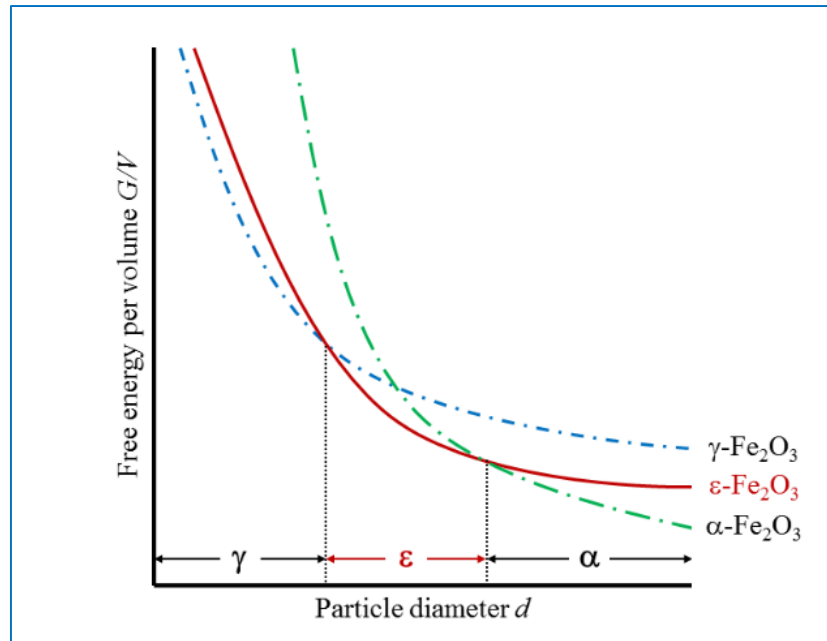


Figure 24: Free energy per volume versus particle diameter in iron oxide (adapted from 40).

As for the case of epsilon ferrite thin films, in the first report on the growth of epitaxial thin films of epsilon ferrite, Gich *et al.* showed the possibility of achieving phase stabilization and epitaxial growth of (001)-oriented films on (111)-oriented SrTiO_3 ⁴⁸. In their manuscript, they ascribed the growth of epsilon ferrite to the lattice match between the substrates and the film, and to the formation of multiple in-plane growth orientations due to the lower symmetry of the film in comparison to the substrates, which helps decreasing the high energy of the (100) surfaces through the formation of domain boundaries^{98,99}.

Consequently, at the start of the project on epsilon ferrite epitaxial thin films, the first choice as substrate for the growth was (111)-oriented strontium titanate (SrTiO_3 – STO), an undistorted perovskite characterized by a cubic crystal structure with lattice parameter $a_{\text{STO}} = 3.905 \text{ \AA}$. Once proved the ability of growing high quality epitaxial films of epsilon ferrite on SrTiO_3 , (111)-oriented lanthanum aluminate/strontium tantalate (LSAT) and lanthanum aluminate (LaAlO_3 – LAO) substrates were also investigated given how they are characterized by the same undistorted cubic perovskite structure with lattice parameter slightly smaller compared to SrTiO_3 (respectively $a_{\text{LSAT}} = 3.868 \text{ \AA}$ and $a_{\text{LAO}} = 3.82 \text{ \AA}$). The main idea was to investigate the effect of increasing strain on the epsilon ferrite epitaxial thin films, given the smaller lattice parameters of LSAT and LAO in comparison to STO.

The best correspondence between the lattice of epsilon ferrite (100) and that of STO (111), which will be called ‘epitaxial match’ in the following, is shown in Figure 25, which will result in the epsilon ferrite film having in-plane lattice parameters equal to $a_\epsilon = \sqrt{6}/2 a_{\text{perovskite}}$ and $b_\epsilon = 3\sqrt{2}/2 a_{\text{perovskite}}$.

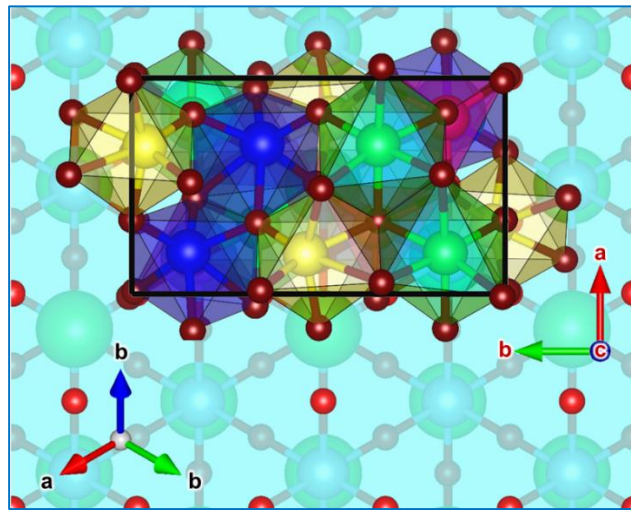


Figure 25: Graphical representation of the (111) plane of cubic perovskites (in light blue) and the epitaxial relation with the epsilon ferrite unit cell. To be noted, the orientation of the substrate (bottom left corner) and on the film (middle right).

Depending on the choice of substrate, given the epitaxial relations, and by using the definition of $mismatch = strain = a_{film} - a_{sub} / a_{sub}$ and the lattice parameters of $\epsilon\text{-Fe}_2\text{O}_3$ reported for nanoparticles, $a = 5.08 \text{ \AA}$, $b = 8.78 \text{ \AA}$, and $c = 9.47 \text{ \AA}$, different lattice mismatch will be obtained for the different substrates, as shown in the Table 1. The positive sign for the mismatch means, given the definition, that in all three cases both lattice parameters of the $\epsilon\text{-Fe}_2\text{O}_3$ film will be under compressive strain.

Substrate	Mismatch a	Mismatch b
STO	6.22 %	5.99 %
LSAT	7.23 %	7.00 %
LAO	8.58 %	8.35 %

Table 1: Lattice mismatch on the in-plane lattice parameters of the $\epsilon\text{-Fe}_2\text{O}_3$ for the three (111)-oriented cubic perovskites.

Another substrate that was chosen for epitaxial stabilization of epsilon ferrite thin film was (100)-oriented yttrium-stabilized zirconia (YSZ), which is characterized by a cubic structure with lattice parameter $a_{\text{YSZ}} = 5.12 \text{ \AA}$. Such choice was inspired by reports showing how GaFeO_3 (GFO), which is isostructural to $\epsilon\text{-Fe}_2\text{O}_3$, grows epitaxially on YSZ (100)¹⁰⁰. In addition, the growth of epitaxial YSZ films on Si (100) is possible and well documented^{101–103}, making it a very relevant choice of substrate for potential future application of $\epsilon\text{-Fe}_2\text{O}_3$ epitaxial thin films in integrated devices. As for the case of epsilon ferrite epitaxial thin films grown on (111)-oriented perovskites, which showed (001)-oriented growth, also the growth of GFO on YSZ (100) was (001)-oriented. In the reports of GFO epitaxial films on YSZ (100) substrate, two distinct in plane epitaxial relationships were found between GFO and YSZ, with the growth being along the (001) orientation in both cases¹⁰⁰. Given the similitude between GaFeO_3 and $\epsilon\text{-Fe}_2\text{O}_3$ structures, an analogous situation was expected to be observed for epsilon ferrite thin films as well. Such two epitaxial matches between $\epsilon\text{-Fe}_2\text{O}_3$ and YSZ (100) are shown below in a graphical representation (Figure 26): the first epitaxial match is given by the parallel alignment of the b_ϵ lattice parameters of epsilon ferrite with the [100] and [010] directions of YSZ. While there is a good match between a_ϵ and a_{YSZ} , the match for b is given by the so-called “tiling”, having $3b_\epsilon \approx 5a_{\text{YSZ}}$ (Figure 26a), our belief is that this is the correct description of the lattice match, given the much lower mismatch it introduces along the b direction compared to the description proposed in ref. ¹⁰⁰). The second match is given by the fact that the diagonal of the unit cell of $\epsilon\text{-Fe}_2\text{O}_3$ equals approximately twice the lattice parameter a_{YSZ} of YSZ: $\sqrt{a_\epsilon^2 + b_\epsilon^2} \approx 2a_{\text{YSZ}}$. In this configuration, the angle between the directions of the b_ϵ lattice parameter with respect to the a_{YSZ} is equal to $\alpha = \cos^{-1}(2a_{\text{YSZ}}/\sqrt{a_\epsilon^2 + b_\epsilon^2}) \approx 30^\circ$ (Figure 26b).

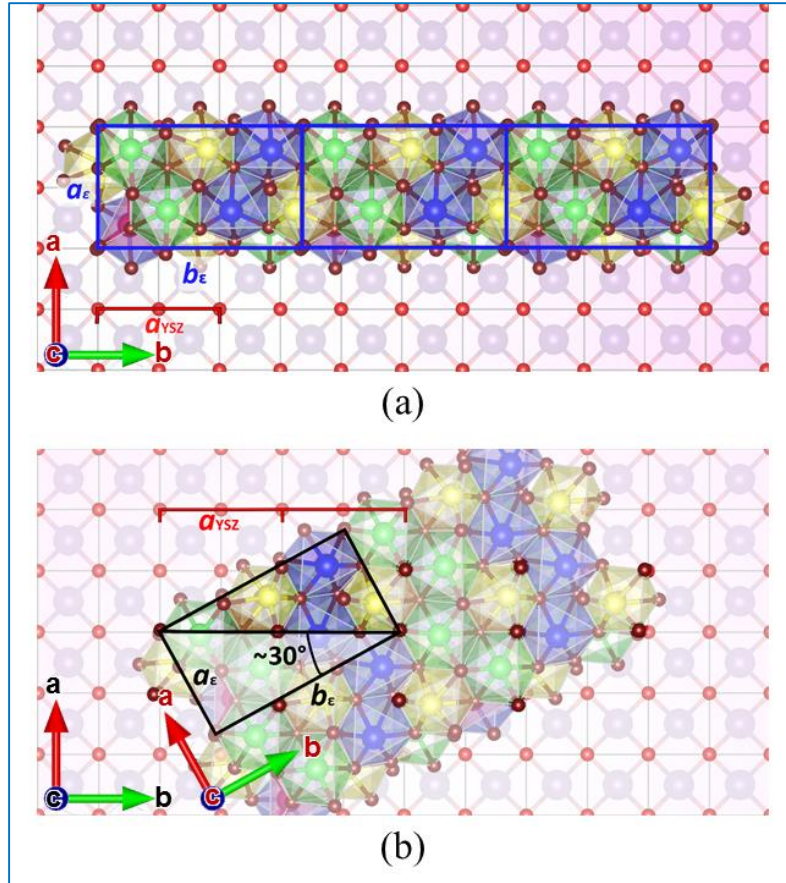


Figure 26: Graphical representation of the (100) plane of YSZ (in pink) and the two epitaxial matches between ϵ -Fe₂O₃ (001) and YSZ (100), (a) “parallel” match and (b) “non-parallel” match. To be noted: the same orientation of the two lattices in the “parallel” case and the presence of a rotation in the “non-parallel” one.

Given the double epitaxial relation given by the substrate, two different strain configuration exist as shown in Table 2.

YSZ relation	Mismatch <i>a</i>	Mismatch <i>b</i>
“parallel”	-0.78 %	2.89 %
“non-parallel”	-	-

Table 2: Lattice mismatch on the in-plane lattice parameters for the two relation in (100)-oriented YSZ.

For the case of the “parallel” match, it has to be noted how there is little difference between the film and the substrate which produces a little tensile strain on the *a* lattice parameter, while the strain over *b* is compressive as in the case of epsilon ferrite grown on (111)-oriented perovskites. For the “non-parallel” relation, an estimation of the values for the mismatch along *a* and *b* is not really possible given the uncommon epitaxial match.

Finally, other substrates such as (111)-oriented lithium niobate (LiNbO_3) (a distorted perovskite), (100)-oriented magnesium oxide (MgO), strontium titanate, (0001)-oriented alumina (or sapphire - Al_2O_3), and bare (100)-oriented silicon were also tested, although they did not yield epitaxial thin films. In such cases, although the epitaxial relation would still give (001)-oriented epsilon ferrite thin films in principle, the mismatch is too high to yield epitaxial growth, or, in case of bare silicon, there is no continuity of the oxygen atoms framework to promote epitaxy. The inability to obtain epitaxial thin film of epsilon ferrite on Al_2O_3 (0001) is of most interest given how this substrate proved to grant epitaxial growth for GaFeO_3 as reported by Thai *et. al.* (GaFeO_3 is actually used as a buffer layer for the growth of $\epsilon\text{-Fe}_2\text{O}_3$ on Al_2O_3 (0001))⁴⁹.

3.1.2 Continuity in the oxygen framework.

Notwithstanding the theory proposed in ref. 48 on the minimization of the energy of the (001) surface of epsilon ferrite by formation of growth domains, which maintains its validity also for films grown on YSZ (100), the stabilization is, in our opinion, mainly given by two phenomena: (i) the presence of strain which acts as size-confinement factor (resembling the effect of the SiO_2 in sol-gel synthesized nanoparticles), and (ii), and most importantly, the continuity of the lattice of oxygen polyhedra granted by the epitaxial matches (see Figure 27 and Figure 28). As introduced earlier when explaining the concept of “hard” epitaxy, the type of chemical bonds at the film/substrate interface and the translational symmetry granted by the substrates, i.e. - in our specific case - essentially the continuity of the oxygen atoms framework in epsilon ferrite which align with the oxygen framework of the underlying substrate, are key factors for epitaxy in materials with different lattice constants and lattice symmetries. Such oxygen framework correspondence can be seen by drawing the upper oxygen layer of a (111)-oriented perovskites and the bottom oxygen layer of epsilon ferrite, as shown in Figure 27. In the picture, the (111) oxygen plane of the STO substrate (bright red smaller spheres) and the first layer of iron (blue/violet bigger spheres) and mostly important oxygen in $\epsilon\text{-Fe}_2\text{O}_3$ (burgundy smaller spheres) are represented. As can be seen, there is very good correspondence between the oxygen

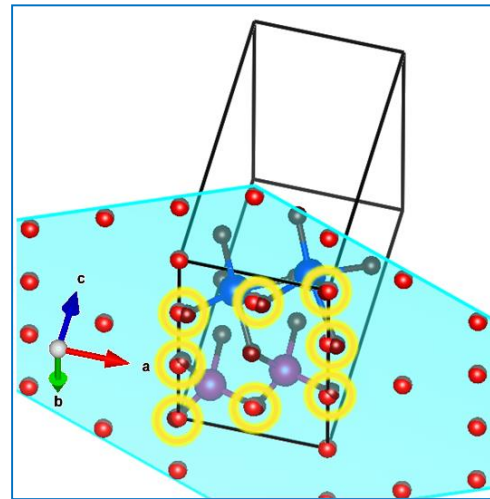


Figure 27: Graphical representation of the good match of the oxygen polyhedra framework in the epsilon ferrite grown film and in the underlying (111)-oriented perovskite substrate.

framework of the substrate and the oxygen polyhedra in the film (the small difference arising from the fact that the atom coordinates used for ϵ -Fe₂O₃ were the one of epsilon ferrite when synthesized as nanoparticles, since there exist no free-standing and totally relaxed crystal of metastable ϵ -Fe₂O₃).

A certain degree of correspondence, although not as high as the one found for films grown on perovskites, can be also found in the case of epsilon ferrite grown on YSZ. Moreover, such correspondence appears to be better for the “parallel” lattice match (Figure 28a) than for the “non-parallel” one (Figure 28b).

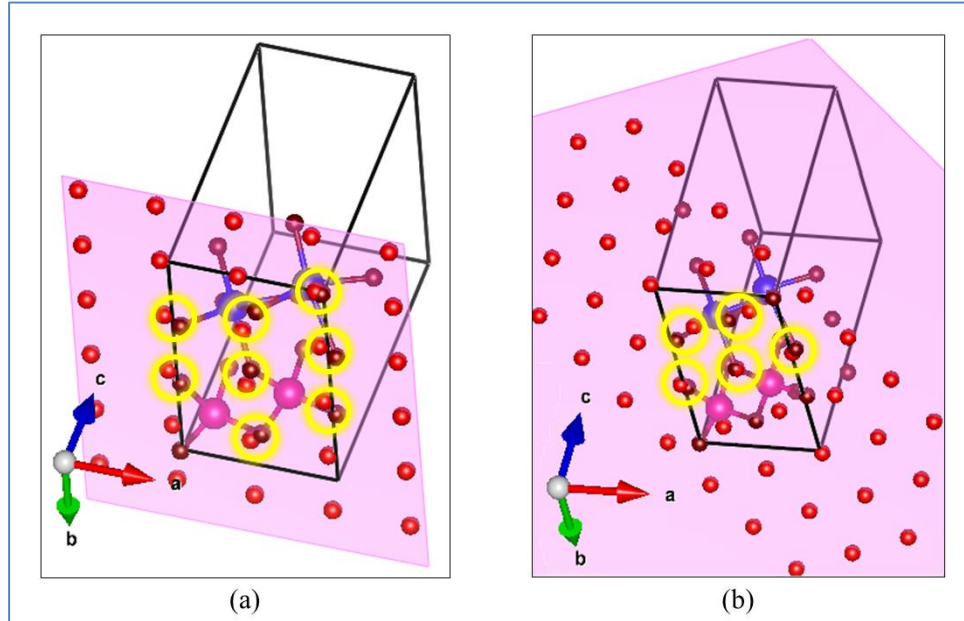


Figure 28: Graphical representation of the continuity of the oxygen polyhedra framework in epsilon ferrite grown on (100)-oriented YSZ. The continuity in the case of the “parallel” epitaxial match (a) seems, from the graphical representation, to be better than for the “non-parallel”, although, in both cases, it is not as good as for the case of epsilon ferrite grown on perovskites (111).

The correspondence between the oxygen frameworks would be also very high for the case of epsilon ferrite thin films grown on (0001)-oriented alumina: however, such substrate would introduce an even higher strain than LAO (111). Moreover, alumina has a lattice expansion coefficient smaller than both the other substrates and smaller than iron oxides, which, given the high temperature at which the growth occur, might induce high mechanical stress and strain, and even phase transitions during cooling. Either one or both of these explanations might be the reason why it is not possible to grow directly epsilon ferrite on top of alumina, but it is indeed possible to do it utilizing a buffer layer of GaFeO₃, which has smaller lattice parameter compared to ϵ -Fe₂O₃.

3.1.3 Thermal expansion coefficient of the utilized substrates.

A major feature of the substrates in relation to epitaxial growth, especially for depositions performed at such high temperature, is their thermal expansion coefficients. The values of the thermal expansion coefficient for the different substrates are listed in Table 3. As can be seen, only alumina holds a major difference compared to the other substrates: moreover, such value is smaller than the value for iron oxides (no data was available for epsilon ferrite, which should however behave similarly to hematite and maghemite). Such difference might be the cause of the non-possibility of achieving epitaxial thin films of epsilon ferrite directly on alumina. Gallium ferrite, which on the other hand grows epitaxially on alumina, being characterized by a thermal expansion coefficient of 7.8^{104} , might help relieving some of the thermal stress when used for buffer layer for the growth of $\epsilon\text{-Fe}_2\text{O}_3$ on LAO.

Substrate	Thermal Expansion Coefficient [10^{-6} K^{-1}]
YSZ	10.5
STO	9.4
LSAT	8 ~ 10
LAO	11.6
Alumina	5.8
GFO	7.8
Iron Oxide	7 ~ 12

Table 3: Thermal expansion coefficients for the different substrates (in red the ones that grant epitaxial growth).

Deposition features and “deposition window”.

As mentioned in the description of the deposition technique, different parameters might be adjusted in the PLD setup in order to obtain epitaxial growth of epsilon ferrite. Starting from the growth parameters reported by Gich *et al.* in the first report on epitaxially stabilized epsilon ferrite thin film deposited on STO (111), the growth parameters were optimized for the PLD chamber used during my doctorate. Thin films of epsilon ferrite were deposited by pulsed laser deposition utilizing a KrF excimer laser (wavelength 248 nm, pulse duration ~22 ns) with a pulse repetition rate of 5 Hz, focused on the surface of a 1 inch diameter ceramic target placed circa 5.5 cm away from the substrates with a fluence of $\sim 1.8 \text{ J/cm}^2$ (focused beam spot size $\approx 0.03 \text{ cm}^2$). The target was prepared by sintering Fe_2O_3 powders (Semiconductor Industries, 99.9% purity), resulting in a mixture of polycrystalline hematite ($\alpha\text{-Fe}_2\text{O}_3$) and amorphous Fe_2O_3 . Growth was performed

at a substrate temperature of 850 °C; such temperature was the maximum temperature achievable in the chamber with the substrate holder used. The synthesis was carried on in oxidizing environment, where the O₂ pressure was maintained at 75 mTorr. To ensure the highest surface quality and to achieve the correct termination, (111)-oriented STO substrates (both regular and miscut) were treated by wet etching using buffered oxide etch solution, composed of a 6:1 volume ratio of (40% NH₄F in water) and (49% HF in water). Furthermore, prior each deposition, the chosen substrates were cleaned in a sonic bath with acetone and isopropanol.

3.1.4 Effect of temperature and pressure on the growth of ϵ -Fe₂O₃ thin films.

Different temperatures and pressures were tested before finding the parameters yielding the best results. Phase stabilization was achieved for a very narrow conditions window.

As mentioned above, the films were grown at the highest temperature possible for the chamber available. Lowering the deposition temperature by more than 50 °C from the target temperature of 850 °C, leads to either non-formation of the epsilon ferrite phase or its non-epitaxial growth: analysis of the crystal structure by XRD of the films grown at temperatures lower than 800 °C resulted in diffractograms where only the peaks belonging to the substrates could be detected. Pressure lower than 65 mTorr lead to the pronounced formation of a secondary phase which was identified as magnetite Fe₃O₄. While such secondary phase was also present in very small quantity for the optimized conditions, synthesis at pressures lower than 65 mTorr lead to more intense peaks belonging to Fe₃O₄ in the x-ray diffractograms (which were non-detectable for growth under optimal conditions). Such behavior can be ascribed to the non-complete oxidation of the iron ions leading to a higher growth rate of magnetite (which includes both Fe³⁺ and Fe²⁺ in its lattice). An upper limit of 85 mTorr for the growth of epsilon ferrite was also found: exceeding this limit instead yielded to non-crystalline or non-epitaxial films. In such case, the non-formation of the epsilon phase could be due to the lower particles energy (higher gas pressure means lower kinetic energy of the plasma plume due to collision with the gas), which can impede the correct growth mode.

However, both tentative explanations on the effect of temperature and pressure on the phase stabilization are only hypotheses which would require a more comprehensive the study of the growth dynamics by an in situ characterization technique such as reflection high-energy electron diffraction (RHEED) in order to be verified.

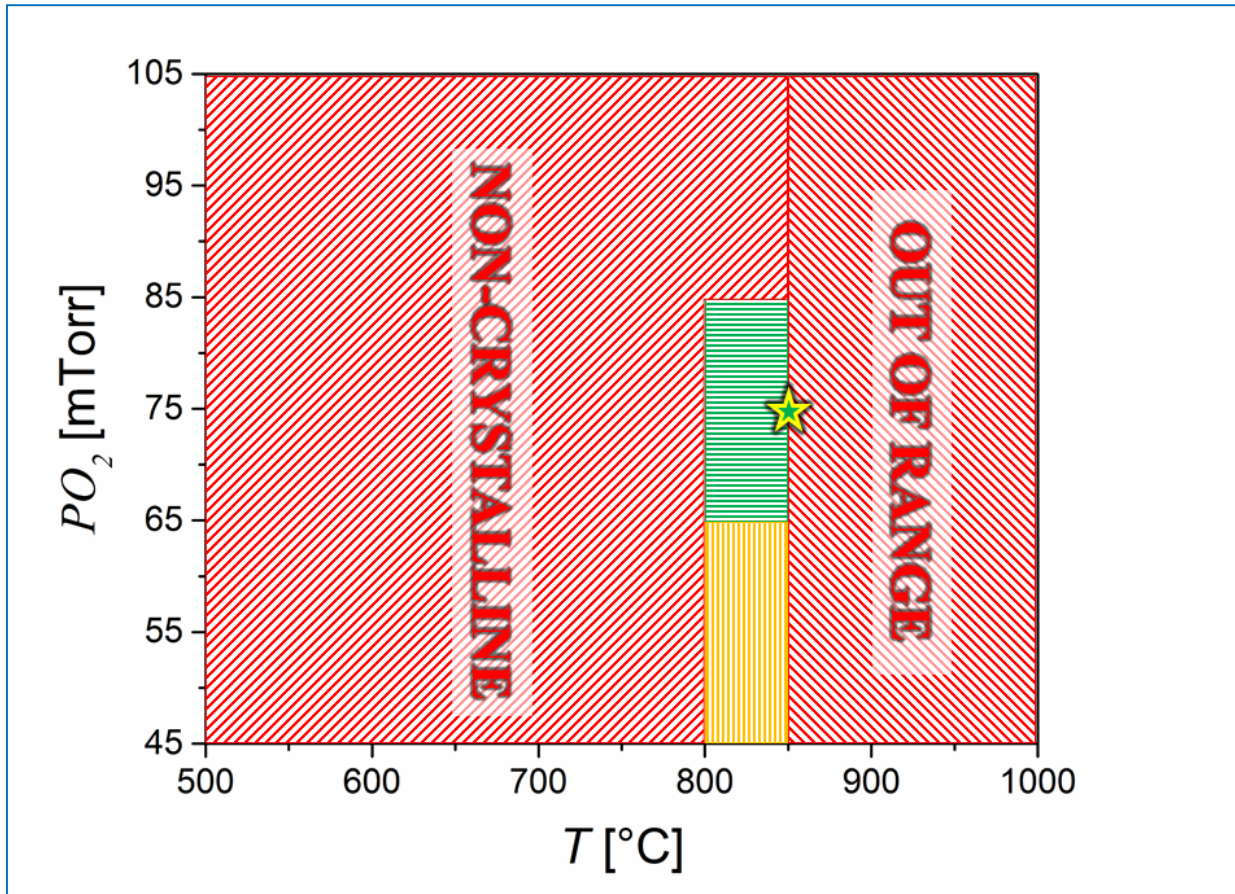


Figure 29: Optimal deposition temperature and pressure (star), and deposition window (in green) for thin films of epsilon ferrite. The area drawn in yellow depicts the condition for which extra magnetite was grown, while the areas in red are either non accessible with the utilized experimental setup or do not yield to the growth of epitaxial thin films.

3.1.5 Determination of the growth-rate and optimal thickness.

Thickness of the grown films was measured by profilometer and Atomic Force Microscopy (AFM), yielding a growth rate of $\sim 0.04 \text{ \AA/pulse}$, which was then used to estimate the thickness of every film given the known number of pulses used during the growth. Once the growth rate was determined, films with thicknesses between 25 and 250 nanometers were synthesized. After growing and characterizing (as described in the next sections) films of different thicknesses, the 50-100 nanometers thickness range was chosen as optimal thickness range, given how (i) above a certain critical thickness (that was detected to be around 150 nm), secondary and undesired secondary iron oxide phases become predominant, and (ii) films thinner than 50 nm are characterized by a very low magnetic moment which is masked by the signal given by the substrate in magnetic measurements.

3.2 Structural characterization of epsilon ferrite thin films.

3.2.1 Confirmation of epitaxial growth.

The films structure was first studied by XRD. Both classical Bragg-Brentano geometry ($\theta/2\theta$) and phi (φ) scans measurements were performed to confirm the epitaxial growth of (001)-oriented epsilon ferrite on the different used substrates (Figure 30). The first configuration was used to determine the out-of-plane orientation of the film and substrates as well as their mutual alignment, while the second helped understanding the in-plane orientation of the film with respect to the crystal structure of the substrate. Given the strong $K\beta$ lines signal arising from the substrates, in particular the one of (111)-oriented perovskites, which partially overlap with the peaks belonging to the film, a nickel filter was used in order to cut these peaks and have a cleaner diffractogram.

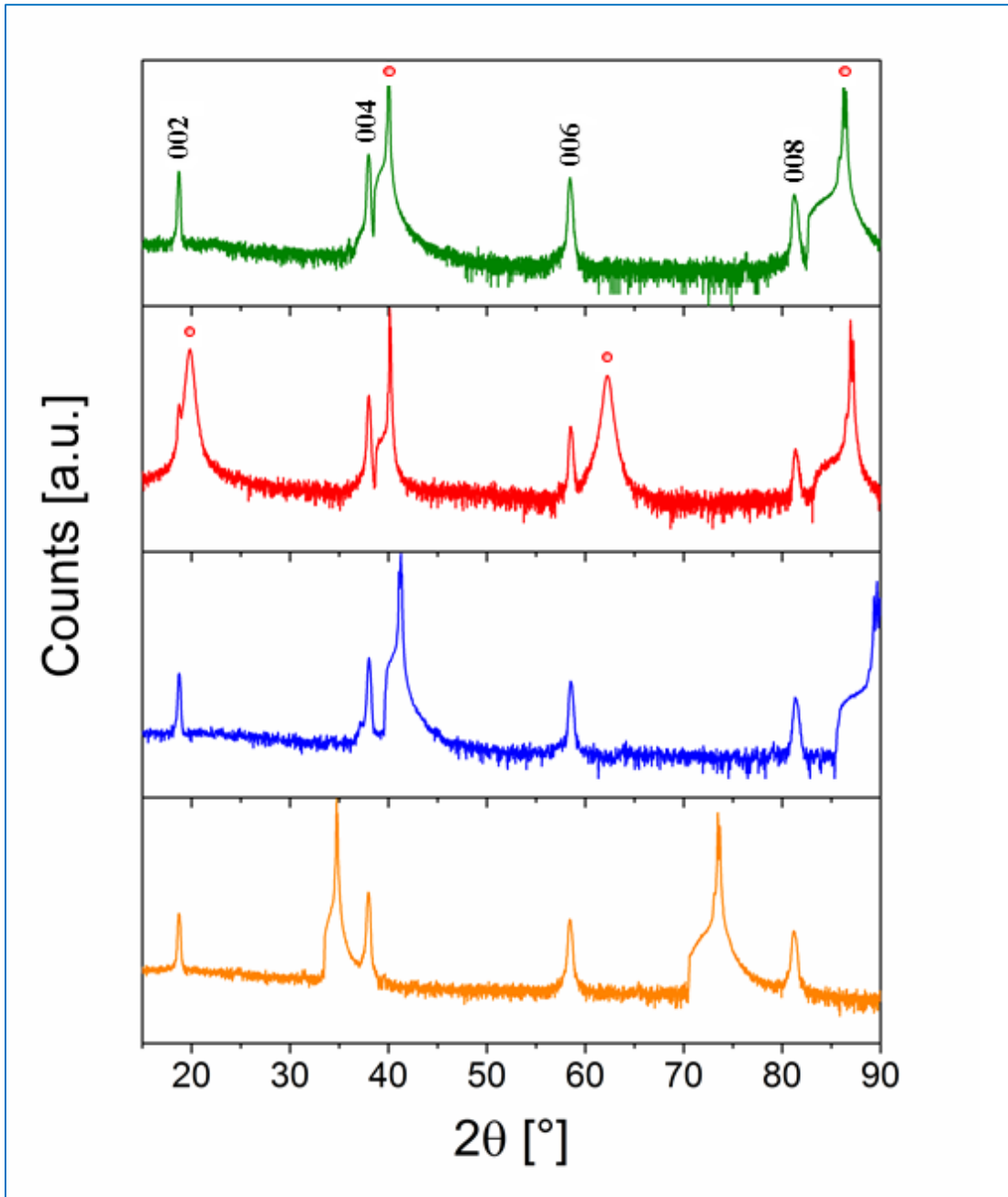


Figure 30: X-ray diffractogram for (001)-oriented thin films of epsilon ferrite grown on STO (111) (green line), LSAT (111) (red line), LAO (111) (blue line), and YSZ (100) (orange line). The peaks belonging to the film are the one of lower intensity marked in the top diffractogram and labeled with the corresponding index. The peaks belonging to the substrates are the high intensity ones marked with red dots in the two top sections.

Prior utilizing the Ni filter, evidences of formation of an extra phase were recorded and the peaks were attributed to highly constraint magnetite (Fe_3O_4) (see Figure 31). The presence of the extra phase was detected both on (111)-oriented perovskites (as shown for STO (111)), and for YSZ (100) substrates (not shown).

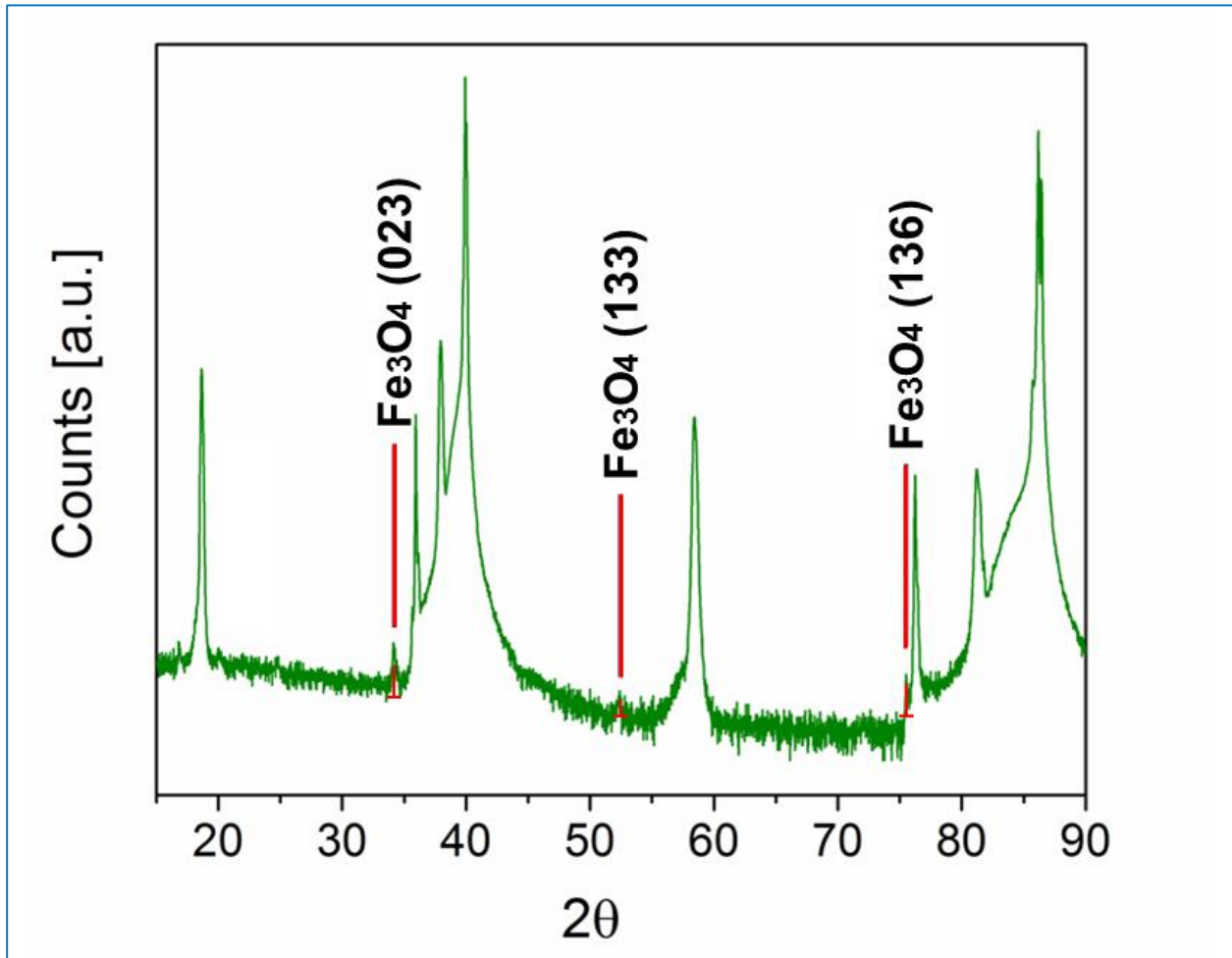


Figure 31: Diffractogram for a thin film of $\epsilon\text{-Fe}_2\text{O}_3$ (001) grown on STO (111). In red the peaks belonging to highly constraint magnetite are noted. Note also the secondary peaks arising from the substrate (marked in red).

One peculiarity detected when analyzing the $\theta/2\theta$ diffractograms of $\epsilon\text{-Fe}_2\text{O}_3$ (001) when grown on different substrates, was how the position of the peaks belonging to epsilon ferrite is independent from the choice of substrate (see Figure 32). Such a behavior means that the out-of-plane inter-planar distances do not vary, even though the in-plane stresses and strains are different. This could be explained by assuming that the oxygen polyhedra constituting part of the framework epsilon ferrite (see the unit cell in Figure 5) are able to rotate enough such as to accommodate the epitaxial strain without modifying the out-of-plane lattice

parameters (which gives the inter-planar distances responsible for the constructive interferences of x-rays resulting in peaks in the diffractogram). This absence of dependence on the substrate (and of the in-plane epitaxial strains induced by the substrate) of the out-of-plane lattice parameters is also seen when the different lattice parameters were calculated (shown below in Table 4).

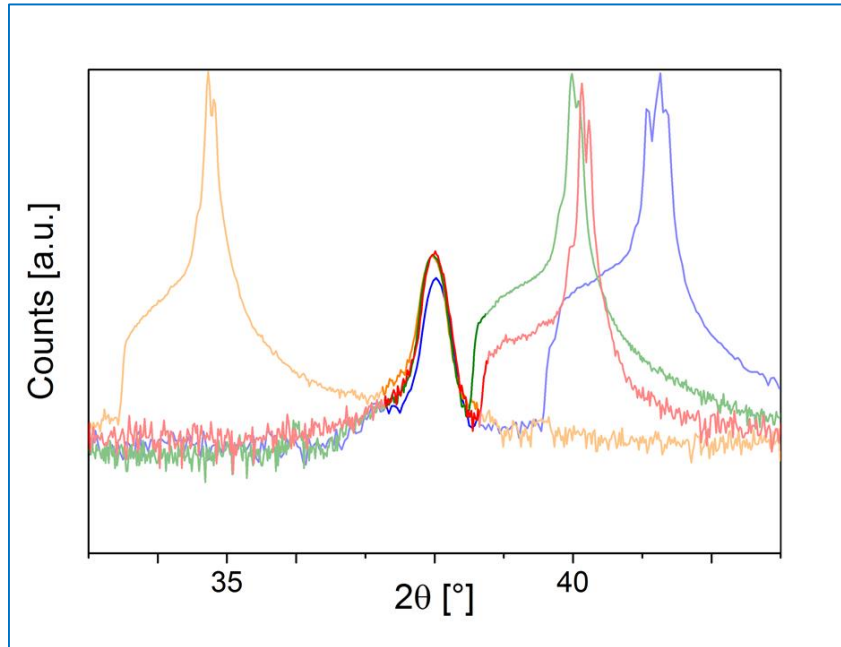


Figure 32: Detail of the 004 peak for thin films of epsilon ferrite grown on different substrates (same color code as Figure 30). Note how the position of the peak does not change with the different substrates.

In order to measure the three lattice parameters characterizing epsilon ferrite, and to confirm the presence of the two different variants of epitaxial ϵ - Fe_2O_3 grown on YSZ (100), the position of peaks associated with planes non-parallel to the film surface were investigated. The planes chosen for determining a and b lattice parameters (c was found easily from the main $\theta/2\theta$ scan), were the 132 and 013, respectively. The initial values of the 2θ angles, to be further refined, were found by simulating the powder diffraction pattern of an epsilon ferrite unit cell with atomic coordinates and lattice parameters of the unit cell of ϵ - Fe_2O_3 reported for nanoparticles (obtained by Rietveld refinement). This allowed us to estimate the value for both the position ($\theta/2\theta$) of the peaks, and the angle between the two planes considered and the surface (χ) (see Figure 20 for the angles in XRD). The values of the three lattice parameters for epitaxial thin films of epsilon ferrite when grown on different substrates are listed in Table 4.

Substrate	a [Å]	b [Å]	c [Å]
ϵ Nanoparticles	5.08	8.78	9.47
STO (111)	5.08	8.79	9.48
LSAT (111)	5.08	8.77	9.48
LAO (111)	5.08	8.78	9.48
YSZ (100)	5.08	8.73	9.48

Table 4: Lattice parameters found for epsilon ferrite epitaxial thin films grown on different substrates, along with the lattice parameters for epsilon ferrite nanoparticles.

By comparing the values of the lattice parameters experimentally found for epsilon ferrite when grown on different substrates with the one reported for nanoparticles, which can be found in the first line of Table 4 and were used as reference, it can be deduced that the films appeared to be completely relaxed independently from the substrates they were grown on. Moreover, almost no difference was found for the two lattice match granted by (100)-oriented YSZ. This evidence can strengthen the hypothesis that indeed the type of chemical bonds and the continuity in the oxygen framework, along with a compatible thermal expansion coefficient, are the essential conditions to insure the epitaxial growth of epsilon ferrite

In order to prove the mutual orientation of the film and the substrate, Phi-scans of the peak corresponding to the 013 plane of ϵ -Fe₂O₃ were performed along with the Phi-scan of the underlying STO and YSZ substrates, as shown in Figure 33.

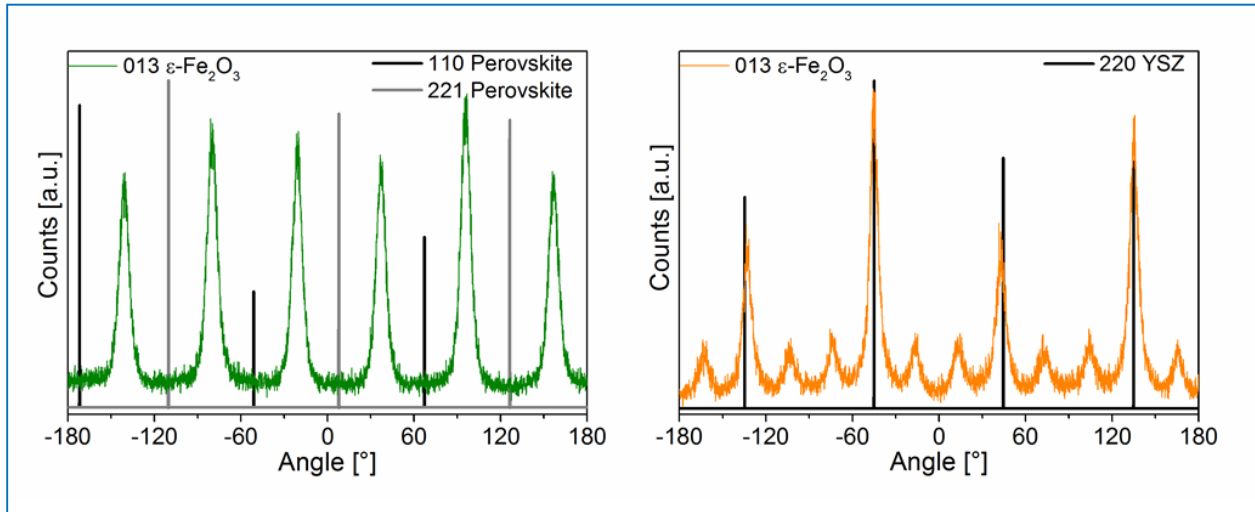


Figure 33: Phi scans for the 013 peak of epsilon ferrite when grown on (111)-oriented perovskites (left) and (100)-oriented YSZ (right), along with the scan of peaks belonging to the substrates, in order to infer the mutual orientation between the films and the substrates.

Films deposited on STO (111) were used as reference for the whole class of perovskite substrates, given how the structural (and functional, as it will be shown later) properties appeared to be consistent for the three perovskite substrates. Such analysis firstly confirmed the formation of twins for both (111)-oriented

perovskites and (100)-oriented zirconia. The different angular dependence originates in the different symmetry of the oxygen terminations of the two classes of substrates, hexagonal in case of (111)-oriented perovskites and cubic for (100)-oriented YSZ, as well as the presence of multiple epitaxial matches in the second case. Moreover, the Phi scan of the 013 peak of films grown on YSZ (100) highlighted how the peaks corresponding to the parallel direction, with a 90° symmetry, are more intense than the non-parallel ones, which appear at circa $\pm 30^\circ$ with respect to the parallel peaks. Very similar behavior was also seen and reported for epitaxial thin films of GFO (001) on YSZ (100)¹⁰⁵.

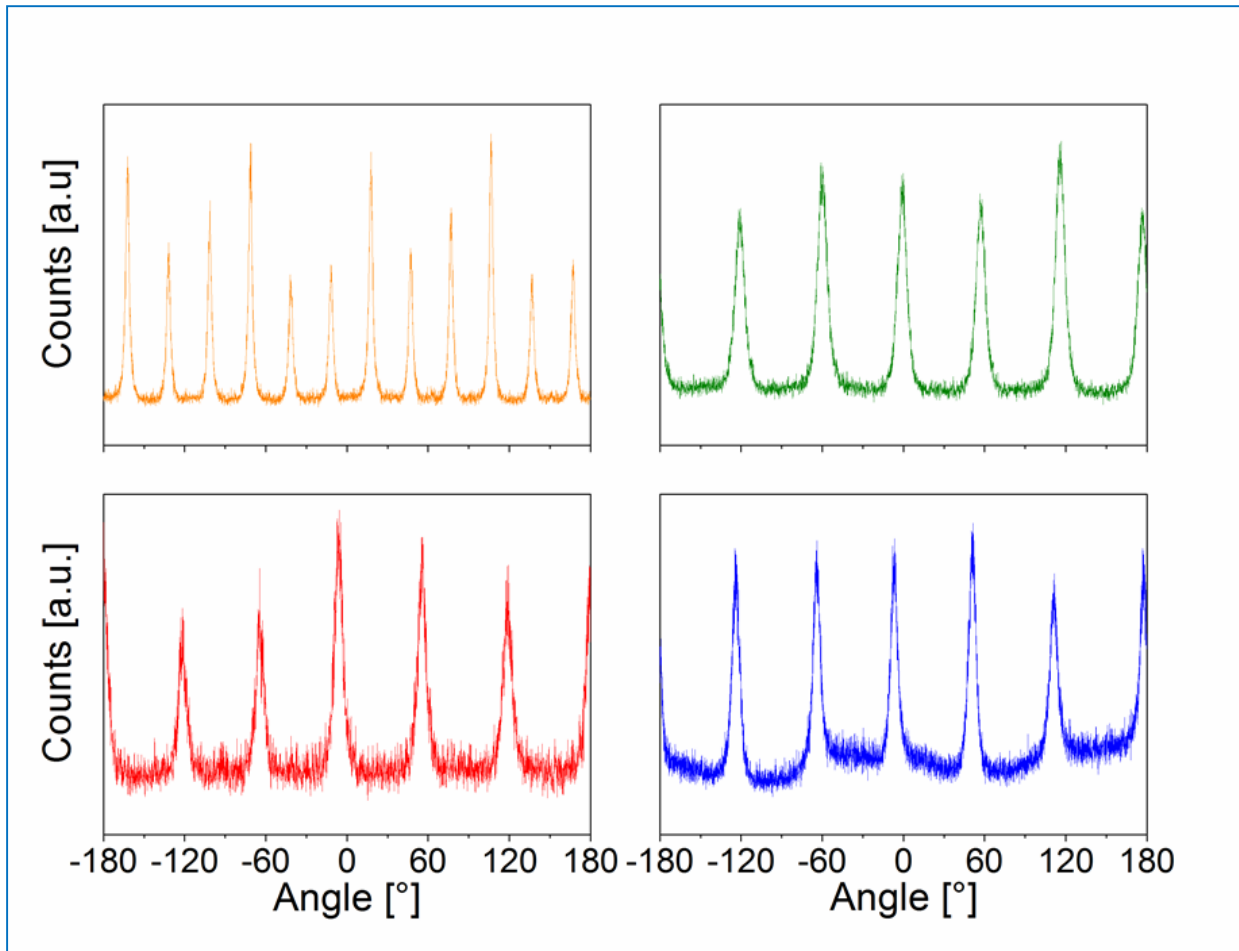


Figure 34: Phi scans for the 013 peak of epsilon ferrite thin films grown on different substrates: from the top left clockwise, on YSZ (100) (orange), STO (111) (green), LAO (111) (blue), and LSAT (111) (red).

Finally, very careful analysis of the structural properties led to the discovery of interstitial growth domains lying in between the main growth orientations that were shown in Figure 34. Such interstitial structures are characterized by smaller a lattice parameters compared to the main growth orientation (4.73 \AA opposed to 5.08 \AA), while b (8.69 \AA vs 8.78 \AA) and c (9.08 \AA in both cases) are almost identical. Such difference was

determined by comparing of the position of the 013 and 132 peaks for the two types of domains for films grown on YSZ (100) (Figure 35).

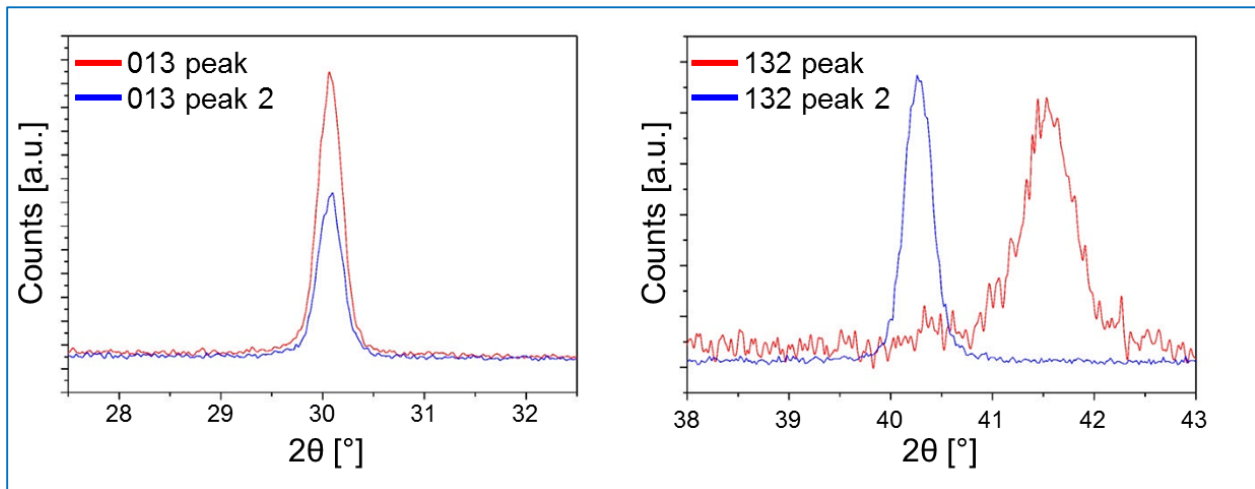


Figure 35: $\theta/2\theta$ scan around the peaks associated with the (013) and the (132) planes of epsilon ferrite. The two different variants (blue line for the “main” growth orientation, red line for the “interstitial”) for the 132 peak confirm the double epitaxy of epsilon ferrite on YSZ (100).

Analysis of the phi scans of the 132 peaks of both the main growth orientation and of the interstitial domains revealed how the interstitial growth domains are located $\pm 14^\circ$ around the main growth domains (Figure 36). Comparison of the counts in the phi scan for the two types of domains revealed how the interstitial domains are more prominent in epitaxial thin films of epsilon ferrite grown on (111)-oriented perovskites, characterized by peaks of amplitude equal in average to 30% the amplitude of the main peaks, compared to the films grown on (100)-oriented YSZ, which peaks have amplitude of less than 10% in average. Under the assumption that these interstitial domains lie at the boundaries of the main growth domains, the lower prominence detected for films grown on YSZ (100) might be due to the fact that there are more angular configuration of domains on YSZ (100), hence less space available for each interstitial domains compared to onto (111)-oriented perovskites. Conversely, there are two times more angular directions for the interstitial domains to grow on YSZ (100) than on (111)-oriented perovskites.

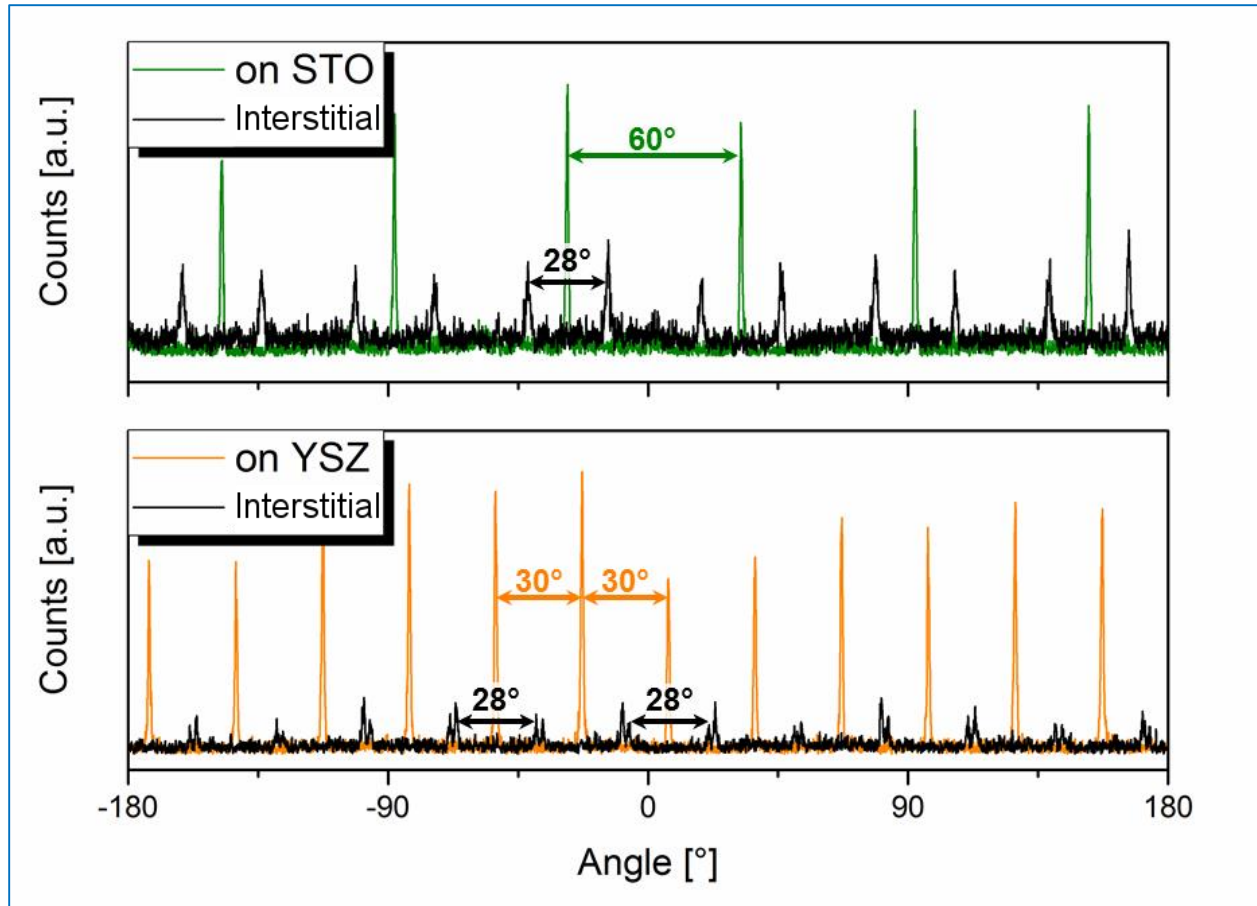


Figure 36: Phi scan for the 132 peaks of the main growth domains of epsilon ferrite grown on STO (111) (top – green) and YSZ (100) (bottom – orange) plotted along the phi scan of the 132 peaks of the interstitial domains, along with the separation between them.

3.2.2 Graphical representation of twins.

An easy graphical representation of the twins and their angular periodicity can be obtained by coupling the information gathered by angular x-ray diffractometry with the epitaxial matches granted by the different substrates that were depicted in Figure 25 and Figure 26, obtaining the two pictures shown in Figure 37.

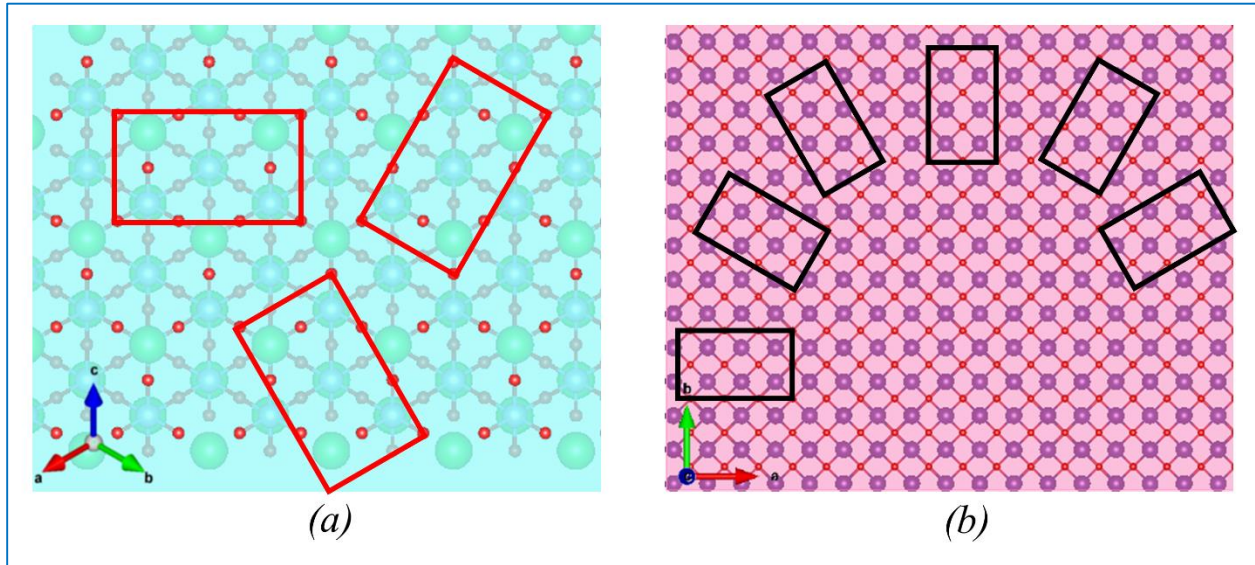


Figure 37: Graphical representation of the different growth orientations possible on (a) (111)-oriented perovskites, and (b) (100)-oriented YSZ.

For the case of epsilon ferrite grown on (111)-oriented perovskite, three epitaxial match were identified (Figure 37a), while six different ones were found for films grown on (100)-oriented YSZ (Figure 37b)^v. The three possible orientations for the epsilon ferrite twins on STO/LSAT/LAO (111) are with the a_ϵ lattice parameter aligned along the $[1 \bar{2} 1]$, $[1 1 \bar{2}]$, $[\bar{2} 1 1]$ directions of the substrate. For films grown on YSZ (100) the six different growth variants found are two “parallel” with b_ϵ aligned along the $[0 1 0]$ and the $[1 0 0]$ direction of the substrate, and four “non-parallel”, aligned along the $[1 \bar{1} 0]$, $[4 \bar{1} 0]$, $[4 1 0]$, and $[1 1 0]$.

^v Each growth orientation allows for a 180° rotation, as shown in Figure 37, thus creating a twice higher number of peaks in XRD Phi-scans.

3.2.3 Mosaicity effects.

By analyzing the broadening of the peaks in the phi-scans, it was possible to infer the presence of a so-called *mosaicity*, which is a certain degree of misalignment between cells belonging to the same growth domain, as schematically shown in Figure 38.

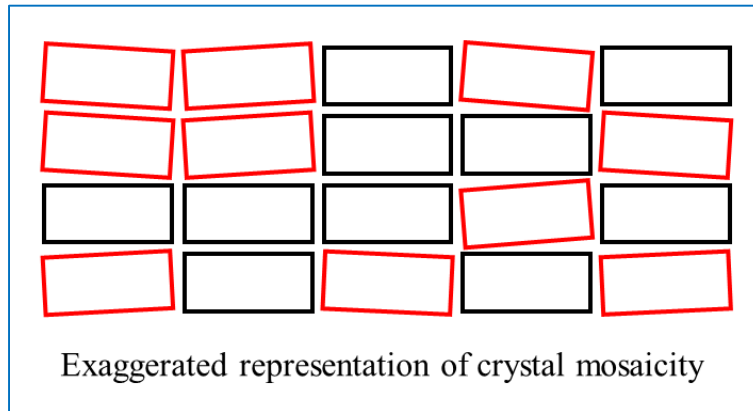


Figure 38: Graphical representation of mosaicity in one particular growth domain in a crystal. Such mosaicity effect can affect both plane parallel to the surface of the sample and perpendicular to it. In the first case, mosaicity will be studied with rocking curve measurements, in the second with Phi-scans.

The degree of lateral mosaicity (mutual in-plane alignment of the different growth orientations) is linked to the standard deviation of the Gaussian distribution which is assumed to describe the crystallite orientation. For the analysis of the mosaicity, the angular distribution of the 013 peaks of films both grown on (111)-oriented perovskites and on (100)-oriented YSZ were analyzed (Figure 39).

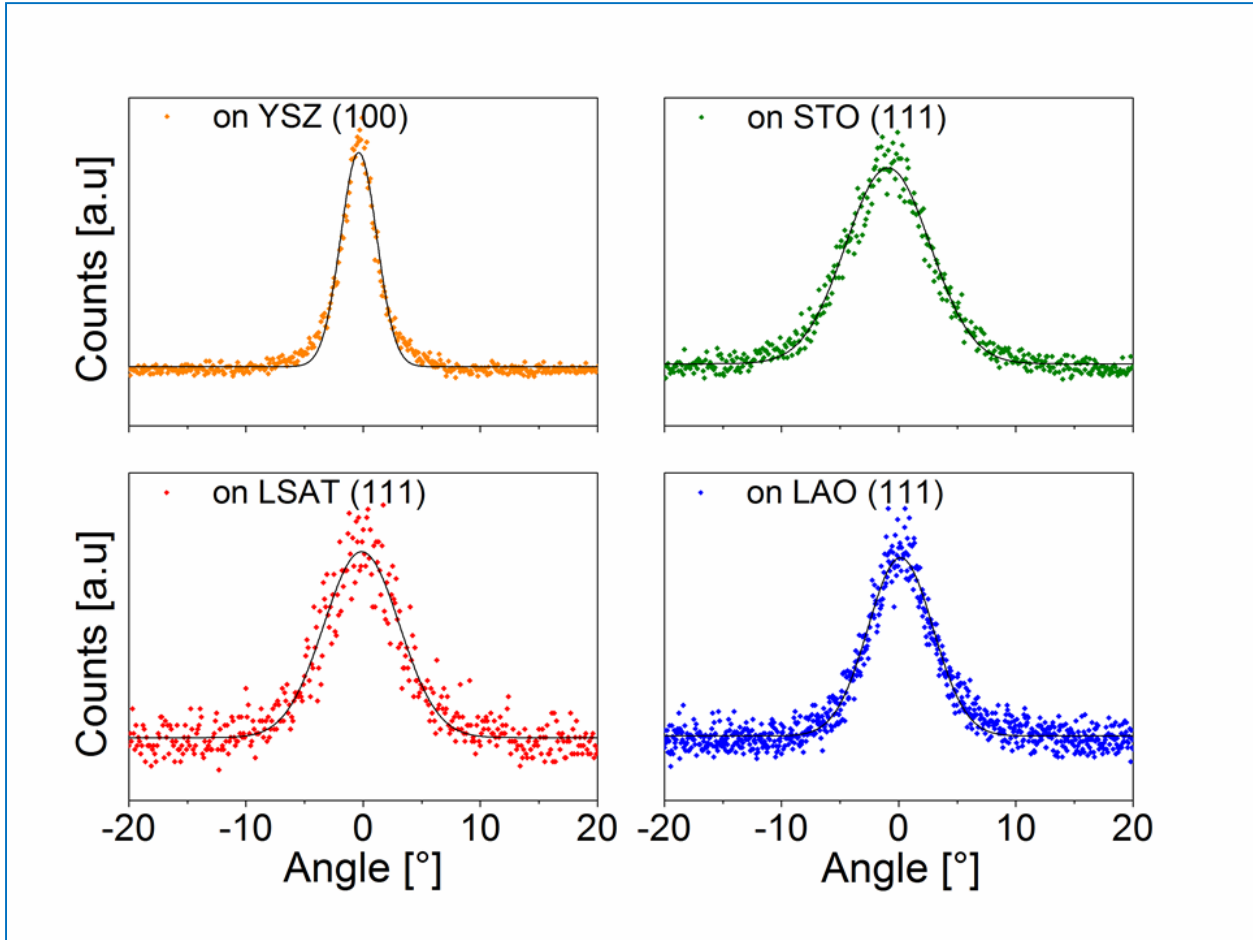


Figure 39: Dispersion in the angular dependence of the 013 peak for epsilon ferrite films: the experimental data are shown as symbols, while the Gaussian fit is represented by the black line. From the top left clockwise, on YSZ (100) (orange), STO (111) (green), LAO (111) (blue), and LSAT (111) (red).

The values found for the different substrates are shown in Table 5; what emerges is that (111)-oriented perovskites yield a higher degree of mosaicity of the ϵ - Fe_2O_3 films compared to (100)-oriented zirconia. Moreover, it appears that the mosaicity decreases for increased compressive strain: this might be due to a higher degree of rotational freedom of the iron polyhedra in epsilon ferrite given by the oxygen termination of the perovskites in comparison with YSZ.

Substrate	SIGMA - Gauss
YSZ (100)	1.54°
STO (111)	3.60°
LSAT (111)	3.23°
LAO (111)	2.78°

Table 5: Values for the standard deviation of the Gaussian fit of the Phi-scan of the 013 peaks for films grown on different substrates.

3.2.4 Rocking curve analysis.

In order to evaluate the degree of alignment between the (00*l*) planes, parallel to the surface of the sample, which is often in the literature defined as out-of-plane mosaicity, the rocking curve of the (004) peaks of ϵ -Fe₂O₃ were studied for each substrate. Similarly, to what was done for the analysis of the Phi-scan, the peaks were fitted and the full-width at half-maximum was used as parameter; this time however, a Lorentzian curve was utilized for the fit, given the better fit given in comparison to a Gaussian fit. As a reference, the width of the Lorentzian function used to fit the rocking curves obtained from a bare STO (111) substrate and a bare YSZ (100) substrate were also measured, finding for both a width circa 0.025°.

The results, summarized in Table 6 and portrayed in Figure 40, show how the films grown on different substrates exhibit low degree of dispersion, signifying that the films are well oriented out-of-plane. This should not come as surprising given how the epitaxial ϵ -Fe₂O₃ films appear to be fully relaxed out-of-plane and it reinforces the idea of the rotation of the epsilon ferrite polyhedra to accommodate the mismatch induced by the different substrates. A slightly higher dispersion was found for the films grown on YSZ (100), which could be due to the higher number of in-plane variants which are allowed on YSZ (100), as explained in section 3.2.2.

Substrate	SIGMA - Lorentz
YSZ (100)	0.32°
STO (111)	0.13°
LSAT (111)	0.2°
LAO (111)	0.18°
Perovskite (111)	0.17°

Table 6: Values of the standard deviation of the Lorentzian fit for the Rocking curve of 004 peaks of epsilon ferrite thin films deposited on different substrates.

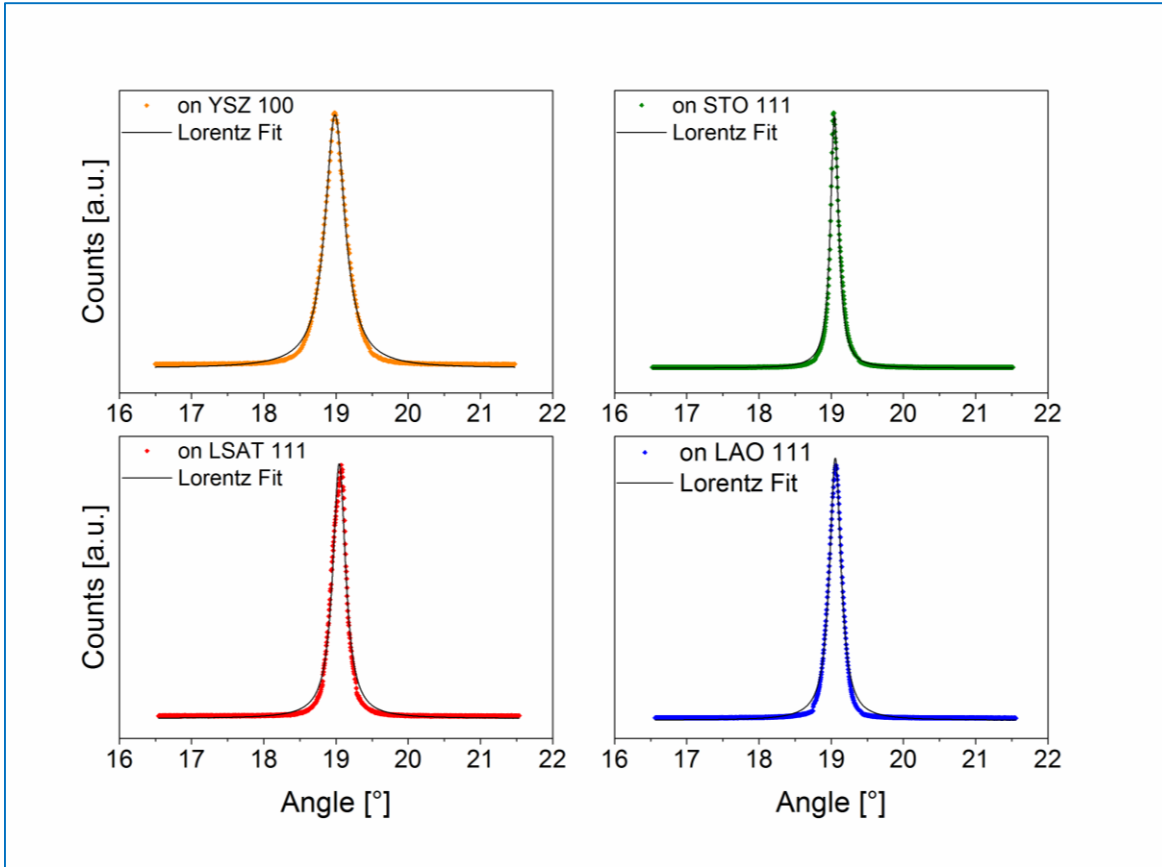


Figure 40: Rocking curve measurements for the 004 peak for epsilon ferrite films: the experimental data are shown as symbols, while the Lorentzian fit is represented by the black line. From the top left clockwise, on YSZ (100) (orange), STO (111) (green), LAO (111) (blue), and LSAT (111) (red).

3.2.5 Structural characterization via transmission electron microscopy.

Aberration corrected Scanning Transmission Electron Microscopy (STEM) high-angle annular dark-field (HAADF) imaging further confirmed the epitaxial growth of epsilon ferrite on STO (111) and YSZ (100); in such case, STO (111) was chosen as the substrate to exemplify the growth of films deposited on (111)-oriented perovskites substrates (the films grown on LSAT and LAO showing similar behavior). In the images recorded for epsilon ferrite thin films grown on STO (111), a very thin 'buffer' layer (few angstroms thick) was detected at the interface between the substrate and the film (Figure 41). Such interfacial buffer layer appears to be more pronounced (few nanometers thick), for $\epsilon\text{-Fe}_2\text{O}_3$ grown on YSZ (100) (Figure 42). The dimension of the buffer layer is consistent with the degree of continuity of the oxygen framework that was discussed in Section 3.1.2 (*i.e.* the better continuity in the oxygen framework for films grown on perovskites than for the ones grown on YSZ). Considering that XRD has indicated the presence of a parasitic phase, which we ascribed to magnetite, this parasitic phase might be located at the boundaries between the different growth domains, or it could be located at the interface with the substrate. In the case of epsilon ferrite thin films grown on YSZ (100), the interfacial layer most probably consists of magnetite. This will be further supported by the magnetic measurements, which will be shown in the following.

The presence of multiple in-plane growth variants (twins) is observed (areas in the TEM images with different contrast) for the films grown on both family of substrates: however, the twins of the films grown on YSZ (100) appear to form pillar-like structures, which is in contrast with the case of films grown on (111)-oriented strontium titanate, where such strong pillar-like structures were not observed (these observations of our group are consistent with what has been reported in the literature⁴⁸). The width of the pillars appear to be of circa 20 nm, which coincides with the average thickness found for epsilon ferrites nanorods⁴⁵. Therefore, it is challenging to tell whether this occurrence represent a hint of island (Volmer-Weber) growth mode, or is related to the maximum width of epsilon ferrite and its growth domains.

Finally, by selecting areas of a highly detailed picture belonging to different growth orientations and using Fourier transform enhancement software to improve the contrast of the image, we were able to pair the different structures observed in the twins with graphical unit cells rotated according to the epitaxial relationships with the substrate described above, thus convincingly confirming the proposed epitaxy relationships derived from XRD analysis.

For the images gathered for thin films grown on (111)-oriented STO, only one of the three possible orientations was detected. By comparing the orientation of the substrate in the high resolution image (Figure 41b) with the graphical representation (shown at the bottom left), it was possible to simulate the three different orientation of the epsilon ferrite twins (shown on the side); of these three orientations, only one

was observed (the twin oriented along $[1\bar{2}1]$ direction, with b_ϵ pointing towards the reader, highlighted in red), as shown in the Fourier transform corrected area (the blue square) and the corresponding epsilon ferrite graphical representation. In the detail, high contrast atomic planes are alternated with lower contrast ones, in good agreement with the graphical representation where plans with high overlap between the iron atoms at different depth of the sample (in such case, the “yellow” and “green” site), alternate with plans with lower overlap (the “blue” and “pink” atoms).

For the case of epsilon ferrite thin films grown on (100)-oriented YSZ, there appears to be reasonable agreement between the experimental observation and calculations of HAADF images and the [010] projection of the ϵ -Fe₂O₃ crystal structure in the red frame and in the [410] or $[4\bar{1}0]$ projection for the green and blue frames (Figure 42b). However, the agreement between the experimental pattern in the images and calculations and projected structure shown, assuming the Fe ions are only visible in HAADF image, assuming the Fe ions are only visible in HAADF image, does not appear to be suitable for the area highlighted in the yellow frame, due to the possible overlap of two crystals in the projection of the foil. Nevertheless, such analysis helps to visualize the clear difference among the different growth orientations and tries to match the different growth domains observed with the possible corresponding unit cell orientation.

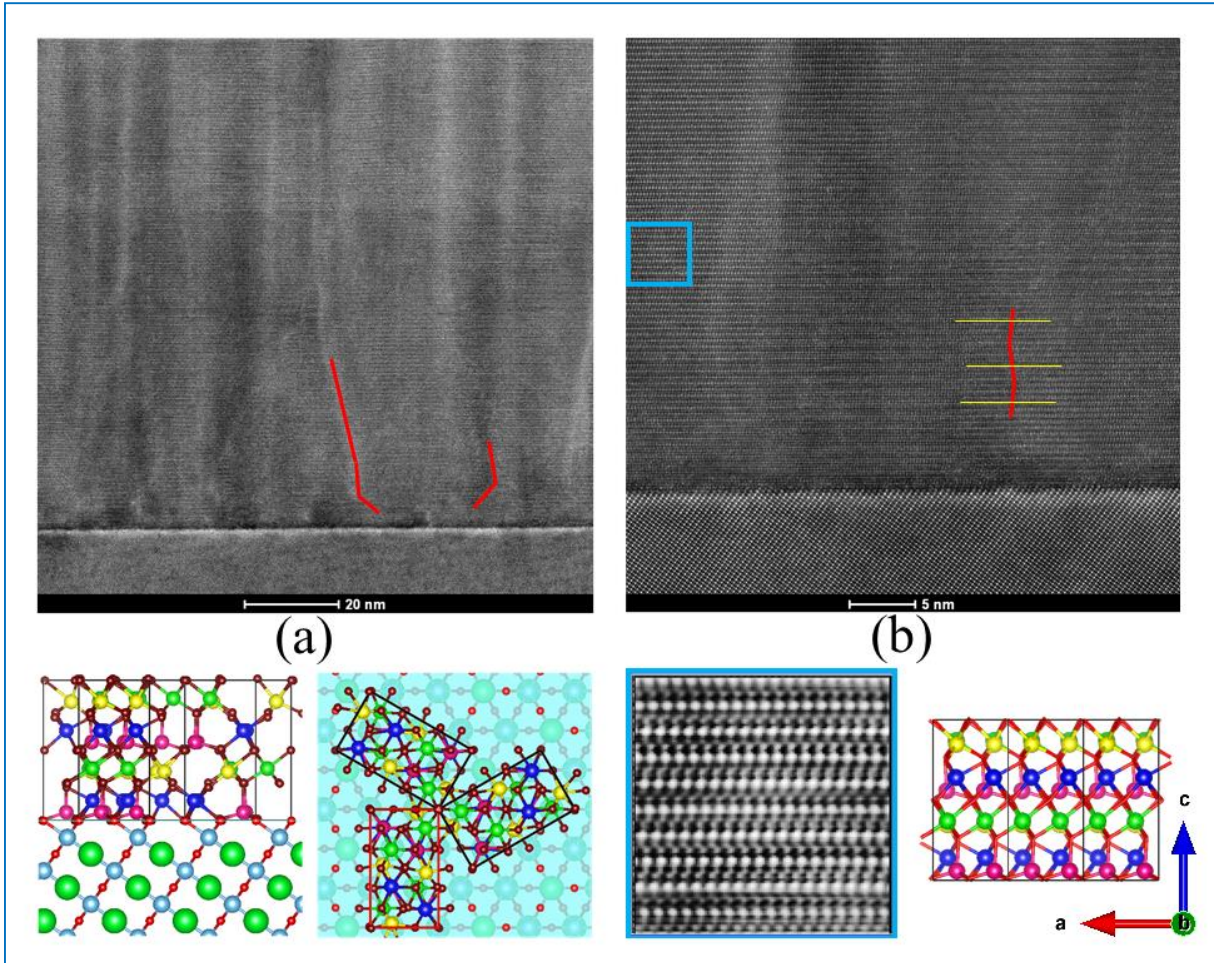


Figure 41: (a) STEM image of a circa 120 nm thick film of epsilon ferrite grown on STO (111), highlighting the formation of twins, denoted by the areas with different contrast, separated by randomly oriented boundaries (as noted by the red lines), (b) detail of the interface between the substrate and the film, showing the really sharp interface between (111)-oriented strontium titanate and epsilon ferrite. Below: (1st from the left) graphical simulation of the interface between STO (111) and epsilon ferrite, portraying the same orientation as STO seen in the TEM image. (2nd from left) top view of the epsilon ferrite twins, with the same orientation kept for the substrate, highlighting (in red) the only detectable orientation, which is magnified in the light blue selected area (3rd from left) which is portrayed next to the simulated ϵ -Fe₂O₃ structure rotated according to the proposed epitaxy relationship (4th from left).

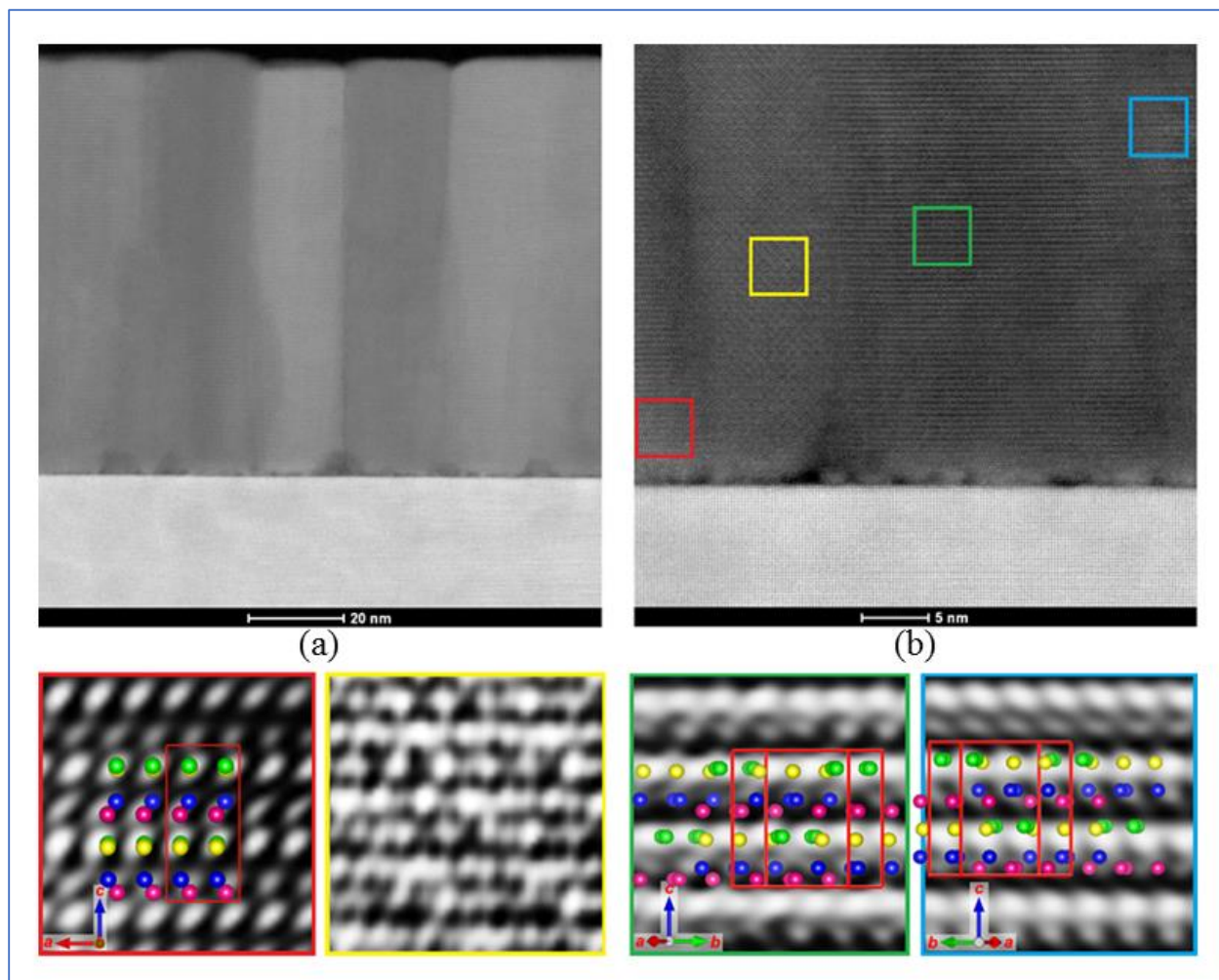


Figure 42: (a) STEM image of a circa 100 nm thick film of $\epsilon\text{-Fe}_2\text{O}_3$ on YSZ (100) highlighting the formation of pillar-like twins, (b) detail of the interface between the substrate and the film, evidencing the formation of ‘bubbles’ of a foreign phase (most likely Fe_3O_4) at the interface. Below: high-magnification of the 4 colored selected areas overlapped with simulated $\epsilon\text{-Fe}_2\text{O}_3$ structures rotated according to the proposed epitaxy relationships to further prove the existence of different growth domains with different in-plane orientations. If the orientation in the red box, with the b axis pointing out-of-plane is taken as 0° , the unit cells depicted in the other boxes are rotated, respectively by 300° (green), and 120° (light blue) (note that the 2 last unit cells (green) and (light blue) have a 180° rotational symmetry). No match was found for the yellow selection, probably due to the overlap of two different growth domains in the depth of the sample and overlapping in the STEM image.

3.3 Conclusions

To conclude, the growth of epitaxial thin films of epsilon ferrite of thickness comprised between 25 and 150 nanometers was achieved on single crystalline (111)-oriented perovskite substrates, and on (100)-oriented single crystalline YSZ. Within the very narrow window for the growth conditions yielding the epsilon phase of Fe_2O_3 , making the synthesis of epsilon ferrite thin films quite challenging, high quality (001)-oriented films were obtained.

The continuity of the oxygen framework, along with a good match of the lattice expansion coefficient, appears to be key to grant epitaxial growth and stabilize the metastable $\epsilon\text{-Fe}_2\text{O}_3$.

Structural characterization performed by x-ray diffractometry confirmed the orientation of the films and how the out-of-plane lattice parameter appears totally relaxed disregarding the thickness of the films.

The in-plane mutual orientation of the films and the substrates was also probe by XRD, revealing how the films are characterized by different growth orientation (twins). Such twins display a 6-fold symmetry for films grown on (111)-oriented perovskites, while the ones grown on (100)-oriented YSZ are characterized by a 12-fold symmetry. Both symmetries are coherent with the symmetry of the oxygen framework of the surface of the substrates and the epitaxial matches found (remember for instance the two possible matches of $\epsilon\text{-Fe}_2\text{O}_3$ on top of YSZ (100)).

A detailed study of the XRD phi scans led to the discovery of interstitial growth domains of epsilon ferrite, growing between the “main” orientations. Such domains are characterized by smaller in-plane lattice parameter, and while always present, are observed more for the case of thin films grown on (111)-oriented perovskites, which display a less “packed” angular dispersion of the main growth domains.

High definition transmission electron microscopy highlighted several difference between the films grown on STO (111) and films grown on YSZ (100). The first appear to have sharper interfaces (only few Angströms thick), while the second are characterized by a rather thick (few nanometers) buffer layer. Moreover, for the films grown on YSZ (100), the different twins appear to form pillar-like structures that extend from the interface with the substrate to the film surface. Such structures were not noted for films grown on STO (111). Finally, for films grown on both substrates, it was possible to pair simulation of epsilon ferrite unit cell with the image recorded by TEM, and for the case of the films grown on YSZ, it was also possible to identify different growth orientations in the same image.

Chapter 4 FUNCTIONAL CHARACTERIZATION OF EPSILON FERRITE THIN FILMS

This chapter presents the characterization of the functional properties of the epsilon ferrite epitaxial thin films grown by pulsed laser deposition described in detail in the previous chapter.

Given the initial scope of the research project, which was to fabricate a material characterized by high magnetocrystalline anisotropy, thus having a very high magnetic coercive field, the first part will be dedicated to a detailed magnetic characterization of $\epsilon\text{-Fe}_2\text{O}_3$ thin films. Magnetic hysteresis loops of films deposited on different substrates were measured with a vibrating sample magnetometer. Given the high in-plane magnetocrystalline anisotropy characterizing epsilon ferrite, both in-plane and out-of-plane loops were recorded and their shape and properties were compared.

Moreover, in order to further investigate the presence of the secondary phase that was discovered during the structural characterization, temperature characterization of the magnetization was performed. An involuntary and unexpected phase transition was also triggered and observed during such measurements.

As was done for structural characterization, the differences in the magnetic properties for films grown on different substrates were investigated. In particular, we focused on the angular dependence of the magnetization, given the very different angular symmetry of the films grown on perovskites compared to films grown on yttrium-stabilized zirconia.

The magnetic properties were also probed on the microscopic scale, by magnetic force microscopy, and although a signal was indeed measured, no clear interpretation could be given.

Ferroelectric characterization was performed on the macroscopic and microscopic scale by using a commercial ferroelectric tester and piezoresponse force microscopy. The macroscopic measurements were characterized by high leakage currents, making impossible to record clear ferroelectric hysteresis loops. Microscopic measurements instead gave clear hints about the presence of polarization.

Last but not least, the ferromagnetic resonance frequency was estimated indirectly, by comparing the in-plane and out-of-plane hysteresis loop and by THz-TDS.

4.1 Magnetic characterization of the epsilon ferrite thin films.

4.1.1 Magnetic hysteresis and temperature dependent measurements.

The macroscopic magnetic properties of epsilon ferrite thin films were analyzed via Vibrating Sample Magnetometry (VSM). The first step in the magnetic characterization was to measure the hysteresis loops of the samples, with the magnetic field applied first parallel (in-plane) and then perpendicular (out-of-plane) to the film surface (Figure 21 for the schematics). In order to obtain solely the film signal, magnetic contributions of the sample holder (glass rod) and the substrates were measured separately and subtracted from the total signal.

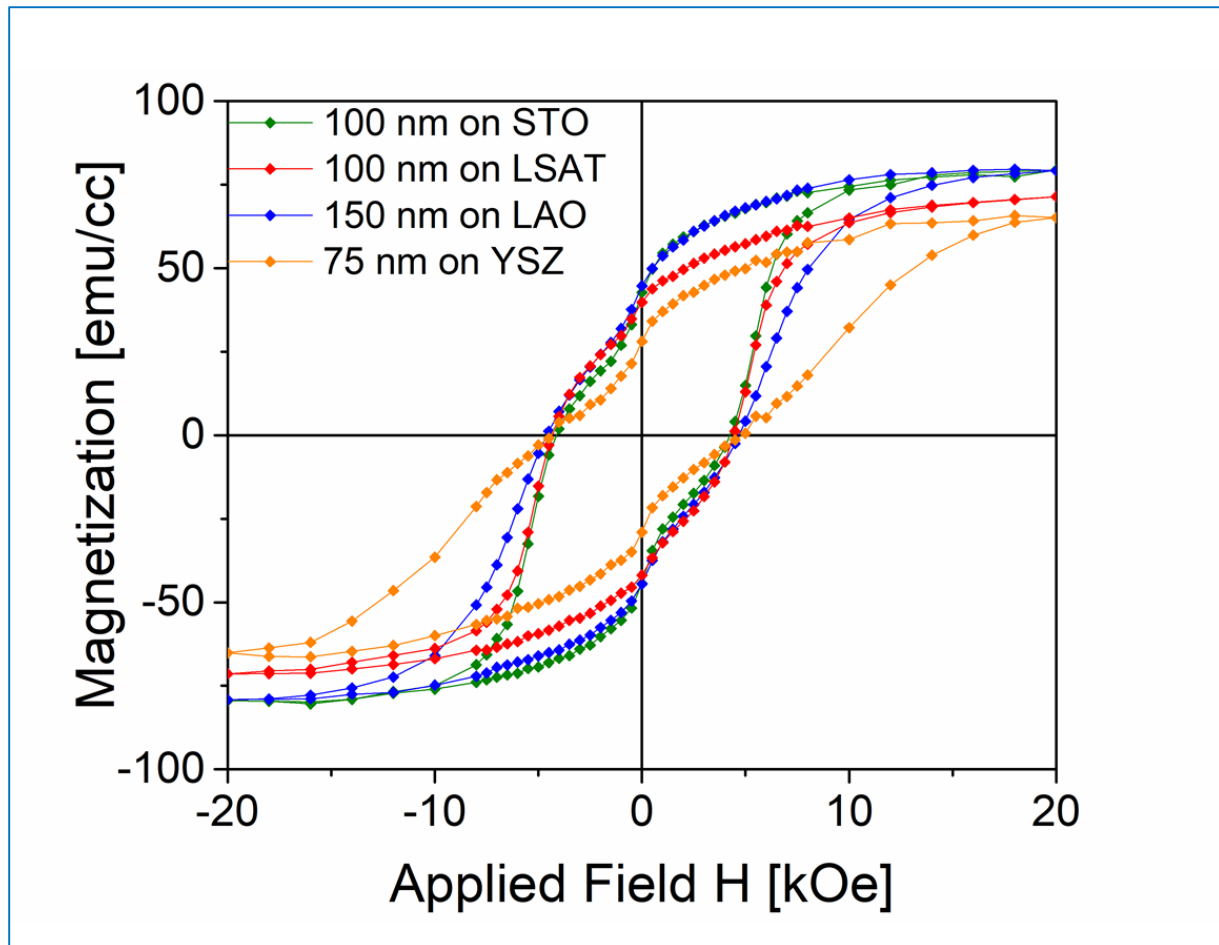


Figure 43: Hysteresis loops recorded in-plane for thin films of epsilon ferrite of various thickness deposited on the four substrates that grant epitaxial growth (same color code as XRD measurements).

As shown in Figure 43, the hysteresis loops are characterized by two notable elements: a high coercive field, and the presence of a shoulder (or “pinch”) for low applied fields in the loops. While the first element is a confirmation of the high anisotropy of the films (high coercive fields are an effect of a strong magnetic

anisotropy), the second can be explained by the simultaneous presence of epsilon ferrite and a secondary magnetic phase; as shown before in the section on structural characterization, such secondary phase was identified as randomly oriented magnetite by x-ray diffractometry. Further evidences of its being magnetite were obtained by studying the temperature dependent properties of the magnetization which will be shown further in this section. This explanation is in contrast to the ones reported in the literature to explain the 'pinched' hysteresis loop, resorting to the presence of antiphase boundaries (APB) between the differently oriented growth domains¹⁰⁶, where the magnetization may, for example, lie perpendicular to the film surface, or to the presence of nanostructures which may grow on top of the film, as reported for CoFe_2O_4 epitaxial thin films¹⁰⁷. However, the belief of my collaborators and myself is that the simplest manner to explain it, overlooked so far in the published literature, is the presence of a soft magnetic phase in addition to epsilon ferrite.

The differences in the values of magnetization at saturation M_S and remanent magnetization M_R for the different loops recorded for films grown on different substrates, can either be ascribed to the error in estimating the thicknesses of the different films, which is calculated by multiplying the estimated growth/rate by the number of pulses of every deposition, or to a not perfect alignment of the applied field along one of the magnetic easy axes of the sample (the dependence of the magnetic properties with varying applied field angle will be described more in detail later in this chapter), or to a difference in the amount of the soft secondary magnetic phase present in the sample. However, the films appear to have consistently exhibit high coercivity irrespective of the type and symmetry of substrates they were grown on.

Finally, and most importantly, the strong difference in the coercive field and in the approach to saturation at the maximum applied field between the in-plane and out-of-plane measurements confirms the high magnetic anisotropy of the epsilon ferrite epitaxial films (see Figure 44 for the comparison of the in-plane and out-of-plane loops for films deposited on YSZ (100)).

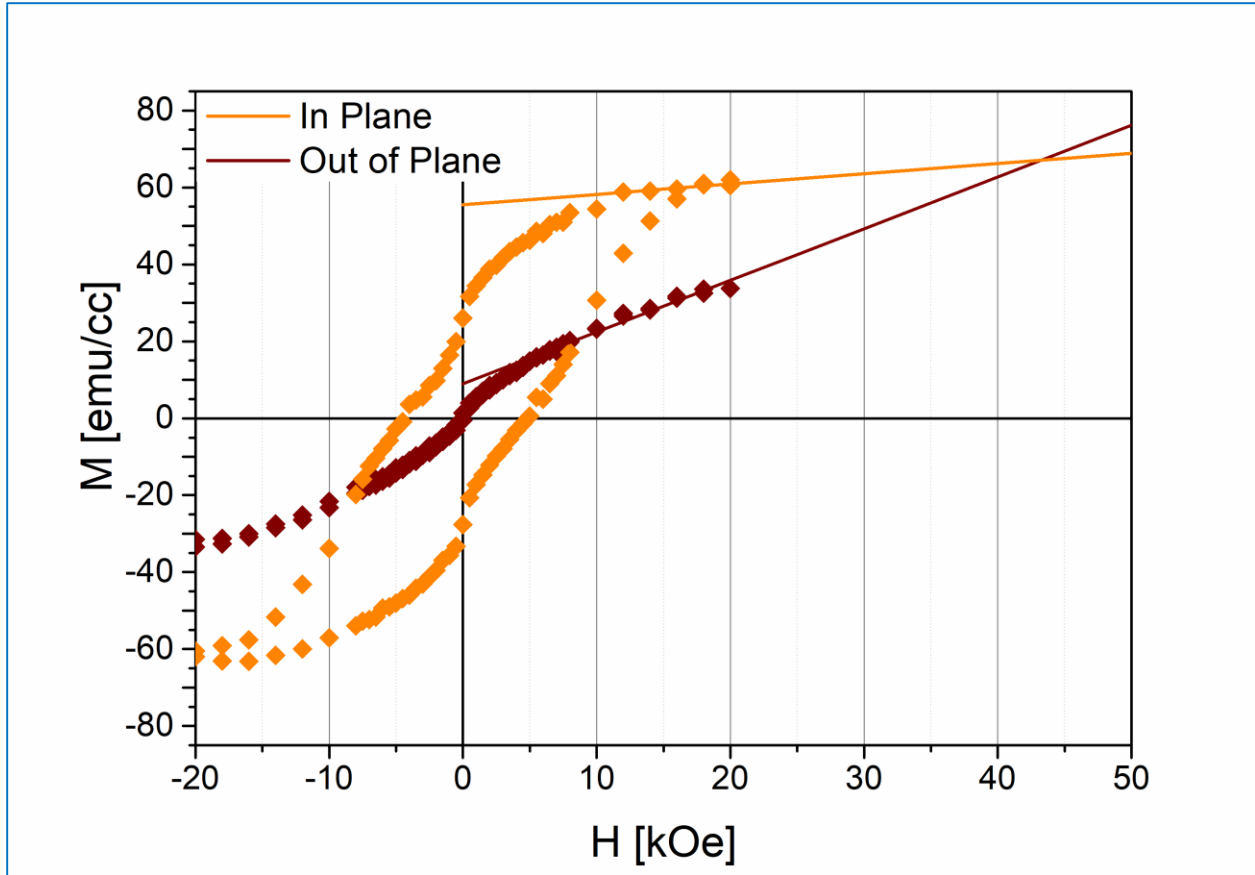


Figure 44: Estimation of the anisotropy field (the point of intersection of the linearization of the saturation part of the loops recorded in and out-of-plane) for a thin film of epsilon ferrite grown on YSZ (100).

The comparison of the loops measured in the two configurations allowed, by extrapolating the values in the linear regime for both the in-plane and out-of-plane hysteresis, to estimate the anisotropy field to be ~ 43 kOe (Figure 44)¹⁰⁸. This value, along with the values of magnetization at saturation and coercive field that were extrapolated from the plot of the hysteresis loops, is smaller than those reported in the case of epsilon ferrite nanoparticles ($M_s \approx 15$ emu/g, which gives $M_s \approx 81$ kA/m using 5.4 g/cc as density for epsilon ferrite, $H_C \approx 20$ kOe and $H_A \approx 65$ kOe)⁴⁰. While nanoparticles would be monodomain, the lower coercivity measured in our epitaxial films can possibly be explained by the presence of multiple growth variants, each with its easy axis in a different direction, thus averaging the magnetic hysteresis loops along several magnetic easy axes. As a consequence, it is possible that our thin films are not completely saturated when subjected to a field of 20 kOe, which is the maximum field of our VSM. As a consequence, the magnetization at saturation, the coercive field and anisotropy field values obtained here can be considered as lower limits.

Temperature dependent measurements of the remanent magnetization under no field and with a small applied magnetic field of 1000 Oe are presented in Figure 45. A ferromagnetic to paramagnetic transition is observed at a temperature of ≈ 460 K, which was attributed to ϵ -Fe₂O₃. The Curie temperature $T_C \approx 460$ K of the ϵ -Fe₂O₃ thin films is slightly lower than the one reported for ϵ -Fe₂O₃ nanoparticles ($T_C \approx 490$ K)⁴³. Measurements under a small applied magnetic field of 1000 Oe, well below the coercive field of the hard magnet ϵ -Fe₂O₃, but larger than the coercive field of a soft magnet, does indeed reveal the presence of a soft secondary ferromagnetic phase with a T_C higher than 550 K, consistent with the presence of some Fe₃O₄ (T_C of Fe₃O₄ = 850 K) observed by XRD.

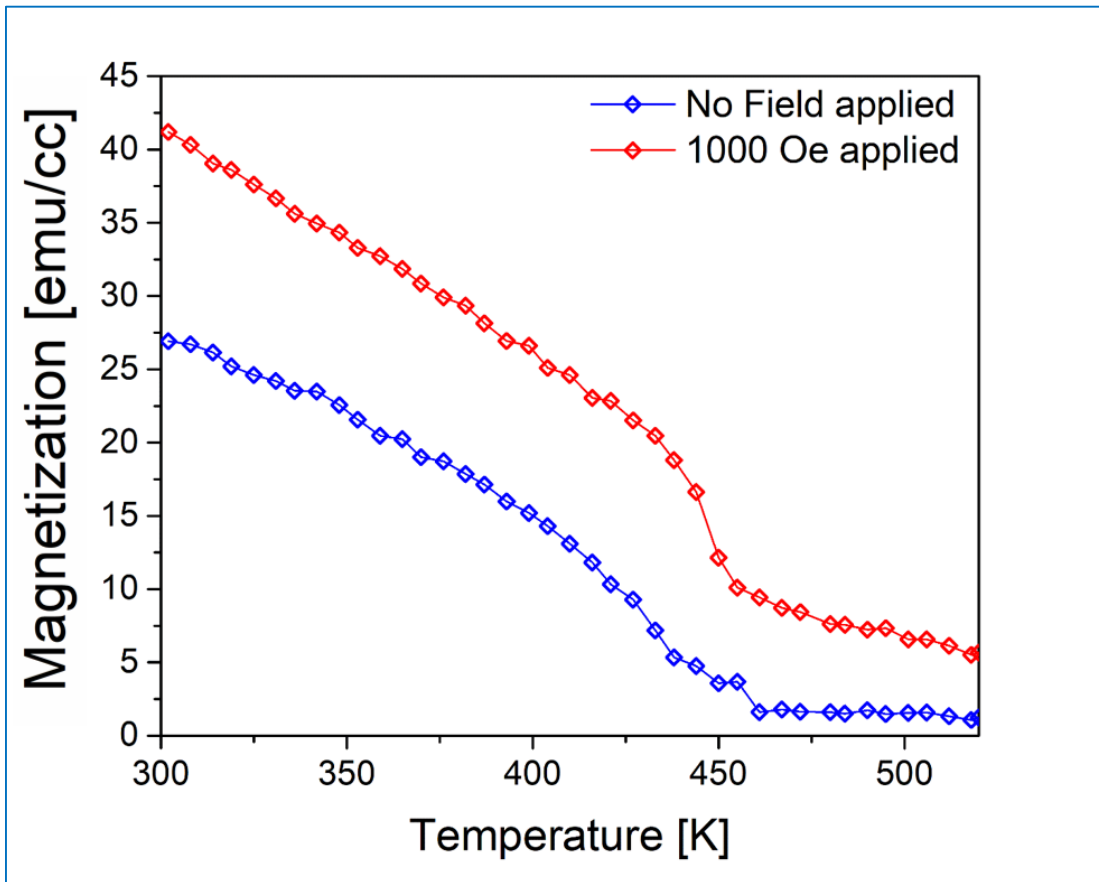


Figure 45: Plot of the dependence of the remanent magnetization M_R (blue dots/line) and under the application of a field of 1000 Oe (red dots/line) versus temperature for an epsilon ferrite thin film.

Moreover, analysis of the magnetization under the application of a field of 1000 Oe in function of the temperature was carried out for a wider range temperature (up to 900K, above the Curie temperature of magnetite). An irreversible phase transition was involuntarily induced in the analyzed sample. Such phase transition, is believed to correspond to the epsilon phase transforming into more stable maghemite (γ - Fe_2O_3). From the plot of magnetization vs temperature for temperature rising from 300 to 900 K under the application of a field of 1000 Oe, it is possible to identify a first “magnetic” transition T at circa 475 K (T_C of ϵ), above which the magnetization is not completely suppressed, thus once more proving the presence of magnetite, a second “phase” transition T at circa 600 K (which is believed to correspond to the transition of ϵ - Fe_2O_3 to γ - Fe_2O_3), a third “magnetic” transition T at circa 755 K (which corresponds to the Curie Temperature of γ - Fe_2O_3), and a final “magnetic” transition T at circa 875 K (T_C of Magnetite). From the analysis of the transitions, it is possible to infer that the original film was composed by the ϵ -phase of Fe_2O_3 plus the magnetite phase, and was transformed above 600 K into γ - Fe_2O_3 plus magnetite. Note that the slight increase of the magnetic transition temperatures compared to values reported in literature is due to the small applied magnetic field.

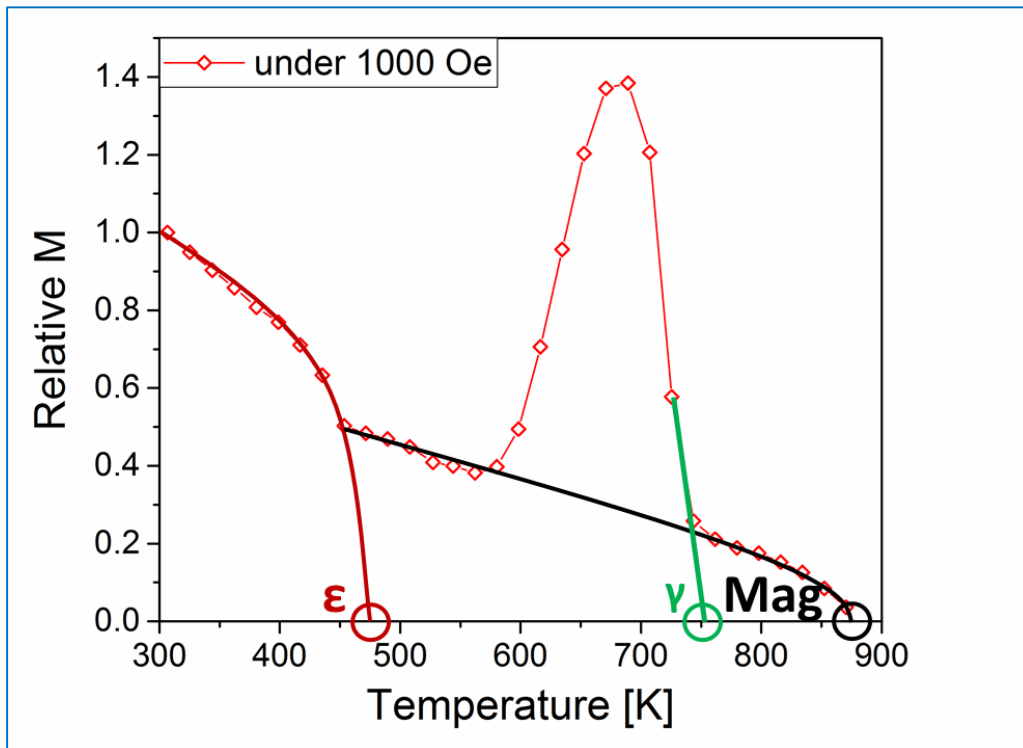


Figure 46: The complex plot of magnetization versus temperature of an epsilon ferrite epitaxial film for temperatures spanning 300 to 900 K.

The dependence of the magnetization versus temperature, under the application of 1000 Oe, was also recorded with decreasing temperature: as can be seen in Figure 47, the magnetic moment of the sample dramatically increases, and the new “material” is characterized by a first Curie temperature at circa 755 K and a second one at circa 855 K, suggesting once more how the epsilon phase of Fe_2O_3 has been transformed into maghemite upon heating to 900 K.

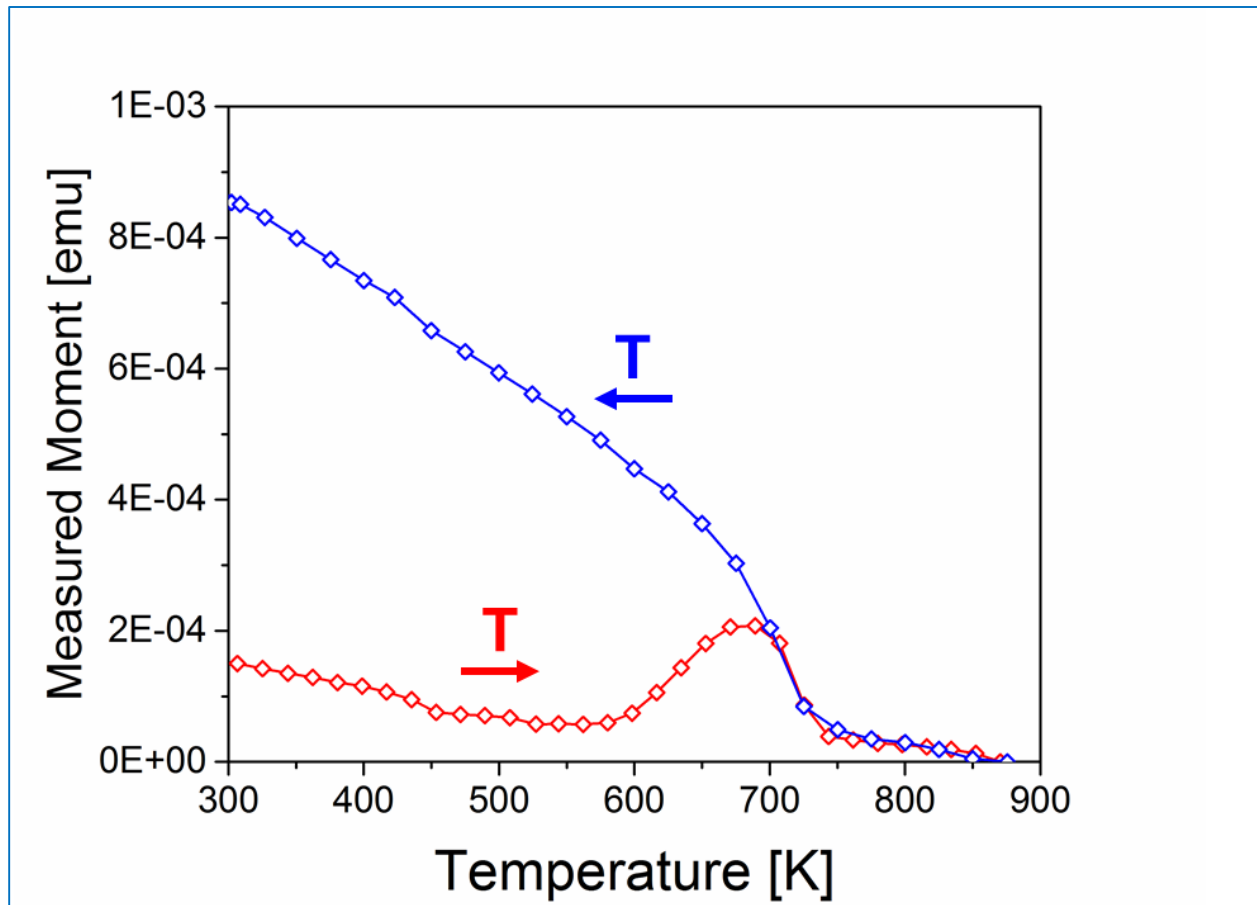


Figure 47: Plot of the dependence of the magnetization versus temperature measured under an applied field of 1000 Oe, for increasing (red – same curve shown above with different scale) and decreasing (blue) temperature.

The in-plane hysteresis loop was measured again for the sample after its “heating to 900 K and cooling to RT transformation to maghemite”; it was observed that the film previously characterized by a typical hysteresis for epsilon ferrite, *i.e.* low magnetization with a strong imprint of the diamagnetic substrate, very wide loop due to the high coercivity of epsilon, and “shoulder” at low field, turned into the typical hysteresis loop of a soft magnetic material characterized by high magnetization and low coercive field, such as the magnetic hysteresis loop of maghemite (see Figure 48 for the measured loop before and after the transition). To further confirm the transition from epsilon ferrite to maghemite, the new experimentally measured

Chapter 4

magnetic moment was compared with an estimation obtained by assuming that the totality of the epsilon phase had been converted into maghemite, and by using the reported values of magnetization for $\gamma\text{-Fe}_2\text{O}_3$. In such way it was possible to predict the magnetic moment of the now converted sample, which resulted in a value very similar to the one experimentally recorded (see the table at bottom part of Figure 47).

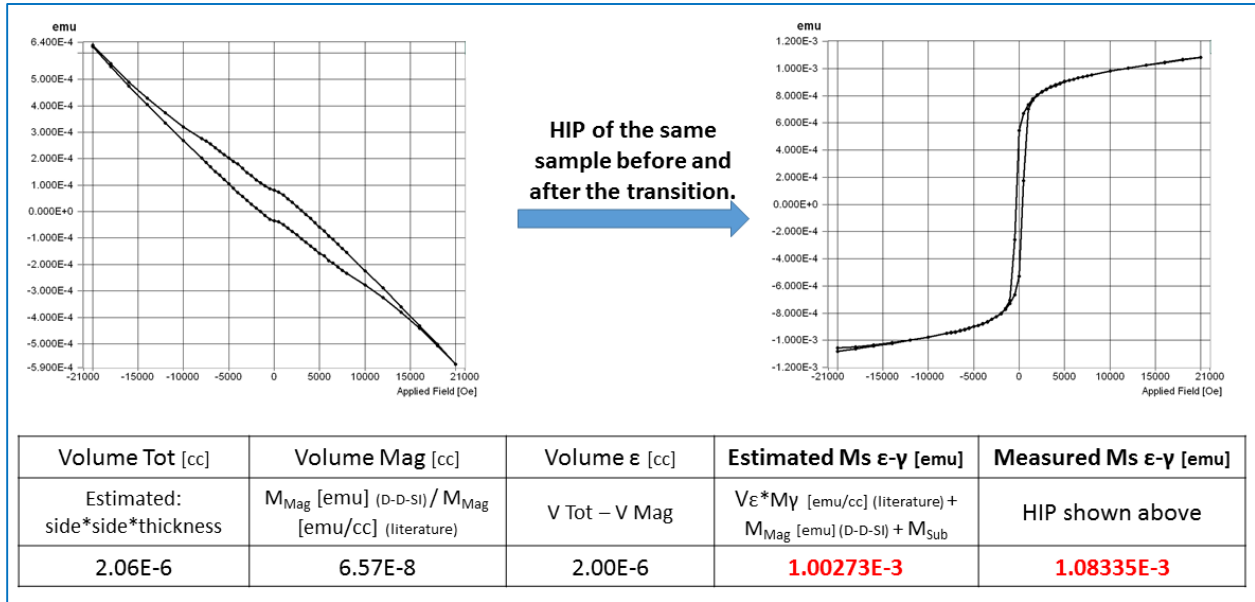


Figure 48: Hysteresis in-plane measured before (left) and after (right) the involuntarily induced phase transition, along with the passage used to estimate the new magnetic moment and the value experimentally measured.

This interesting phenomenon is currently under further investigation in our group: at the moment, no clear application are envisioned, although being able to pattern a hard magnet (*i.e.* epsilon ferrite) with a soft one (*i.e.* maghemite), for example by inducing the phase transition by laser heating, might represent an innovation in the field of micro-fabricated magnetic waveguides.

Chapter 4

In order to determine the relative contribution of the two magnetic phases ϵ -Fe₂O₃ and Fe₃O₄ to the measured magnetic hysteresis loop, a method consisting in differentiating the measured loop was developed, consisting in fitting the various peaks of the 1st derivative by using a summation of Voigt distributions in addition to a constant. This method permits to deconvolute the signals originating from the different magnetic phases (which simply correspond to the different peaks). Integrating exclusively and independently each Voigt functions (see ANNEX I and ref. ⁸⁷) yields the individual magnetic hysteresis loop of the different magnetic phases found without contributions of any other phase. The technique, which was named D-D-SI, from “Derivative - Deconvolution - Selective Integration”, allows both to (i) discriminate the various contributions originating from different magnetic phases, and also to (ii) eliminate every linear contribution due to the paramagnetic and/or diamagnetic signals arising either from the vibrating rod or/and from the substrate, along with any further linear contribution possibly coming from the film.

The reconstructed loops obtained from the D-D-SI technique are shown in Figure 49 for the two ϵ -Fe₂O₃ and Fe₃O₄ magnetic phases (red and yellow lines) and the sum of the two magnetic contributions (blue line). For comparison, the hysteresis loop obtained using the conventional way, *i.e.* by subtracting the measured contributions of the substrate and the rod from the measured signal of the thin film is also shown (blue symbols). In order to compare the two loops and demonstrate that the experimentally measured loop is well described by their sum (the small residual being a linear contribution that has not been captured in the modeling), the magnetic moment is shown, as measured [emu] rather than the magnetization (moment/volume). Plotting the magnetizations in SI units [A/m] (see Figure 50), would make this comparison and graphical addition more difficult given the higher magnetization of magnetite compared to epsilon (3-4 times higher) and the different volumes of the soft magnetite and hard epsilon ferrite phases (circa 1:10 volume ratio). As discussed in ANNEX I and in a publication by our group⁸⁷, the difference observed between the hysteresis loops obtained using the D-D-SI method and the hysteresis loop obtained using the conventional method corresponds to a linear contribution. This linear contribution can originate from different sources, as for example, an error measurement of 7.5% on the magnetic contribution of the substrate and sample holder or alternately, the presence of ferromagnetic domains in the thin films, whose hard axis are parallel to the applied field direction.

The experimental results indicate that the presence of the magnetite parasitic soft magnetic phase, which possesses a coercive field of ~100 Oe, has the drastic effect of strongly reducing the coercive field of the hysteresis loop of the whole film ($H_c \sim 5$ kOe). In comparison, the epsilon ferrite domains are individually characterized by a magnetization at saturation of $M_s \approx 40$ kA/m and a coercive field $H_c \approx 8$ kOe.

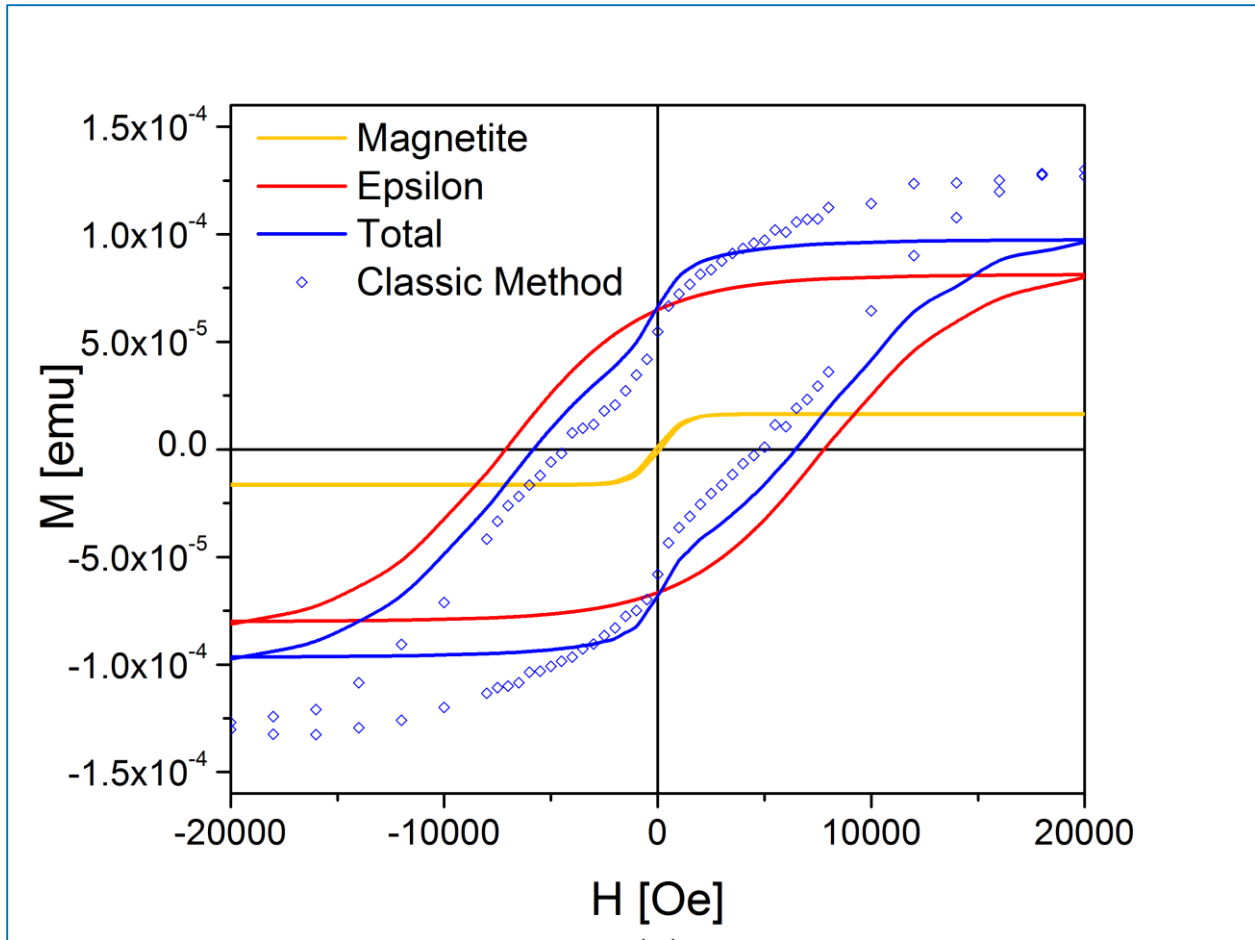


Figure 49: Practical application of the D-D-SI technique to separate the contributions of the two phases to the measured magnetic moment in an epsilon ferrite thin film deposited on YSZ (100).

In order to separate the magnetization curve for each phase, and to determine M_s in S.I. units, we estimated the volume of each phase (ϵ = epsilon ferrite $\epsilon\text{-Fe}_2\text{O}_3$ and Mag = magnetite Fe_3O_4) using the following methodology:

- Estimation of the total volume of our sample by knowing the growth rate (thus the thickness t) and measuring the surface area (S) of our films: $V_{\text{Tot}} = t \cdot S$;
- The values of the total magnetic moment in [emu] for epsilon ferrite and magnetite were found by using the “D-D-SI” method, extracting the two individual contributions (ref. ⁸⁷);
- The volume of magnetite was estimated by taking the normalized magnetization value reported in literature for Fe_3O_4 nanostructures $M_s = 309$ [emu/cc] and using $V_{\text{Mag}} = m_s$ [emu] (moment at saturation measured for the film)/ M_s [emu/cc]^{109–113}. It is important to note how this value is significantly lower than the value for bulk magnetite ($M_s = 480$ [emu/cc])⁶⁷, which, if used, would result in a lower volume.

- The volume of epsilon was found by subtracting the Magnetite volume from the total: $V_{\epsilon} = V_{\text{Tot}} - V_{\text{Mag}}$;
- By using V_{ϵ} and V_{Mag} (which are circa 10:1 in ratio), the magnetization in [A/m] for each phase was found.

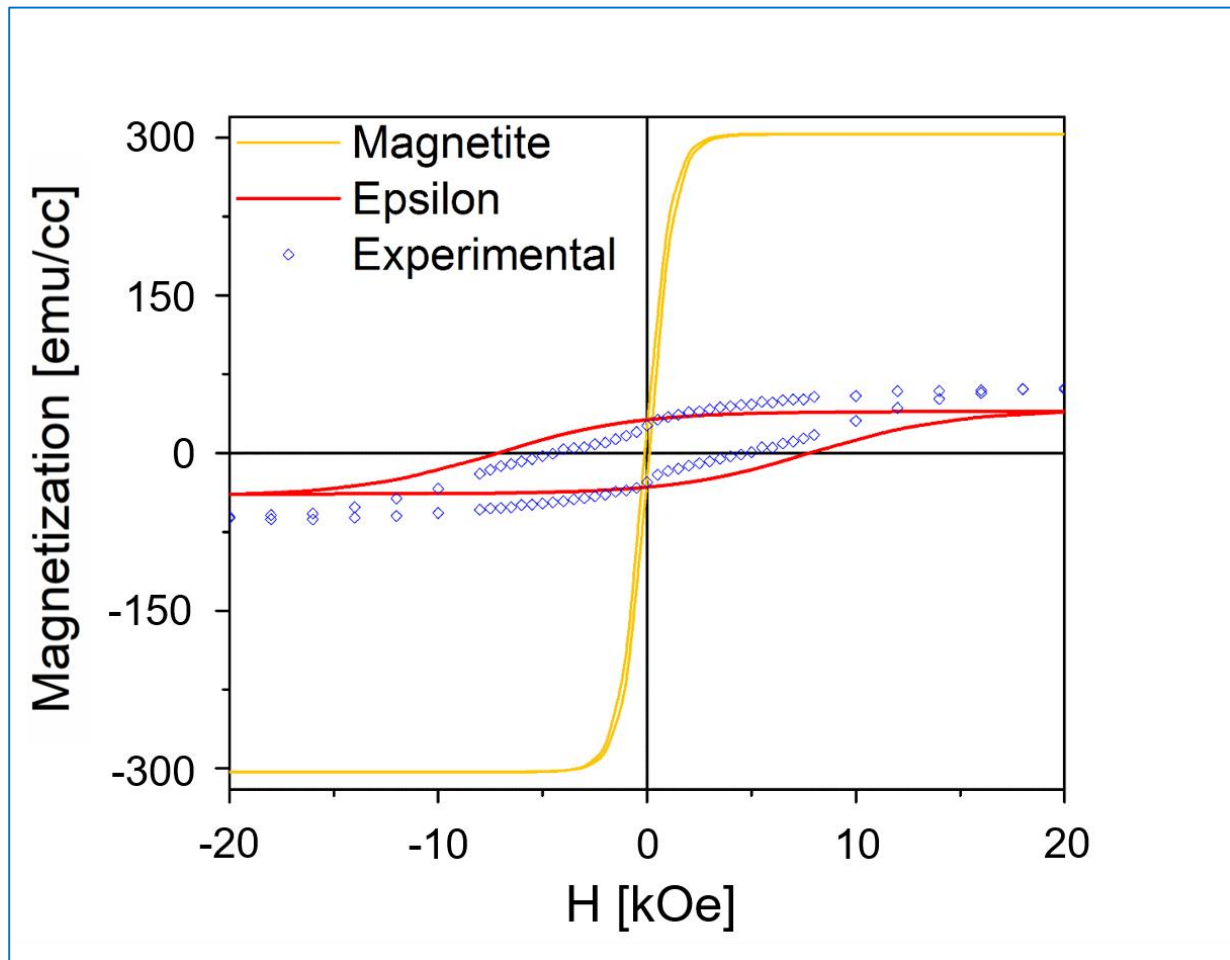


Figure 50: Graph of the magnetization (in SI units) for the epsilon and the magnetite phase in a thin film of epsilon ferrite.

Being able to separate the two components allows us to study both the influence of the chosen substrate and the influence of the sample thickness on the magnetic properties of our films.

After having developed the D-D-SI technique, the first step was to compare the in-plane hysteresis loops for films grown on YSZ (100) and on STO (111), the latter being used to exemplify the behavior of all the samples grown on (111)-oriented perovskites. In order to evaluate solely the properties of epsilon ferrite, the D-D-SI technique was used to isolate its contribution to the measured hysteresis loop. In order to be

sure to compare the loops with applied field parallel to the magnetic easy axis, the loops with the higher coercive fields measured during the magnetic angular characterization were used for this analysis (which will be shown in detail in the next section).

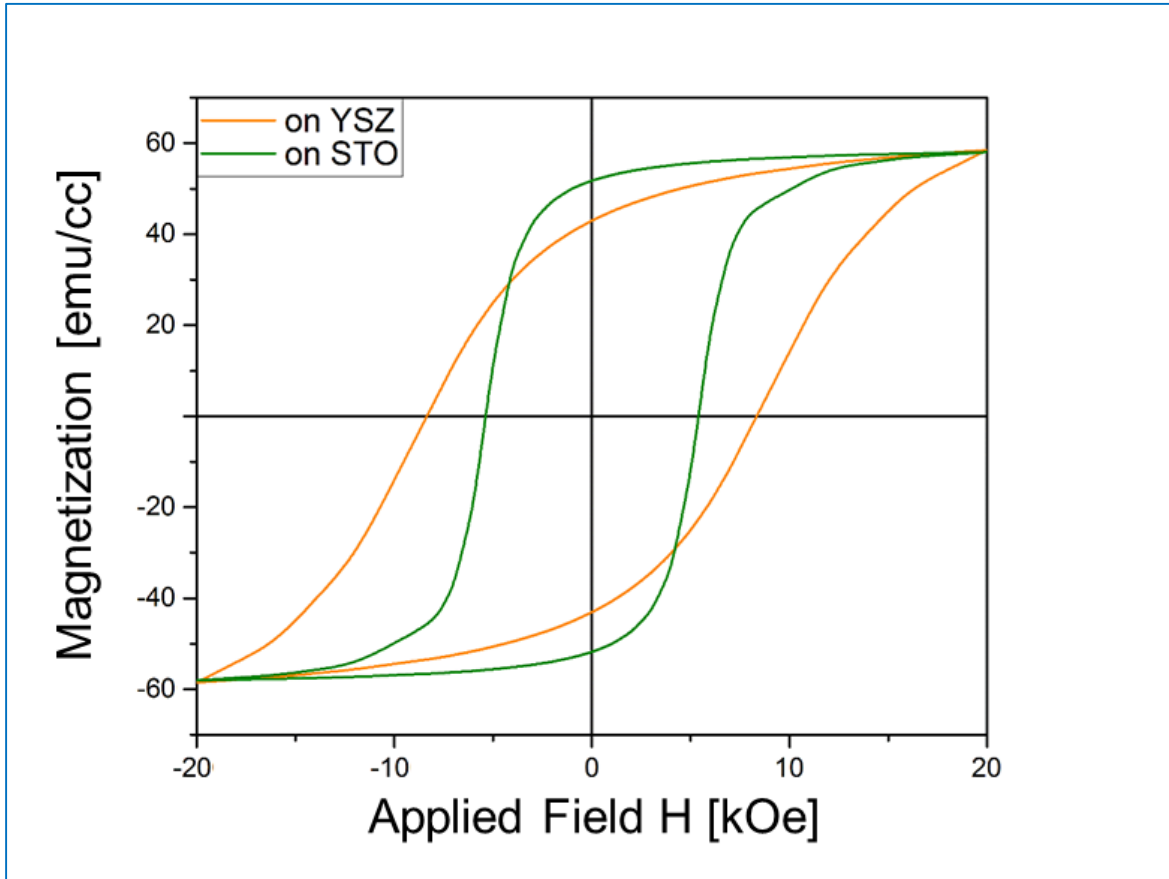


Figure 51: Hysteresis in plane for two thin films of epsilon ferrite grown on YSZ (100) (orange line) and STO (111) (green line).

What comes out of this analysis is that, although the geometry of the substrate does not affect the magnetization at saturation of the samples, the $\epsilon\text{-Fe}_2\text{O}_3$ film grown on YSZ (100) is characterized by a quite higher coercive field and lower remanent magnetization compared to the one on STO (100) (coercive field of circa 8300 Oe and remanent magnetization of circa 43000 A/m for the sample grown on YSZ, and coercive field of circa 5400 Oe and remanent magnetization of circa 52000 A/m for the sample grown on STO). Although it is rather difficult to determine a precise cause of such phenomena, which would require a much deeper analysis in order to obtain a definitive answer, it is possible to make some educated guesses based on the structural and magnetic analysis that have been performed. The higher coercive field for the film deposited on (100)-oriented YSZ than for the one deposited on (111)-oriented perovskites, might be caused by the presence of two main orientations (which were defined as “parallel” in section 3.1.1) which

are separated by a 90° angle for epsilon ferrite on YSZ, in comparison with the 3 different ones separated by 60° for films grown on perovskites. As for the shape of the hysteresis loops, the more “squared” loop for films grown on STO (111) might be due to a lower pinning energy for magnetic domain given by the boundaries between the different growth orientations domains or grains. However, as mentioned before, this are only hypothesis that would require further analysis in order to be confirmed.

4.1.2 Angle dependent measurements.

The angle-dependent magnetic properties were obtained by recording in-plane hysteresis loops every 2 degrees. The in-plane angle dependence of the remanent magnetization M_R was extracted from the measured loops. To explain the azimuthal dependence of M_R , a simple model which averages the remanence of the different growth variants parallel to the measured axis was used⁸⁸. Such model is based on the assumption that, at zero applied field, the magnetization inside each crystal is uniform and aligned along their magnetic easy axis (a -axis). This assumption is supported by a critical dimension analysis based on the anisotropy field values and also by the dimensions of the epsilon ferrite crystals obtained from TEM (see Figure 41 and Figure 42) which both allow to infer that the crystals are essentially ferromagnetic monodomains^{88,89}.

First, the different growth orientations for epsilon ferrite on STO (111) (which was used as model for the other perovskites) and YSZ (100) were identified^{VI}. Three different main variant were identified for epsilon ferrite thin films grown on STO (111), aligned respectively along the $[1 \bar{2} 1]$, $[1 1 \bar{2}]$, and $[\bar{2} 1 1]$ directions of the substrate crystalline lattice. Moreover, as shown in Figure 36, non-negligible interstitial twins with an intermediate orientation approximately $\pm 14^\circ$ off from the main growth orientations were also detected by XRD.

As for films grown on YSZ, six different growth variants (two “parallel” with \mathbf{b} aligned along the $[0 1 0]$ and the $[1 0 0]$ direction of the substrate, and four “non-parallel”, aligned along the $[1 \bar{1} 0]$, $[4 \bar{1} 0]$, $[4 1 0]$, and $[1 1 0]$) were found. In such case, the interstitial twins were not considered in our model, given their low counts relatively to the main orientations (Figure 36).

^{VI} Given the use of the absolute value of a sinusoidal function to model the evolution of the remanent magnetization with varying angle, the different variant only need to be defined over a 180° symmetry.

The need of implementing the “interstitial” domains in the modeling of the angular dependence of the magnetic properties for films grown on STO (111) was made evident when analyzing the angular evolution of the coercive field H_C , where an anomalous behavior, only explainable by the presence of “interstitial” domains was noted, as shown in Figure 52. While the global maxima every 60° clearly corresponds to the different main growth orientations, the local maxima every 30° must result from the presence of interstitial domains (compare to Figure 36).

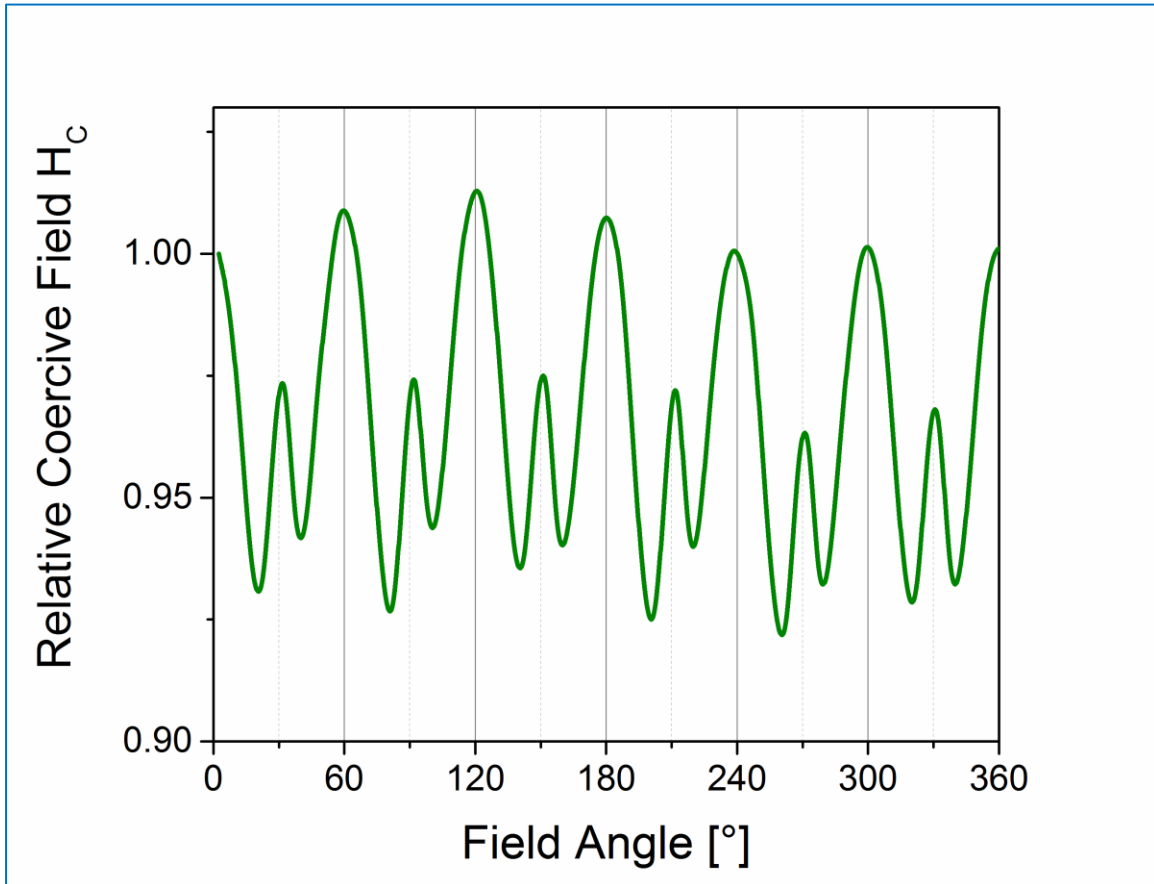


Figure 52: Plot of the angular evolution of the coercive field, relative to 0° , measured for a film of epsilon ferrite grown on STO (111).

According to the Stoner-Wohlfarth model, the angular dependence of the remanent magnetization of a single-domain can be modeled using the absolute value of $\cos(x+\varphi)$, where x is the angle between the applied magnetic field and a “0” direction of the substrate ($[1\bar{2}1]$ for STO and $[010]$ for YSZ) and φ is the angle between the b -axis and the “0” direction. It has to be noted how the normalized remanent magnetization (M_R) of a growth variant is then 1 when the magnetic field is applied along its magnetic easy axis, and 0 when the magnetic field is applied along its hard axis. Following these rules and the orientation

of the main (and interstitial, in the case of films grown on STO (111)) growth directions, it will be possible to create a model to fit the measured data.

The total angular dependence of M_R for film grown on STO can be expressed as:

$$M_{R\ Total} = x(1) * abs(\cos(x)) + x(2) * abs\left(\cos\left(x - \frac{\pi}{6}\right)\right) + x(3) * abs\left(\cos\left(x - \frac{\pi}{3}\right)\right) + x(4) * \left[abs\left(\cos\left(x - \frac{\pi}{12}\right)\right) + abs\left(\cos\left(x - \frac{5\pi}{12}\right)\right) + abs\left(\cos\left(x - \frac{3\pi}{4}\right)\right)\right] + x(5) * \left[abs\left(\cos\left(x - \frac{\pi}{4}\right)\right) + abs\left(\cos\left(x - \frac{7\pi}{12}\right)\right) + abs\left(\cos\left(x - \frac{11\pi}{12}\right)\right)\right],$$

where $x(1)$, $x(2)$ and $x(3)$ correspond to weight factors representing the volume fraction for each main growth variant, while $x(4)$ and $x(5)$ correspond respectively to the “left” and “right” interstitial twins. Although initially one weight factor for all the “interstitial” twins was taken, in agreement with XRD data (see Figure 36), it was decided to split them in two group in order to achieve better fit for the model.

For the case of thin films grown on YSZ, the model “only” has to account for the “main” growth orientations, given how introduction of the interstitial domain did not yield to appreciable improvement of the fit. Thus the total angular dependence of M_R can be expressed as:

$$M_{R\ Total} = x(1) * abs(\cos(x)) + x(2) * abs\left(\cos\left(x - \frac{\pi}{2}\right)\right) + x(3) * \left[abs\left(\cos\left(x - \frac{\pi}{6}\right)\right) + abs\left(\cos\left(x - \frac{\pi}{3}\right)\right) + abs\left(\cos\left(x - \frac{2\pi}{3}\right)\right) + abs\left(\cos\left(x - \frac{5\pi}{6}\right)\right)\right].$$

As for the case of the model describing the remanent magnetization for thin films grown on STO (111), also in this case the weight factors were taken in agreement with x-ray diffractometry data (see Figure 33 and results discussion after Figure 54).

The contribution of each variant to the total M_R vs angle evolution in a thin film of epsilon ferrite grown on STO (111) was weighted in order to fit satisfactorily the measured data with our model (see Figure 53). However, the outcome of the best fit of the experimental data with our model is that the contribution of the interstitial twins to the total magnetization is slightly higher than the one of the main peaks, accounting for 55% of the total. This result is contradicting what was found by x-ray diffractometry, according to which the “interstitial” domain accounted for 40% the total volume. Furthermore, according to the fit, the satellite peaks can be divided in two groups: a “left” and a “right” group with the latter one being predominant by a factor of circa 1.8:1. Although the difference between the measured data and the model is outside the usual “tolerance” that was found in previous instances of using such a model, it can be attributed to the non-concentric rotation of the rod holding the sample during the measurements^{114,115}. Moreover, it has to be noted how the magnetic properties of main and “interstitial” domains were assumed to be equal, which

might not be the case given how the smaller lattice “ a ” parameter in the “interstitial” domains might induce a stronger anisotropy (given by a stronger hybridization of the more overlapped $\text{Fe}_{3d}\text{-O}_{2p}$ bonds).

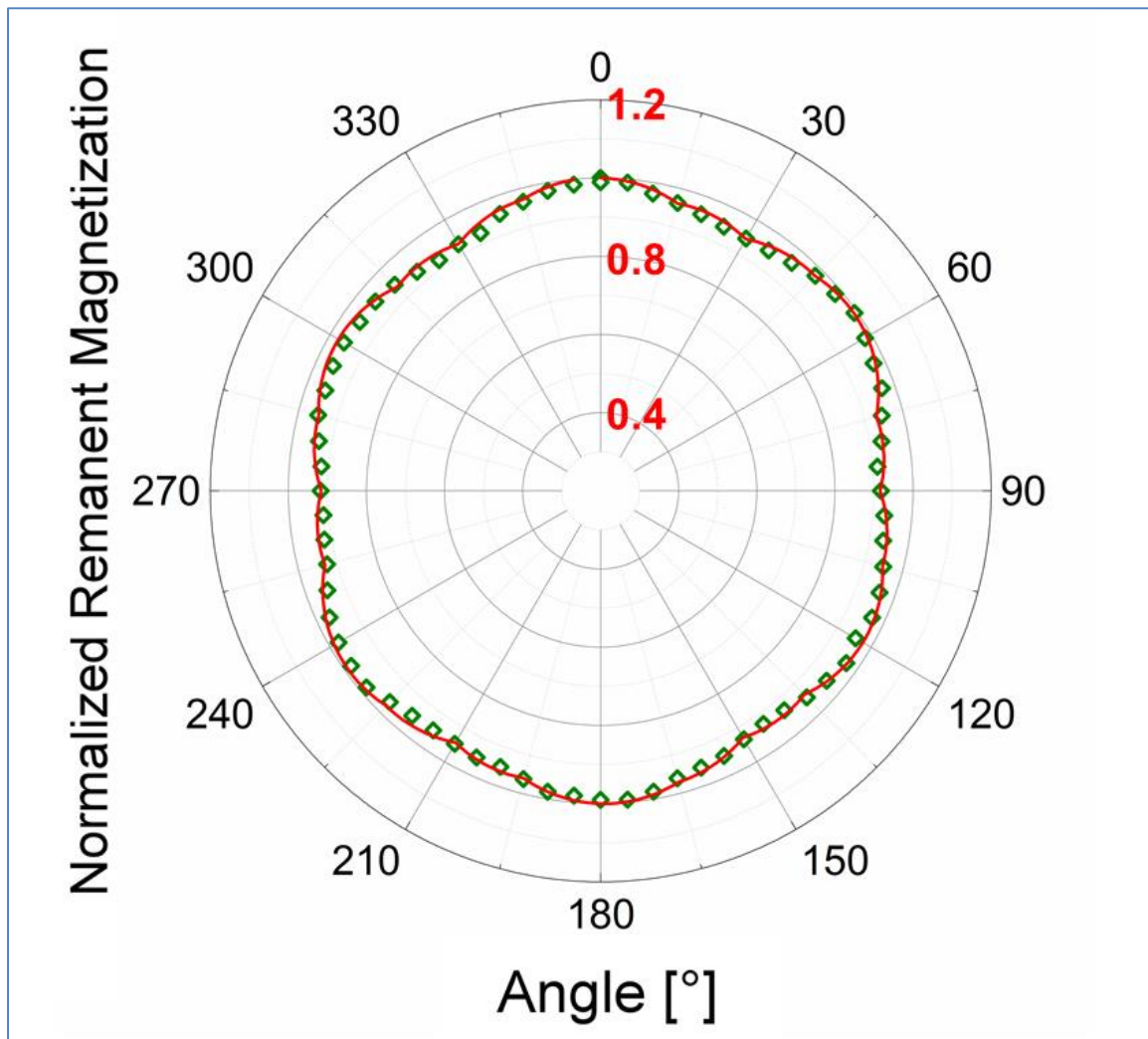


Figure 53: Polar plot of the evolution of the measured M_R versus angle (green diamonds) and of the fitted curve (red line) for a sample of epsilon ferrite grown on STO (111).

Like it was done for the film grown on STO (111), the contribution of each variant to the total angular distribution of M_R in a thin film of epsilon ferrite grown on YSZ (100) was weighted in order to fit satisfactorily the measured data with our model (see Figure 54).

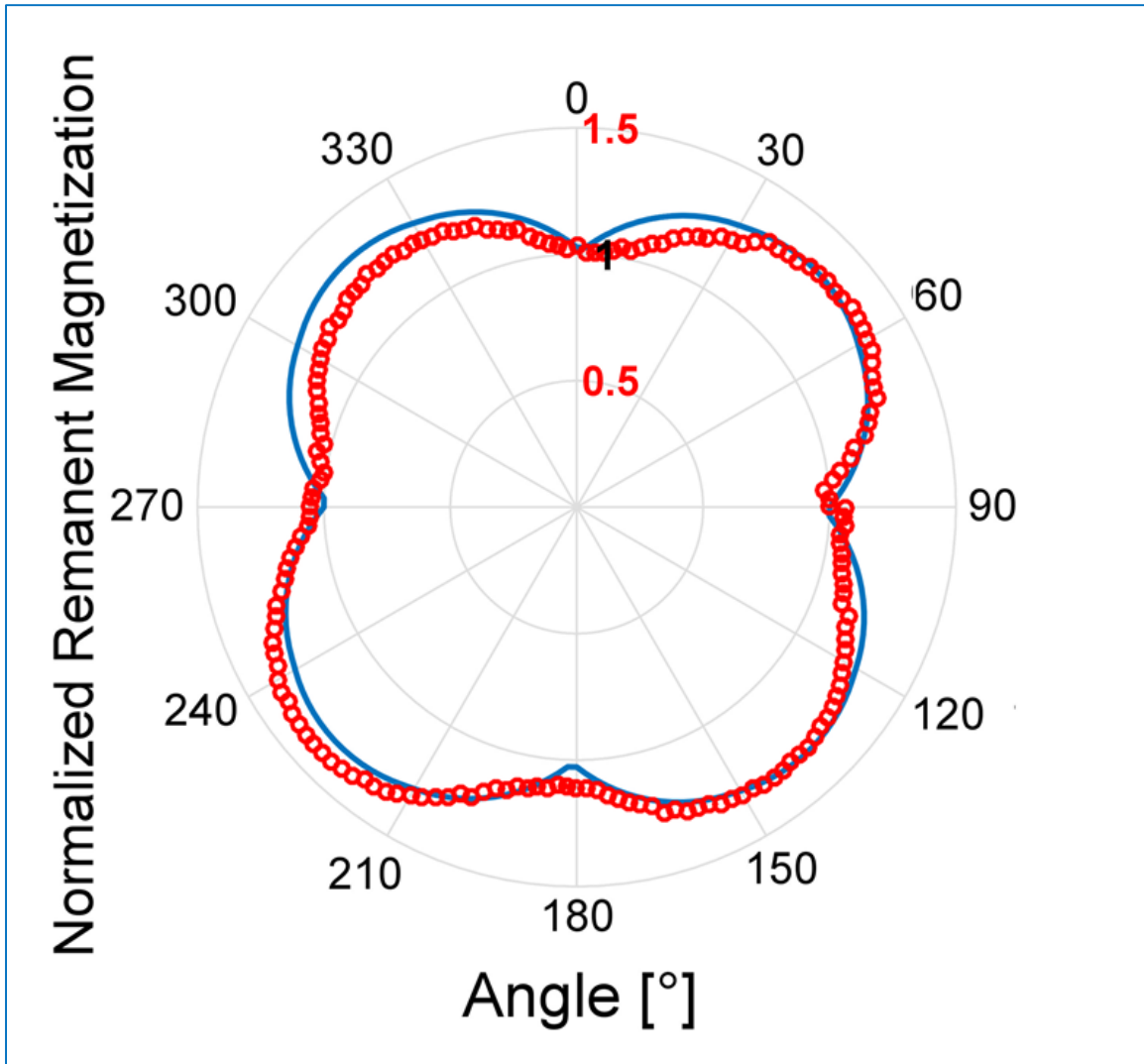


Figure 54: Polar plot of the evolution of the measured M_R versus angle (red dots) and of the fitted curve (blue line) for a sample of epsilon ferrite grown on YSZ (100).

The results for the fitting of the angular dependence of a film^{VII} grown on YSZ indicate that the magnetic contribution of the two “parallel” variants account for the larger contribution (~93% of the total remanent magnetization), which is consistent with the data found by angular XRD (~85% of the counts, Figure 33). In this case, the difference between the measured data and the model can be solely attributed to the non-concentric rotation of the rod holding the sample during the measurements^{114,115}.

^{VII} Although the model will fit satisfactorily any film, the values found describe in particular the sample which XRD phi scan is show in Figure 32.

4.1.3 Microscopic magnetic characterization via magnetic force microscopy.

Microscopic magnetic characterization was conducted by magnetic force microscopy (MFM). Given the concept and operation of a MFM, where the magnetic tip is attracted/repelled by the magnetic field/fields exiting the surface of the sample and going out of plane (more specifically, the force acting on the tip is related to the magnetic field gradients *above* the magnetic sample surface), it becomes really hard to interpret the contrast detected in some MFM imaging of thin films of epsilon ferrite, which are characterized by a very strong in-plane anisotropy.

Although a clear MFM contrast was detected for different samples of epsilon ferrite, as can be seen in Figure 55, it was not possible to relate them to different magnetic domains forming in the epitaxial thin film.

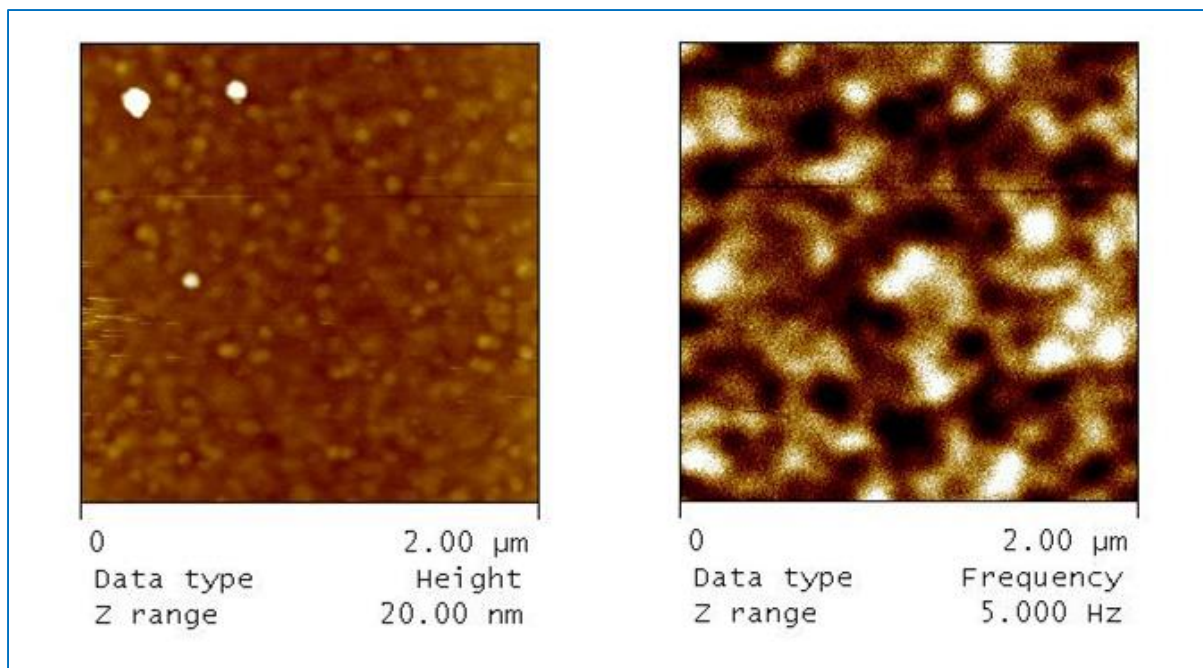


Figure 55: Topography (left) and magnetic contrast (right) measured for a thin film of epsilon ferrite.

4.2 Ferroelectric characterization of epsilon ferrite thin films.

The macroscopic ferroelectric loops of epsilon ferrite thin films were recorded with the FE-Module of a TF Analyzer 2000 system by aixACT Systems GmbH (Aachen, Germany). In order to measure their polarization and its hysteresis, the films were deposited on (111)-oriented 0.5% niobium-doped STO substrates. These substrates are characterized by a lower sheet resistance compared to the undoped substrate which allows them to be used as bottom electrode for electrical measurements, and in particular for ferroelectric characterization. Moreover, given the small amount of dopant in the lattice, the crystal structure of the Nb-doped films remains unchanged allowing the same epitaxial stabilization as it was seen for (111)-oriented undoped STO. To serve as top electrode, circular platinum contacts with diameter of 300 μm and thickness of circa 30 nm were deposited on top of the epsilon ferrite thin films by sputtering. The final structure of the film and electrodes is portrayed in Figure 56.

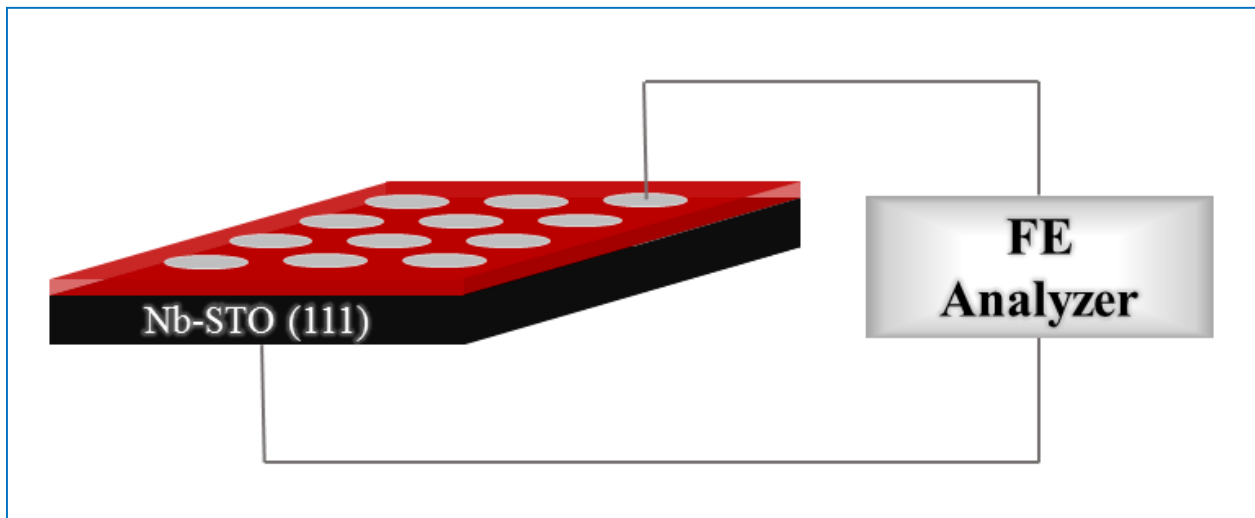


Figure 56: Schematics of the sample structure for ferroelectric characterization: the epsilon ferrite thin film is depicted in red, while the platinum electrodes are drawn, magnified, in silver.

The ferroelectric measurements revealed how the polarization versus field (also called PE) hysteresis loops of thin films of epsilon ferrite are dominated by leakage currents (Figure 57). By analyzing the switching currents (IE) loops, it is evident that the leakage current is of the same order of magnitude as the switching current reported in literature, of few μA the loops reported in the literature were, however, recorded at low temperatures, where the effect of leakage is greatly reduced⁵⁰; it becomes therefore extremely difficult to detect the currents generated by the polarization switching, and to separate them from the leakage currents. Such high leakage can be explained by the presence of free electrons due to the formation of non-fully oxidized Fe^{2+} ions (whose presence was confirmed by the finding of magnetite, Fe_3O_4 , both by XRD and by magnetic measurements), which can then hop between the different iron ions (Fe^{3+} and Fe^{2+})¹¹⁶.

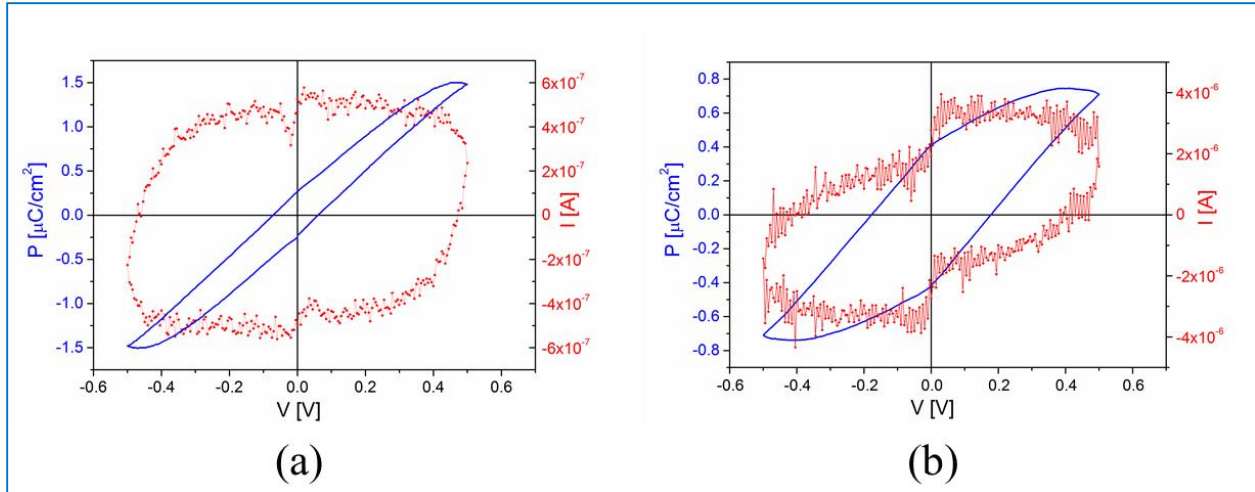


Figure 57: Polarization and Current vs cyclic voltage plot for a thin film of epsilon ferrite grown on Nb-STO (111), recorded at a driving frequency of (a) 100 Hz and (b) 2KHz.

Microscopic analysis of the dielectric properties of epsilon ferrite thin films was also performed via piezoresponse force microscopy known to be less sensitive to leakage current: although the results were not consistent, analysis of a multi-layered sample composed of a 90 nm thick film of ϵ - Fe_2O_3 grown on top of a 10nm film of a AlFeO_3 itself grown on a Nb-STO (111) substrate (in order to replicate results reported in the literature)⁵⁰, indeed showed piezoresponse. As can be seen in Figure 58, once the linear electrostatic component – *i.e.* the linear contribution– is removed from the measured signal (black dots and red line), a loop resembling a hysteresis curve (magenta line) is obtained. It has to be noted however that it was not possible to switch back the polarization on that particular grain, at least by applying a voltage of 20 V (the maximum voltage available in our setup, corresponding, given the thickness of the film, of a field of circa $2 \cdot 10^8$ V/m). The impossibility of switching the grain back might be due to pinning caused by the strong magnetic interaction; other reasons behind the pinning could be the presence of defects or of electric fields at the interface. However, until proven more rigorously, these remain only speculations.

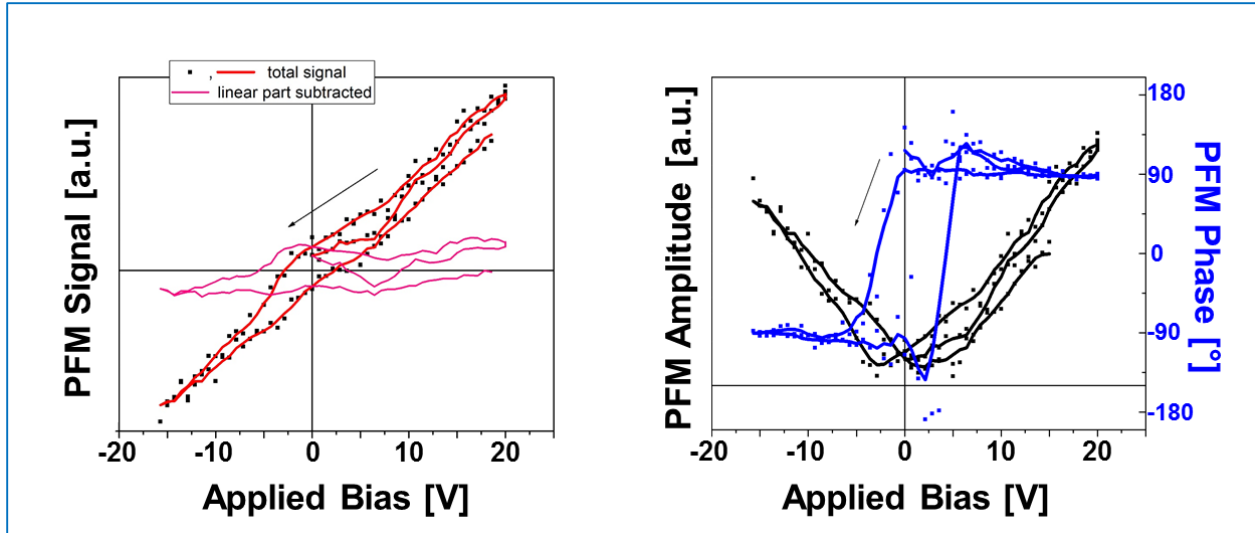


Figure 58: PFM signal as measured (black dots and red line), and without the linear electrostatic response (magenta line), and PFM amplitude and phase (right); the recorded signals hint to the presence of a non-switchable polarization (see the magenta line in the PFM signal).

4.3 Direct and indirect measurement of the ferromagnetic resonance frequency.

Since the primary goal of my investigation was to obtain a material which ferromagnetic resonance (FMR) frequency would fall in the low THz range, in order to try to induce magnetization switching by using ultrafast THz pulses, the characterization of the FMR frequency of thin films of epsilon ferrite by different techniques was attempted. Besides the indirect estimation of the anisotropy field that can give an estimation of the FMR frequency, obtained by comparing of the hysteresis loops recorded in-plane and out-of-plane that was shown previously (see Figure 44), measurement of the FMR frequency were performed both directly, and indirectly via THz time domain spectroscopy (THz-TDS).

Direct characterization proved very challenging due to the small magnetic moment of the epsilon ferrite thin films and to the absence of a resonant cavity with its resonance frequency close to the values expected for the resonance of epsilon ferrite of circa 190 GHz⁴⁰. A quick test between 160 and 200 GHz was realized using a vector network analyzer and a coplanar waveguide but the FMR peak of epsilon ferrite could not be observed. The reason was that the FMR peak was probably much smaller than the setup noise, indicating that an appropriate resonant cavity is indeed required in order to increase the signal-to-noise ratio. Different “field sweep” measurements were performed for sample of $\epsilon\text{-Fe}_2\text{O}_3$ and AlFeO_3 grown on YSZ (100) and for the YSZ (100) substrate using a resonant cavity at 24 GHz to make sure that no “low-frequency” resonances were detected in the epsilon ferrite samples. In “field sweep” measurement, an increasing DC field (H - from 0 to 20kOe) is applied to the sample while the absorption at a resonance frequency (R) equal to the cavity resonance frequency (*i.e.* 24 GHz) is measured. As can be seen in Figure 59, for the FMR measurement of the bare YSZ substrate (blue curve), two peaks are observed (4000 and 16000 Oe) which originate either from the cavity itself or from the bare YSZ substrate. For the FMR measurement of the $\epsilon\text{-Fe}_2\text{O}_3$ sample, no additional peaks are seen indicating that no FMR due to $\epsilon\text{-Fe}_2\text{O}_3$ is observed at 24 GHz, which is consistent with the fact that the FMR frequency expected is at a much higher frequency (190 GHz). For the FMR measurement of the AlFeO_3 sample, we observe an additional small and broad signal (8000

Oe), originating from AlFeO_3 . The fact that it is broad is possibly due to the fact that the sample is randomly oriented in combination with a small magnetocrystalline anisotropy.

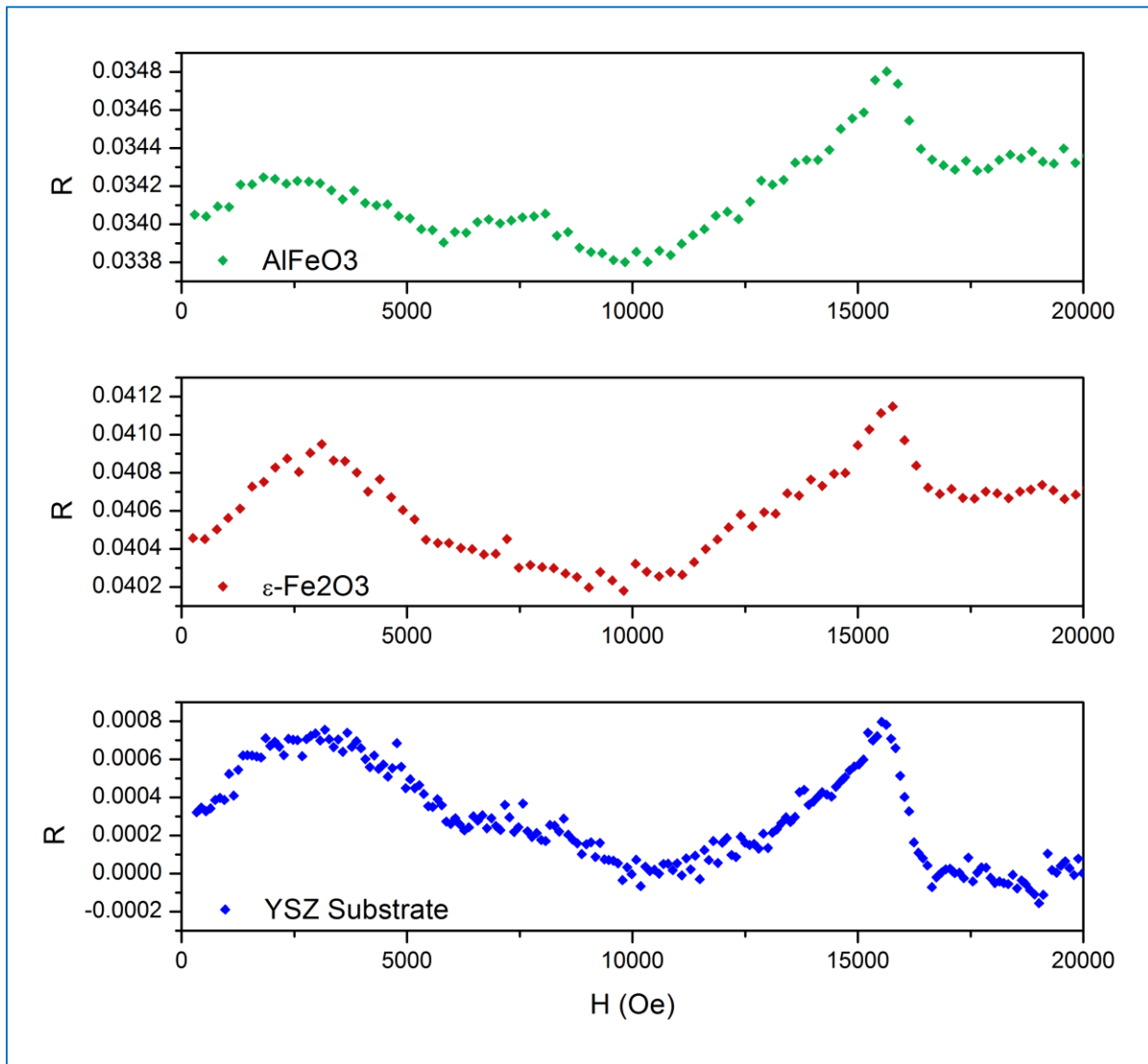


Figure 59: Field sweep with frequency set at 24GHz for thin films of aluminum ferrite (top green) and epsilon ferrite (middle red) grow on YSZ (100), along with the signal from the bare substrate (blue bottom).

Given the difficulties that have been encountered in directly measure the FMR frequency in epsilon ferrite thin films, the team directed by Professor Ménard and advised by Dr. Lacroix, is currently working towards the realization of a cavity with resonance close to the FMR of epsilon ferrite; succeeding in this very challenging task will likely make direct measurements of the FMR frequency possible.

Measurements of the FMR frequency of epsilon ferrite were also attempted using THz time domain spectroscopy (TDS). The results were unfortunately also not conclusive. In this case, the main problem was linked to the extreme thinness of the epsilon ferrite films, which gave a very limited absorption. Moreover, what came even more surprising was the detection of a higher overall transmittance for the sample constituted by the epsilon ferrite film on the YSZ (100) substrate than for the bare YSZ (100) substrate only. This might be due to the fact that the epsilon ferrite film is acting as an anti-reflective coating for THz radiation, as was shown for thin films of other semiconductors¹¹⁷. Nevertheless, a noticeable absorption was detected in the 60-175 GHz (0.06-0.175 THz), as can be seen in **Figure 60**, which was obtained from the measured spectrogram by applying a fast Fourier transform. Even with the reduced resolution of the measurement, which was due to reaching the minimum interval sampling in the TDS of 0.05 ps, this is a first clear evidence of absorption in epitaxial thin films around the FMR frequency, previously reported for epsilon ferrite nanoparticles (190 GHz). A lower FMR frequency would not be surprising given the lower coercive field that was recorded in epsilon ferrite thin films compared to nanoparticles (see section 4.1.1).

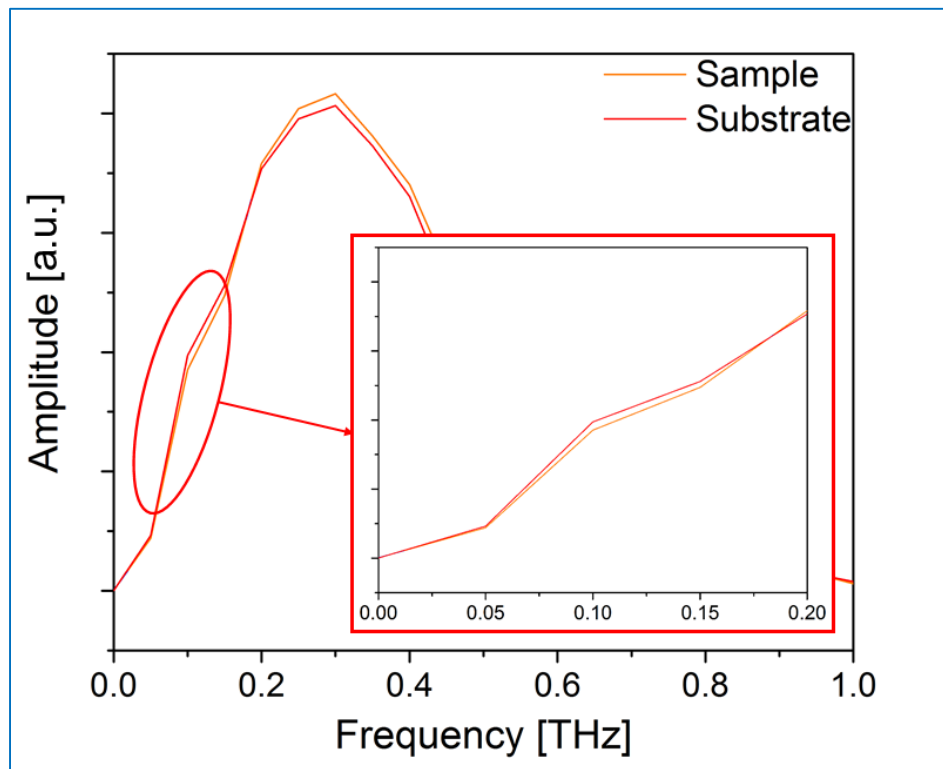


Figure 60: Amplitude of a THz pulse transmitted through an epsilon ferrite thin film grown on YSZ (100) (orange line), and through a YSZ (100) bare substrate (red line), showing absorption in the 0.1-0.15 THz (100-150 GHz) range.

4.4 Conclusions

The functional properties of epsilon ferrite epitaxial thin films were studied. Given the main scope of the research, which was to create a material characterized by ferromagnetic resonance frequency in the low THz range, the focus was initially placed on the magnetic properties. Ferromagnetic hysteresis loops were measured in-plane (thus with the field applied parallel to the surface of the sample) and out-of-plane (field applied perpendicular to the surface) by vibrating sample magnetometry. In-plane hysteresis loops showed high values for the coercive field, as expected given the high in-plane magnetocrystalline anisotropy characterizing epsilon ferrite.

Moreover, the loops are characterized by a “shoulder” at low applied field: such behavior was attributed to the presence of a secondary soft magnetic phase. This simple explanation has always been overlooked in the literature, where more complicated interface or surface effects were invoked to explain this behavior. In order to verify that indeed the shoulder was given by the presence of a secondary soft magnetic phase, measurements of the magnetization versus temperature were performed under an applied field of 1 kOe. Such field would not be enough to saturate epsilon ferrite, but it is necessary to have a measurable response from the secondary soft phase.

The magnetization versus temperature measurement lead to the discovery that the magnetization does not vanish completely for the Curie temperature of epsilon ferrite (circa 470 K), confirming the presence of a secondary magnetic phase. In order to further verify the nature of such secondary phase, that was in the meantime identified as randomly oriented magnetite (Fe_3O_4) by x-ray diffractometry, its Curie temperature was investigated. Our measurements determined that the secondary magnetic phase is characterized by a Curie temperature of 870 K, confirming it is magnetite.

Moreover, during such measurement, an irreversible involuntary phase transition of epsilon ferrite into maghemite ($\gamma\text{-Fe}_2\text{O}_3$) was promoted at a temperature of circa 600 K.

In order to evaluate the main magnetic properties of epsilon ferrite, namely coercive field, magnetization at remanence and at saturation, an analytical technique to separate the two contributions (hard epsilon ferrite and soft magnetite) was developed. The technique (which is described in detail in the ANNEX at the end of this thesis) allows to reconstruct solely the hysteresis loop of epsilon ferrite, and most importantly, determine with precision the characteristic magnetic properties of epsilon ferrite. The most interesting result relates to the differences when epsilon ferrite is deposited on the two classes of materials: films grown on YSZ (100) appear to have higher coercive field but less squared loop compared to films grown on perovskites (111). Differences between films grown on the two substrates appear even more relevant when

Chapter 4

analyzing the angular dependence of the magnetization. Reflecting what was measured by XRD phi-scans, different geometries were found for films deposited on the two classes of substrates.

The ferromagnetic resonance frequency of epsilon ferrite thin films was also probed both directly, by ferromagnetic resonance frequency measurements, and indirectly, via estimation of the anisotropy field and THz time domain spectroscopy. While direct measurements were inconclusive, given the small magnetic moments of our samples, indirect measurements lead to finding that the ferromagnetic resonance frequency lies between 0.05 and 0.15 THz centered around 0.12 THz.

Finally, the dielectric properties of epitaxial thin films of $\epsilon\text{-Fe}_2\text{O}_3$ were analyzed both macroscopically and microscopically. Ferroelectric hysteresis loops were measured with a ferroelectric measurements setup. However, due to the high leakage currents characterizing epsilon ferrite thin films, it was not possible to measure a clear ferroelectric (PE) hysteresis loops. Nevertheless, microscopic characterization performed by piezoresponse force microscopy, revealed a typical 180° phase switch of the piezoresponse, which is characteristic of materials characterized by (albeit in this case apparently non-switchable) spontaneous polarization.

Chapter 5 GROWTH AND CHARACTERIZATION OF ALUMINUM-SUBSTITUTED EPSILON FERRITE THIN FILMS

After the “rediscovery” of epsilon ferrite in early 2000, the focus, especially the one of the group supervised by professor Ohkoshi, who is currently the leading expert on ϵ -Fe₂O₃ nanoparticles, has shifted to the study of the effect of metal substitution into epsilon ferrite (ϵ -M_xFe_{2-x}O₃) nanoparticles, in particular regarding its effect on the FMR frequency (therefore on the absorption in the so-called millimeter wave range). In different reports, Ohkoshi *et al.* showed that substitution of Fe³⁺ ions in ϵ -Fe₂O₃ with metals having a smaller ionic radius, such as Al³⁺ and Ga³⁺, results in a lowering of the FMR frequency⁴¹⁻⁴³, while through substitution with larger ions like Rh³⁺, an increase of the FMR is observed⁴⁴. It is interesting to note that AlFeO₃ and GaFeO₃, which are isostructural to ϵ -Fe₂O₃, are known room temperature ferroelectrics characterized by spontaneous magnetic ordering at cryogenic temperatures^{100,118,119}. The substitution of Indium for iron in nanoparticles has been reported as well, but while it lowers the Curie temperature and the saturation magnetization of epsilon-ferrite, no effect on the FMR frequency was measured⁴⁵.

Once demonstrated the possibility of growing high quality epsilon ferrite thin films, the focus of my research moved to investigating the effects of metal substitution into the ϵ -Fe₂O₃ lattice: the main goal was to try to replicate in thin films the effects shown for nanoparticles, with a major interest towards the lowering of the FMR frequency by Al or Ga substitution. Furthermore, given the good ferroelectric properties displayed by aluminum ferrite and gallium ferrite, which hold an even further distorted/non-centrosymmetric structure in comparison to epsilon ferrite, my hope was to improve the ferroelectric properties of my hard magnetic films.

5.1 Growth and structural characterization of Al-substituted epsilon ferrite thin films.

Once the possibility of growing both Al and Ga substituted films was verified, we choose to focus exclusively on aluminum given the toxic nature of the gallium oxide powders necessary to fabricate the ceramic PLD target.

Epitaxial thin films of $\epsilon\text{-Al}_x\text{Fe}_{2-x}\text{O}_3$ of thickness of circa 50 nm, which was the targeted thickness given the optimal functional properties exhibited by $\epsilon\text{-Fe}_2\text{O}_3$ at such thickness, were grown on single crystalline (111)-oriented STO and (100)-oriented YSZ substrates and the effect of Al substitution on the structural and magnetic properties were studied. Although they have different symmetry, give different epitaxial match and result in different twins formation (as explained in section 3.2.2), the films grown on the two substrates show very similar structural and functional properties as well as the same trends with increasing aluminum substitution.

The films were grown under the same conditions as normal thin films of epsilon ferrite, as explained in section 0; the only difference was that, in order to obtain films with different percentage of dopant, the growth was performed by alternatively ablating a standard Fe_2O_3 target and a second target of AlFeO_3 . Different Al substitution percentages were then obtained by changing the ratio of the number of pulses shot on each target. In order to achieve a homogenous distribution of aluminum, the films were grown circa one monolayer at the time, alternating the targets in order to get the desired composition. Pure samples of AlFeO_3 (*i.e.* $x = 1$) were also prepared to estimate its growth rate and for comparison with the $\epsilon\text{-Al}_x\text{Fe}_{2-x}\text{O}_3$ films. Films with Al concentration ranging from pure $\epsilon\text{-Fe}_2\text{O}_3$ to $\epsilon\text{-Al}_{0.5}\text{Fe}_{1.5}\text{O}_3$ ($0 < x < 0.5$) were then prepared.

The Al-substituted films underwent the same characterization shown than undoped epsilon ferrite thin films. Goniometer ($\theta/2\theta$) scans confirmed that $\epsilon\text{-Al}_x\text{Fe}_{2-x}\text{O}_3$ grows epitaxially both on STO (111) and YSZ (100). As expected, the films hold the same orientation as the one portrayed by the pure films, which are (001)-oriented, as shown by the diffraction patterns of pure $\epsilon\text{-Fe}_2\text{O}_3$, $\epsilon\text{-Al}_{0.1}\text{Fe}_{1.9}\text{O}_3$, and pure AlFeO_3 grown on STO (111) (Figure 61). A shift towards higher θ angles with increasing Al concentration is observed, which was expected given the smaller ionic radius of Al^{3+} (53.5 pm) compared to Fe^{3+} (64.5 pm).

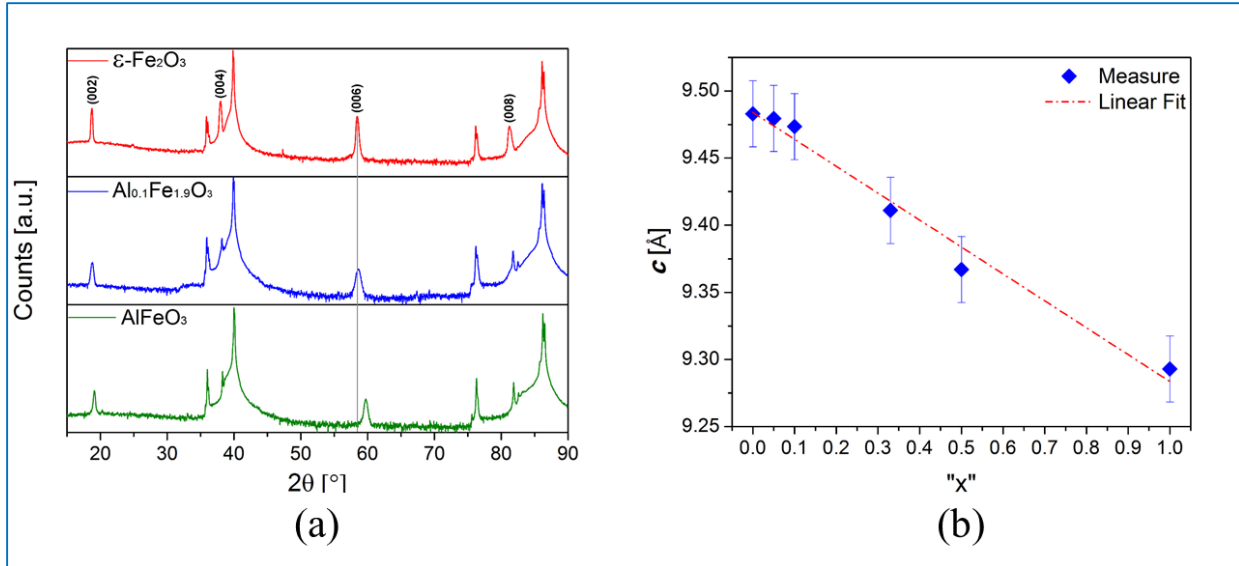


Figure 61: (a) $\theta/2\theta$ scans of (100)-oriented ϵ -Fe₂O₃, ϵ -Al_{0.1}Fe_{1.9}O₃, and AlFeO₃ thin film, revealing how all the three materials grow epitaxially on (111)-oriented STO. The line drawn in grey helps visualizing the shift in the position of the (006) peak for the Al-substituted films in comparison to pure ϵ -Fe₂O₃. (b) Evolution of the lattice parameter “ c ” with increasing Al concentration “ x ”.

The out-of-plane lattice parameter “ c ” was calculated from the measured goniometer scans, averaging the values found utilizing the inter-planar distances corresponding to the four $00l$ peaks ($l = 2, 4, 6, 8$). A linear decrease in the out-of-plane lattice parameter with increasing aluminum content was found, as shown in the graph in Figure 61b and reported in reference ⁴².

5.2 The effect of aluminum substitution on the magnetic properties.

Hysteresis loops were recorded at room temperature for all the aluminum-substituted epsilon ferrite thin films, with the magnetic field applied both parallel (in-plane) and perpendicular (out-of-plane) to the film surface. Once again, in order to obtain solely the signal arising from the thin films, the contribution of the vibrating rod holding the samples and the contribution of the substrate were measured and subtracted from the measured hysteresis loops. Following the results published on Al-substituted ϵ -Fe₂O₃ nanoparticles, we expect to observe two effects related to the metal substitution: The first is the decrease of the coercivity given the non-magnetic nature of the Al³⁺ ions (completely filled 2p⁶ shell). The second effect expected is the increase of the magnetization at saturation up to a concentration of circa 40% of Al⁴⁰. This effect was shown for gallium-substituted nanoparticles (which have a behavior similar to that of Al-substituted nanoparticles), where the increase of the magnetization was ascribed to the preferential substitution of the iron located in the tetragonal site “D” of the lattice (Figure 5) by the doping metal ions (gallium in ref. ⁴⁰, aluminum in our case), due to their ionic radius smaller than that of Fe³⁺. This results in a decrease of the “D”-site magnetic moment, hence to an increase of the total magnetic moment (Figure 5)⁴⁰. The measured magnetic hysteresis loops of a film with $x = 0$ and $x = 0.1$ are shown in Figure 62.

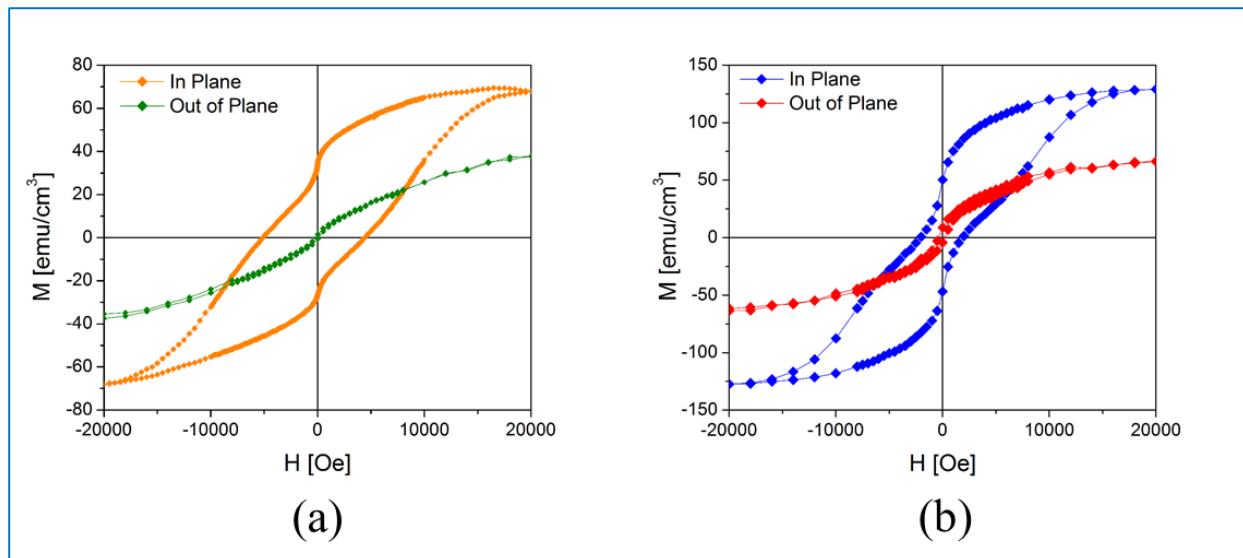


Figure 62: (a) In-plane (orange) and out-of-plane (green) hysteresis loop measured for a pure ϵ -Fe₂O₃ epitaxial thin film, and (b), In-plane (blue) and out-of-plane (red) hysteresis loop measured for a ϵ -Al_{0.1}Fe_{1.9}O₃ epitaxial thin film, both grown on YSZ (100). In both cases we can infer the high magnetic anisotropy of the two samples.

A shoulder at low applied fields was detected for the hysteresis loops of ϵ -Al_xFe_{2-x}O₃ thin films like it was the case for ϵ -Fe₂O₃. As in the case of pure epsilon ferrite films, the shoulder originates from the presence of a secondary soft magnetic phase which was identified as magnetite (Fe₃O₄) from XRD measurements.

Comparison between the two loops (pure and Al-substituted) revealed, as expected, (i) how the aluminum-substituted film preserved its in-plane anisotropy (see the difference between the in-plane and the out-of-plane measurement), (ii) that the Al-doped film is characterized by a lower coercive field and a higher saturation magnetization than pure epsilon ferrite films. Temperature dependence of the magnetization was also measured for the $\epsilon\text{-Al}_{0.1}\text{Fe}_{1.9}\text{O}_3$ film under a field of 1000 Oe. A paramagnetic-to-ferromagnetic phase transition is observed at $T \approx 475$ K (see Figure 63a). No phase transition is observed close to 300 K, which is the Curie temperature of AlFeO_3 ¹¹⁹. This indicates that aluminum substitution in the lattice of $\epsilon\text{-Fe}_2\text{O}_3$ was successfully achieved and that the resulting film is homogeneous, *i.e.* it does not consist of a mixture of AlFeO_3 and $\epsilon\text{-Fe}_2\text{O}_3$. Moreover, we observe once again that the magnetization does not fall to zero at temperatures higher than the Curie temperature of $\epsilon\text{-Fe}_2\text{O}_3$ ($T_C \approx 475$ K).

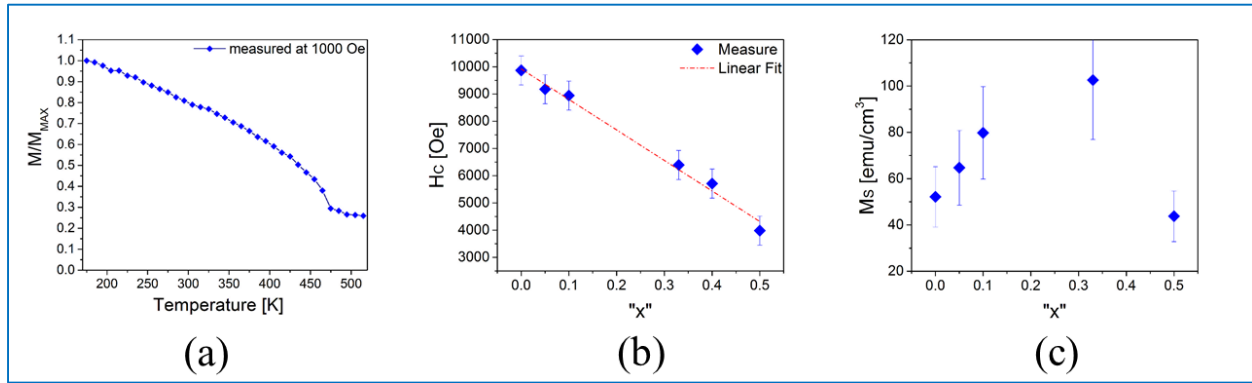


Figure 63: (a) Dependence of the magnetization (M) on the temperature for a $\epsilon\text{-Al}_{0.1}\text{Fe}_{1.9}\text{O}_3$ thin film grown on YSZ (100), recorded under a field of 1000 Oersted applied in $-$ plane. (b) Evolution of the coercive field H_c and (c) of the magnetization at saturation M_s in function of the aluminum concentration “ x ”.

To separate the contribution originating from $\epsilon\text{-Al}_x\text{Fe}_{2-x}\text{O}_3$ and Fe_3O_4 in the hysteresis loops, we used the D-D-SI technique described in the ANNEX I and in reference⁸⁷. This allowed us to obtain the coercive field and the magnetization at saturation for the sole $\epsilon\text{-Al}_x\text{Fe}_{2-x}\text{O}_3$ phase for different Al concentrations (see Figure 63b and c). As expected, the coercive field decreases linearly when the aluminum concentration increases indicating that the magnetic anisotropy decreases linearly with aluminum concentration⁴¹. We thus expect that the natural ferromagnetic resonance frequency should also decrease linearly with aluminum concentration^{40,42}. We also observe that, as the Al concentration increases, the saturation magnetization increases up to a factor of 2 at $x = 0.33$ where it reaches a maximum and then decreases. The decrease is due to the fact that above this threshold, Fe ions have been replaced by Al in all the “D” sites and further Al substitution occurs both at the iron “B” and “C” octahedral sites, thus decreasing the total magnetization⁴².

5.3 The effect of aluminum substitution on the ferroelectric properties.

Although aluminum substitution was hoped to improve the ferroelectric properties in epsilon ferrite thin films, given the better ferroelectric properties displayed by pure aluminum ferrite thin films, the $\epsilon\text{-Al}_x\text{Fe}_{2-x}\text{O}_3$ still exhibit very high leakage current which render the detection of any switching current impossible. Once again, the effect can be ascribed to the formation of conductive paths promoted by the hopping of the free electrons created by the presence of non-fully oxidized iron ions.

5.4 Conclusions

To conclude, epitaxial thin films of $\epsilon\text{-Al}_x\text{Fe}_{2-x}\text{O}_3$ were grown on SrTiO_3 (111) and on YSZ (100). Substitution over a wide range ($x=0.03$ to 0.5 , as well as $x = 1$) was achieved. Al substitution proved to linearly reduce the coercive field with increasing aluminum concentration indicating a diminution of the magnetocrystalline anisotropy with aluminum concentration. Moreover, increase of the saturation magnetization up to a threshold of $x = 0.33$ was shown, in accordance with the results previously reported for aluminum and gallium-substituted epsilon-ferrite nanoparticles.

Chapter 6 THE DEPOSITION ON MISCUT SUBSTRATES.

As seen in section 4.1.2, the presence of multiple in-plane growth orientation results in the presence of multiple in-plane magnetic easy axes. Depending on the choice of substrate the thin film will have either three (such is the case for epsilon ferrite grown on (111)-oriented perovskites) or six (for films grown on (100)-oriented YSZ) magnetic easy axes (Figure 64). Such phenomenon is detrimental for applications in which a unique magnetic easy axis is needed, as for example in magnetic memories.

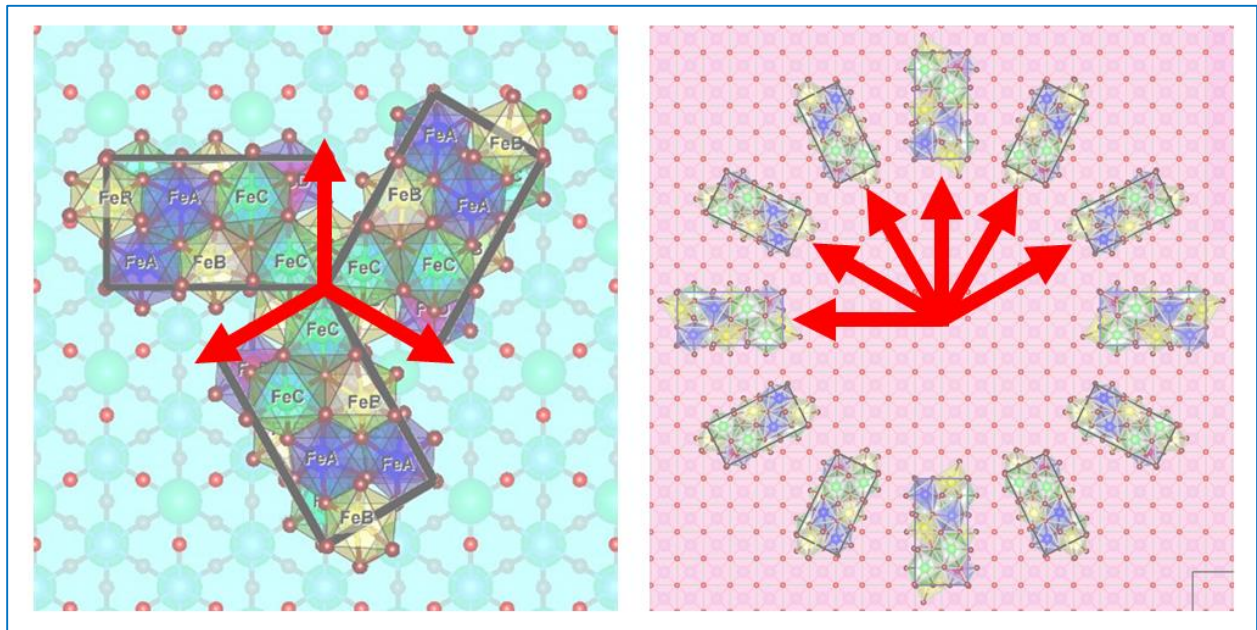


Figure 64: The magnetic easy axis that arise due to the different epitaxial matches and twinning in thin films of epsilon ferrite grown on (111)-oriented perovskites (left) and on (100)-oriented YSZ (right).

In order to promote the growth along only one crystallographic direction, the possibility of growing epitaxial thin films on substrates with high degree of miscut (5, 10, 15, and 20 degrees) was investigated. The idea is to take advantage of the reduce terrace width and the preferential direction they determine in the miscut substrates compared to the regular ones, to promote the growth perpendicular to the miscut direction (Figure 65 and Table 7).

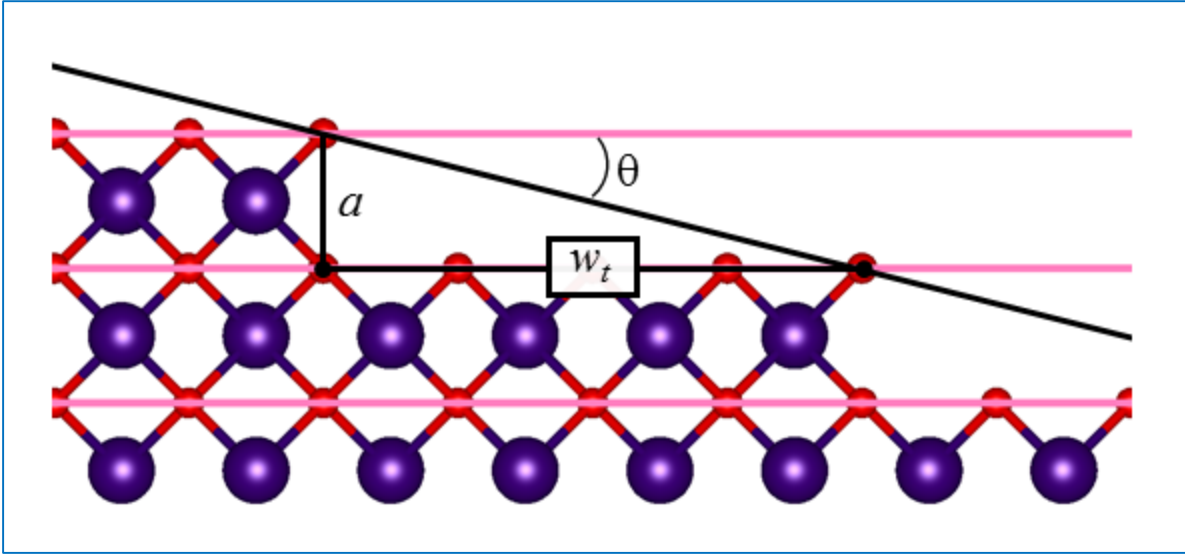


Figure 65: Graphical representation of a section of a (100)-oriented YSZ substrate with a miscut of circa 15° and terraces $\sim 19 \text{ \AA}$ wide.

As shown in the figure, the width of the terrace is inversely proportional to the degree of miscut: if we define θ as the degree of miscut, as a , the out-of-plane interplanar distance, which will be the lattice parameter for YSZ (100) ($a_{\text{YSZ}} = 5.12 \text{ \AA}$) and the body diagonal for STO (111) ($\sqrt{3} * a_{\text{STO}} = 6.76 \text{ \AA}$), the terrace width w_t by the following relation:

$$w_t = a \cot \theta. \quad (6.1)$$

The resulting terrace width for the different substrates and miscut angles are shown in Table 7.

Substrate	Miscut [$^\circ$]	w_t [\AA]
STO (111)	0.05	7746.39
	5	77.27
	10	38.34
	15	25.23
	20	18.57
YSZ (100)	0.05	5867.09
	5	58.52
	10	29.04
	15	19.11
	20	14.07

Table 7: calculated width of the terrace for miscut YSZ (100) and STO (111) for increasing degrees of miscut. The 0.05° degrees, which is often the tolerance on regular substrates and is considered having no-miscut, is shown for comparison.

6.1 Growth of epsilon ferrite thin films on miscut substrates.

Growth of thin films of epsilon ferrite on STO (111) and YSZ (100) (*Crystal GmbH*) miscut substrates was performed keeping the same optimal growth parameters that were utilized to grow films on regular substrates (see section 0). With the intent of increasing the quality of the crystal lattice, the films were grown using the interval deposition technique (as explained in section 2.1.4): by pausing the growth after the ablation of a quantity of material necessary to obtain approximately one monolayer, the goal was to achieve a “step-flow” growth, in order to have for the adatoms, after landing on the surface of either the substrate or the growing film, the possibility to diffuse to a step edge before nucleating a surface island. Following this approach, 50 nm thick films were deposited by alternatively shooting sequences of 220 pulses on the Fe₂O₃ target (44’’, at a repetition rate of 5 pulses/s), and waiting 1’45’’ afterward each deposition sequence.

6.2 Structural characterization of epsilon ferrite thin films on miscut substrates.

Epitaxial growth was achieved on STO (111) and YSZ (100) substrates having miscut from 5 to 20 degrees. Cross sectional STEM images of two 50nm films of epsilon ferrite grown on 5° miscut STO (111) (Figure 66a) and YSZ (100) (Figure 66b), revealed how growth on miscut substrates results in highly crystalline films, which hold the same orientation as the films grown on regular substrates, as shown by the XRD goniometer diffractogram of the same films in Figure 66c. An overall high quality growth was achieved for all the films grown on miscut STO (111) substrates, as shown by the $\theta/2\theta$ x-ray diffractogram in Figure 67. As for the films grown on YSZ, an overall lower quality in the crystallinity was detected for increased degree of miscut: such phenomenon could be given by the lower continuity in the oxygen framework, as explained in section 3.1.2.

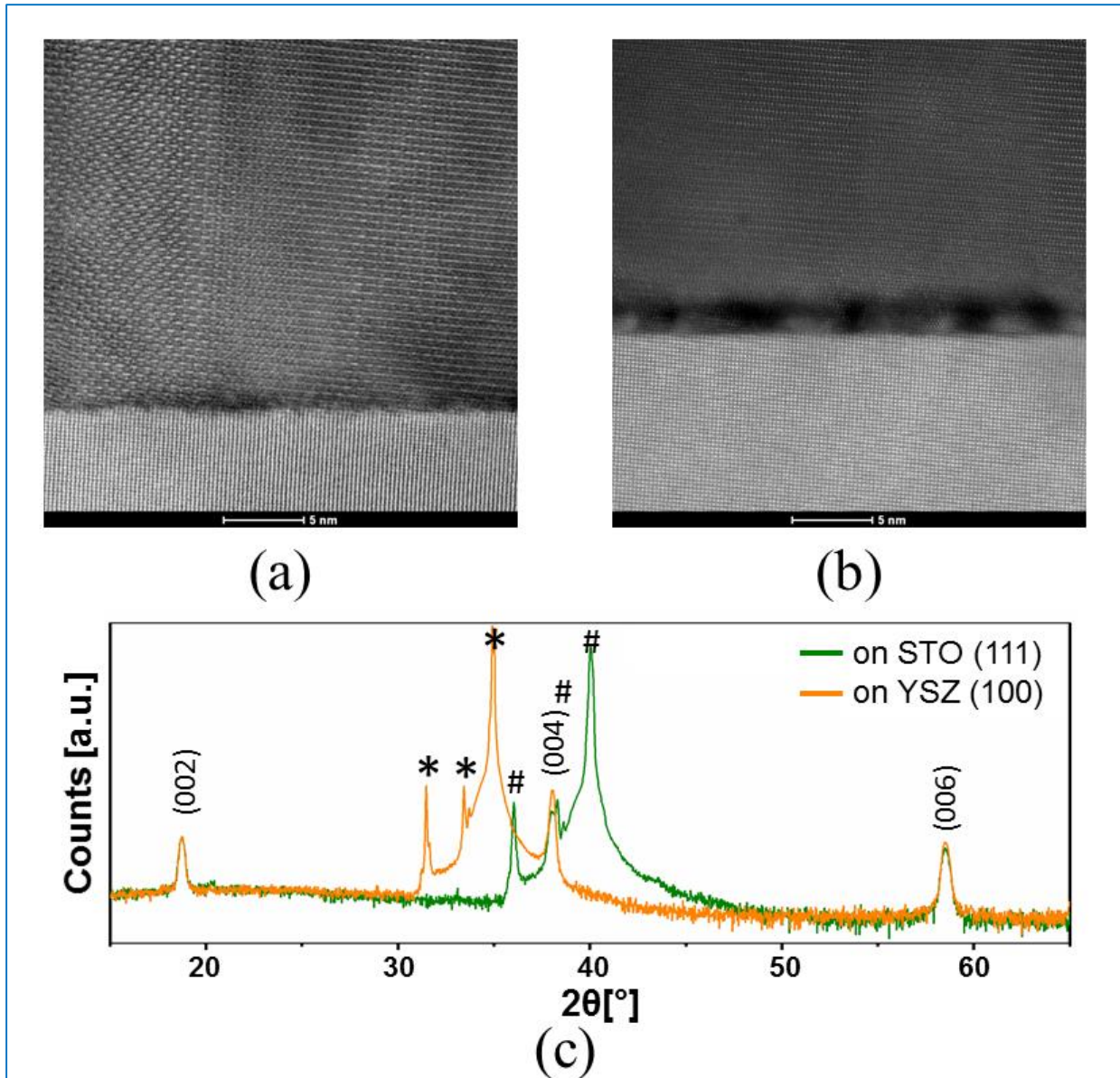


Figure 66: STEM picture for 50 nm films of epsilon ferrite grown on (a) STO (111) 5° miscut and (b) on YSZ (100) 5° miscut. As was observed for films grown on regular substrates, growth on STO (111) results in sharper interfaces than growth on YSZ (100). (c) Goniometer scan (2θ) of the films shown in the STEM images, revealing that the films grow along the same (001) direction as when grown on regular substrates. The peaks labeled by pound (#) and asterisk (*) belong respectively to the STO (111) and YSZ (100) substrates.

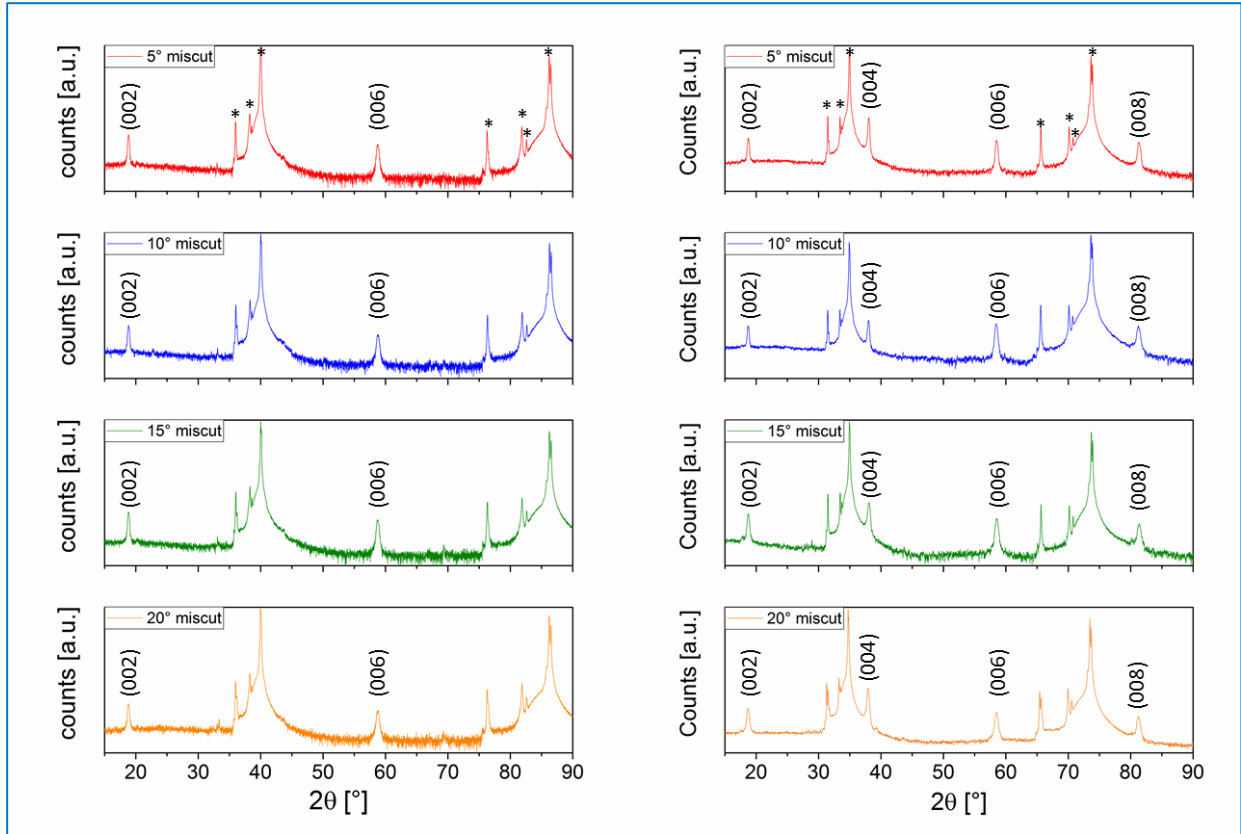


Figure 67: Goniometer scan of 50 nm thick epsilon ferrite epitaxial thin films grown on STO (111) (left) and YSZ (100) right, with increasing degree of miscut. As it was the case for epsilon ferrite thin films grown on regular substrates, the films are (001)-oriented.

In order to evaluate the effect of the miscut substrates on the twin formations, Phi scans of the (013) lattice planes were recorded (Figure 68). Comparison between the Phi scans of films grown on miscut substrate with the ones grown on regular substrates, clearly shows how higher degree of miscut reduces the formation of twins, preferentially selecting one orientation domain and giving a preferential orientation for the growth. Moreover, besides the disappearance of some growth orientation, the appearance of new growth directions, was detected for films grown on substrates with miscut higher than 10° at angles that do not correspond to any growth orientation detected for films grown on regular substrates. Such behavior was not expected and is still not completely clear, given how there were no indications of the presence of such directions for epitaxial thin films grown on regular substrates.

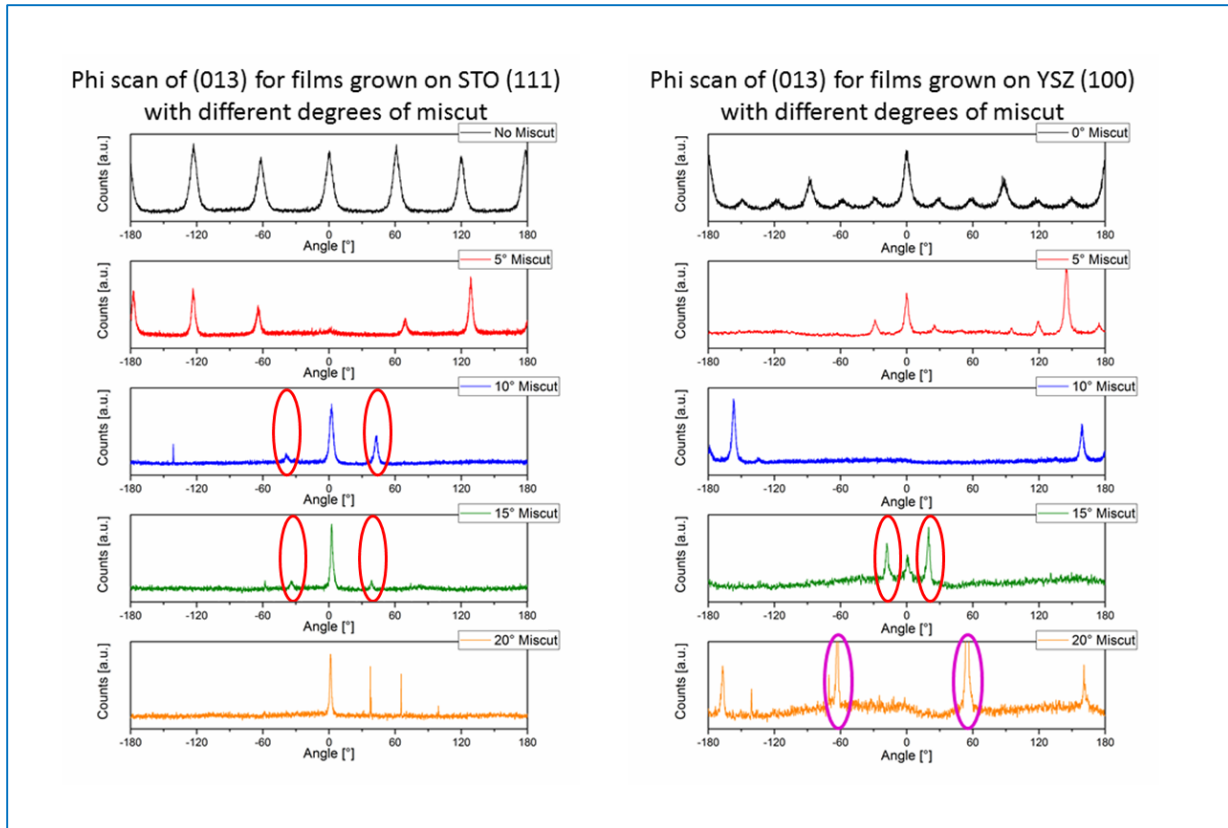


Figure 68: Phi scans of the (013) planes for 50 nm thick films of epsilon ferrite grown on STO (111) (left) and YSZ (100) (right) thin films with increasing miscut (0° - 5° - 10° - 15° - 20°). The reduction of the multiplicity of the peaks hints to a reduction of the growth orientations. It has to be noted how higher degrees of miscut (higher than 10°) lead to the formation of new growth orientations, highlighted by red circles, given the novel angular distribution of the peaks that was detected. Finally, the two main peaks detected for thin films grown on YSZ (100) miscut 20° circled in violet belong to the substrate and not the film.

As previously introduced, aberration corrected Scanning Transmission Electron Microscopy (STEM) high-angle annular dark-field (HAADF) imaging was performed on epsilon ferrite thin films grown on 5° miscut STO (111) and YSZ (100) substrates (Figure 69 and Figure 70). By analyzing the STEM images different useful information can be obtained. First, the width of the terraces is of circa 5 nm for both STO (111) and YSZ (100) 5° miscut, slightly smaller than what was estimated using equation 3.2. Second, the interface between the films and the substrates is sharper in the case of the film grown on STO than the case of YSZ, whereas in both cases a few monolayers thick buffer layer and/or some area of amorphous or differently oriented material are detected. The same behavior was also observed in films grown on regular substrates (Figure 41 and Figure 42). Third, the growth domains appear, at least for the case of films grown on substrates with 5° miscut, to extend themselves over several steps of the substrate (see Figure 69).

Finally, as was the case for films grown on regular substrates, it is possible to detect different growth orientations: such difference is particularly evident for the case of films grown on films grown on 5° miscut STO (111), as can be seen in Figure 69, where two different twins can be identified.

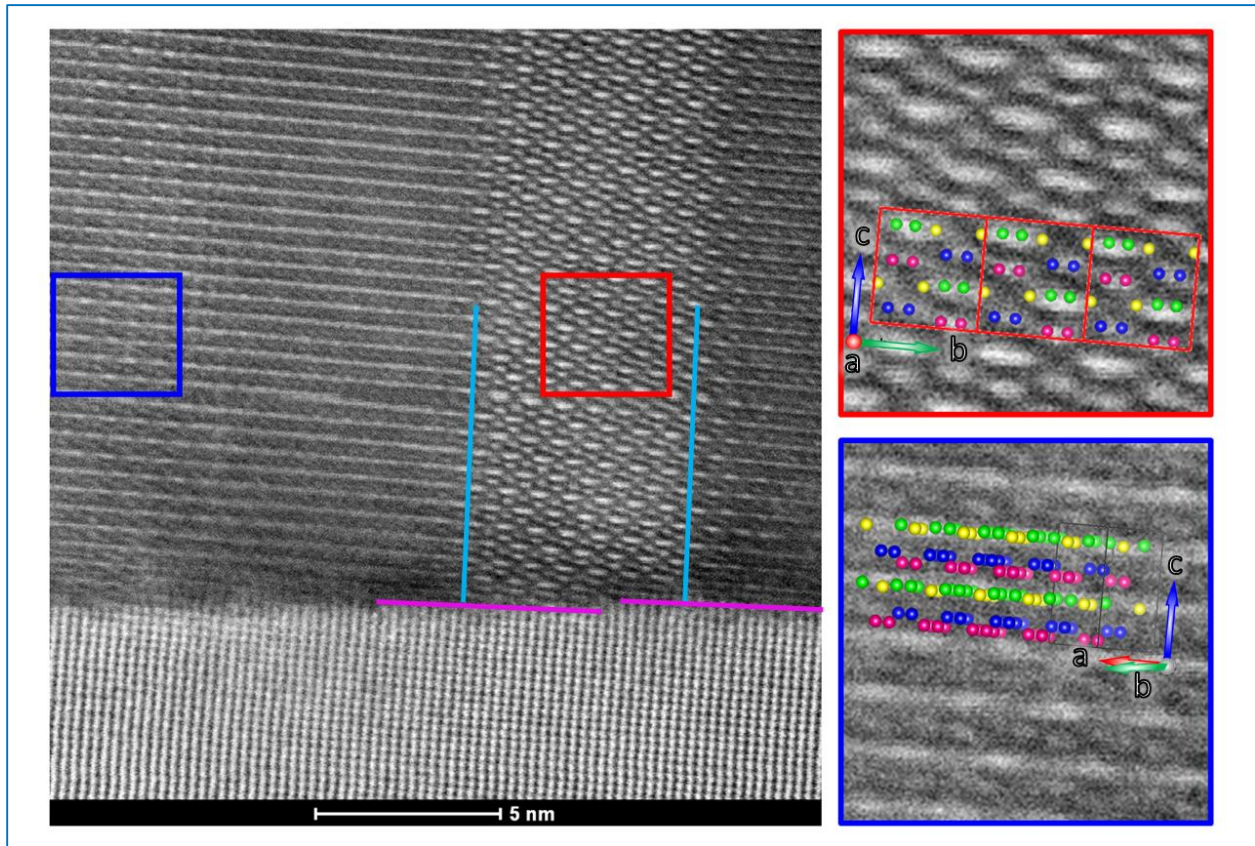


Figure 69: STEM image of the interface between a STO (111) 5° miscut substrate and the epitaxial thin film of epsilon ferrite grown on top of it. Note how one growth domain, which boundaries (blue lines), extends over several step edges of the substrate (violet lines). In the two boxes, magnification of two areas picturing two different twins, overlapped with graphical simulation of the unit cell of epsilon ferrite.

One of the two directions recorded is the one with the a lattice parameter of epsilon ferrite parallel to the terrace direction (thus pointing out of plane of the image, see the red box in Figure 69). It has to be noted how growth with the a lattice parameter parallel to the terrace (perpendicular to the miscut direction) helps decreasing the demagnetizing field, minimizing the divergence of the spontaneous magnetization \mathbf{M} inside such twin (for a detailed review on magnetic domain formations and demagnetizing fields, please refer to 67). However, such phenomenon might not be related to the growth of such twin, given how the growth temperature is way above the Curie temperature of epsilon ferrite. The second direction identified, shown in the blue box, is a 60° counter-clockwise rotation of the detail in the red box. Formations of such domain

was indeed expected and anticipated given the symmetry of the STO (111) substrate and the epitaxial relations (see section 3.1.1).

As for the STEM image of a thin film of epsilon ferrite grown on YSZ (100) miscut 5° , two different twins can be identified (red and blue box in Figure 70); the two twins are characterized by a 180° rotational symmetry, both having the b lattice parameter of epsilon (the $[010]_\epsilon$ direction) parallel to the terraces direction (thus respectively having $[010]_\epsilon$ pointing in and out of the plane of the image).

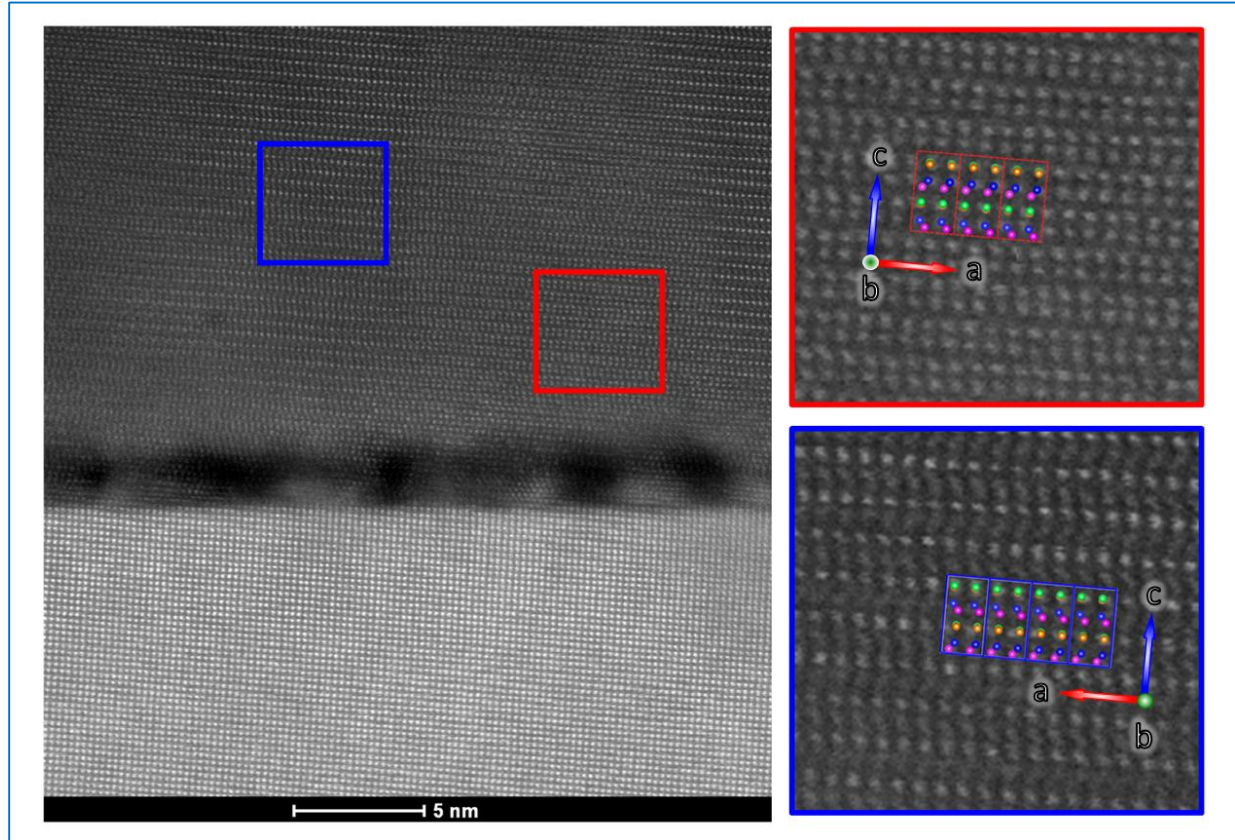


Figure 70: STEM image of the interface between a YSZ (100) 5° miscut substrate and the epitaxial thin film of epsilon ferrite grown on top of it. In the two boxes, magnification of two areas picturing two different twins, overlapped with graphical simulation of the epsilon ferrite unit cell.

6.3 Magnetic characterization of epsilon ferrite thin films on miscut substrates.

The magnetic properties of the epitaxial thin films grown on miscut substrates were characterized following the same procedure explained in section 2.2.4 for films grown on regular substrates.

Analysis of the in-plane hysteresis loops of thin films grown on 5° miscut substrates (Figure 71) revealed how the films retain (i) their high coercivity and are characterized by values of magnetization at saturation comparable to the ones measured for films grown on substrate without any miscut, and (ii) their characteristic shoulder at low applied fields, showing how the miscut does not impede the formation of the secondary magnetite phase (as was also hinted by STEM image in Figure 70). Such secondary magnetite phase appears to be more relevant for films grown on YSZ (100) (Figure 71b) substrates than on STO (111) (Figure 71a), confirming what was already observed for films grown on regular substrates and detected by STEM imaging.

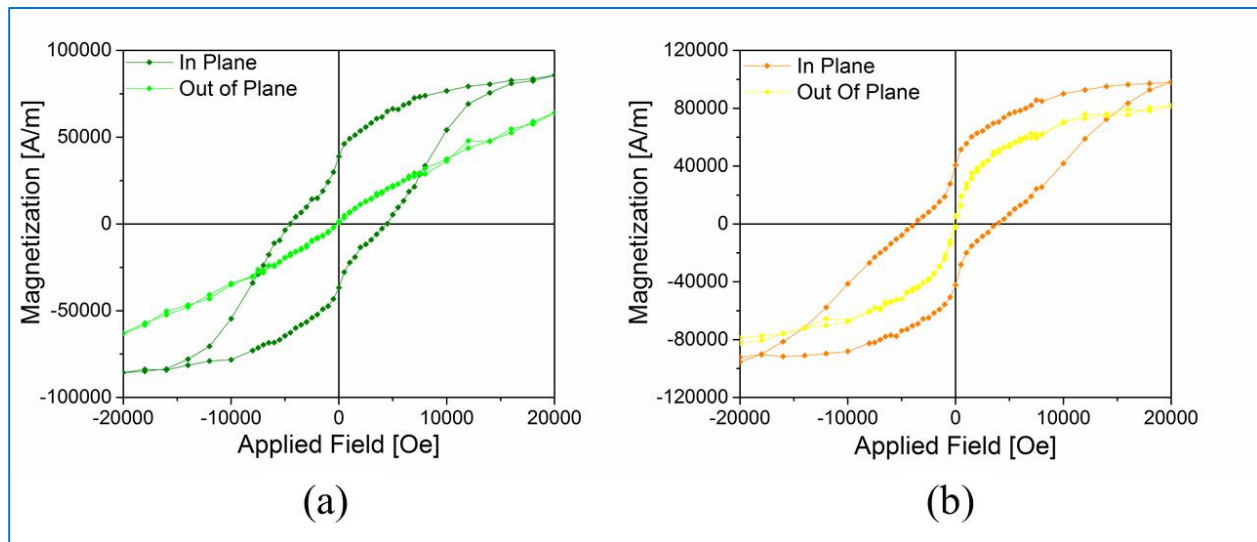


Figure 71: Magnetic hysteresis in-plane and out-of-plane measured for two 50 nm thick thin films of epsilon ferrite grown on 5° miscut STO (111) (a) and YSZ (100) (b).

Measurement conducted with the applied field perpendicular to the film surface (the so-called out-of-plane measurements), once more confirmed the strong in-plane anisotropy of the epsilon ferrite thin films. It has to be noted that the out-of-plane hysteresis loop of the film grown on 5° miscut YSZ (100) is dominated by the contribution of the soft magnetite, further confirming how such phase is more significant when epsilon ferrite is grown on the cubic YSZ.

In order to confirm the reduction of twins formation (*i.e.* of an increased “global” magnetic anisotropy) that were evidenced through phi scans by x-ray diffractometry, an analysis of the angular distribution of the magnetic properties of epsilon ferrite thin films grown on miscut substrates was performed. The angular dependence of the remanent magnetization was studied for films grown on substrates with increasing degrees of miscut: as can be seen in Figure 72, the growth on miscut substrate, both STO (111) and YSZ (100), does indeed reduce the multiplicity of the maxima hinting to the selection of one orientation domain over the others and the formation of an anisotropic configuration for films grown on miscut substrates higher than 10°.

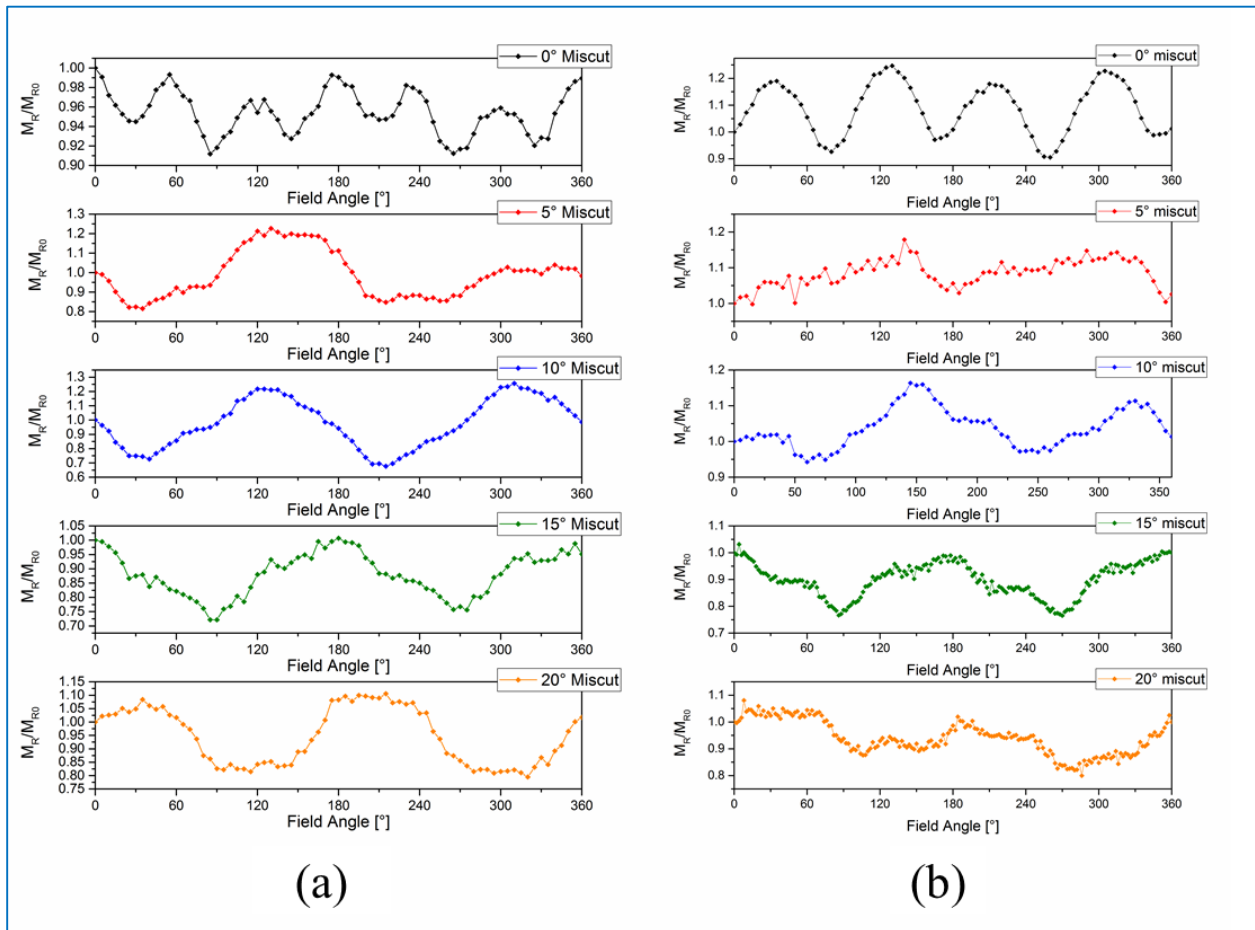


Figure 72: Evolution of the remanent magnetization in thin films of epsilon ferrite grown on STO (111) (a) and YSZ (100) (b) with increasing degree of miscut. The measurements hint to an increase in “global” anisotropy for films grown on substrates with miscut higher than 10°, as shown by the decrease in the number of local maxima and the progression to a 180° symmetry.

6.4 Conclusions.

Epitaxial thin films of epsilon ferrite with thickness of circa 50 nm were grown on STO (111) and YSZ (100) substrates characterized by miscut with degrees ranging from 5 to 20°, with the objective of reducing the formation of in-plane growth orientation domains (also called twins) which could be detrimental for some applications (*i.e.* for magnetic permanent memories). In order to improve the quality of the lattice of the grown films, with the goal to achieve a step-flow growth regime, the so-called interval deposition technique was used, by alternatively ablating a quantity of material sufficient to deposit one monolayer and pausing the deposition to let the adatoms sufficient time to diffuse towards the step-edges.

Transmission electron microscopy, coupled with x-ray goniometer scans, revealed how the epsilon ferrite thin films maintain their good crystallinity and (001) growth epitaxial growth, as was the case for films grown on regular substrates. Structural (via phi-scan x-ray diffractometry) and magnetic (via vibrating sample magnetometry) characterization revealed how the growth on miscut substrate does indeed reduce the twins formation, resulting, especially for films grown on substrates with miscut higher than 10°, in a quasi-uniaxial anisotropy.

Chapter 6

Chapter 7 GENERAL CONCLUSIONS AND PERSPECTIVES.

7.1 General conclusions

The growth of epitaxial thin films of epsilon ferrite $\epsilon\text{-Fe}_2\text{O}_3$ of thickness comprised between 25 and 150 nanometers was achieved on (111)-oriented perovskites, such as SrTiO_3 , LSAT and LaAlO_3 (LAO), as well as on (100)-oriented yttrium-stabilized zirconia (YSZ) by pulsed laser deposition. While the growth of epsilon ferrite on SrTiO_3 (111) had already been reported, growth of $\epsilon\text{-Fe}_2\text{O}_3$ on LSAT (111), LAO (111) and YSZ (100) is unprecedented. The possibility of growing epitaxial thin films of epsilon ferrite on YSZ (100) is of great significance for applications given how yttrium-stabilized zirconia is often used as a buffer layer to facilitate the growth of complex oxides on silicon.

A thorough analysis of the relations between the crystal structure of epsilon ferrite and that of the underlying substrates promoting epitaxial growth in spite of their different symmetry and crystal structure, lead to the conclusion that we took advantage of an “unusual” heteroepitaxial growth regime, *hard heteroepitaxy*, to achieve the epitaxial growth mode enabling the stabilization of epsilon ferrite, a metastable phase of Fe_2O_3 . Hard heteroepitaxy is used to describe the growth of films for which either the structure, the lattice parameters, or the type of chemical bonds differs between the film and the underlying substrate. In the case of epsilon ferrite epitaxial thin film, the epitaxial growth is promoted by the continuity of the oxygen framework between the substrates and the film.

Detailed characterization performed by x-ray diffractometry and scanning transmission electron microscopy revealed the high quality of the PLD-grown epitaxial thin films of epsilon ferrite, and how, independently from the choice of substrates, the films obtained were (001)-oriented (thus with their c lattice parameter out-of-plane) and fully relaxed (the measured lattice parameters were equal to the one reported for the unit cell of epsilon ferrite in nanoparticles) irrespective of the substrate. The fully-relaxed nature of the films was ascribed to the presence of oxygen polyhedra which can rotate to accommodate the epitaxial stresses and strains introduced by the substrates.

STEM analysis focused at the interface between the substrates and epsilon ferrite revealed how films grown on SrTiO_3 (111) possesses a sharp interface, only few Angstroms thick, while a few nanometers thick buffer

layer characterizes the ones grown on YSZ (100). The evidences of fully-relaxed films and of thinner buffer layer at the interface of films grown on SrTiO₃ (111), strengthen the hypothesis that it is indeed the continuity of the network of oxygen polyhedra that stabilize the metastable epsilon ferrite, given how there is a better continuity of this network in the case of films grown on STO (111) than for films grown on YSZ (100).

Structural characterization highlighted how the films are characterized by multiple in-plane growth variant (twins) and how their geometry depends on the choice of substrates. On (111)-oriented perovskites, which possess oxygen termination having a hexagonal symmetry, the orientation of the twins differs by an angle of 60°. On the other hand, for films grown on YSZ (100), the orientation of the twins differs by an angle of 30°. This is due, in the latter case, to the existence of two different epitaxial matches for ϵ -Fe₂O₃ grown on YSZ (100). Evidence of the presence of all these different oriented twins was gathered both by x-ray diffractometry and by scanning transmission electron microscopy.

Analysis of the angular dispersion of the peaks in the XRD phi scans of films grown on different substrates showed that the films grown on YSZ (100) are characterized by a lower in-plane mosaicity compare to the ones grown on (111)-oriented perovskites. This can be explained by the higher “angular density” of the twins for films grown on YSZ (every 30° opposed to every 60° for films grown on (111)-oriented perovskites).

Finally, the presence of interstitial domain was revealed by a careful study of the XRD phi scans. Such domains appear to be present irrespective of the type of substrate the films are grown on, and are characterized by a smaller *a* lattice parameter compared to the “regular” domains.

Macroscopic magnetic characterization performed using a vibrating sample magnetometer (VSM) confirmed the highly anisotropic nature of epsilon ferrite thin films. The in-plane hysteresis loops are characterized by a high coercive field of circa 8 kOe. This value is smaller than the coercive field measured for epsilon ferrite nanoparticles, which was found to be as high as 20kOe. Comparison of the in-plane and out-of-plane magnetic hysteresis, however, confirmed the high in-plane anisotropy of the epitaxial thin films, and led to an estimation of the anisotropy field of circa 43 kOe. By estimating the anisotropy field, it was also possible to approximate the ferromagnetic resonance frequency, which was estimated to be 130 GHz. Also in this case, the FMR frequency values estimated for thin films are lower than the one reported for nanoparticles which were reported to be 63 kOe and 190 GHz. The lower values of the coercive field, anisotropy field and FMR frequency can be explained by the fact that the nanoparticles are single magnetic domains, while the thin films are likely characterized by a multiple domains configuration.

Chapter 7

Another major feature that was noticed from the analysis of the in-plane hysteresis loops is the presence of a “shoulder” at low coercive fields resulting in ‘pinched’ hysteresis loops, which was explained by the presence of a secondary soft magnetic phase. Analysis of the dependence of the magnetization with increasing temperature helped identifying the secondary phase as being magnetite. Moreover, during such analysis, an irreversible epsilon ferrite to maghemite phase transition was detected at a temperature of circa 600 °C.

Finally, the in-plane angular dependence of the magnetic properties was probed by measuring hysteresis loops every 2°. The angular distribution of the remanent magnetization shown the same symmetry highlighted during the structural characterization and was fitted satisfactorily by a model developed using the information gathered via angular x-ray measurements.

Microscopic magnetic characterization was also performed using magnetic force microscopy. Although images with contrast different from the topology of the surface were gathered, it was not possible to interpret them in terms of magnetic domains, given the inherent complexity of magnetic force microscopy and the in-plane anisotropy of the epsilon ferrite thin films.

The macroscopic ferroelectric properties of epitaxial thin films of epsilon ferrite were probed using a ferroelectric tester. In order to perform such measurements, the thin films were grown on conductive Nb doped SrTiO₃ (111) substrates and circular platinum electrodes were deposited on top of the films by sputtering. The measured ferroelectric hysteresis loops are characterized by strong leakage currents, which impede the detection of switching currents. Presence of paths of low resistance might be due by the simultaneous occurrence of Fe³⁺ and Fe²⁺ (which, for example, characterize magnetite Fe₃O₄, the presence of Fe²⁺ itself possibly originating from the small quantity of magnetite present in the films) which creates a quantity of free electrons which can then hop between the two different iron sites.

Microscopic ferroelectric measurements were performed by piezoresponse force microscopy that are less sensitive to leakage current: a piezoelectric response was indeed detected for some of the grains analyzed, although it was not possible to switch them back. Such impossibility might be due to pinning caused by the strong magnetic interaction; other reasons behind the pinning could be the presence of defects or of fields at the interface. In any case, such behavior was non-consistent and further analysis has to be performed in order to confirm piezoresponse in thin films of epsilon ferrite.

The ferromagnetic resonance (FMR) frequency was also probed directly by ferromagnetic resonance measurements and by time domain spectroscopy. Direct characterization did not yield any measurements of the ferromagnetic resonance frequency due to the small magnetic moment of the epsilon ferrite thin films

and to the unavailability of a resonant cavity with its resonance frequency close to the values expected for the resonance of epsilon ferrite that would be needed to provide the necessary amplification. Precise measurements of the FMR frequency of epsilon ferrite were not possible either by THz time domain spectroscopy (THz-TDS). However, higher absorption for epsilon ferrite thin films deposited on YSZ (100) compared to the YSZ (100) bare substrate was recorded in the 50-150 GHz range, providing a hint that the FMR frequency for epsilon ferrite thin films falls in this range.

Aluminum substituted epsilon ferrite ($\epsilon\text{-Al}_x\text{Fe}_{2-x}\text{O}_3$) epitaxial thin films were then grown on SrTiO_3 (111) and on YSZ (100). Substitution over a wide range ($x = 0.03 - 0.5$) was achieved. Al substitution proved to linearly reduce the out-of-plane lattice parameter with increasing aluminum concentration, as was expected given the smaller ionic radius of aluminum ions in comparison to iron. A linear decrease the coercive field with increased Al content was detected, along with an increase of the remanent magnetization up to a threshold of $x = 0.33$, in accordance with the results previously reported for aluminum and gallium substituted nanoparticles. The increase and then decrease of the remanent magnetization is due to preferential targeting of one of the four iron sites by the diamagnetic aluminum ions (M_r increase) until all these sites are substituted and then substitution occurs at other sites (M_r decrease). The potential ferroelectric nature of aluminum-substituted epsilon ferrite thin films was probed on the macroscopic and microscopic scales: an improvement of the ferroelectric properties was indeed expected given the switchable polarization reported for AlFeO_3 . Unfortunately, however, the films were still characterized by very high leakage currents which hampered detection of the switching currents.

Finally, the possibility of growing epitaxial films of epsilon ferrite characterized by selective growth orientation by depositing them on miscut substrates was investigated. This study was prompted by the fact that formation of multiple growth orientations, thus multiple magnetic easy axes, is detrimental for some applications, such as, for instance, magnetic memories. High quality (100)-oriented epitaxial thin films of epsilon ferrite were grown SrTiO_3 (111) and on YSZ (100) with high and increasing degree of miscut (substrates with 5° , 10° , 15° and 20° were utilized). Structural characterization performed by XRD and STEM showed how it is indeed possible to reduce the angular distribution of the twins by growing the thin films on miscut substrates. Measurements of the angular dependence of the magnetic properties highlighted how films grown on miscut substrates, in particular the ones grown with miscut higher than 10° , are characterized by growth along a selected orientation, thus start exhibiting a resemblance of a single magnetic “easy” axis.

7.2 Perspectives

In order to further clarify the mechanism behind the stabilization of $\epsilon\text{-Fe}_2\text{O}_3$, and to better understand which epitaxial growth mode characterizes the growth of epsilon ferrite thin films, real time monitoring of the growth would be of great interest. Being able to deposit films while characterizing their surface by reflection high-energy electron diffraction (RHEED) would give useful insights on the growth regime (layer-by-layer, island growth, etc.), allowing better understanding of the hard heteroepitaxial growth regime. Developing a rigorous description of such heteroepitaxial growth mode could prompt the investigation of the epitaxial growth of complex materials, which thus far have not been investigated due to the lack of “classic” heteroepitaxial matches. Moreover, growth on miscut substrates would also greatly benefit from real-time monitoring of the crystal growth, allowing to precisely achieving a step-flow growth mode which would significantly increase the quality of the films.

Given the successful deposition of high quality epitaxial thin films of epsilon ferrite on YSZ (100), and how YSZ is often used as a buffer layer for growth of complex oxides on silicon substrates, the growth of epsilon ferrite on silicon should be investigated. Showing how it is possible to achieve high quality epsilon ferrite thin films on epitaxial YSZ on silicon will certainly increase the interest on such material as well, given how it would open the door to designing $\epsilon\text{-Fe}_2\text{O}_3$ -based devices easily integrable into consumer electronics. In particular, epsilon ferrite epitaxial thin films, given its “magnetic” stability, could find potential applications in nanomagnetic logic (NML)^{120,121}, an exciting new field where transmission and computation of data are accomplished using magnetic fields instead of electrical current, as happens in the widely used complementary metal–oxide semiconductor (CMOS). Moreover, being able to expand the list of substrates on which it is possible to achieve epitaxial growth will also help confirming the hypothesis we made on the continuity of the oxygen framework as the key element for the successful growth of epitaxial $\epsilon\text{-Fe}_2\text{O}_3$, validating the use of hard epitaxy as a useful growth mode to possibly extend the variety of substrates - or at least having more insight on choosing them - on which epitaxial films could be grown.

Further investigation on the ferromagnetic resonance frequency of epsilon ferrite epitaxial thin film will also be needed. As it was for epsilon ferrite nanoparticles, showing that also thin films are characterized by a FMR frequency in the low THz regime, and how such frequency is tunable, for example by substituting aluminum into the lattice, will probably constitute a breakthrough which will spur the interest towards epsilon ferrite thin films for millimeter waves or THz applications. Once this task will be achieved, the possibility of tuning “up” the FMR frequency, for example by rhodium substitution should also be

investigated. Considering the amount of publications on the generation and manipulation of THz radiation (see the recent creation of an IEEE journal only dedicated to the topic, IEEE Transactions on Terahertz Science and Technology), having thin films of a simple material capable of interacting with such frequency range will surely attract great interest. Moreover, a precise measurement of the FMR frequency of epsilon ferrite thin films, coupled with the efforts that were made in order to achieve growth along a single in-plane orientation, can prompt significant advancements towards the possibility of achieving magnetization switching through optical manipulation. Being able to show, even if only as a proof of concept, that it is indeed possible to fabricate an optically writable, and readable, magnetic memory could represent a technological breakthrough for the field of non-volatile magnetic memories.

After having been able to precisely identify the nature of the secondary magnetic phase, efforts are presently being conducted by the group of Professor G. Botton to *identify the location* of the ‘parasitic’ magnetite through electron energy loss spectroscopy (EELS). Although not detrimental for magnetism-based applications, the phenomena around the formation of Fe_3O_4 need to be better understood in order to produce epitaxial thin films of epsilon ferrite of even higher quality. Moreover, the secondary magnetite phase is most probably indirectly responsible of the impossibility of measuring and switching the ferroelectric polarization which characterizes epsilon ferrite. One way to reduce the formation of magnetite could be doping the films with low quantity of magnesium (around 2%), which has already proved to help decrease leakage currents in the isostructural GaFeO_3 ^{116,122}. Efforts towards obtaining a “magnetite-free” films should be coupled with an investigation of the optimal materials to use as bottom and top electrode (instead of the currently used Nb-doped STO and platinum) in dielectric/piezoelectric/ferroelectric $\epsilon\text{-Fe}_2\text{O}_3$ -based devices. Showing multiferroic behavior for an inexpensive, and somehow simple, single phase material such as epsilon ferrite, could re-spark the interest for single phase multiferroics/magnetoelectrics that has slightly faded in the latest years due to the lack of simple materials exhibiting both ferromagnetism and ferroelectricity at room temperature. When it will be possible to detect macroscopic switchable polarization at room temperature, the next step will be to find how such polarization is coupled with the magnetic ordering. Showing magnetoelectric coupling would allow to further expand the possible application of epsilon ferrite thin films to multiferroic memories, where switch of the magnetization could be achieved by applying electric fields instead of magnetic fields, greatly increasing the bit-density, thus the memory capacity, and also reducing energy consumption^{123–125}.

Chapter 8 SYNOPSIS IN FRENCH

Les nanostructures à base d'oxydes de fer sont un sujet de recherche attrayant au sein de la communauté scientifique, compte tenu des nombreuses applications envisagées^{7,126,127}. Les propriétés magnétiques intrinsèques des oxydes de fer, par ex. leur haute magnétisation spontanée à température ambiante et leur haute température de Curie, les rendent appropriés non seulement pour des applications technologiques générales telles que des supports d'enregistrement magnétiques ou des aimants permanents^{1,128}, mais aussi pour des applications dans divers domaines de la médecine tels que la délivrance de médicaments, le diagnostic médical, car au-delà de leur propriétés magnétiques, elles ne sont pas toxiques, sont biodégradables et biocompatibles^{14,129-135}. En outre, les nanostructures d'oxydes de fer sont souvent utilisées comme modèles dans des études théoriques pour clarifier les caractéristiques magnétiques particulières des systèmes nanométriques non observables dans leurs homologues massifs¹³⁶. Enfin, les diverses formes d'oxydes de fer constituent les composés de fer les plus courants dans la nature et sont généralement faciles à synthétiser.

Bien que ne soit pas aussi facile à synthétiser que les autres polymorphes, en raison de son instabilité intrinsèque à l'état ambiant (ce qui n'a toutefois pas empêché les artisans chinois Jian de l'utiliser comme pigment noir pour leur vases il y a plus de 800 ans)²⁶, ϵ -Fe₂O₃ mérite tout notre attention, en effet, étant une phase intermédiaire de Fe₂O₃ entre la maghémite (γ -Fe₂O₃) et l'hématite (α -Fe₂O₃) avec une structure cristalline orthorhombique complexe (Figure 4). La phase Epsilon de l'oxyde ferrique (oxyde de fer (III)) a d'abord été synthétisé en 1934, lorsque Forestier et Guiot-Guillain ont signalé l'existence d'un oxyde de fer(III) différent de α -Fe₂O₃ et γ -Fe₂O₃²⁷. Ensuite, en 1963, Schrader et Buttner²⁸, et à peu près au même moment Walter-Levy et Quemeneur²⁹, ont pu synthétiser ce matériau, pour en mesurer le diagramme de diffraction des rayons X (DRX) pour la première fois. La phase pure a ensuite été obtenue par Trautmann et Forestier en 1965³⁰. En effet, en raison de son instabilité structurelle et chimique intrinsèque dans les conditions ambiantes, ϵ -Fe₂O₃ doit être stabilisé par un confinement de taille. Par exemple, il a été démontré que ϵ -Fe₂O₃ pourrait être synthétisé sous la forme de nanoparticules encapsulées dans une matrice de silice (SiO₂) par des méthodes sol-gel³¹, ou comme nano-fils¹³⁷. Ces nanostructures se sont révélées magnétiques avec une température de Curie $T_C \approx 490$ K⁴³ et présentent des valeurs remarquablement élevées du champ coercitif à température ambiante, $H_C \approx 20$ kOe⁴³. Le champ coercitif très élevé des nanoparticules de ϵ -Fe₂O₃ en font un matériau prometteur pour les mémoires non volatiles ou les aimants permanents, malgré leur aimantation spontanée inférieure à celles de la maghémite et de l'hématite.

Le dichroïsme circulaire magnétique de rayons-X a montré que la grande coercivité des nanoparticules du ϵ -Fe₂O₃ provient de la présence d'une grande anisotropie magnétocristalline⁶³. Cette grande anisotropie magnétocristalline, induite par les distorsions du réseau des polyèdres de coordination du Fe³⁺, conduit à une forte hybridation entre les orbitales Fe_{3d} et O_{2p}, ce qui donne un moment magnétique orbital L non nul, ce qui, en conséquence du couplage spin-orbite, définit un axe magnétique-facile. De plus, les premiers calculs *ab initio* ont soutenu la découverte expérimentale, prédisant que l'axe magnétique facile se situe dans la direction de l'axe a de la cellule cristalline unitaire⁶⁴.

En raison de son anisotropie magnétocristalline élevée, l'oxyde ferrique Epsilon est l'un des rares matériaux ayant sa fréquence de résonance ferromagnétique naturelle, donc à température ambiante et sans appliquer de champ magnétique, supérieure à 100 GHz, dans la gamme THz (c. à d. entre 0,1 et 100 THz). Cette caractéristique est intéressante étant donné que les fréquences THz ont récemment reçu beaucoup d'attention en termes de physique fondamentale et d'applications dans divers domaines, tels que les communications, la défense / sécurité, l'imagerie médicale, la biologie et l'astronomie¹³⁸⁻¹⁴². En outre, comme ϵ -Fe₂O₃ se caractérise par une structure cristalline orthorhombique appartenant au groupe spatial non-centrosymétrique et polaire $Pna2_1$ (Figure 73), elle doit présenter au moins des propriétés de pyroélectricité, ce qui en fera un nouveau membre de la famille des oxydes magnéto-électrique⁸⁹, ou encore un nouvel oxyde multiferroïque à température ambiante. Enfin, il a été récemment démontré que l'oxyde ferrique Epsilon est également un catalyseur très efficace pour la génération solaire d'hydrogène activé par la lumière à partir de solutions d'eau et de divers oxydes⁴⁷.

Afin d'intégrer ϵ -Fe₂O₃ dans des dispositifs semi-conducteurs, les nanoparticules ne sont généralement pas la forme la plus appropriée. Néanmoins, le dépôt d'un mélange de nanorods ϵ -Fe₂O₃ et β -Fe₂O₃ supportés sur une plaquette de silicium synthétisé par dépôt chimique en phase vapeur a été démontré⁴⁶. Cependant, ces nanostructures ne possèdent pas les mêmes propriétés fonctionnelles que leurs homologues sous forme de nanoparticules ; en particulier, ils présentent un champ coercitif beaucoup plus faible. En outre, ils ne présentent pas une structure complètement ordonnée, ce qui les rend inadéquats pour les applications où une telle commande est nécessaire. Afin de favoriser l'intégration de ϵ -Fe₂O₃ dans les dispositifs et de profiter de l'ordre magnétique, et peut-être ferroélectrique, caractérisant la phase Epsilon de l'oxyde ferrique, la forme la plus appropriée serait des couches minces épitaxiées. Il se trouve que le dépôt de ces couches épitaxiées de ϵ -Fe₂O₃ par ablation laser pulsé a été récemment signalée⁴⁸, où la stabilisation de la phase epsilon métastable a été réalisée en mettant à profit la contrainte épitaxiale induite par le substrat de titanate de strontium (SrTiO₃) monocristallin utilisé. Plus récemment encore, la croissance sur des substrats autres que SrTiO₃, à savoir l'alumine et la zircone stabilisée à l'yttrium (YSZ), a été réalisée, bien que non directement sur YSZ, mais avec une couche tampon de GaFeO₃ (GFO) de 50 nm d'épaisseur sur YSZ

utilisée pour favoriser la croissance de ϵ -Fe₂O₃⁴⁹. En outre, bien que le comportement ferroélectrique des films d'oxyde de fer Epsilon pur n'a jamais été étudié, la présence d'une polarisation spontanée réversible a aussi récemment été rapportée dans une structure en couches de SrTiO₃:Nb / AlFeO₃ / SrRuO₃ / ϵ -Fe₂O₃⁵⁰.

Dans ce contexte, mes recherches se sont concentrées sur l'expansion des connaissances actuelles sur la croissance de couches minces épitaxiés d'oxyde ferrique Epsilon sur différents substrats monocristallins par ablation laser pulsé et sur leurs propriétés structurelles et fonctionnelles. Au départ, l'idée d'étudier le ϵ -Fe₂O₃ a été motivée par une publication d'Ohkoshi *et al.* qui a montré comment il était possible d'induire la précession de l'aimantation dans des nanoparticules de ce matériau en utilisant une radiation THz de fréquence égale à sa fréquence de résonance magnétique (FMR)⁵¹. En plus d'une recherche plus fondamentale sur la physique sous-jacente de la magnétisation/démagnétisation ultra-rapide induite par des impulsions laser femtoseconde⁵²⁻⁵⁴, cette étude a suscité un grand intérêt à l'INRS-EMT, compte tenu de l'expertise de notre propre groupe - le Ferroic Lab - dans la croissance de films minces épitaxiés d'oxydes complexes multifonctionnels ainsi que de l'existence à INRS-EMT d'un laboratoire de pointe pour la g En effet ϵ -Fe₂O₃, en raison de sa fréquence FMR naturelle dans la gamme THz basse était un matériau de choix idéal pour approfondir une telle recherche. Le but ultime de ce projet initial était d'obtenir une commutation ultra-rapide de l'aimantation en utilisant des impulsions THz asymétriques de haute intensité. Un tel exploit augmenterait considérablement la vitesse d'inversion de l'aimantation, qui est une caractéristique clé dans le stockage de données magnétiques, sans oublier qu'il s'agirait également d'un processus de commutation déclenché à distance donc sans avoir besoin d'électrodes. Dans la technologie de l'enregistrement magnétique l'état de l'art en ce qui concerne la commutation de la magnétisation, c'est-à-dire l'inversion complète de la direction du vecteur de magnétisation **M**, se produit sur une échelle de temps de l'ordre de la nanoseconde, beaucoup plus grande que le temps de précession caractéristique de l'aimantation – qui est lui de l'ordre des picosecondes⁶⁰. Avoir des couches minces épitaxiés plutôt que des nanoparticules, permet d'avoir une structure cristalline ordonnée sur une relativement grande surface et est également très favorable à leur éventuelle intégration dans les dispositifs électroniques.

Le premier défi rencontré fut d'obtenir la croissance de couches minces épitaxiés par PLD et de comprendre les mécanismes expliquant la stabilisation de la phase Epsilon. Ensuite, les propriétés fonctionnelles des films d'oxyde ferrique Epsilon ont été caractérisées afin de les comparer à celles des nanoparticules. Au début de notre étude, nous nous intéressions principalement au champ coercitif élevé qui est un effet de l'anisotropie magnétocristalline élevée, laquelle est également responsable de la fréquence de résonance magnétique (FMR) dans la gamme THz basse. L'étape suivante, étant donné la structure cristalline non-centrosymétrique de nos films, a été d'étudier leurs propriétés diélectriques dans l'espoir - en cas de détection d'une polarisation commutable - d'obtenir un nouveau matériau monophasé multiferroïque avec

une composition chimique très simple et fonctionnant à température ambiante. Enfin, nous avons examiné l'effet de la substitution partielle du fer dans $\epsilon\text{-Fe}_2\text{O}_3$, en mettant l'accent sur les effets de l'aluminium, pour essayer de reproduire les études publiées dans la case nanoparticules de $\epsilon\text{-Fe}_2\text{O}_3$. Nous avons enfin étudié la possibilité de croître $\epsilon\text{-Fe}_2\text{O}_3$ sur des substrats vicinaux fortement tronqués afin de réduire la formation des macles cristallines qui caractérisent les films minces épitaxiés déposés sur des substrats normaux sans troncature (idéalement sans terrasse ou avec des terrasses beaucoup plus larges) et dont la présence est due à la symétrie plus élevée du substrat par rapport à celle de la couche déposée.

Ce manuscrit sera donc organisé de la manière suivante :

*La **Partie I** comprend le contexte théorique et la description des techniques expérimentales utilisées au cours de mon doctorat. Il est divisé en deux chapitres :*

Chapitre 1 : Contexte théorique. Le chapitre 1 présentera la physique derrière le développement de mes recherches. Tout d'abord, je donnerai plus de détails sur $\epsilon\text{-Fe}_2\text{O}_3$; Ensuite, je discuterai de l'ordre magnétique, puis de la ferroélectricité, et conclurai en introduisant le concept de multiferroïcité.

Chapitre 2 : Expérimental. Ce chapitre sera divisé en deux parties : la première abordera la technique de dépôt utilisée dans ce travail, c'est-à-dire le dépôt par ablation laser pulsé, tant du point de vue théorique que pratique. La deuxième partie examinera les principales méthodes de caractérisation qui ont été utilisées au cours de toute l'étude.

La **Partie II** traitera des différents résultats expérimentaux obtenus dans mes recherches. Il sera divisé en cinq chapitres :

Chapitre 3-4-5-6 : Résultats et discussion. Les résultats expérimentaux seront répertoriés ici. Tout d'abord, les caractéristiques de la croissance de couches minces épitaxiales de $\epsilon\text{-Fe}_2\text{O}_3$ par ablation laser pulsé seront présentées. Ensuite, les données expérimentales collectées seront analysées, en commençant par les résultats structuraux mesurés par diffractométrie aux rayons-X et par microscopie électronique en transmission, puis par caractérisation magnétique et diélectrique. Une description détaillée de la croissance des couches minces épitaxiales d'oxyde ferrique epsilon dopé avec aluminium ($\epsilon\text{-Al}_x\text{Fe}_{2-x}\text{O}_3$) sera donnée, mettant en évidence comment, en modifiant la concentration d'aluminium dans les films, il est possible de contrôler le champ coercitif et l'aimantation rémanente. Enfin, l'étude de l'effet de la croissance sur des substrats à haut degré de « miscut » sera présentée, en se concentrant sur l'effet des différents substrats sur la réduction du nombre d'orientations de croissance dans le plan.

Chapitre 7 : Conclusions et perspectives. Finalement, ce chapitre servira de conclusion générale de la thèse et aussi à décrire les travaux futurs nécessaires à encore améliorer les couches minces de $\epsilon\text{-Fe}_2\text{O}_3$ et leurs propriétés, ainsi qu'à leur l'intégration dans de possibles dispositifs.

Cette thèse contient un rapport détaillé sur la croissance et la caractérisation des films minces de $\epsilon\text{-Fe}_2\text{O}_3$ stabilisés épitaxialement déposés directement sur des substrats monocristallins - pérovskites orientés (111) et zircono stabilisée à l'yttrium (YSZ) orientées (100) - en utilisant le dépôt par ablation laser pulsé (PLD), sans utiliser de couche tampon, contrairement aux études publiées antérieurement⁴⁹.

Le choix de la PLD est dû à ses succès bien connus pour le dépôt de matériaux de composition et de structure compliquées, en particulier d'oxyde complexes, et au fait qu'il est possible d'obtenir un transfert stœchiométrique des éléments de la cible aux films déposés. Ceci est notamment dû à la nature hors équilibre du processus, ainsi qu'aux nombreux paramètres qui peuvent être contrôlés indépendamment pendant le dépôt. Tous ces éléments sont essentiels pour obtenir une stabilisation épitaxiales de couches minces de $\epsilon\text{-Fe}_2\text{O}_3$.

La structure des films a été d'abord étudiée par diffraction des rayons X en utilisant le rayonnement K_α du cuivre ($\lambda = 1,5407 \text{ \AA}$) dans un diffractomètre PANalytical X'Pert PRO MRD. Des mesures dans les configurations classiques Bragg-Brentano ($\theta/2\theta$) et phi-scans (ϕ -scans) ont été effectuées, la première pour vérifier le caractère épitaxié de nos couches, c'est-à-dire l'alignement mutuel des plans cristallins des films et des substrats, tandis que la seconde détermine l'orientation dans le plan de nos films par rapport aux substrats. Étant donné le signal fort des lignes K_β provenant des substrats monocristallins, en particulier celui des pérovskites orientées (111), qui se chevauchent partiellement avec certains pics appartenant au film, un filtre de nickel a été utilisé pour couper ces lignes K_β et avoir un diffractogramme plus propre.

L'imagerie par microscopie électronique par balayage en transmission (STEM) avec correction d'aberrations a été utilisée pour étudier en détail la structure des films, avec un accent particulier sur les interfaces entre les films et les substrats. Les mesures ont été effectuées à l'Université McMaster au centre canadien de microscopie électronique par l'équipe dirigée par le professeur Gianluigi Botton. Les échantillons de microscopie électronique à transmission en coupe transverse ont été préparés selon un procédé éprouvé pour minimiser les dommages et la perte d'oxygène⁸⁶.

Les propriétés magnétiques des films ont été sondées par un magnétomètre à échantillons vibrants (VSM) EV9 fabriqué par ADE Technologies (MicroSense, Lowell MA, USA). Les cycles d'hystérésis magnétique ont été enregistrés à température ambiante avec un champ magnétique, variant entre $\pm 20\,000 \text{ Oe}$, appliqué en parallèle (dans le plan), et perpendiculaire (hors-plan) à la surface du film. Afin d'obtenir uniquement le signal du film, les contributions magnétiques du porte-échantillon (tige de verre) et des substrats ont été

mesurés séparément et soustraits du signal total. Les cycles d'hystérésis avec champ magnétique dans le plan ont été enregistrés tous les 2 degrés afin d'extraire la dépendance angulaire des propriétés magnétiques. Les propriétés magnétiques microscopiques ont été analysées en utilisant un microscope à force atomique modifié (AFM) équipé d'une pointe magnétique, ce qui en fait un microscope à force magnétique (MFM).

Les cycles d'hystérésis ferroélectriques macroscopiques ont été enregistrés avec le module FE d'un système TF Analyzer 2000 par aixACT Systems GmbH (Aachen, Allemagne). Afin de mesurer le comportement hystérétique de la polarisation, les films doivent être déposés sur des substrats conducteurs, et des électrodes métalliques doivent être déposées sur leur surface supérieure, afin d'avoir une géométrie de condensateur plan où le matériau ferroélectrique agit comme diélectrique. La réponse piézoélectrique microscopique et son éventuel comportement hystérétique ont été utilisés pour confirmer la présence des propriétés polaires et possiblement ferroélectriques à l'échelle microscopique. La réponse piézoélectrique a été mesurée en utilisant un le même AFM que celui utilisé pour les mesures MFM, cette fois équipé d'une pointe conductrice et modifié pour mesurer la réponse piézoélectrique, appelé en général un microscope à force piézoélectrique (PFM).

Enfin, la fréquence de résonance ferromagnétique a été sondée avec deux techniques différentes : des mesures directes ont été effectuées à *Polytechnique Montréal* avec un équipement spécifique, équipé de cavités spéciales permettant de mesurer la fréquence de résonance ferromagnétique, tandis que la spectroscopie dans le domaine temporel (TDS) a été la seconde technique utilisée pour sonder la résonance ferromagnétique de mes échantillons.

Avant la description des résultats expérimentaux, un mode de croissance épitaxié "inhabituel" - hétéroépitaxie difficile - est introduit afin d'essayer de mieux expliquer les phénomènes derrière la stabilisation épitaxiale des couches de ϵ -Fe₂O₃ métastable.

Les nombreuses études menées par Ohkoshi *et al.*, ont permis de clarifier les mécanismes de stabilisation de la ϵ -Fe₂O₃ lorsqu'ils sont synthétisés sous forme de nanoparticules. Dans leurs travaux, il a été montré comment ϵ -Fe₂O₃ peut être obtenu par un procédé sol-gel au moyen d'un contrôle précis de la taille des nanoparticules en les faisant croître dans une matrice de SiO₂ nano-poreuse: la stabilisation est obtenue en raison d'une certaine plage de dimensions où la phase Epsilon de l'oxyde ferrique, et non pas les phases Gamma (maghémite) ou alpha (Hématite) généralement plus stables, possède la plus basse énergie libre par unité de volume (G/V)⁶¹.

En ce qui concerne le cas des couches minces épitaxiées de ϵ -Fe₂O₃, il a très peu été publié à sur le sujet. Un rapport de Gich *et al.* a montré la possibilité d'une croissance épitaxiée selon la direction (001) de

couches minces de $\epsilon\text{-Fe}_2\text{O}_3$ sur SrTiO_3 (111)⁴⁸. Ils ont attribué la stabilisation de la phase Epsilon et l'orientation des films à la haute énergie de surface des surfaces (100) de minces épitaxiées, ainsi qu'à la formation de multiples orientations de croissance dans le plan en raison de la symétrie inférieure du film par rapport à les substrats, ce qui aide à la diminution de cette énergie grâce à la formation de plusieurs macles et donc de l'existence de nombreuses parois de domaine^{98,99}.

Dans cette thèse, nous avons démontré la possibilité de faire croître des couches minces épitaxiées de $\epsilon\text{-Fe}_2\text{O}_3$ sur des substrats de pérovskites orienté selon l'axe (111) et, pour la première fois, sur YSZ orienté selon l'axe (100) sans aucune couche tampon. Le titanate de strontium (SrTiO_3) (111) a été le premier substrat utilisé pour obtenir la croissance épitaxiée de $\epsilon\text{-Fe}_2\text{O}_3$ ⁴⁸. Afin de faire varier les contraintes épitaxiales, l'aluminate de lanthane (LaAlO_3) (111) et LSAT (111) ont été sélectionnés car ils sont caractérisés par la même structure de la pérovskite que SrTiO_3 mais avec paramètre de maille légèrement plus petit. En outre, des substrats monocristallins de YSZ (100) ont aussi été choisis, car ils ont été démontré qu'ils favorisent la croissance épitaxiée de GaFeO_3 (GFO)¹⁰⁰, qui est isostructural à $\epsilon\text{-Fe}_2\text{O}_3$. De plus, YSZ (100) est un substrat très intéressant car la croissance de films épitaxiées de YSZ sur Si (100) est possible et bien documenté¹⁰¹⁻¹⁰³, ce qui en fait un choix de substrat très pertinent pour toute application future des couches minces épitaxiées de $\epsilon\text{-Fe}_2\text{O}_3$ dans des dispositifs intégrés.

Compte tenu de la présence de multiples orientations de croissance (macles) dans le plan des couches minces déposées sur chacun des substrats choisis, la théorie de la minimisation de l'énergie de surface de la surface (100) de $\epsilon\text{-Fe}_2\text{O}_3$ est toujours valide. Cependant, sans forcément remettre en question la théorie proposée dans la réf. ³³ basée sur l'énergie de surface, nous avançons une hypothèse basée d'avantage sur la structure des réseaux cristallins et selon laquelle la stabilisation de la phase epsilon est essentiellement favorisée par la continuité entre les polyèdres d'oxygène de la couche d'oxyde épitaxiée et ceux du substrat.

La relation épitaxiale entre $\epsilon\text{-Fe}_2\text{O}_3$ et les substrats sous-jacents est représentée sur la Figure 73. La même relation est valide pour LSAT et LaAlO_3 , qui sont caractérisés par la même structure que SrTiO_3 (pérovskite cubique), mais avec un paramètre de maille plus petite ($a_{\text{STO}} = 3,905 \text{ \AA} > a_{\text{LSAT}} = 3,868 \text{ \AA} > a_{\text{LAO}} = 3,820 \text{ \AA}$).

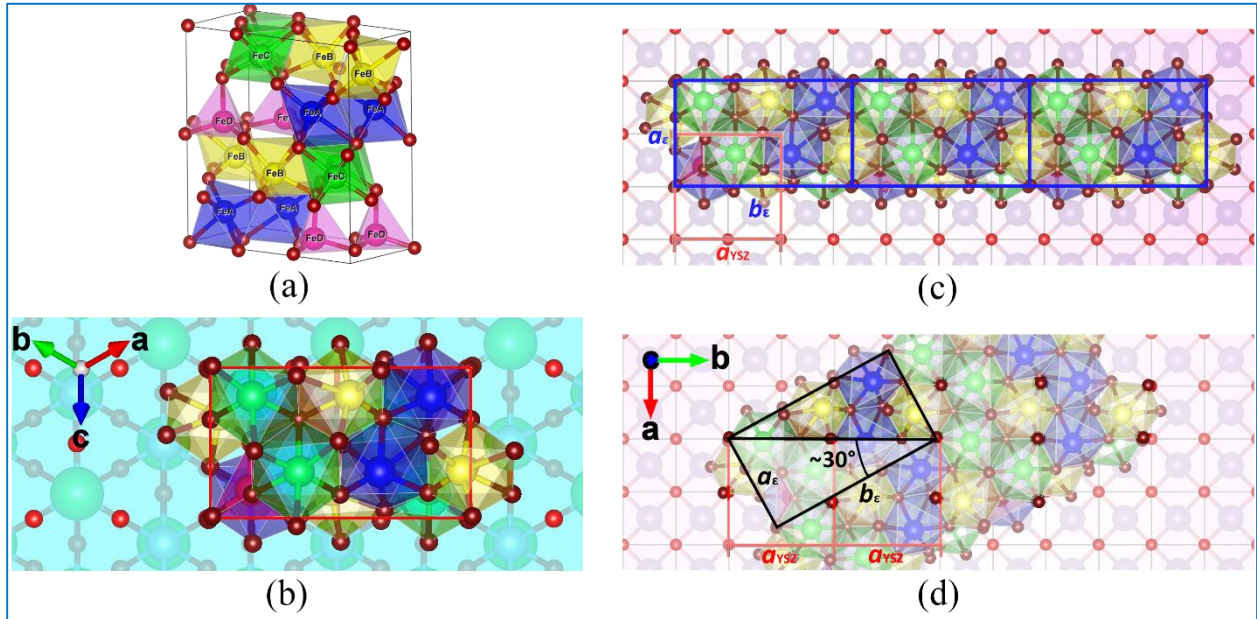


Figure 73: (a) la maille cristalline élémentaire de ϵ -Fe₂O₃. Relations d'épitaxie entre ϵ -Fe₂O₃ et (b) la surface (111) des pérovskites et, (c) et (d), les deux correspondances pour la surface (100) de YSZ.

En raison de la nature métastable de ϵ -Fe₂O₃ et de son existence uniquement dans un état confiné et/ou contraint comme par exemple dans des nanostructures, il est possible de définir les paramètres de réseau de ϵ -Fe₂O₃ massif et relaxé. Par conséquent, il est difficile de bien définir la déformation et l'état de contrainte induit par le substrat sur le. Dans ce travail, ce sont les valeurs des paramètres de réseau de ϵ -Fe₂O₃ lorsqu'elles sont synthétisées sous forme de nanoparticules qui sont utilisées comme référence. Compte tenu des différentes relations d'épitaxie avec les différents substrats, les désaccords de maille sont les suivants :

<i>Substrats</i>	<i>Relation a</i>	<i>Mismatch a</i>	<i>Relation b</i>	<i>Mismatch b</i>
<i>SrTiO₃</i>	$= \sqrt{6}/2 a_{sub}$	6.22 %	$= 3\sqrt{2}/2 a_{sub}$	5.99 %
<i>LSAT</i>	$= \sqrt{6}/2 a_{sub}$	7.23 %	$= 3\sqrt{2}/2 a_{sub}$	7.00 %
<i>LaAlO₃</i>	$= \sqrt{6}/2 a_{sub}$	8.58 %	$= 3\sqrt{2}/2 a_{sub}$	8.35 %
<i>YSZ 1</i>	$a_{film} = a_{sub}$	-0.78 %	$3b_{film} = 5a_{sub}$	2.89 %
<i>YSZ 2</i>	$\sqrt{a_{film}^2 + b_{film}^2} = 2 * a_{sub}$			

Tableau 8: Désaccords de maille entre paramètre de maille a et b de ϵ -Fe₂O₃ et les substrats choisis pour obtenir une croissance épitaxiale. Le désaccord de maille a été calculé en utilisant 'mismatch' = $(a_{film} - a_{sub})/a_{sub}$. En raison des relations d'épitaxie inhabituelles, il n'est pas possible de définir les désaccords de maille pour le cas YSZ "non-parallèle" (ici appelé YSZ 2).

Comme on peut le voir dans le Tableau 8, il existe un désaccord de maille relativement élevé entre le substrat et le film lorsque ce dernier est déposé sur la surface (111) de pérovskites, en particulier pour le cas de couches minces de $\epsilon\text{-Fe}_2\text{O}_3$ sur LaAlO_3 (111). Ces désaccords de maille important entre couches minces et substrats, ainsi que les relations d'épitaxie très inhabituelles entre le film et les substrats, nous conduisent à considérer une approche différente pour décrire la croissance épitaxiale de la $\epsilon\text{-Fe}_2\text{O}_3$. Au lieu de s'appuyer sur l'hétéroépitaxie « classique », une meilleure description de la correspondance des deux réseaux cristallins de la couche et du substrat, peut être trouvée dans l'hétéroépitaxie dite « difficile ». La définition de l'hétéroépitaxie difficile est la croissance d'un film sur un substrat cristallin qui diffère fortement du film pour une ou plusieurs des caractéristiques suivantes: structure cristalline, paramètres de maille, et / ou la nature des liaisons chimiques⁸¹. Dans le cas de la $\epsilon\text{-Fe}_2\text{O}_3$, la structure cristalline et les paramètres du réseau différent de ceux des substrats choisis (bien que des relations d'épitaxie 'inhabituelles' puissent être identifiées). Cependant, la nature des liaisons chimiques dans la couche épitaxiée est similaire à celle des substrats - les deux réseaux cristallins étant caractérisés par polyèdres d'oxygène, ce qui - à notre avis - est la clé pour promouvoir une croissance épitaxiale. Le problème fondamental de l'hétéroépitaxie difficile réside dans le concept du couplage satisfaisant et harmonieux des deux réseaux cristallins. Pour les systèmes caractérisés par une hétéroépitaxie difficile, le critère "classique" du couplage du réseau basé sur la comparaison des constantes de réseau du matériau massif relaxé ne s'applique plus. Une nouvelle définition du couplage du réseau, plus pertinent pour l'hétéroépitaxie difficile, sera: « deux réseaux sont cristallographiquement compatibles si la symétrie de translation de l'interface est compatible avec la symétrie des réseaux cristallins des deux côtés de l'interface (donc de la couche mince et du substrat), ceci à l'intérieur d'une précision donnée »⁸². La correspondance de la maille dans ce nouveau contexte signifie donc que l'interface bidimensionnelle possède une symétrie translationnelle compatible avec celle du volume des deux côtés de l'interface. Une telle compatibilité, qui a été bien démontrée pour la $\epsilon\text{-Fe}_2\text{O}_3$ et les substrats de la Figure 1, permet aux structures locales de l'interface de se répéter périodiquement sur de grandes distances. Il convient de souligner que pour l'hétéroépitaxie difficile l'effet du désaccord de maille du réseau est secondaire en importance à la chimie de l'interface, qui jouera toujours un rôle majeur en ce qui concerne la croissance épitaxiale. Des exemples de systèmes caractérisés par une épitaxie difficile sont $\text{CdTe}(111)/\text{GaAs}(100)$ ⁸³ et $\text{CdTe}(111)/\text{Al}_2\text{O}_3$ ⁸⁴.

Le motif formé par la couche supérieure d'oxygène des substrats qui assurent l'épitaxie et celui de la couche inférieure d'oxygène de $\epsilon\text{-Fe}_2\text{O}_3$ révèle une similitude qui permet la continuité du réseau des polyèdres d'oxygène. Comme on peut le voir sur la Figure 74 a, il y a une très bonne correspondance entre le réseau d'oxygène du substrat (sphères rouges) et les polyèdres de $\epsilon\text{-Fe}_2\text{O}_3$ (sphères de couleur mauve) pour les couches minces épitaxiées déposées sur des pérovskites orientées (111); la petite différence découle plutôt du fait que les coordonnées des atomes utilisées étaient celles qui appartiennent à $\epsilon\text{-Fe}_2\text{O}_3$ lorsqu'elles sont

synthétisées sous forme de nanoparticules. Une certaine correspondance peut également être trouvée dans le cas de ϵ -Fe₂O₃ déposé sur YSZ, bien que pas bonne que celle trouvée pour les films déposés sur les pérovskites. De plus, cette correspondance semble être meilleure pour la correspondance de réseau « parallèle » (Figure 74b) que pour une « non-parallèle » (Figure 74c). Il est également à noter que les rotations des polyèdres d'oxygène peuvent correspondre au « décalage » dépeint afin d'obtenir une meilleure continuité.

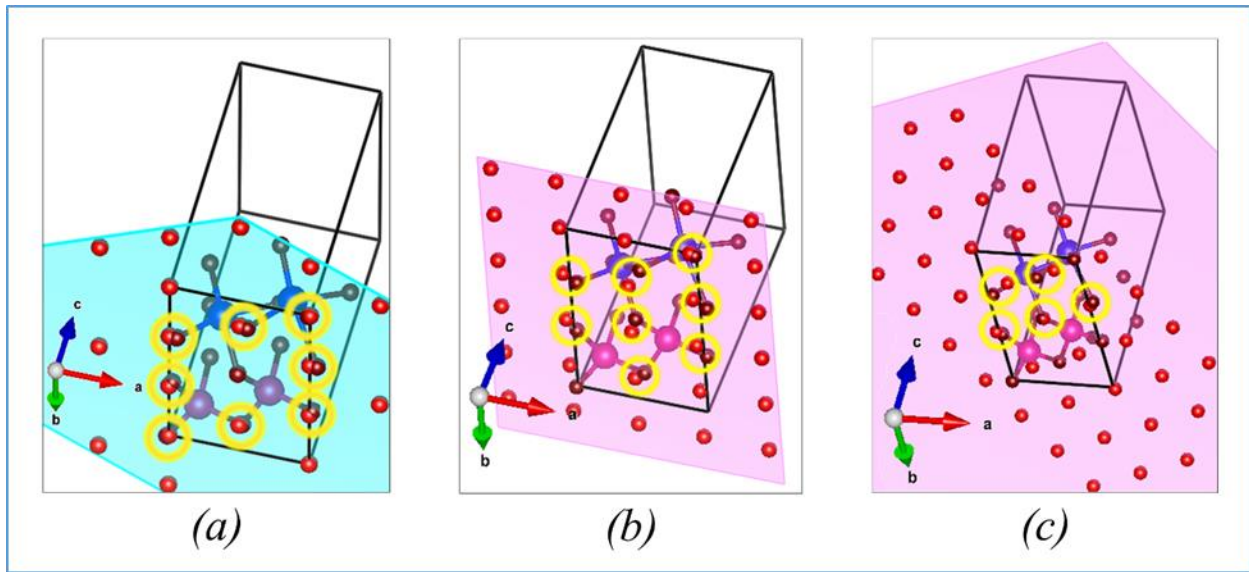


Figure 74: Représentation graphique de la continuité du réseau de polyèdres d'oxygène de films d' ϵ -Fe₂O₃ déposés sur (a) des pérovskites orientées (111) et (b et c) du YSZ orienté (100). La continuité dans le cas de la relation d'épitaxie "parallèle" YSZ (100) semble, à partir de la représentation graphique, être meilleure que pour la relation d'épitaxie "non parallèle" (c). Il faut noter cependant que la correspondance dans les cas (b) et (c) n'est pas aussi bonne que dans le cas d' ϵ -Fe₂O₃ déposé sur des pérovskites orientées (111).

La correspondance entre les réseaux d'oxygène serait également très bonne dans le cas de couches minces de ferrite epsilon déposées sur la surface (0001) de l'alumine : cependant, un tel substrat introduirait un désaccord de maille encore plus élevé que LAO (111). En outre, l'alumine possède un coefficient de dilatation plus petit que ceux des deux autres substrats et des oxydes de fer, ce qui, en raison de la température élevée à laquelle la croissance se produit, pourrait induire des transitions de phase pendant le refroidissement. L'une ou l'autre de ces explications pourrait être la raison pour laquelle il n'est pas possible de faire croître ϵ -Fe₂O₃ directement sur la surface de l'alumine, mais qu'il est possible de le faire en utilisant une couche tampon de GaFeO₃, qui a un paramètre de maille plus petit que celui de ϵ -Fe₂O₃.

La structure des films a d'abord été étudiée par diffraction de rayons X. Les mesures dans la géométrie Bragg-Brentano classique ($\theta/2\theta$) et phi-scan (ϕ -scan) ont été effectuées pour confirmer la croissance épitaxiale de la phase Gamma de l'oxyde ferrique orientée (001) sur les différents substrats utilisés (pour

plus de détail, se référer au texte principal). La configuration Bragg-Brentano ($\theta/2\theta$) a été utilisée pour déterminer l'orientation hors-plan de la couche mince et l'alignement mutuel des plans cristallins du film et du substrat. Tandis que les mesures phi-scan ont aidé à comprendre l'orientation dans le plan du réseau cristallin du film. En raison du fort signal des lignes K_β issues des substrats monocristallins, en particulier celui des pérovskites orientées (111), qui se chevauchent partiellement avec les pics des films, un filtre de nickel a été utilisé pour les couper et avoir un diffractogramme plus propre. Avant l'utilisation du filtre Ni (qui nécessairement diminuent l'intensité de tous les pics), des preuves de formation d'une phase supplémentaire ont été enregistrées et les pics de faible intensité de cette phase supplémentaire ont été attribués à la phase magnétite (Fe_3O_4) fortement contrainte. La présence de cette phase supplémentaire a été détectée à la fois pour les couches déposées sur les pérovskites orientées (111), et sur YSZ (100) (référence voir le texte principal pour plus de détail).

Une particularité révélée lors de l'analyse des diffractogrammes $\theta/2\theta$ de couches minces épitaxiales de $\epsilon\text{-Fe}_2\text{O}_3$ (001) déposées sur différents substrats est que la position des pics appartenant à $\epsilon\text{-Fe}_2\text{O}_3$ est fondamentalement indépendante du choix du substrat (voir Figure 75). Cela peut s'expliquer en supposant que les polyèdres d'oxygène constituant la couche d' $\epsilon\text{-Fe}_2\text{O}_3$ stabilisé (voir la cellule unitaire de la Figure 73a) peuvent tourner de manière à accommoder la relation d'épitaxie difficile à l'interface sans modifier les paramètres de maille hors-plan.

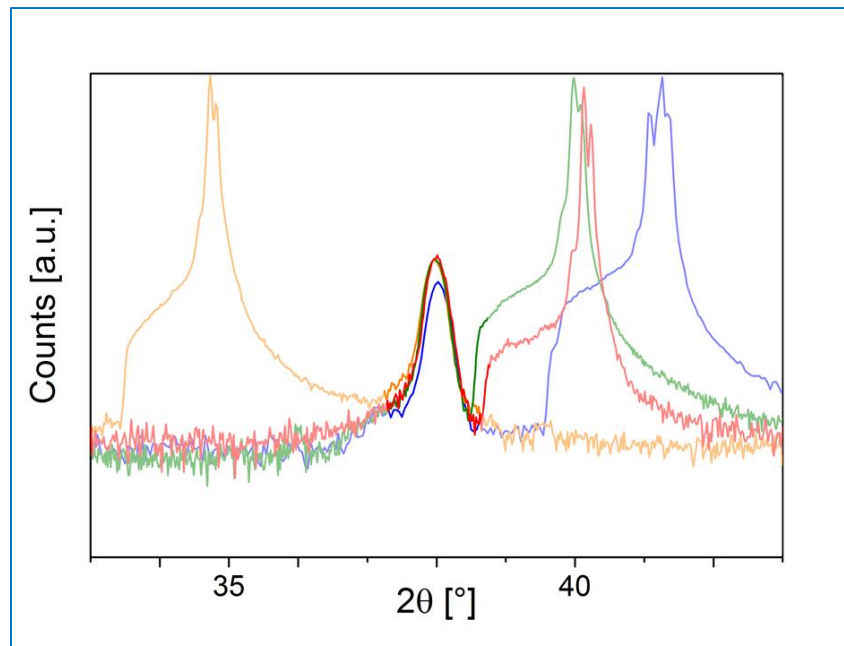


Figure 75: Détail du pic de diffraction 004 pour des films minces de $\epsilon\text{-Fe}_2\text{O}_3$ déposés sur des substrats différents. À Noter : la position du pic ne change pas avec les différents substrats.

Afin de mesurer les trois paramètres de maille caractérisant ϵ -Fe₂O₃, la position des pics associés aux plans non parallèles à la surface du film a aussi été étudiée. Les plans choisis pour déterminer les paramètres de réseau a et b (c a été trouvé facilement à partir du diffractogramme $\theta/2\theta$), étaient les pics 132 et 013, respectivement. Ces valeurs ont été raffinées en simulant le diagramme de diffraction de poudre de ϵ -Fe₂O₃, où les coordonnées atomiques fractionnaires et les paramètres de maille initiaux de la maille élémentaire de ϵ -Fe₂O₃ pour des nanoparticules ont été utilisées puis en effectuant un raffinement de Rietveld. Cela nous a entre autre permis d'estimer la valeur à la fois de la position ($\theta/2\theta$) des pics, et de l'angle entre les deux plans considérés et la surface (χ). Les valeurs des trois paramètres réticulaires de couches minces épitaxiales de ϵ -Fe₂O₃ lorsqu'elles sont déposées sur des substrats différents sont répertoriés dans le Tableau 9.

<i>Substrats</i>	<i>a</i> [Å]	<i>b</i> [Å]	<i>c</i> [Å]
ϵ Nanoparticules	5.08	8.78	9.47
STO (111)	5.08	8.79	9.48
LSAT (111)	5.08	8.77	9.48
LAO (111)	5.08	8.78	9.48
YSZ (100)	5.08	8.73	9.48

Tableau 9: Paramètres de mailles trouvés pour les films minces épitaxiés ϵ -Fe₂O₃ déposés sur des substrats différents, ainsi que les paramètres de maille de nanoparticules de ϵ -Fe₂O₃.

En comparant les valeurs des paramètres de maille trouvées expérimentalement pour ϵ -Fe₂O₃ lorsqu'elles sont déposées sur des substrats différents avec celles rapportées pour les nanoparticules⁴⁰, qui peut être trouvée dans la première ligne du Tableau 9, il est possible de déduire que les films sont complètement relaxés indépendamment des substrats sur lesquels ils ont été déposés. En outre, une analyse plus approfondie pour les paramètres de réseau des films de ϵ -Fe₂O₃ déposés sur YSZ (100), révèlent qu'il n'y a presque aucune différence dans les dimensions du réseau cristallin pour les domaines de croissance donnés par les deux différentes correspondances de réseau esquissées à la Fig. 1c et 1d. Le fait que l'on observe une relaxation complète de ϵ -Fe₂O₃ renforce l'hypothèse que se sont en effet les liaisons chimiques et la continuité des polyèdres d'oxygène, ainsi qu'un coefficient de dilatation thermique compatible, qui assurent la croissance épitaxiale de la ϵ -Fe₂O₃.

Afin de déterminer l'orientation mutuelle du film et du substrat, les analyses 'Phi scan' du pic correspondant au plan 013 de ϵ -Fe₂O₃ ont été réalisées en même temps que celles des pics 110 et 221 des substrats sous-jacent de STO et des pics 220 de YSZ, comme représenté sur la Figure 76.

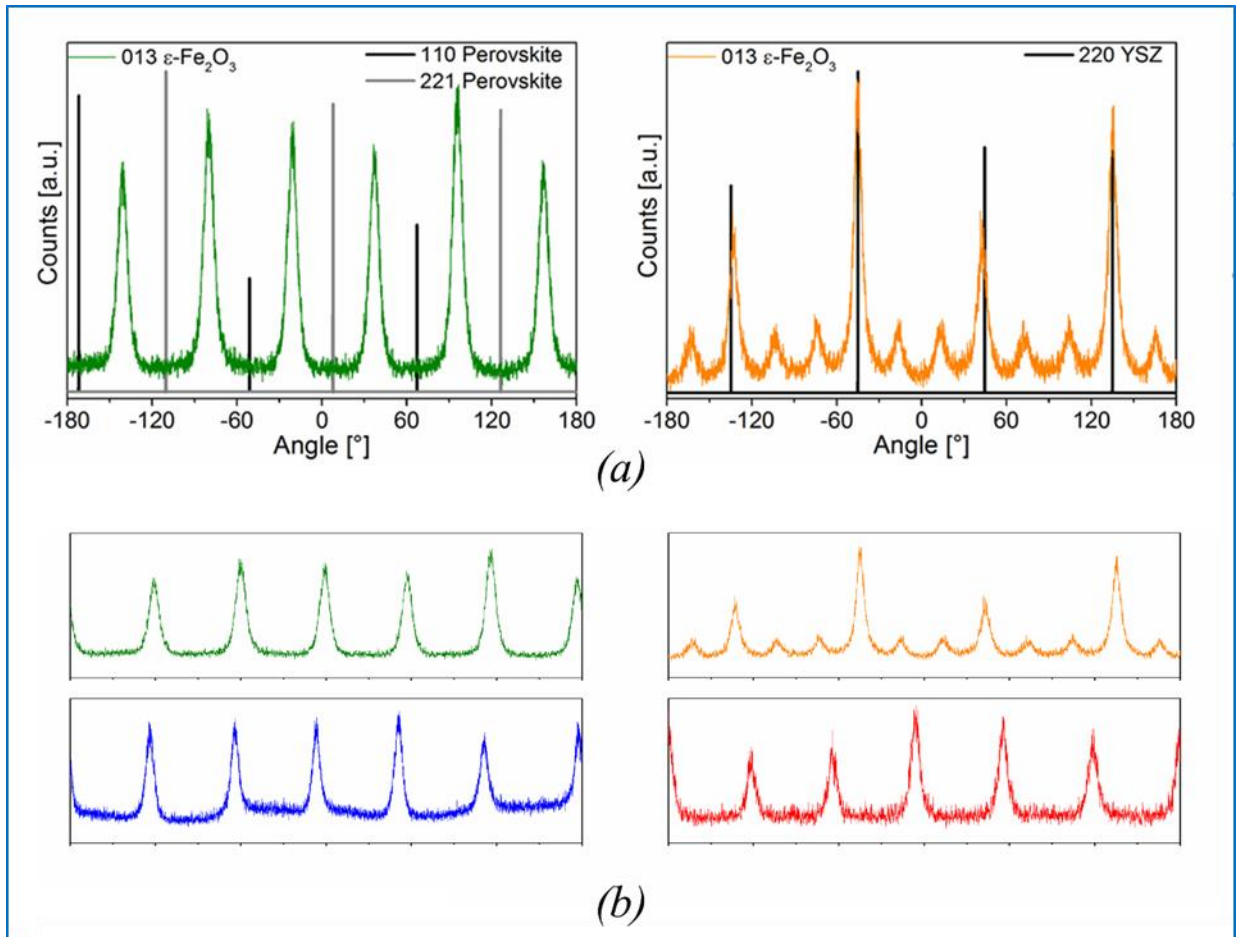


Figure 76: (a) Analyse Phi scan pour le pic 013 de $\epsilon\text{-Fe}_2\text{O}_3$ lorsqu'il est déposé sur des pérovskites orientées (111) (à gauche) et sur et sur YSZ (100) (à droite), ainsi que les pour les pics 110 et 221 des substrats pérovskite, e des pics 220 des substrats de YSZ, afin de déterminer l'orientation mutuelle entre les films et les substrats. (b) Les mêmes phi-scans pour les pics 013 de $\epsilon\text{-Fe}_2\text{O}_3$ sur les différents substrats qui assurent une croissance épitaxiale : d'en haut à gauche dans le sens des aiguilles d'une montre, sur STO (111) (vert), YSZ (100) (orange), LSAT (111) (rouge) et LAO (111) (bleu).

Les films déposés sur STO (111) ont été utilisés comme modèle pour toute la classe de substrats de type pérovskite, compte tenu de la manière dont les propriétés structurales (et fonctionnelles, comme on le verra plus loin) semblent être similaires et cohérentes pour les trois substrats (STO, LSAT et LAO). Une telle analyse a d'abord confirmé la formation de macles (« twins ») pour les pérovskites orientées (111) et la zirconne orientées (100). La dépendance angulaire différente pour les pérovskites et YSZ est donnée par la différente symétrie des terminaisons d'oxygène des deux classes de substrats, hexagonales dans le cas des pérovskites orientées (111) et cubiques pour YSZ orientée (100), cette dernière symétrie permettant la présence de deux relations d'épitaxie différentes. De plus, le balayage en Phi (Phi-scan) du pic 013 des films déposés sur YSZ (100) a révélé que les pics dans le cas de la correspondance de réseau « parallèle » (Figure 73b), avec une symétrie de 90° , sont plus intenses que dans le cas de la correspondance « non-

parallèle » (Figure 73c), pour laquelle ils apparaissent à environ $\pm 30^\circ$ par rapport aux pics du cas parallèle. Un comportement très similaire a été observé aussi pour des couches minces épitaxiées de GFO (001) sur YSZ (100)¹⁰⁰.

En associant les informations recueillies par diffractométrie de rayons X avec balayage angulaire en Phi avec les relations d'épithaxie difficiles trouvées pour les différents substrats et représentées à la Figure 73, il est possible d'obtenir une correspondance des macles et de leur périodicité angulaire facilement représentable graphiquement (voir information complémentaire). Pour le cas de la ϵ -Fe₂O₃ déposé sur des substrats de structure pérovskite et orienté (111), trois orientations azimutales de croissance ont été identifiées, tandis que six autres ont été trouvés pour les films déposés sur (YSZ) orientés (100). Chaque orientation de croissance permet une rotation de 180°, résultant ainsi en un nombre de pics deux fois plus élevé dans les spectres XRD de balayage en Phi. Les trois orientations possibles pour les macles de ϵ -Fe₂O₃ sur STO/LSAT/LAO (111) sont telles que le paramètre de maille a_ϵ est orienté selon les directions cristallographiques $[1 \bar{2} 1]$, $[1 1 \bar{2}]$, et $[\bar{2} 1 1]$ du substrat. Pour les films déposés sur YSZ (100), les six variantes de croissance différentes trouvées sont deux orientations « parallèle » avec b_ϵ aligné le long de les directions cristallographiques $[0 1 0]$ et $[1 0 0]$ du substrat, et quatre orientations « non-parallèle », où b_ϵ est aligné le long des directions $[1 \bar{1} 0]$, $[4 \bar{1} 0]$, $[4 1 0]$, et $[1 1 0]$.

En analysant l'élargissement des pics dans le phi scan, il a été possible d'inférer la présence de ce qu'on appelle *la mosaïcité*. Le degré de mosaïcité latérale (alignement mutuel des différentes cristallites dans le plan pour chaque différente orientation de croissance) est lié à l'écart type de la distribution gaussienne décrivant la dispersion angulaire. Pour l'analyse de la mosaïcité, la distribution angulaire de spics 013 des films déposés à la fois sur des pérovskites orientées (111) et sur YSZ (100) ont été analysés (Figure 77).

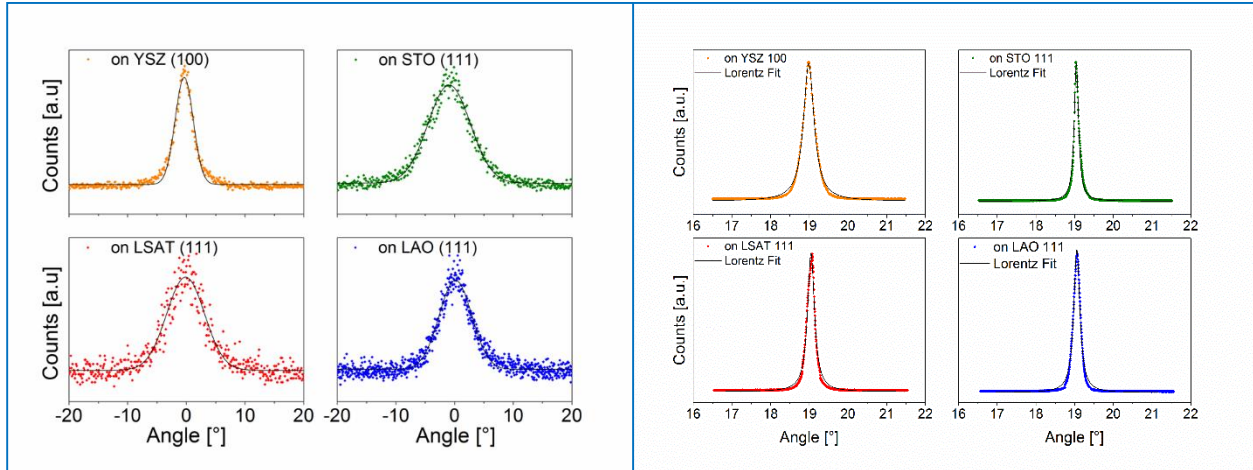


Figure 77: (Planche de gauche) Dispersion de la dépendance angulaire du pic 013 pour les films de $\epsilon\text{-Fe}_2\text{O}_3$: les données expérimentales sont présentées sous forme de symboles discrets, tandis que le fit Gaussien est représenté par la ligne noire continue. En haut à gauche dans le sens des aiguilles d'une montre, dépendance angulaire du pic 013 de $\epsilon\text{-Fe}_2\text{O}_3$ déposé sur YSZ (100), STO (111), LAO (111) et LSAT (111). (Planche de droite) Mesures « rocking curve » pour le pic 004 des films de $\epsilon\text{-Fe}_2\text{O}_3$: les données expérimentales sont présentées sous forme de symboles discrets, tandis que l'ajustement de Lorentz est représenté par la ligne continue noire. En haut à gauche dans le sens des aiguilles d'une montre, pic 004 des films de $\epsilon\text{-Fe}_2\text{O}_3$ déposés sur YSZ (100), STO (111), LAO (111) et LSAT (111).

Afin d'évaluer le degré d'alignement entre les plans (00*l*) des films de $\epsilon\text{-Fe}_2\text{O}_3$ et des plans (00*l*) du substrat, parallèles à la surface de l'échantillon, ce qui est souvent définie comme étant *la mosaïcité hors-plan*, la « rocking curve » des pics (004) de $\epsilon\text{-Fe}_2\text{O}_3$ a été étudiée (Figure 77). De manière identique à ce qui a été fait pour l'analyse des courbes « phi-scans », les pics ont été modélisés - cette fois par une distribution de Lorentz - et la largeur totale à mi-hauteur (FWHM) a été évaluée. Comme référence, on a également mesuré la largeur de la fonction de Lorentz utilisée pour effectuer le fit des courbes mesurées pour les substrats STO (111) et YSZ (100), et avons trouvé pour ces substrats monocristallins un FWHM d'environ 0,025°.

Les valeurs trouvées pour la mosaïcité dans le plan et hors-plan pour des couches minces de $\epsilon\text{-Fe}_2\text{O}_3$ déposées sur différents substrats sont présentés dans le Tableau 10. On y constate que, pour le cas de la mosaïcité dans le plan, les couches déposées sur des pérovskites orientées (111) ont un degré de mosaïcité plus élevé ceux déposés sur de la zircone orientée (100). En outre, il semble que la mosaïcité diminue lorsque la contrainte compressive augmente.

En ce qui concerne la mosaïcité hors-plan, nos résultats montrent que les films que l'on a fait croître sur différents substrats présentent un degré de dispersion faible et comparable, ce qui signifie que les films sont bien alignés parallèlement à la surface du substrat, et cet alignement est meilleur sur des substrat pérovskites que sur YSZ, probablement dû à la meilleure qualité et moindre rugosité de surface des premiers. Cela ne devrait pas surprenant étant donné la façon dont ils semblent être complètement relaxé hors du plan et ceci renforce l'idée que c'est bien la rotation des polyèdres de $\epsilon\text{-Fe}_2\text{O}_3$ pour être recevoir la non-concordance

donnée par les différents substrats. Une légère dispersion plus élevée a été trouvée pour les films développés sur YSZ (100), ce qui pourrait être dû au nombre plus élevé de variantes dans le plan autorisées sur YSZ (100).

<i>Substrats</i>	<i>SIGMA - Gauss</i>	<i>SIGMA - Lorentz</i>
YSZ (100)	1.54°	0.32°
STO (111)	3.60°	0.13°
LSAT (111)	3.23°	0.2°
LAO (111)	2.78°	0.18°

Tableau 10: Valeurs de l'écart - type du fit gaussien permettant d'évaluer la mosaïcité dans le plan, et du fit Lorentzien, pour évaluer la mosaïcité hors-plan, pour le pic 013 des en balayage « phi » et de la « rocking curve » du pic 004 des couches minces de ϵ -Fe₂O₃ déposé sur différents substrats.

L'imagerie HAADF (High Angle Dark Field field) obtenue par microscopie électronique par balayage en transmission (STEM) avec correction d'aberrations a de nouveau confirmé de manière indépendante la croissance épitaxiale de la ϵ -Fe₂O₃ sur STO (111) et YSZ (100) ; une fois encore, STO (111) a été choisi comme substrat modèle pour les films déposés sur des substrats de pérovskites orientés (111) (les autres substrats étant LSAT et LAO). Dans les images enregistrées pour des couches minces de ϵ -Fe₂O₃ déposées sur STO (111), une couche interfaciale ou « couche tampon » très mince (quelques angströms d'épaisseur) a été détectée à l'interface entre le substrat et la couche (Figure 78a). Une telle couche interfaciale semble être plus prononcée (quelques nanomètres d'épaisseur), pour des films déposés sur YSZ (100) (Figure 78b). L'épaisseur de cette couche interfaciale semble être corrélée au degré de continuité du réseau de polyèdres d'oxygène qui a été discuté précédemment, à *savoir* une meilleure continuité du réseau d'oxygène pour les films déposés sur des pérovskites que pour une ceux dont la croissance a lieu sur YSZ. Suivant ce qui a été trouvé par XRD au sujet de la présence d'une phase secondaire, que nous avons identifié comme étant de la magnétite, les images STEM indiquent comment cette phase pourrait être localisée aux frontières des différents domaines de croissance ou, en particulier pour les films minces de ϵ -Fe₂O₃ sur le YSZ (100), à l'interface entre le substrat et le film, agissant ainsi comme couche tampon. Cela sera pris en compte lors de l'interprétation des mesures magnétiques, qui seront discutées ci-après. La présence de multiples variantes de croissance dans le plan (« twins ») a été observée (les zones avec un contraste différent) pour les films déposés sur tous les substrats : cependant, les macles des films déposés sur YSZ (100) semblent former des structures colonnaires, ce qui contraste avec le cas des films déposés sur du titanate de strontium orienté (111), où de telles structures avec des interfaces verticales nettes et rectilignes ne sont pas observées. La largeur des piliers, lorsque présents, semblent être d'environ 20 nm, ce qui coïncide avec l'épaisseur

moyenne trouvée pour de nanofils de $\epsilon\text{-Fe}_2\text{O}_3$ ³⁷. Par conséquent, il est difficile de dire si cette occurrence représente un indice du mode de croissance 3D (Volmer-Weber) des couches, ou si cela est lié à la dimension maximale des cristallites de $\epsilon\text{-Fe}_2\text{O}_3$ et de ses divers domaines de croissance.

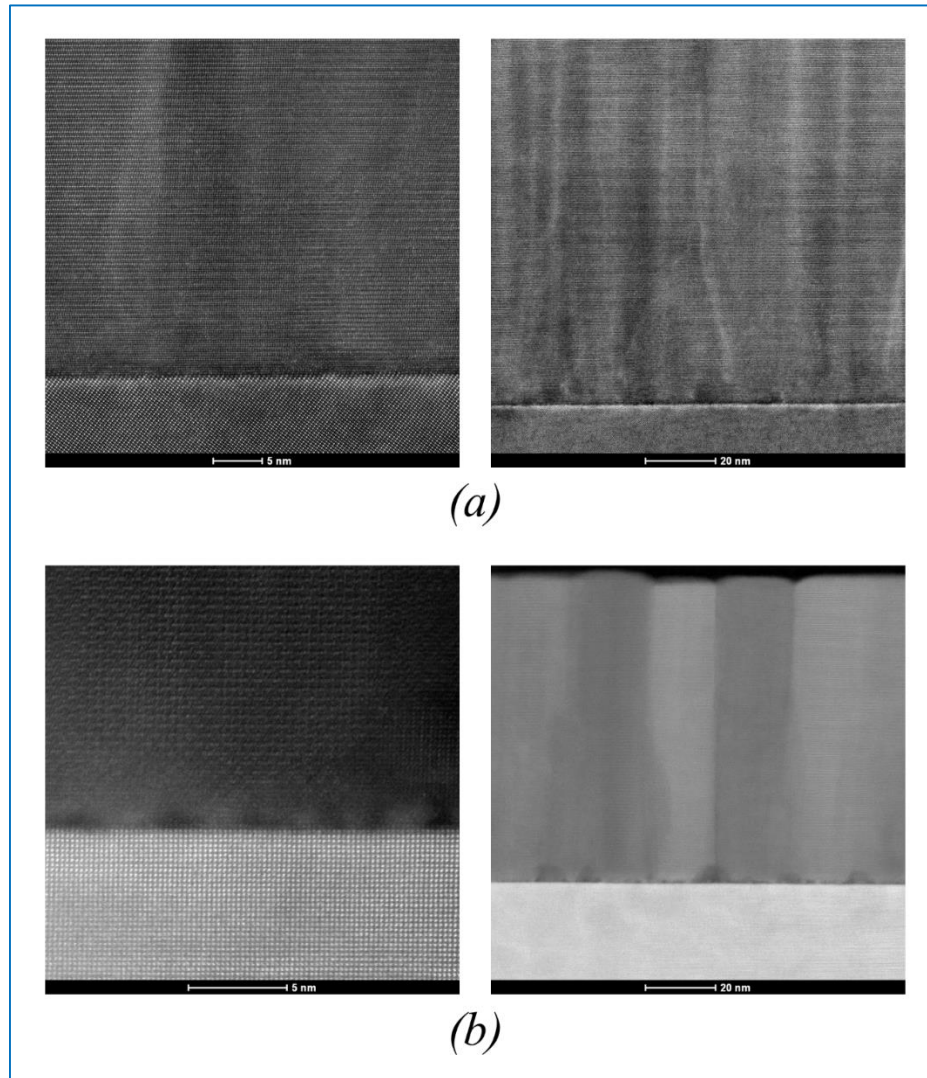


Figure 78: (a) Image STEM d'un film d'une épaisseur d'environ 125nm de $\epsilon\text{-Fe}_2\text{O}_3$ sur STO (111) et (b) sur YSZ (100) mettant en évidence la différence de l'épaisseur de la couche tampon - quelques angströms dans le premier cas , plusieurs nanomètres dans le second - et la différence de morphologie des « twins » - désordonnés pour les films déposés sur STO, et en forme de pilier régulier pour les films déposés sur YSZ.

Chapter 8

Les propriétés magnétiques macroscopiques des couches minces oxyde ferrique epsilon ont été analysées via la magnéto-métrie à échantillon vibrant ("vibrating sample magnetometer" - VSM). La première étape de la caractérisation magnétique a été de mesurer les cycles d'hystérésis des échantillons avec le champ magnétique appliqué d'abord parallèle (dans le plan) puis perpendiculaire (hors de plan) à la surface de la couche. Afin d'obtenir uniquement le signal de la couche, les contributions magnétiques du porte-échantillon (tige de verre) et les substrats ont été mesurées séparément et soustraites du signal total.

Comme le montre la Figure 79a, les cycles d'hystérésis se caractérisent par deux éléments remarquables: un champ coercitif élevé, et la présence d'un épaulement (ou « pincement » du cycle d'hystérésis) pour les champs appliqués faibles. Alors que le premier est une confirmation de l'anisotropie magnétique élevée des couches, le second s'explique par la présence simultanée d'oxyde ferrique epsilon ($\epsilon\text{-Fe}_2\text{O}_3$) et d'une phase magnétique secondaire ; comme indiqué précédemment dans la section sur la caractérisation structurale, cette phase secondaire a été identifiée par diffractométrie aux rayons X comme étant de la magnétite (Fe_3O_4) polycristalline. De plus, la forte différence dans le champ coercitif et dans l'aimantation à saturation (déterminée au champ maximal expérimentalement appliqué) entre les mesures dans le plan et hors-plan confirment l'anisotropie magnétique élevée des couches épitaxiales d'oxyde ferrique epsilon. La comparaison des cycles d'hystérésis enregistrés pour des couches minces épitaxiales d'oxyde ferrique epsilon déposées sur différents substrats a révélé des différences dans les valeurs de l'aimantation à saturation M_S et rémanente M_R pour les différents cycles enregistrés (Figure 43). Ces différences peuvent être attribuée soit à l'erreur d'estimation des épaisseurs des différentes couches, qui est calculée en multipliant le taux de dépôt (en nm/pulse) estimé par le nombre de pulses laser durant chaque dépôt, soit à un alignement imparfait du champ appliqué le long d'un des axes magnétiques faciles de l'échantillon, ou encore à une différence de la quantité de la phase magnétique secondaire présente dans l'échantillon. Cependant, les couches semblent toutes avoir une coercivité élevée et constante, indépendamment du type et de la symétrie des substrats sur lesquels ils ont été développés.

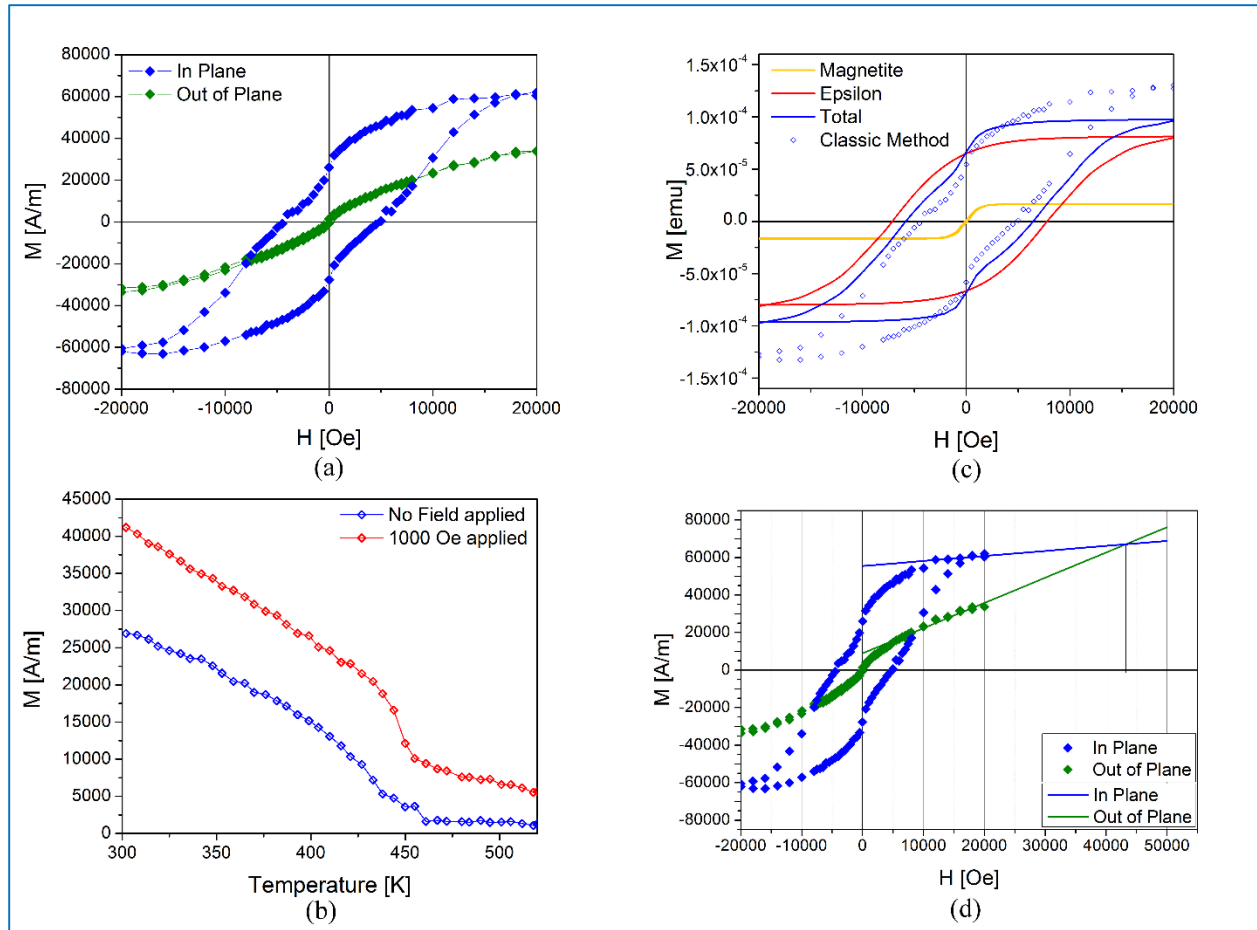


Figure 79: (a) Dépendance de l'aimantation d'une couche mince $\epsilon\text{-Fe}_2\text{O}_3$ déposée sur YSZ (100) avec le champ magnétique appliqué dans le plan de l'échantillon (symboles bleus) et hors du plan de l'échantillon (symboles verts), montrant l'anisotropie magnétique de $\epsilon\text{-Fe}_2\text{O}_3$. (b) Graphe de M en fonction de T mesuré sous champ nul (bleu) et sous un faible champ magnétique appliqué de 1000 Oe (rouge), montrant que M ne disparaît pas pour une température supérieure à la température de Curie de $\epsilon\text{-Fe}_2\text{O}_3$ de 460 K lorsqu'un un faible champ magnétique est appliqué, révélant la présence d'une phase 'parasite' correspondant à un matériau magnétique doux ayant un TC plus élevé et ayant été assignée à une petite quantité de Fe_3O_4 . (c) Mesure de M - H corrigée où les contributions du substrat et du porte-échantillon expérimentalement mesurées (symboles bleus) et analytiquement déterminées (ligne bleue) ont été soustraites, ainsi que les deux cycles d'hystérésis correspondants à la phase d'oxyde ferrique epsilon ($\epsilon\text{-Fe}_2\text{O}_3$ - rouge) et la magnétite (Fe_3O_4 - jaune). (d) Estimation de l'anisotropie magnétique en comparant les cycles d'hystérésis mesurées dans le plan et hors du plan.

La mesure de l'aimantation rémanente sous champ nul et avec un faible champ magnétique appliqué de 1000 Oe en fonction de la température est présentée à la Figure 79b. Une transition ferromagnétique à paramagnétique est observée à une température de ≈ 460 K, que nous attribuons à ϵ -Fe₂O₃. Nous notons que la température de Curie $T_C \approx 460$ K de nos couches minces ϵ -Fe₂O₃ est légèrement inférieure à celle rapportée pour les nanoparticules ϵ -Fe₂O₃ ($T_C \approx 490$ K)⁴⁰. De plus, les mesures sous un petit champ magnétique appliqué de 1000 Oe, bien au-dessous du champ coercitif du matériau ferromagnétique dur ϵ -Fe₂O₃, mais plus grand que le champ coercitif d'un matériau ferromagnétique doux, révèle en effet la présence d'une phase ferromagnétique secondaire avec un T_C supérieur à 550 K, compatible avec la présence d'une certaine quantité de Fe₃O₄ ($T_C = 850$ K) observée par XRD. Contrairement à certaines explications rapportées dans la littérature qui recourent à la présence de multiples macles pour expliquer la forme particulière du cycle d'hystérésis, et comme nous le verrons plus loin, la nature 'pincée' du cycle d'hystérésis s'explique simplement par la présence simultanée d'oxyde ferrique epsilon et de magnétite. Afin de déterminer la contribution relative des deux phases magnétiques ϵ -Fe₂O₃ et Fe₃O₄ au cycle d'hystérésis magnétique mesuré, nous avons développé une méthode consistant à prendre la dérivée par rapport à la tension appliquée de la courbe mesurée, en ajustant les différents pics de la 1ère dérivée en les modélisant comme la somme de distributions de Voigt et d'une constante. Ceci permet de séparer les signaux provenant des différentes phases magnétiques (qui correspondent simplement aux différents pics) et finalement, de reconstruire le cycle d'hystérèse en intégrant de manière indépendante toutes les fonctions de Voigt utilisées⁸⁷. Notre technique, que nous appelons D-D-SI, pour "Derivative - Deconvolution – Selective Integration", nous permet de discriminer les différentes contributions provenant de différentes phases magnétiques et aussi d'éliminer toute contribution linéaire due aux signaux paramagnétiques et /ou diamagnétiques provenant soit de la tige vibrante, soit du substrat, ainsi que toute autre contribution linéaire pouvant provenir de la couche. Les cycles reconstitués obtenus à partir de la technique D-D-SI sont présentés sur la Figure 79c pour les deux phases magnétiques ϵ -Fe₂O₃ et Fe₃O₄ (lignes rouge et jaune) ainsi que leur somme (ligne bleue). À titre de comparaison, le cycle d'hystérésis obtenu de manière classique, c'est-à-dire en mesurant de manière indépendante les contributions du substrat et de la tige et en les soustrayant du signal de l'échantillon (couches mince + substrat + tige) expérimentalement mesuré est également représentée (symboles bleus).

Enfin, nous notons qu'un cycle d'hystérésis avec une forme 'pincée' a également été observé dans des couches minces épitaxiées orientées (001) de oxyde ferrique epsilon déposées sur les pérovskites (SrTiO₃, LaAlO₃ et LSAT) orientées (111) (Figure 43), ainsi que dans des couches minces d'oxyde ferrique epsilon synthétisés par d'autres groupes sur SrTiO₃ (111)^{48,50}. Il faut noter également que d'autres effets peuvent contribuer à la nature pincée de la courbe représentant le cycle d'hystérésis magnétique, comme la présence de parois de domaine en antiphases (APB) entre les différents domaines de croissance avec différentes

orientations¹⁰⁶, où l'aimantation peut, par exemple, être perpendiculaire à la surface de la couche, ou encore à la présence de nanostructures qui peuvent se développer sur le dessus du couche, comme cela est le cas pour les couches minces épitaxiales du CoFe_2O_4 ¹⁰⁷. Cependant, nous croyons que la manière la plus simple d'expliquer la forme particulière de ces cycles d'hystérésis, négligée jusqu'à présent dans la littérature, est la présence d'une phase magnétique douce en plus de la phase d'oxyde ferrique epsilon.

Ce qui en résulte, est que la nature du substrat n'affecte pas l'aimantation à saturation des échantillons, que les couches minces déposées sur YSZ (100) sont caractérisées par un champ coercitif plutôt élevé et par une aimantation rémanente inférieure aux couches déposées sur STO (100) (champ coercitif d'environ 8300 Oe et aimantation rémanente de environ 43000 A/m pour $\epsilon\text{-Fe}_2\text{O}_3$ déposé sur YSZ, et champ coercitif de environ 5400 Oe et aimantation rémanente d'environ 52.000 A/m pour $\epsilon\text{-Fe}_2\text{O}_3$ déposé sur STO). Bien qu'il soit assez difficile de déterminer une cause précise expliquant ces observations, ce qui nécessiterait une analyse beaucoup plus approfondie, il est possible d'avancer quelques suppositions en fonction des analyses structurales et magnétiques qui ont été menées. En ce qui concerne le champ coercitif plus élevée pour le couche déposé sur YSZ (100) que celle déposée sur les pérovskites (111), cet effet pourrait être causé par la présence de deux orientations principales qui sont séparées par un angle de 90° pour l'oxyde ferrique epsilon sur YSZ, alors qu'il y en aurait trois séparées de 60° pour les couches déposées sur des pérovskites (Figure 36). En ce qui concerne la forme des cycles d'hystérésis, la forme « carrée » des cycles d'hystérésis des couches déposées sur STO (111) pourrait être due à une énergie plus faible pour le blocage des domaines magnétiques causés par les parois entre les différents domaines de croissance avec différentes orientations ou entre différents joints grains. Une analyse plus approfondie sera menée afin de confirmer ces hypothèses.

Les propriétés magnétiques dépendant de l'angle ont été obtenues en enregistrant cycles de hystérésis dans le plan chaque 2 degrés. La dépendance de la magnétisation rémanente M_R en fonction de l'angle dans le plan a été extraite des cycles mesurés. Pour expliquer la dépendance azimutale de M_R , un modèle simple, qui fait la moyenne de l'aimantation rémanente des différentes variantes de croissance parallèlement à la direction mesurée, a été utilisé⁸⁸. Ce modèle est basé sur l'hypothèse que, à zéro champ appliqué, l'aimantation à l'intérieur de chaque cristallite est uniforme et alignée le long de son axe magnétique facile (l'axe a de la maille unitaire). Cette hypothèse est supportée par les valeurs élevées de l'anisotropie magnétocristalline de $\epsilon\text{-Fe}_2\text{O}_3$ et repose sur une analyse critique de la taille de chaque cristallite obtenue à partir d'images MET (voir Figure 41 et Figure 42) qui permettent de déduire que les cristallite sont essentiellement des monodomaines ferromagnétiques^{88,89}. La dépendance angulaire de l'aimantation rémanente normalisée pour une orientation cristalline peut donc être modélisée par la valeur absolue de \cos (*angle + décalage*) où l'*angle* est l'angle à lequel les valeurs de M_r sont enregistrées, et le *décalage* représente la direction de l'axe magnétique facile du monodomaine par rapport à un 0° .

La contribution de chaque variante à la valeur totale du M_R en fonction de l'angle pour les couches minces d'oxyde ferrique epsilon déposées sur STO (111) et sur YSZ (100) a été pondérée afin que notre modèle corresponde de manière satisfaisante aux données mesurées (Figure 53 et Figure 54). La différence entre les données mesurées et le modèle peut être attribuée à la rotation non concentrique de la tige qui maintient l'échantillon pendant les mesures^{114,115}.

La caractérisation magnétique microscopique a été effectuée par microscopie à force magnétique (MFM). Compte tenu du concept et du fonctionnement d'un MFM, où la pointe magnétique est attirée vers le haut / bas par une force proportionnelle au gradient du champ de dispersion magnétique de la surface de l'échantillon, il devient vraiment difficile d'interpréter le contraste détecté dans une image MFM de couches minces de $\epsilon\text{-Fe}_2\text{O}_3$, qui sont caractérisée par une très forte anisotropie dans le plan. Bien qu'un contraste clair ait été détecté pour différents échantillons de oxyde ferrique epsilon, comme on peut le voir sur la figure (Figure 55), il n'est pas possible de déterminer si les différents domaines magnétiques se forment dans le film mince épitaxiale.

Les propriétés ferroélectriques macroscopiques de couches minces oxyde ferrique epsilon ont été enregistrées avec le module FE d'un système TF Analyzer 2000 par aixACT Systems GmbH (Aachen, Allemagne), tandis que les propriétés microscopiques ont été mesurées par microscopie à force piézoélectrique (piezoresponse force microscopy - PFM). Afin de mesurer leur polarisation et son hystérésis macroscopique, les couches ont été déposées sur des substrats du STO (111) dopés avec 0,5% de niobium. Comme électrode supérieure, des contacts circulaires en platine d'un diamètre de 300 μm et une d'épaisseur d'environ 30 nm ont été déposés sur la surface des couches minces par pulvérisation cathodique.

Les mesures ferroélectriques macroscopiques ont révélé que les cycles de polarisation en fonction du champ électrique appliqué (également appelées PE) de couches minces de oxyde ferrique epsilon sont dominées par des courants de fuite (Figure 57). En analysant les courbe du courant de commutation (IE), il est évident que le courant de fuite est du même ordre de grandeur du courant de commutation mentionné dans la littérature, soit de quelques μA (dans ce cas cependant, les boucles étaient probablement enregistrées à basse température, et par conséquent l'effet des fuites était considérablement réduit)⁵⁰; il devient donc impossible de détecter les courants générés par d'éventuels changements de polarisation. L'analyse microscopique des propriétés diélectriques des couches minces d'oxyde ferrique epsilon a en effet montré une réponse piézoélectrique dans un échantillon multicouche composé d'une couche épaisse de 90 nm d' $\epsilon\text{-Fe}_2\text{O}_3$ sur une couche de 10 nm d'un AlFeO_3 et un substrat Nb-STO (111). Comme on peut le voir sur la Figure 58, une fois que la composante électrostatique linéaire - c'est-à-dire la contribution linéaire - est soustraite du signal mesuré (points noirs et ligne rouge), une courbe ressemblant à un cycle d'hystérésis

(ligne magenta) est obtenue. Il faut noter cependant qu'il n'a pas été possible de saturer la polarisation sur ce grain particulier, même en appliquant une tension maximale de 20 V (correspondant à un champ électrique de $2 \cdot 10^6$ V/m). L'impossibilité de renverser la polarisation du grain peut être due à un blocage provoqué par une forte interaction magnétique ; d'autres raisons pour un tel blocage pourraient être la présence de défauts ou de champs électriques à l'interface. Cependant, jusqu'à ce cela soit démontré de manière rigoureuse, cela ne reste que des spéculations.

Étant donné que l'objectif principal de mon étude était d'obtenir un matériau dont la fréquence de résonance ferromagnétique (FMR) tomberait dans la gamme des basses fréquences THz, afin d'essayer d'induire une commutation de la magnétisation en utilisant des impulsions THz ultra-rapides, différentes mesures ont été faites pour caractériser la fréquence FMR de couches minces de ϵ -Fe₂O₃. Outre l'estimation indirecte de l'anisotropie du champ magnétique, qui permet d'estimer la fréquence FMR, obtenue en comparant les boucles d'hystérésis enregistrées en plan et hors plan qui ont été montrées précédemment (Figure 44), la mesure de la fréquence FMR a été effectuée à la fois directement, et indirectement via la spectroscopie THz dans le domaine temporel. La caractérisation directe s'est révélée très difficile en raison de l'absence d'une cavité résonnante avec une fréquence de résonance proche des valeurs attendues pour la résonance du ϵ -Fe₂O₃ d'environ 190 GHz⁴⁰, ce qui ne permet pas de tirer parti des mesures par cavité qui amplifient considérablement le ratio signal sur bruit. Un test rapide entre 160 et 200 GHz a néanmoins été réalisé à l'aide d'un analyseur de réseau vectoriel et d'un guide d'ondes coplanaire, mais le pic FMR de la couche d'oxyde ferrique epsilon n'a pas pu être observé. La raison en est que le pic FMR était probablement beaucoup plus petit que le bruit de configuration, ce qui indique qu'une cavité résonante est absolument nécessaire pour augmenter le rapport signal sur bruit et pouvoir mesurer la résonance.

Malheureusement, des mesures précises de la fréquence FMR de ϵ -Fe₂O₃ n'étaient pas possibles ni par la spectroscopie THz dans le domaine temporel (TDS). Dans ce cas, la problématique principale était liée à la minceur extrême des couches d'oxyde ferrique epsilon, qui ont pour conséquence une absorption très limitée. De plus, les pérovskites orientées (111) utilisées comme substrats pour les couches de ϵ -Fe₂O₃ se sont révélées avoir une absorption élevée dans la gamme de fréquences sondées, et ne sont donc pas très bien adaptées à ces types de mesures. Cette mesure TDS a toutefois quand même été réalisée et a mené à un résultat expérimental surprenant : En effet, une transmittance globale plus élevée a été mesurée pour l'échantillon constitué par la couche d'oxyde ferrique epsilon et le substrat YSZ (100) que pour le substrat YSZ (100) seul ! Cela peut être dû au fait que la couche de ϵ -Fe₂O₃ agit comme un revêtement antireflet pour le rayonnement THz, comme cela a été montré pour les couches minces d'autres semi-conducteurs¹¹⁷. Néanmoins, une absorption notable a été enregistrée dans les 60-175 GHz (0.06-0.175 THz), comme on

peut le voir sur la **Figure 60**, qui a été obtenue à partir du spectrogramme TDS expérimentalement mesuré en appliquant une transformée de Fourier rapide. Même avec la réduction de la résolution de la mesure, qui était due à un échantillonnage minimal de 0,05 ps, ceci est une première preuve claire de l'absorption dans les couches minces épitaxiales autour de la fréquence FMR rapportée pour les nanoparticules oxyde ferrique epsilon (190 GHz)⁴⁰. Une baisse de cette fréquence ne serait pas surprenante étant donné le champ coercitif inférieur qui a été enregistré dans les couches minces oxyde ferrique epsilon par rapport aux nanoparticules (voir la section 3.3.1).

Après la «redécouverte» de l'oxyde ferrique epsilon au début des années 1990, la direction principale de la recherche, en particulier celle du groupe supervisé par le professeur Ohkoshi, qui est actuellement le principal expert en nanoparticules de $\epsilon\text{-Fe}_2\text{O}_3$, s'est déplacé vers l'étude de l'effet de la substitution partielle du fer par d'autres métaux dans les nanoparticules d'oxyde ferrique epsilon ($\epsilon\text{-M}_x\text{Fe}_{2-x}\text{O}_3$), en particulier en ce qui concerne son effet sur la fréquence FMR (donc sur l'absorption dans la gamme dite des ondes millimétriques). Dans différents rapports, Ohkoshi et al. ont montré que la substitution des ions Fe^{3+} dans $\epsilon\text{-Fe}_2\text{O}_3$ par des métaux ayant un rayon ionique plus petit, tel que Al^{3+} et Ga^{3+} , entraîne une diminution de la fréquence FMR⁴¹⁻⁴³, tandis que pour une substitution avec des ions plus grands comme Rh^{3+} , une augmentation de la FMR est observée⁴⁴. Il est intéressant de noter que AlFeO_3 et GaFeO_3 , qui sont isostructuraux à $\epsilon\text{-Fe}_2\text{O}_3$, sont des ferroélectriques à température ambiante, connus pour être aussi caractérisés par un ordre magnétique spontané à des températures cryogéniques^{100,118,119}. Une fois démontré la possibilité de développer des couches minces de $\epsilon\text{-Fe}_2\text{O}_3$ de haute qualité, l'objectif de ma recherche s'est déplacé vers l'étude de la substitution du fer par d'autres métaux dans le réseau $\epsilon\text{-Fe}_2\text{O}_3$: l'objectif principal était d'essayer de reproduire dans les couches minces les effets montrés pour les nanoparticules avec un intérêt majeur pour l'abaissement de la fréquence FMR par une substitution partielle du Fe par Al ou Ga. En outre, compte tenu des meilleures propriétés ferroélectriques observée pour la ferrite d'aluminium et la ferrite de gallium (qui possède aussi une structure non-centrosymétrique et légèrement déformée par rapport à l'oxyde ferrique epsilon), j'espérais améliorer les propriétés ferroélectriques de mes couches en effectuant ces substitutions. Des couches minces épitaxiales de $\epsilon\text{-Al}_x\text{Fe}_{2-x}\text{O}_3$ ont donc été déposées sur SrTiO_3 (111) et sur YSZ (100). La substitution sur une large gamme de composition ($x = 0,03$ à $0,5$, ainsi que $x = 1$) a été obtenue. La substitution d'Al a permis de réduire linéairement le paramètre de réseau dans le plan des couches minces (Figure 61) ainsi que le champ coercitif avec une augmentation de la concentration d'aluminium, indiquant une diminution de l'anisotropie magnétocristalline avec la concentration en aluminium (Figure 62). De plus, une augmentation de l'aimantation à saturation jusqu'à un seuil de substitution de $x = 0,33$ a été montrée, conformément aux résultats précédemment rapportés

pour les nanoparticules d'epsilon-ferrite avec substitution d'aluminium et de gallium. En raison de la résolution limitée des mesures TDS, aucune différence appréciable n'a été mesurée pour la FMR des couches substituées avec de l'aluminium. Enfin, les fuites élevées détectées dans les couches minces purs de $\epsilon\text{-Fe}_2\text{O}_3$, caractérisent encore les couches minces substitués en aluminium, avec pour conséquence que les courants de commutation ne sont toujours pas mesurables.

Comme on l'a vu à la section 3.3.2, la présence de multiples orientations de croissance dans le plan entraîne la présence de multiples axes magnétiques faciles dans le plan. Selon le choix du substrat, la couche mince aura soit trois axes magnétiques faciles, comme c'est le cas pour $\epsilon\text{-Fe}_2\text{O}_3$ déposé sur des pérovskites orientées (111), ou six axes faciles, pour les couches déposées sur YSZ (100) (Figure 64). Un tel phénomène est préjudiciable pour les applications dans lesquelles un axe facile magnétique unique est nécessaire, comme par exemple pour les mémoires magnétiques. Afin de favoriser la croissance selon une seule direction cristallographique, nous avons étudié la possibilité de déposer des couches minces épitaxiales sur des substrats ayant un haut degré de miscut (5, 10, 15 et 20 degrés). L'idée est de profiter de la largeur réduite des terrasses dans ces substrats beaucoup plus faible que pour des substrats réguliers, afin de favoriser une direction de croissance parallèle ou perpendiculaire à la direction du miscut (Tableau 11).

Substrats	Miscut [°]	w_t [Å]
STO (111)	0.05	7746.39
	5	77.27
	10	38.34
	15	25.23
	20	18.57
YSZ (100)	0.05	5867.09
	5	58.52
	10	29.04
	15	19.11
	20	14.07

Tableau 11: Largeur calculée des terrasses pour des substrats de YSZ (100) et de STO (111) pour des degrés croissants de miscut, calculées selon la formule: largeur = paramètre de maille * cos (angle de miscut). Un miscut de 0,05 °, souvent tolérés sur des substrats réguliers, sont présentés à titre de comparaison.

Des films minces épitaxiales de $\epsilon\text{-Fe}_2\text{O}_3$ de l'épaisseur d'environ 50 nm ont été déposées sur des substrats STO (111) et YSZ (100) caractérisés par une mauvaise coupe avec des degrés allant de 5° à 20.

Chapter 8

Pour augmenter la qualité du réseau cristallin, les couches ont été déposées en utilisant la méthode de dépôt par intervalles (comme expliqué dans la section 2.1.4): en arrêtant pendant un certain temps la séquence de croissance après l'ablation d'une quantité de matériau nécessaire pour obtenir environ une monocouche avant de la reprendre, l'objectif était de réaliser une croissance «step-flow». À la suite de cette approche, des couches épaisses de 50 nm ont été déposés en tirant alternativement 220 impulsions sur la cible de Fe_2O_3 (44", à un taux de répétition de 5 impulsions/s) et en attendant 1'45" après la séquence de dépôt.

La microscopie électronique à transmission, associée à la diffraction de rayons X, ont révélé que la croissance sur les substrats de STO (111) et YSZ (100) avec miscut aboutit à des couches hautement cristallines qui ont la même l'orientation que les couches déposées sur des substrats réguliers, mais où une orientation dans le plan domine.

La microscopie électronique à transmission, associée à la diffraction de rayons X, ont révélé que la croissance sur les substrats de STO (111) et YSZ (100) avec miscut aboutit à des couches hautement cristallines qui ont la même l'orientation que les couches déposées sur des substrats réguliers, mais où une orientation domine clairement.

La caractérisation structurale (par XRD) et la magnétométrie (via VSM) ont révélé comment la croissance sur les substrats avec miscut réduit en effet la formation de macles résultant, en particulier pour les couches sur des substrats avec un miscut supérieure à 10° , à une croissance quasi-uniaxiale.

BIBLIOGRAPHY

- (1) Cornell, R. M.; Schwertmann, U. *The Iron Oxides: Structure, Properties, Reactions, Occurrence and Uses*; Wiley-VCH: Weinheim, Germany, 2003.
- (2) Faivre, D. *Iron Oxide: from Nature to Applications*; Faivre, D., Ed.; Wiley-VCH, 2016.
- (3) Azharuddin, M.; Tsuda, H.; Wu, S.; Sasaoka, E. *Fuel* **2008**, *87* (4–5), 451–459.
- (4) Lowrie, W. *Fundamentals of Geophysics*; Cambridge University Press: Cambridge, 2007.
- (5) Malaguti, F. *C. R. Acad. Sci. Paris* **1862**, *55*, 350.
- (6) Wagner, P. A. *Econ. Geol.* **1927**, *22* (8), 845–846.
- (7) Teja, A. S.; Koh, P.-Y. *Prog. Cryst. Growth Charact. Mater.* **2009**, *55*, 22–45.
- (8) Chen, J.; Xu, L.; Li, W.; Gou, X. *Adv. Mater.* **2005**, *17* (5), 582–586.
- (9) Sun, Z.; Yuan, H.; Liu, Z.; Han, B.; Zhang, X. *Adv. Mater.* **2005**, *17* (24), 2993–2997.
- (10) Zheng, Y.; Cheng, Y.; Wang, Y.; Bao, F.; Zhou, L.; Wei, X.; Zhang, Y.; Zheng, Q. *J. Phys. Chem. B* **2006**, *110* (7), 3093–3097.
- (11) Li, L.; Chu, Y.; Liu, Y.; Dong, L. *J. Phys. Chem. C* **2007**, *111* (5), 2123–2127.
- (12) Zhong, L.-S.; Hu, J.-S.; Liang, H.-P.; Cao, A.-M.; Song, W.-G.; Wan, L.-J. *Adv. Mater.* **2006**, *18* (18), 2426–2431.
- (13) Wu, W.; Wu, Z.; Yu, T.; Jiang, C.; Kim, W.-S.; Wei, W.; Zhaohui, W.; Taekyung, Y.; Changzhong, J.; Woo-Sik, K. *Sci. Technol. Adv. Mater.* **2015**, *16* (2), 23501.
- (14) Pankhurst, Q. A.; Connolly, J.; Jones, S. K.; Dobson, J. *J. Phys. D Appl. Phys.* **2003**, *36*, R167–R181.
- (15) Duran, J. D. G.; Arias, J. L.; Gallardo, V.; Delgado, A. V. *J. Pharm. Sci.* **2008**, *97* (8), 2948–2983.
- (16) Mahmoudi, M.; Sant, S.; Wang, B.; Laurent, S.; Sen, T. *Adv. Drug Deliv. Rev.* **2011**, *63* (1–2), 24–46.
- (17) Basly, B.; Felder-Flesch, D.; Perriat, P.; Billotey, C.; Taleb, J.; Pourroy, G.; Begin-Colin, S. *Chem. Commun.* **2010**, *46* (6), 985–987.
- (18) Múzquiz-Ramos, E. M.; Guerrero-Chávez, V.; Macías-Martínez, B. I.; López-Badillo, C. M.; García-Cerda, L. A. *Ceram. Int.* **2015**, *41* (1), 397–402.

Bibliography

- (19) O'Grady, K. *J. Phys. D. Appl. Phys.* **2009**, *42* (22), 220301–220301.
- (20) Haun, J. B.; Yoon, T.-J.; Lee, H.; Weissleder, R. *Wiley Interdiscip. Rev. Nanomedicine Nanobiotechnology* **2010**, *2* (3), 291–304.
- (21) Shao, D.; Xu, K.; Song, X.; Hu, J.; Yang, W.; Wang, C. *J. Colloid Interface Sci.* **2009**, *336* (2), 526–532.
- (22) Magro, M.; Domeneghetti, S.; Baratella, D.; Jakubec, P.; Salviulo, G.; Bonaiuto, E.; Venier, P.; Malina, O.; Tuček, J.; Ranc, V.; Zoppellaro, G.; Zbořil, R.; Vianello, F. *Chem. - A Eur. J.* **2016**, *22* (40), 14219–14226.
- (23) Lin, Y.-F.; Chen, J.-L. *RSC Adv.* **2013**, *3* (35), 15344.
- (24) Li, C.; Shen, Y.; Jia, M.; Sheng, S.; Adebajo, M. O.; Zhu, H. *Catal. Commun.* **2008**, *9* (3), 355–361.
- (25) Shi, F.; Tse, M.; Pohl, M.-M.; Brückner, A.; Zhang, S.; Beller, M. *Angew. Chemie Int. Ed.* **2007**, *46* (46), 8866–8868.
- (26) Dejoie, C.; Sciau, P.; Li, W.; Noe, L.; Mehta, A.; Chen, K.; Luo, H.; Kunz, M.; Tamura, N.; Liu, Z. *Sci. Rep.* **2014**, *4*, 4941.
- (27) Forestier, H.; Guiot-Guillain, G. *C. R. Acad. Sci.* **1934**, *199*, 720–723.
- (28) Buttner, R.; Schrader, G. *Z. Anorg. Allg. Chem.* **1963**, *320*, 220–234.
- (29) Quemeneur, L.; Walter-Levy, E. *C. R. Acad. Sci.* **1963**, *257*, 3410–3413.
- (30) Trautmann, J. M.; Forestier, H. *C. R. Acad. Sci.* **1965**, *261*, 4423–4425.
- (31) Tronc, E.; Chanéac, C.; Jolivet, J. P. *J. Solid State Chem.* **1998**, *139*, 93–104.
- (32) Savii, C.; Popovici, M.; Enache, C.; Subrt, J.; Niznansky, D.; Bakardzieva, S.; Caizer, C.; Hrianca, I.; Cecilia Savii Corina Enache, J. Subrt, D. Niznansky, Snejana Bakardzieva, C. Caizer and I. Hrianca, M. P. *Solid State Ionics* **2002**, *151*, 219–227.
- (33) Zboril, R.; Mashlan, M.; Petridis, D. *Chem. Mater.* **2002**, *14*, 969–982.
- (34) Jin, J.; Ohkoshi, S.; Ashimoto, K. *Adv. Mater.* **2004**, *16* (1), 48–51.
- (35) Gich, M.; Roig, A.; Frontera, C.; Molins, E.; Sort, J.; Popovici, M.; Chouteau, G.; Martín y Marero, D.; Nogués, J. *J. Appl. Phys.* **2005**, *98* (4), 44307.
- (36) Ding, Y.; Morber, J. R.; Snyder, R. L.; Wang, Z. L. *Adv. Funct. Mater.* **2007**, *17* (7), 1172–1178.
- (37) Morber, J. R.; Ding, Y.; Haluska, M. S.; Li, Y.; Liu, J. P.; Wang, Z. L.; Snyder, R. L. *J. Phys. Chem.*

Bibliography

- B* **2006**, 110.
- (38) Sakurai, S.; Shimoyama, J.; Hashimoto, K.; Ohkoshi, S. *Chem. Phys. Lett.* **2008**, 458 (4–6), 333–336.
- (39) Sakurai, S.; Tomita, K.; Hashimoto, K.; Yashiro, H.; Ohkoshi, S. *J. Phys. Chem. C* **2008**, 112 (51), 20212–20216.
- (40) Ohkoshi, S.; Tokoro, H. *Bull. Chem. Soc. Jpn.* **2013**, 86 (8), 897–907.
- (41) Tucek, J.; Zboril, R.; Namai, A.; Ohkoshi, S. *Chem. Mater.* **2010**, 22, 6483–6505.
- (42) Namai, A.; Sakurai, S.; Nakajima, M.; Suemoto, T.; Matsumoto, K.; Goto, M.; Sasaki, S.; Ohkoshi, S. *J. Am. Chem. Soc.* **2009**, 131 (3), 1170–1173.
- (43) Ohkoshi, S.; Kuroki, S.; Sakurai, S.; Matsumoto, K.; Sato, K.; Sasaki, S. *Angew. Chem. Int. Ed. Engl.* **2007**, 46 (44), 8392–8395.
- (44) Namai, A.; Yoshikiyo, M.; Yamada, K.; Sakurai, S.; Goto, T.; Yoshida, T.; Miyazaki, T.; Nakajima, M.; Suemoto, T.; Tokoro, H.; Ohkoshi, S. *Nat. Commun.* **2012**, 3, 1035.
- (45) Sakurai, S.; Kuroki, S.; Tokoro, H.; Hashimoto, K.; Ohkoshi, S. *Adv. Funct. Mater.* **2007**, 17, 2278–2282.
- (46) Carraro, G.; Barreca, D.; Maccato, C.; Bontempi, E.; Depero, L. E.; de Julian Fernandez, C.; Caneschi, A. *CrystEngComm* **2013**, 15, 1039–1042.
- (47) Carraro, G.; Maccato, C.; Gasparotto, A.; Montini, T.; Turner, S.; Lebedev, O. I.; Gombac, V.; Adami, G.; Van Tendeloo, G.; Barreca, D.; Fornasiero, P. *Adv. Funct. Mater.* **2014**, 24, 372–378.
- (48) Gich, M.; Gazquez, J.; Roig, A.; Crespi, A.; Fontcuberta, J.; Idrobo, J. C.; Pennycook, S. J.; Varela, M.; Skumryev, V.; Varela, M. *Appl. Phys. Lett.* **2010**, 96 (11), 112508.
- (49) Thai, T. M. N.; Nguyen, D. T.; Lee, N.-S.; Rhyee, J.-S.; Song, J.; Kim, H.-J. *J. Appl. Phys.* **2016**, 120 (18), 185304.
- (50) Gich, M.; Fina, I.; Morelli, A.; Sánchez, F.; Alexe, M.; Gàzquez, J.; Fontcuberta, J.; Roig, A. *Adv. Mater.* **2014**, 26 (27), 4645–4652.
- (51) Nakajima, M.; Namai, A.; Ohkoshi, S.; Suemoto, T. *Opt. Express* **2010**, 18.
- (52) Bigot, J.-Y.; Vomir, M.; Beaurepaire, E. *Nat. Phys.* **2009**, 5.
- (53) Boeglin, C.; Beaurepaire, E.; Halte, V.; Lopez-Flores, V.; Stamm, C.; Pontius, N.; Durr, H. A.; Bigot, J. Y. *Nature* **2010**, 465 (7297), 458–461.

Bibliography

- (54) Zhang, G. P.; Lefkidis, G.; Hübner, W.; Bai, Y. *J. Appl. Phys.* **2011**, *109* (7), 07D303.
- (55) Kirilyuk, A.; Kimel, A. V; Rasing, T. *Rev. Mod. Phys.* **2010**, *82* (3), 2731–2784.
- (56) de Jong, J. A.; Kimel, A. V; Pisarev, R. V; Kirilyuk, A.; Rasing, T. *Phys. Rev. B* **2011**, *84* (10), 104421.
- (57) Medapalli, R.; Razdolski, I.; Savoini, M.; Khorsand, A. R.; Kirilyuk, A.; Kimel, A. V; Rasing, T.; Kalashnikova, A. M.; Tsukamoto, A.; Itoh, A. *Phys. Rev. B* **2012**, *86* (5), 54442.
- (58) Reid, A. H. M.; Astakhov, G. V; Kimel, A. V; Schott, G. M.; Ossau, W.; Brunner, K.; Kirilyuk, A.; Molenkamp, L. W.; Rasing, T. *Appl. Phys. Lett.* **2010**, *97* (23), 232503.
- (59) Blanchard, F.; Razzari, L.; Bandulet, H. C.; Sharma, G.; Morandotti, R.; Kieffer, J. C.; Ozaki, T.; Reid, M.; Tiedje, H. F.; Haugen, H. K.; Hegmann, F. a. *Opt. Express* **2007**, *15* (20), 13212–13220.
- (60) Xing, X. *J. Appl. Phys.* **2008**, *103* (7), 07F522.
- (61) Ohkoshi, S.; Sakurai, S.; Jin, J.; Hashimoto, K. *J. Appl. Phys.* **2005**, *97* (10), 10K312.
- (62) Kurmoo, M.; Rehspringer, J.-L.; Hutlova, A.; D’Orléans, C.; Vilminot, S.; Estournès, C.; Niznansky, D. *Chem. Mater.* **2005**, *17* (5), 1106–1114.
- (63) Tseng, Y.-C.; Souza-Neto, N. M.; Haskel, D.; Gich, M.; Frontera, C.; Roig, A.; van Veenendaal, M.; Nogués, J. *Phys. Rev. B* **2009**, *79* (9), 94404.
- (64) Yoshikiyo, M.; Yamada, K.; Namai, A.; Ohkoshi, S. *J. Phys. Chem. C* **2012**, *116* (15), 8688–8691.
- (65) Nakajima, M.; Namai, A.; Ohkoshi, S.; Suemoto, T. *Opt. Express* **2010**, *18* (17), 18260–18268.
- (66) Blundell, S. *Magnetism in Condensed Matter*; Oxford University Press: Oxford, 2001.
- (67) Coey, J. M. D. *Magnetism and Magnetic Materials*; Cambridge University Press: Cambridge, 2010.
- (68) Nusbbaum, C.; Vinal, G. W.; Ritchie, L. M.; White, W. P.; Curtis, H. L.; Duncan, R. C.; Hull, G. F.; Eckhardt, E. a; Dorsey, H. G.; Fletcher, H.; Jones, A. T.; Miller, D. C.; Firestone, F. a; Quayle, P. P.; Stephenson, E. B.; Wright, F. E.; Littleton, J. T.; Pietenpol, W. B.; Tolman, R. C.; Lewis, G. N.; Gibson, G. E.; Gray, A. W.; Mauchly, S. J.; Thomson, A.; Bauer, L. a; Peters, W. J.; Barnett, S. J.; Wenner, F.; Grover, F. W.; Shrader, J. E.; Powers, W. F.; Hubbard, J. C.; Pfund, a H.; Sawtelle, W. O.; Valasek, J.; Priest, I. G.; Hyde, E. P.; Forsythe, W. E.; Randall, H. M.; Colby, W. F.; Paton, R. F.; Laird, E. R.; Howes, H. L.; Blackwood, O.; Millikan, R. a; Comton, K. T.; Olmstead, P. S.; Lilly, E.; Hull, A. W.; Duane, W.; Patterson, R. a; Richtmyer, F. K.; Grant, K.; Stuhlmann Jr., O.; Williams, E. H.; Kunz, J.; Seiler, E. F.; Fazel, C. S.; Hulburt, E. O.; Breit, G.; Davisson, C.; Pidgeon, H. a; Mohler, F. L.; Foote, P. D.; Purington, E. S.; Hull, L. M.; Whittemore, L. E.; Colvin, C. H.

Bibliography

- Phys. Rev.* **1920**, 15 (6), 505–564.
- (69) Bibes, M.; Barthélémy, A. *Nat. Mater.* **2008**, 7 (6), 425–426.
- (70) Nan, C. W.; Bichurin, M. I.; Dong, S.; Viehland, D.; Srinivasan, G. *J. Appl. Phys.* **2008**, 103 (3).
- (71) Smith, H. M.; Turner, A. F. *Appl. Opt.* **1965**, 4 (1), 147, 148.
- (72) Dijkkamp, D.; Venkatesan, T.; Wu, X. D.; Shaheen, S. A.; Jisrawi, N.; Min-Lee, Y. H.; McLean, W. L.; Croft, M. *Appl. Phys. Lett.* **1987**, 51 (8), 619–621.
- (73) Markov, V. A.; Pchelyakov, O. P.; Sokolov, L. V.; Stenin, S. I.; Stoyanov, S. *Surf. Sci.* **1991**, 250 (1–3), 229–234.
- (74) Royer, L. M. *Bull. la Soc. Fr. Mineral. Cristallogr.* **1928**, 51, 7.
- (75) Green, J. E. In *Multicomponent and Multilayered Thin Films for Advanced Microtechnologies*; Auciello, O., Engemann, J., Eds.; Kluwer Academic Publishers: Bad Windsheim (Germany), 1993; pp 39–87.
- (76) Venables, J. A. *Phys. Rev. B* **1987**, 36 (8), 4153–4162.
- (77) Rosenfeld, G.; Poelsema, B.; Comsa, G. In *Growth and Properties of Ultrathin Epitaxial Layers*; King, D. A., Woodruff, D. P., Eds.; Elsevier, 1997; pp 66–101.
- (78) Frank, F. C.; van der Merwe, J. H. *Proc. R. Soc. A Math. Phys. Eng. Sci.* **1949**, 198 (1053), 205–216.
- (79) Herman, M. A.; Sitter, H. *Molecular Beam Epitaxy - Fundamentals and Current Status*, 2nd ed.; Springer: Berlin, Heidelberg, 1996.
- (80) Ayers, J. E. *Heteroepitaxy of Semiconductors - Theory, growth, and characterization.*; Taylor & Francis: Boca Raton, FL, FL, 2007; Vol. 31.
- (81) Griesche, J.; Enderlein, R.; Schikora, D. *Phys. Status Solidi* **1988**, 109 (1), 11–38.
- (82) Zur, A.; McGill, T. C. *J. Appl. Phys.* **1984**, 55 (2), 378–386.
- (83) Faurie, J. P.; Hsu, C.; Sivananthan, S.; Chu, X. *Surf. Sci.* **1986**, 168 (1–3), 473–482.
- (84) Myers, T. H.; Lo, Y.; Bicknell, R. N.; Schetzina, J. F. *Appl. Phys. Lett.* **1983**, 42 (3), 247–248.
- (85) Ruska, E. *Angew. Chemie Int. Ed. English* **1987**, 26 (7), 595–605.
- (86) Gauquelin, N.; Hawthorn, D. G.; Sawatzky, G. a; Liang, R. X.; Bonn, D. a; Hardy, W. N.; Botton, G. a. *Nat. Commun.* **2014**, 5, 4275.

Bibliography

- (87) Corbellini, L.; Plathier, J.; Lacroix, C.; Harnagea, C.; Ménard, D.; Pignolet, A. *J. Appl. Phys.* **2016**, *120*, 124101.
- (88) Lacroix, C.; Lambert-Milot, S.; Desjardins, P.; Masut, R. A.; Ménard, D. *J. Appl. Phys.* **2009**, *105* (7), 07C119.
- (89) Ohkoshi, S.-I.; Namai, A.; Imoto, K.; Yoshikiyo, M.; Tarora, W.; Nakagawa, K.; Komine, M.; Miyamoto, Y.; Nasu, T.; Oka, S.; Tokoro, H. *Scientific Reports*. 2015, p 14414.
- (90) Binnig, G.; Rohrer, H.; Gerber, C.; Weibel, E. *Phys. Rev. Lett.* **1982**, *49* (1), 57–61.
- (91) Binnig, G.; Rohrer, H.; Gerber, C.; Weibel, E. *Appl. Phys. Lett.* **1982**, *40* (2), 178–180.
- (92) Binnig, G.; Rohrer, H. *IBM J. Res. Dev.* **1986**, *30* (4), 355–369.
- (93) Lacroix, C. Propriétés magnétiques de nanoagrégats ferromagnétiques encastrés dans une épicoche semi-conductrice, Ecole Polytechnique de Montréal, 2010.
- (94) Pickwell, E.; Wallace, V. P. *J. Phys. D. Appl. Phys.* **2006**, *39* (17), R301–R310.
- (95) Hoffmann, M. C.; Fülöp, J. A. *J. Phys. D. Appl. Phys.* **2011**, *44* (8), 83001.
- (96) Dhillon, S. S.; Vitiello, M. S.; Linfield, E. H.; Davies, A. G.; Hoffmann, M. C.; Booske, J.; Paoloni, C.; Gensch, M.; Weightman, P.; Williams, G. P.; Castro-Camus, E.; Cumming, D. R. S.; Simoens, F.; Escorcia-Carranza, I.; Grant, J.; Lucyszyn, S.; Kuwata-Gonokami, M.; Konishi, K.; Koch, M.; Schmuttenmaer, C. A.; Cocker, T. L.; Huber, R.; Markelz, A. G.; Taylor, Z. D.; Wallace, V. P.; Axel Zeitler, J.; Sibik, J.; Korter, T. M.; Ellison, B.; Rea, S.; Goldsmith, P.; Cooper, K. B.; Appleby, R.; Pardo, D.; Huggard, P. G.; Krozer, V.; Shams, H.; Fice, M.; Renaud, C.; Seeds, A.; Stöhr, A.; Naftaly, M.; Ridler, N.; Clarke, R.; Cunningham, J. E.; Johnston, M. B. *J. Phys. D. Appl. Phys.* **2017**, *50* (4), 43001.
- (97) Dhillon, S. S.; Vitiello, M. S.; Linfield, E. H.; Davies, A. G.; Hoffmann, M. C.; Booske, J.; Paoloni, C.; Gensch, M.; Weightman, P.; Williams, G. P.; Castro-Camus, E.; Cumming, D. R. S.; Simoens, F.; Escorcia-Carranza, I.; Grant, J.; Lucyszyn, S.; Kuwata-Gonokami, M.; Konishi, K.; Koch, M.; Schmuttenmaer, C. A.; Cocker, T. L.; Huber, R.; Markelz, A. G.; Taylor, Z. D.; Wallace, V. P.; Axel Zeitler, J.; Sibik, J.; Korter, T. M.; Ellison, B.; Rea, S.; Goldsmith, P.; Cooper, K. B.; Appleby, R.; Pardo, D.; Huggard, P. G.; Krozer, V.; Shams, H.; Fice, M.; Renaud, C.; Seeds, A.; Stöhr, A.; Naftaly, M.; Ridler, N.; Clarke, R.; Cunningham, J. E.; Johnston, M. B. *J. Phys. D. Appl. Phys.* **2017**, *50* (4), 43001.
- (98) Kusano, Y.; Fujii, T.; Takada, J.; Fukuhara, M.; Doi, A.; Ikeda, Y.; Takano, M. *Chem. Mater.* **2008**, *20* (1), 151–156.

Bibliography

- (99) Taboada, E.; Gich, M.; Roig, A. *ACS nano*. 2009, pp 3377–3382.
- (100) Trassin, M.; Viart, N.; Versini, G.; Loison, J. L.; Vola, J. P.; Schmerber, G.; Crégut, O.; Barre, S.; Pourroy, G.; Lee, J. H.; Jo, W.; Mény, C. *Appl. Phys. Lett.* **2007**, *91* (20), 202504.
- (101) Lee, H. N.; Senz, S.; Zakharov, N. D.; Harnagea, C.; Pignolet, A.; Hesse, D.; Gosele, U. *Appl. Phys. Lett.* **2000**, *77* (20), 3260–3262.
- (102) Jia, Q. X.; Song, S. G.; Wu, X. D.; Cho, J. H.; Foltyn, S. R.; Findikoglu, A. T.; Smith, J. L. *Appl. Phys. Lett.* **1996**, *68* (8), 1069–1071.
- (103) Jun, S.; Kim, Y. S.; Lee, J.; Kim, Y. W. *Appl. Phys. Lett.* **2001**, *78* (17), 2542–2544.
- (104) Roy, A.; Mukherjee, S.; Gupta, R.; Prasad, R.; Garg, A. *Ferroelectrics* **2014**, *473* (1), 154–170.
- (105) Mukherjee, S.; Roy, A.; Auluck, S.; Prasad, R.; Gupta, R.; Garg, A. *Phys. Rev. Lett.* **2013**, *111* (8), 1–5.
- (106) Sofin, R. G. S.; Wu, H.-C.; Shvets, I. V. *Phys. Rev. B* **2011**, *84* (21), 212403.
- (107) Rigato, F.; Geshev, J.; Skumryev, V.; Fontcuberta, J. *J. Appl. Phys.* **2009**, *106* (11), 113924.
- (108) Kurt, H.; Rode, K.; Venkatesan, M.; Stamenov, P.; Coey, J. M. D. *Phys. Rev. B* **2011**, *83* (2), 20405.
- (109) Wei, Y.; Han, B.; Hu, X.; Lin, Y.; Wang, X.; Deng, X. *Procedia Eng.* **2012**, *27*, 632–637.
- (110) Angermann, A.; Töpfer, J. *J. Mater. Sci.* **2008**, *43* (15), 5123–5130.
- (111) Caruntu, D.; Caruntu, G.; O'Connor, C. J. *J. Phys. D: Appl. Phys.* **2007**, *40* (19), 5801–5809.
- (112) Roca, A. G.; Morales, M. P.; O'Grady, K.; Serna, C. J. *Nanotechnology* **2006**, *17* (11), 2783–2788.
- (113) Yan, F.; Li, J.; Zhang, J.; Liu, F.; Yang, W. *J. Nanoparticle Res.* **2009**, *11* (2), 289–296.
- (114) Lacroix, C.; Lambert-Milot, S.; Masut, R. A.; Desjardins, P.; Ménard, D. *Phys. Rev. B* **2013**, *87* (2), 24412.
- (115) Lambert-Milot, S.; Gaudet, S.; Lacroix, C.; Ménard, D.; Masut, R. A.; Lavoie, C.; Desjardins, P. *J. Vac. Sci. Technol. A* **2012**, *30*, 61510.
- (116) Lefevre, C.; Shin, R. H.; Lee, J. H.; Oh, S. H.; Roulland, F.; Thomasson, A.; Autissier, E.; Meny, C.; Jo, W.; Viart, N. *Appl. Phys. Lett.* **2012**, *100* (26), 1–5.
- (117) Chen, Y. W.; Zhang, X.-C. *Front. Optoelectron.* **2014**, *7* (2), 243–262.
- (118) Sharma, K.; Raghavendra Reddy, V.; Gupta, A.; Choudhary, R. J.; Phase, D. M.; Ganesan, V. *Appl. Phys. Lett.* **2013**, *102* (21), 212401.

Bibliography

- (119) Hamasaki, Y.; Shimizu, T.; Taniguchi, H.; Taniyama, T.; Yasui, S.; Itoh, M. *Appl. Phys. Lett.* **2014**, *104* (8), 82906.
- (120) Cowburn, R. P. *Science* (80-.). **2000**, *287* (5457), 1466–1468.
- (121) Niemier, M. *Nat. Nanotechnol.* **2014**, *9* (1), 14–15.
- (122) Thomasson, A.; Cherifi, S.; Lefevre, C.; Roulland, F.; Gautier, B.; Albertini, D.; Meny, C.; Viart, N. *J. Appl. Phys.* **2013**, *113* (21), 214101.
- (123) Hu, J. M.; Li, Z.; Chen, L. Q.; Nan, C. W. *Nat. Commun.* **2011**, *2* (1), 553–558.
- (124) Shen, J.; Cong, J.; Shang, D.; Chai, Y.; Shen, S.; Zhai, K.; Sun, Y. *Sci. Rep.* **2016**, *6*, 1–6.
- (125) Klimov, A.; Tiercelin, N.; Dusch, Y.; Giordano, S.; Mathurin, T.; Pernod, P.; Preobrazhensky, V.; Churbanov, A.; Nikitov, S. *Appl. Phys. Lett.* **2017**, *110* (22).
- (126) Lu, A.-H.; Salabas, E. L.; Schuth, F. *Angew. Chem. Int. Ed.* **2007**, *46*, 1222–1244.
- (127) Wu, W.; He, Q. G.; Jiang, C. Z. *Nanoscale Res. Lett.* **2008**, *3*, 397.
- (128) Gonzalez, J.; Chubykalo, O.; Gonzalez, J. M. *Encyclopedia of Nanoscience and Nanotechnology*; S., N. H., Ed.; American Scientific Publishers: Stevenson Ranch, CA, 2004; Vol. 10.
- (129) Bulte, J. W. M.; Kraitchman, D. L. *NMR Biomed.* **2004**, *17*, 484–499.
- (130) Berry, C. C.; Curtis, A. S. G. *J. Phys. D Appl. Phys.* **2003**, *36*, R198–R206.
- (131) Gupta, A. K.; Gupta, M. *Biomaterials* **2005**, *26*, 3995–4021.
- (132) Laurent, S.; Forge, D.; Port, M.; Roch, A.; Robic, C.; Elst, L. V.; Muller, R. N. *Chem. Rev.* **2008**, *108*, 2064.
- (133) Mornet, S.; Vasseur, S.; Grasset, F.; Duguet, E. *J. Mater. Chem.* **2004**, *14* (14), 2161–2175.
- (134) Tartaj, P.; del Puerto Morales, M.; Veintemillas-Verdaguer, S.; Gonzalez-Carreno, T.; Serna, C. J. *J. Phys. D Appl. Phys.* **2003**, *36*, R182–197.
- (135) Thorek, D. L. J.; Chen, A. K.; Czupyrna, J.; Tsourkas, A. *Ann. Biomed. Eng.* **2006**, *34* (1), 23–38.
- (136) Dormann, J. L.; Fiorani, D.; Tronc, E. In *Advances in Chemical Physics*; Prigogine, I., Rice, S. A., Eds.; John Wiley: New York, 1997; Vol. 98, pp 283–494.
- (137) Popovici, M.; Savii, C.; Nižòanský, D.; Enache, C.; Ionescu, C.; Radu, R. *Mater. Struct.* **2006**, *13* (2), 79–81.
- (138) Chan, W. L.; Deibel, J.; Mittleman, D. M. *Reports Prog. Phys.* **2007**, *70* (8), 1325.

Bibliography

- (139) Ferguson, B.; Zhang, X.-C. *Nat. Mater.* **2002**, *1* (1), 26–33.
- (140) Huber, R.; Tauser, F.; Brodschelm, a; Bichler, M.; Abstreiter, G.; Leitenstorfer, a. *Nature* **2001**, *414* (6861), 286–289.
- (141) Nuss, M. C.; Orenstein, J. In *Millimeter and Submillimeter Wave Spectroscopy of Solids*; Grüner, G., Ed.; Springer Berlin Heidelberg: Berlin, Heidelberg, 1998; pp 7–50.
- (142) Nagel, M.; Haring Bolivar, P.; Brucherseifer, M.; Kurz, H.; Bosserhoff, A.; Büttner, R. *Appl. Phys. Lett.* **2002**, *80* (1), 154–156.
- (143) Bertotti, G.; Mayergoyz, I. D.; Mayergoyz, I. *The Science of Hysteresis*; Elsevier, 2006.
- (144) Hodenberg, R. V.; Salje, E. *Mater. Res. Bull.* **1977**, *12*, 1029–1034.
- (145) Xiong, Z. H.; Wu, D.; Vardeny, Z. V.; Shi, J. *Nature* **2004**, *427*, 821–824.
- (146) Nakano, M.; Shibuya, K.; Okuyama, D.; Hatano, T.; Ono, S.; Kawasaki, M.; Iwasa, Y.; Tokura, Y. *Nature* **2012**, *487* (7408), 459–462.
- (147) *Handbook of Magnetism and Advanced Magnetic Materials*; Kronmüller, H., Parkin, S., Eds.; John Wiley and Sons, Inc., 2007.
- (148) Lines, M. E.; Glass, A. M. *Principles and Applications of Ferroelectrics and Related Materials*; Oxford University Press: Oxford, 1977.
- (149) *Thin Film Ferroelectric Materials and Devices*; Ramesh, R., Ed.; Springer Science + Business Media: New York, 1997.
- (150) Krafft, C. S.; Josephs, R. M.; Crompton, D. S. *IEEE Trans. Magn.* **1986**, *22* (5), 662–664.
- (151) Zhao, Z. C.; Wang, H.; Xiao, S. Q.; Xia, Y. X.; McGuire, J. a.; Ren, Y.; Jin, Q. Y.; Gao, T. R. *J. Appl. Phys.* **2007**, *101*, 16105.
- (152) Scott, J. F. *J. Phys. Condens. Matter* **2008**, *20* (2), 21001.
- (153) Gupta, P.; Gupta, A.; Franco, V.; Conde, A. *J. Appl. Phys.* **2007**, *101* (3), 33909.
- (154) Kurlyandskaya, G. V.; Barandiarán, J. M.; Muñoz, J. L.; Gutiérrez, J.; Vázquez, M.; Garcia, D.; Vas'kovskiy, V. O. *J. Appl. Phys.* **2000**, *87* (9), 4822.
- (155) Wernsdorfer, W.; Aliaga-Alcalde, N.; Christou, G.; Hendrickson, D. N. *Nature* **2002**, *416*, 406–409.
- (156) Smith, R. C.; Massad, J. E. In *Proceedings of the 2001 ASME Design Engineering Technical Conferences and Computers and Information in Engineering Conference*; 2001; pp 1389–1398.

Bibliography

- (157) Li, J.; Li, F.; Zhang, S. *J. Am. Ceram. Soc.* **2014**, *97* (1), 1–27.
- (158) Pintilie, L.; Alexe, M. *Appl. Phys. Lett.* **2005**, *87* (September), 11–13.
- (159) Pintilie, L. In *Ferroelectrics - Physical Effects*; Lallart, M., Ed.; InTech, 2011; pp 101–134.
- (160) Nechache, R.; Harnagea, C.; Carignan, L.-P.; Gautreau, O.; Pintilie, L.; Singh, M. P.; Ménard, D.; Fournier, P.; Alexe, M.; Pignolet, A. *J. Appl. Phys.* **2009**, *105* (6), 61621.
- (161) Nechache, R.; Harnagea, C.; Ruediger, A.; Rosei, F.; Pignolet, A. *Funct. Mater. Lett.* **2010**, *3* (1), 83–88.
- (162) Momma, K.; Izumi, F. *J. Appl. Crystallogr.* **2011**, *44*, 1272–1276.

APPENDIX I Hysteresis Loops Revisited: An Efficient Method to Analyze Ferroic Materials.

Hysteresis, a term coined by Sir James Alfred Ewing, a Scottish physicist and engineer (1855-1935), is the dependence of the state of a system on the history of such state. Consequently, the system can reach different output values for the same input parameter depending on its history, resulting in the existence of a ‘hysteresis loop’ in the graph of the output of the system versus its input upon cycling the input parameter. Hysteresis can simply be caused by a dynamic lag between the output and the input, in which case a ‘rate-dependent hysteresis’ is observed, or more interestingly, it can be characterized by a more robust memory effect (e.g. the presence and motion of domains in ferroelectric and magnetic materials) and the memory of the past remains even after the transient input has died out, giving a ‘rate-independent hysteresis’. Such effect characterizes many different processes, belonging not only to fields such as physics, chemistry, biology, and engineering, but also to less-obvious ones such as economics and sociology¹⁴³.

Focusing on physics and more specifically on materials science, (rate-independent) hysteretic behavior is the main characteristic of ferroic materials like ferromagnets, ferroelectrics and ferroelastic materials, and also of materials characterized by piezoelectricity, giant magneto-resistance and metal-insulator transition^{144–146}. However, we will here restrict our interest to ferroic materials, in particular to ferromagnets and ferroelectrics which, given their multifunctional properties, have been extensively studied and are nowadays utilized in a wide range of applications^{67,147–149}. In such materials, hysteresis is due to the formation and growth of domains, and the related domain wall motions, under the effect of an external input (respectively a magnetic or an electric field).

Measurements of the hysteretic behavior of a material, be it a ferromagnet or a ferroelectric, can be performed in many ways. Direct measurement of the magnetization and of the spontaneous dielectric polarization can be obtained respectively through a magnetometer, like via a Vibrating Sample Magnetometer (VSM) or a Superconducting Quantum Interference Device (SQUID), and with ferroelectricity measurements setups like a ferroelectric analyzer or via a Piezoresponse Force Microscopy (PFM). In both cases, hysteresis can also be observed via optical measurements^{150,151}.

APPENDIX I

Although these measurements may not be experimentally challenging, it may, however, be difficult to extract a specific ferroic contribution from the experimental hysteresis loop. For example, spurious contributions to the measured magnetic or dielectric polarization originating from various external factors have to be subtracted from the measured curve. Such contributions can originate from the diamagnetic or paramagnetic contribution of the substrate on which the sample is deposited or from the sample holder in a magnetometer, or can be due to some external circuit capacitive components or to the effect of leakage currents in a ferroelectric measurement. Accounting for such contributions associated either with the ferroic phase, or with non ferroic phases, or with experimental artifacts, may be tricky (e.g. the parasitic leakage effect in ferroelectrics, or the contribution of the substrate in magnetic measurements of a thin film at high field). Having a data processing technique that allows to separate the various contributions and extract reliable values of the quantities of interest, such as remanent and saturation values of the magnetization and of the polarization, along with the values of respective coercive fields (i.e. the value of the external input signal at which there is reversal of the order parameter) may, under the right assumption on the nature of the measured hysteretic signal, greatly ease the task of interpreting and analyzing any kind of hysteresis measurement. Such a procedure becomes crucial when the measured loop is dominated by some parasitic effect, like in leaky ferroelectrics, and it may also help to identify the presence of several ferroic phases or to avoid misinterpretation of data such as reported in the famous article entitled ‘Ferroelectrics go bananas’¹⁵².

Here, a method is proposed that allows to easily and reliably extract the contribution from the measured hysteresis loop associated to different ferromagnetic or a ferroelectric phases in a material. In the case of multiphase materials, or of materials with multiple coercive fields, the proposed technique allows us to separate each individual contribution and to reconstruct separate hysteresis loops for each individual hysteretic phenomenon. While the technique can be applied to any hysteresis loops like the one listed above, for example to obtain the precise value of the coercive stress for a ferroelastic loop, or the exact transition temperature in a metal-insulator transition, such systems will not be discussed in this manuscript.

The method is based on the well-known procedure in the field of magnetism which uses the derivative of the hysteresis loop and which has been extensively used to analyze loops belonging to multiphase magnetic materials and materials with multiple magnetic configurations¹⁵³⁻¹⁵⁵. However, to the best of the authors’ knowledge, the ‘reconstruction’ of the hysteresis loops via integration to fit the experimental data has not been reported - even for magnetic hysteresis loops - and such technique has never been used to isolate the various contributions from measured ferroelectric hysteresis loops or to realize a more detailed in-depth study.

I.1 Separating the different contributions to the measured hysteresis loops

The data analysis we propose was initially developed to analyze magnetic hysteresis loops of epitaxial thin films of epsilon iron ferrite ($\epsilon\text{-Fe}_2\text{O}_3$) grown on different single crystal substrates. It was then extended to the analysis of other ferromagnetic and ferroelectric materials. The motivation for developing the method was to separate what we believed to be two distinct contributions to the hysteresis loop of such material, as it will be thoroughly discussed below. We also noticed how such a method could really ease the removal of spurious contributions to the hysteresis loop (whether them being the simple contributions of the substrates in magnetic measurements or more intricate ones in ferroelectric measurements). The technique includes several steps, involving differentiating the originally measured hysteresis loop, fitting the resulting curve utilizing the sum of (i) a constant, (ii) a polynomial contribution, and (iii) a Voigt distribution (which is the convolution between a Gaussian and a Lorentz distribution, of the form $V(x; \sigma, \gamma) = \int_{-\infty}^{\infty} G(x'; \sigma)L(x - x'; \gamma)dx'$, where $G(x; \sigma) \equiv \frac{e^{-x^2/2\sigma^2}}{\sigma\sqrt{2\pi}}$ is the centered Gaussian function, and $L(x; \gamma) \equiv \frac{\gamma}{\pi(x^2 + \gamma^2)}$ is the centered Lorentzian function), and finally integrating only the Voigt fitting function to obtain the sole ferroic contribution. Given the different steps involved in order to obtain solely the ferroic contribution, the technique was coined ‘Derivative - Deconvolution - Selective Integration’ or ‘D-D-SI’, which will be used hereafter in the manuscript. While the idea of differentiating the hysteresis loop in order to highlight the different coercive fields was already used in the papers cited above^{153–155}, we developed it further by fitting the 1st derivative with Voigt distributions and further separating the different hysteresis loop by integrating the fit functions, as well as extending such method to the analysis of ferroelectric loops. In the fitting procedure, the constant offset represents the linear contribution of the measured hysteresis loop (i.e. the diamagnetic and paramagnetic or dielectric and paraelectric contributions), the polynomial series represents both the instrumental contribution and the leakage current in the ferroelectric measurements, while usually there is no such instrumental contribution for magnetic measurements, and the Voigt distributions represents the nonlinear response of the ferroic material. In the case of the analysis of films/materials with multiple contributions to the total signal, two or more Voigt functions can be used for the fit. Further integration of the individual Voigt functions results in one hysteresis loop for each of the ferroic phases. Finally, centering each integrated Voigt curve by adjusting the integration constant, under the assumption that the values at positive and negative saturation are the same, gives the hysteresis reconstructed loop corresponding to each phase, allowing to extract the true coercive and remanent values of the sole hysteretic phenomenon.

APPENDIX I

Besides the symmetry at saturation (for example in the case of ferromagnets, the saturation magnetization is the same for positive and negative magnetic fields: $|M_{S+}| = |M_{S-}|$), there are three more assumptions involved in the procedure:

- Absence of any significant ‘linear’ contribution to the measured hysteresis loop of the phase of interest, whether it is diamagnetic and/or paramagnetic, or dielectric and/or paraelectric;
- Linear regime for both paramagnetic or paraelectric phases of the substrate, sample holder, or anything contributing to the total measured signal;
- Absence of interaction between the ferroic phases and/or with the substrate.

The first two assumptions apply in particular to the analysis of magnetometric data carried on a VSM, for which the magnetization of the sample is of comparable magnitude of the signal given by the substrate or the vibrating rod. In such cases, any ‘linear’ contribution coming from the ferroic phases of interest would be indistinguishable from the signal of the substrate or the rod, all contributing to a constant offset after differentiating the original signal. The last assumption applies, for example, to the study of exchange bias of bilayers or multilayers or to ensemble of nanoparticles with significant dipolar interactions. For such cases, the D-D-SI technique leads to magnetic characteristics “dressed” by the interactions, that is, non-intrinsic to the phase of interest. For example, the exchange bias would shift the measured hysteresis loop and the dipolar interaction could lead to shape dependent effective magnetic anisotropy fields. In such cases, further information or assumptions are required in order to reconstruct the intrinsic loops for each phase.

In order to be able to work with differentiable mathematical functions, the measured hysteresis loops were split into an upward and a downward curve, corresponding to the external field applied being swept with increasing and decreasing values, from negative to positive saturation and vice versa, and which will be presented in the following in red and blue. The choice of a Voigt function for fitting was made for two reasons: the first comes from a practical point of view, given how such a function is standard and implemented in almost any data analysis software. The second reason is that it can be used to fit peaks of various shape since it corresponds to the convolution of a Gaussian and a Lorentzian. For example, a Voigt function can represent fairly well the first derivative of functions such as $\tanh(x)$ or $\coth(x) - \frac{1}{x}$, which correspond respectively to the widely used Ising and Langevin models for ferroelectric and ferromagnetic hysteresis¹⁵⁶. Moreover, by using the D-D-SI (using Voigt functions), it is possible to easily extract the main parameters characterizing the hysteresis loop, either obtaining them by analyzing the different features

of the fitting functions, or graphically from the reconstructed hysteresis curve(s) stemming from the sole ferroic contribution derived from the application of the technique.

Finally, it is worth mentioning that independent superparamagnetic nanoparticles, which are indeed described by Langevin function, would yield a peak centered at zero field, provided the cycled field is strong enough. However, further work and assumptions are needed in order to extract the intrinsic physical information if the particles are interacting. Additional details about the choice of the fitting function are presented in the Supplementary Material.

I.2 Validation of the technique

The magnetic data were acquired with a commercial EV9 Vibrating Sample Magnetometer (VSM) from ADE Technologies while the ferroelectric ones with an aixACCT TF Analyzer 2000 FerroElectric module (the same experimental setups used for functional characterization of epsilon ferrite thin films).

Before analyzing the complex hysteresis loops of a ϵ -Fe₂O₃ thin films, the validity of the method is demonstrated by analyzing the measured hysteresis loops of a ‘standard’ material, namely the widely used and well-known hard ferromagnetic material barium hexaferrite (BaFe₁₂O₁₉). In Figure Appendix 1(a) are shown the measured hysteresis loop of compressed powders of polycrystalline barium hexaferrite (symbols), along with the reconstructed hysteresis loop (blue and red solid lines), and the error between the measurement and the fit (orange line). In Figure Appendix 1(b), the 1st derivative of the measured hysteresis loop (symbols) and their respective Voigt fitting functions (red and blue lines) are displayed. As it can be seen in the figures, Voigt functions provide good fit for the first derivatives of the hysteresis loop obtained experimentally, which in turn allow us to reconstruct the ferroic contribution to the hysteresis adequately. For the case of our barium hexaferrite sample, which possesses a very high magnetic moment, there is no need of removing the constant, since the main contribution to the magnetization comes indeed from the ferromagnetic material itself and not from the diamagnetic vibrating rod of the VSM.

APPENDIX I

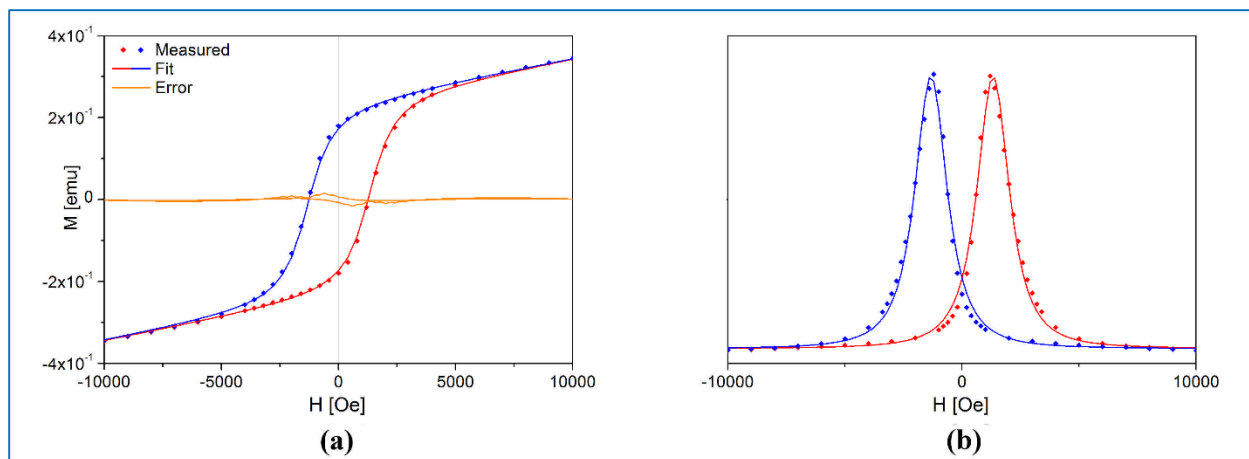


Figure Appendix 1: (a) The good fit achievable by using the presented D-D-SI is evident in the plot of both the measured (dot) and reconstructed (red and blue lines) hysteresis loops of barium hexaferrite, as shown by the error between the measured and the fitted values.

In the case of the hysteresis loop measured from an epsilon ferrite epitaxial thin film grown by our group on a strontium titanate (SrTiO_3) single crystal substrate (Figure Appendix 2(a)), we notice two features worth mentioning. First, we observe the presence of a strong diamagnetic contribution. This diamagnetic contribution originates from the substrate, on which the epsilon ferrite thin film is deposited, and also from the sample holder (made of glass). We note that for the case of the barium hexaferrite sample, the diamagnetic contribution of the sample holder was not visible due to the high magnetic moment of barium hexaferrite (three orders of magnitude higher than the one of the epsilon ferrite thin film). The conventional way to isolate the response of the sole epsilon ferrite films, is to measure the diamagnetic contribution of a substrate of similar dimension of the one on which the film is deposited (Figure Appendix 2 (b)), and to subtract it from the total signal to obtain a loop like the one shown in blue symbols in Figure Appendix 3. Second, the presence of a ‘shoulder’ in the measured loop for applied fields close to zero is observed. Using the presented D-D-SI, the derivative of the measured hysteresis loop (Figure Appendix 2 (c)) is numerically calculated, allowing for the subtraction of all linear contributions due to the substrate and sample holder. It is also easy to see on the derivative of the experimental data that two Voigt functions for each (red and blue) branch were required for a proper fit (Figure Appendix 2 (d)).

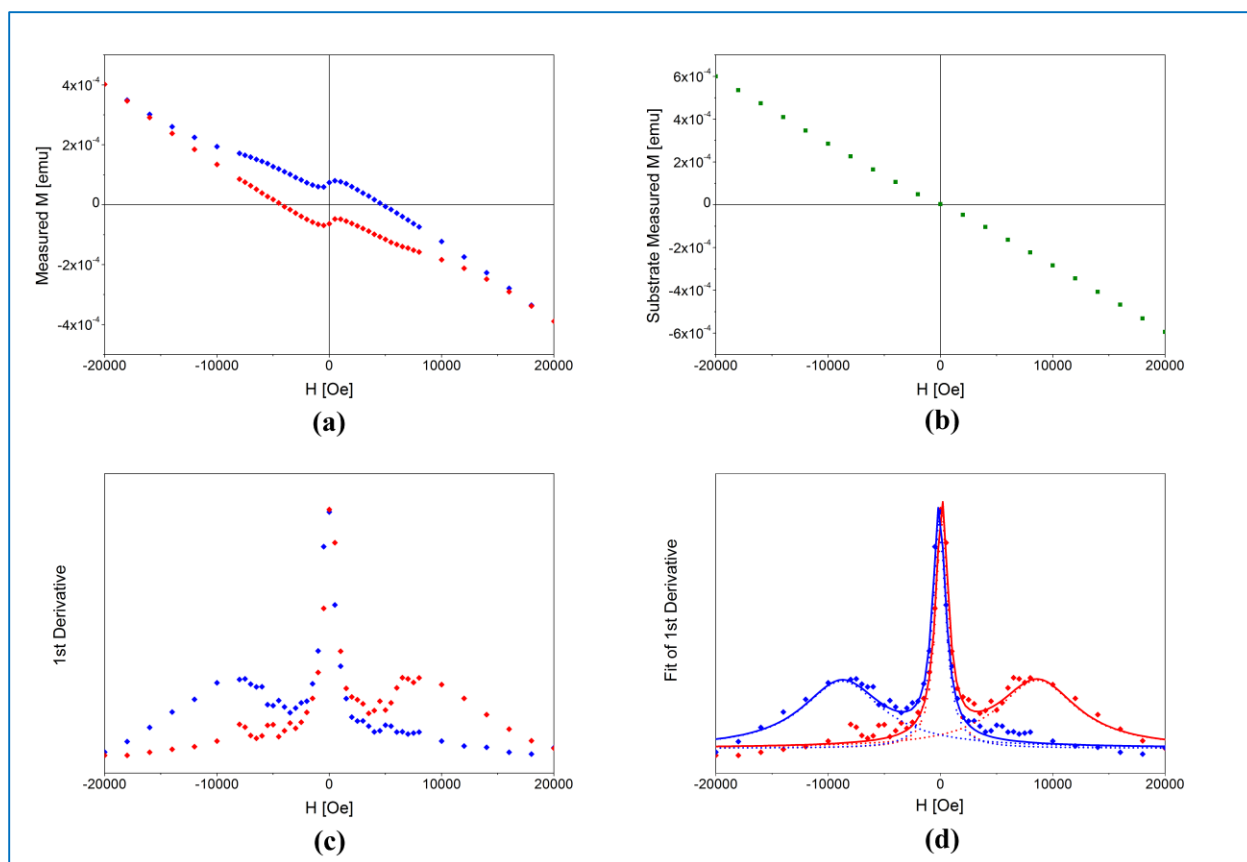


Figure Appendix 2: The measured hysteresis loop of a thin film of ϵ - Fe_2O_3 (a) (dots), shows strong diamagnetic contribution signal of the substrates and of the rod holding the sample, along with double coercivities due to the presence of a secondary magnetic phase. Without using the D-D-SI presented here, additional measurements of the bare substrate (b) are needed in order to isolate the ferromagnetic contribution. Using the presented technique, removal of the signal of the substrate and sample holder, as well as determination of the true hysteretic behavior – in this case the hysteresis loops belonging to two magnetic phases - can be achieved by plotting the 1st derivative of the magnetic hysteresis loop (c) (dots) and fitting it by using a constant offset and two Voigt distributions for each curve (d) (red and blue lines).

Once separated, the two Voigt functions allowed us to reconstruct two distinct hysteresis loops that we attribute respectively to an epsilon ferrite phase (the loop with high coercive field), and to a secondary phase that is thought to be magnetite (Fe_3O_4 , the loop with low coercivity), as shown in Figure Appendix 3, which displays the hysteresis loop of the two phases (epsilon ferrite drawn in dashed burgundy and magnetite in dotted yellow lines) as well as the sum of the two loops (blue lines). By comparing the loop obtained by measuring and subtracting the substrate contribution (blue symbols in Figure Appendix 3) and the one obtained by fitting the derivatives by Voigt functions and reconstructing the hysteresis loops via integration of the sole Voigt functions (blue solid lines in Figure Appendix 3), we observe that the hysteresis

obtained ‘experimentally’ after correction for the diamagnetic rod (symbols) differs from the hysteresis obtained from the fit of the derivative using Voigt functions especially at high fields.

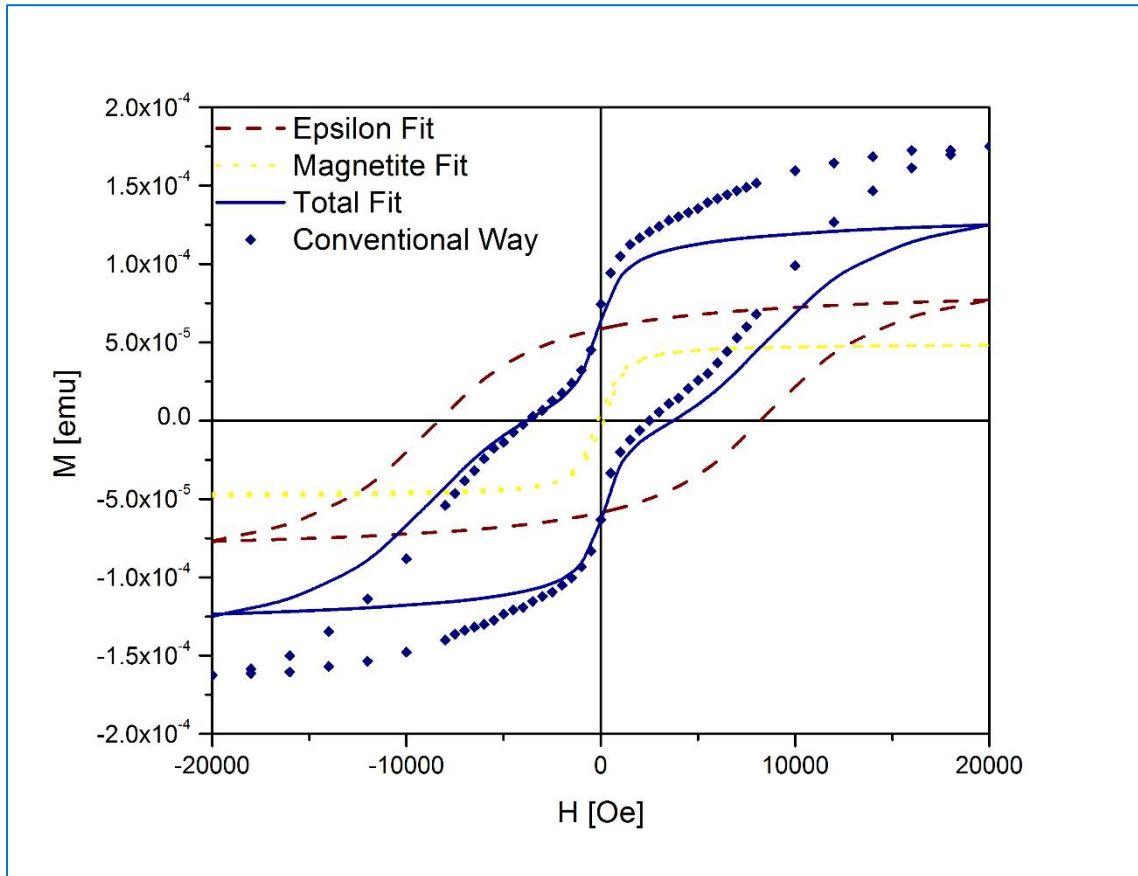


Figure Appendix 3: By separating and reconstructing the isolated contribution to the total loop, it is possible to highlight the actual functional parameters (M_S , M_R , and H_C) of epsilon ferrite (burgundy dashed lines), and magnetite (yellow dotted lines). Moreover, the sum of the two curves (blue lines), yields the total hysteretic signal of the ferroic material devoid of any secondary contributions, giving a more precise result in comparison to the results obtained by subtracting the signal of the vibrating rod (substrate holder) and of the substrate (blue dots).

The main reason explaining this difference is the difficulty to measure the exact contribution of the substrate and of the sample holder, which become larger as the field is increased. In spite of being most careful, it is difficult to measure the magnetic response of the sample holder or substrate considering that any difference in position between the measured values of the sample and of a similar (but distinct) substrate alone, as well as any imprecision in the determination of the shape or size of the sample or substrate can induce variations in the resulting calculated values of the magnetization. Such difficulties may lead towards incorrect estimation of the characteristic parameters of a magnetic material, especially if such material is characterized by low magnetic moment so that the contributions of the substrate and sample holder

APPENDIX I

dominate the experimental data (such as in Figure Appendix 2(a)). The quantity which is affected the most is the magnetization at saturation (given how it is measured at the maximum available field), which, in the case depicted in Figure Appendix 4, can be overestimated by as much as 40%. By comparing the curve obtained by utilizing the D-D-SI with the data obtained following the conventional way, we found that, in this specific case, by decreasing by 7.5% the contribution of the diamagnetic substrate (orange dots), a much better correspondence between the ‘corrected experimental’ (red dots) and the fit data (blue line) is found (Figure Appendix 4). It can be concluded that in this specific case, such an error of approximately 7.5% has been made in estimating the contribution of the substrate and sample holder, which may very easily arise for example from a misplacement of the sample or substrate on the sample holder by less than 0.5 mm or an incorrect measurement of the area of any of the two sample and/or the substrate (which in our case were of circa 5x5mm) by a minute amount.

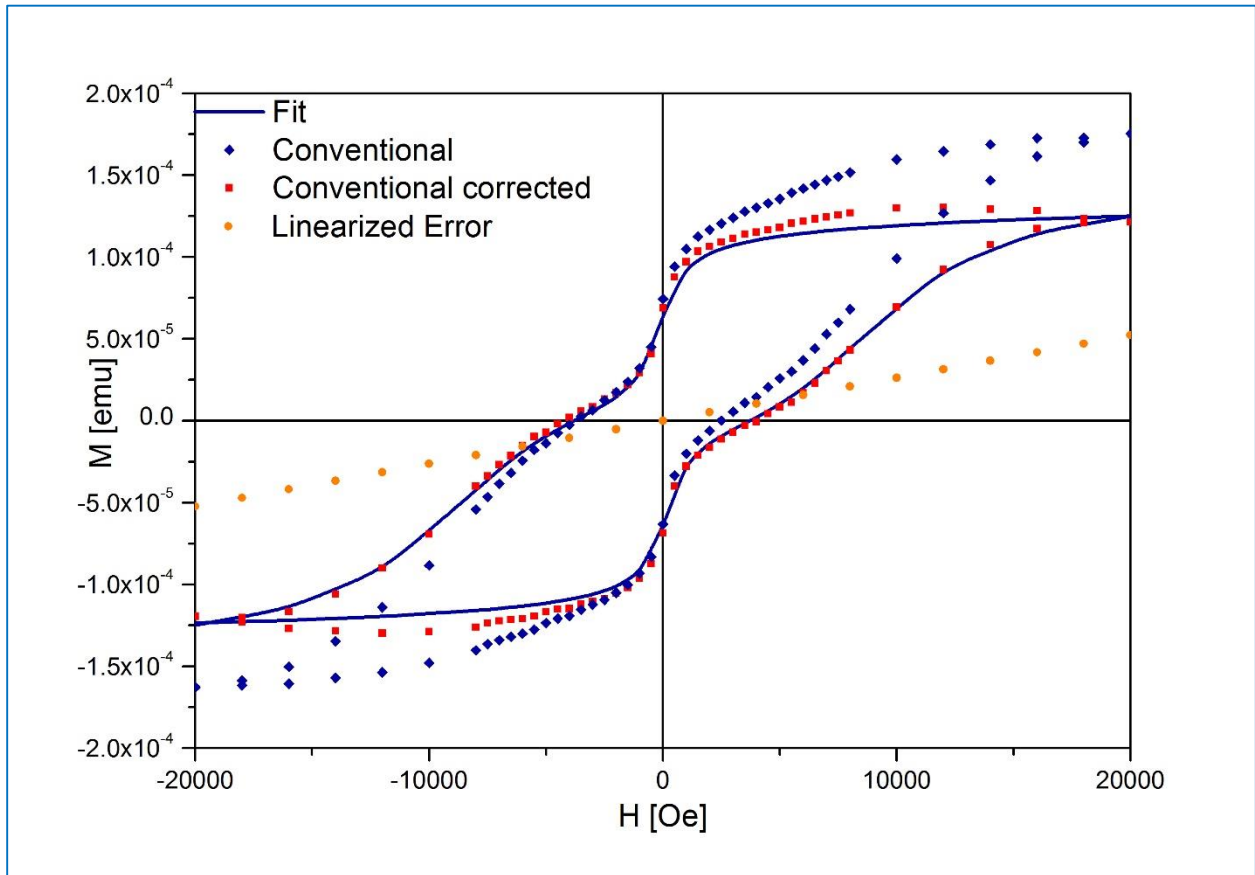


Figure Appendix 4: The data obtained following the ‘conventional’ way (blue diamond dots) lead to a linear error between such data and the one obtained by D-D-SI (orange round dots). Correction of such error was achieved by changing the magnitude of the diamagnetic signal by 7.5% (red square dots). In such a way, much better correspondence was found. The difference which is still present in the picture is due to low magnetic moment of the sample which results in a rather noisy, therefore difficult to fit, plot the 1st derivative as see in Figure Appendix 2 (d).

APPENDIX I

It is thus important to note that the reconstructed hysteresis loop using D-D-SI gives a much better estimate of the real properties of the materials investigated than the hysteresis loop obtain using the ‘conventional way’. The D-D-SI technique allows to remove all the presumably linear spurious contributions very easily, such as diamagnetic contribution of holder and substrate as well as paramagnetic contribution of the material investigated, since it corresponds to an offset in the derivative of the hysteresis loop. It thus eliminates the need to do additional and relatively difficult measurements of the contribution of the substrate (in the case of thin film) and of the sample holder when measuring samples with low magnetic moments. Most importantly, it easily allows to more precisely determine the true characteristic parameters of the studied ferroic material. Moreover, for complex magnetic materials such as epsilon ferrite epitaxial thin films, the possibility of separating the different contributions to the loop is a key feature that helps to fully understand their properties, as well as the complex dynamic that may occur during growth and leading to the formation of secondary phases.

Once the validity of the presented method to analyze ferromagnetic hysteresis loops was demonstrated, we examined the possibility to extend it to ferroelectric hysteresis loops. We believe that a technique that allows isolating solely the ferroic contribution to a ferroelectric hysteresis loop represents an important step towards a better understanding of the behavior of ferroelectrics, providing valuable information about the properties and structures of such materials. For example, besides the obvious parameters such as coercive field, spontaneous, and remanent polarizations, one can infer from a ferroelectric loop, many important elements, including the effect of grain size and grain boundary and other materials related properties (doping, anisotropy, thickness), as well as the effects of aging, and of the measurement conditions¹⁵⁷. For the analysis of ferroelectric hysteresis loops, three different samples were investigated: a loop recorded from a thin film of the well-known ferroelectric lead zirconate titanate ($\text{Pb}[\text{Zr}_{0.2}\text{Ti}_{0.8}]\text{O}_3$ - PZT), an epitaxial thin film of the multiferroic $\text{Bi}_2\text{FeCrO}_6$ (BFCO), which is characterized by high leakage currents, and a low quality thin film of Tetragonal Tungsten Bronze (TTB) which will be used as an example to show how artifacts can lead to misinterpretation of experimental data due to its resemblance to an hysteresis loop.

First, the loop recorded from lead zirconate titanate will serve to validate the D-D-SI technique for the case of ferroelectric materials. It is worth mentioning that the quantity measured in typical macroscopic ferroelectric measurements is the displacement current generated by polarization switching which is integrated over time in order to obtain the electric displacement $\mathbf{D} = \epsilon_0 \mathbf{E} + \mathbf{P}$ (generally the dielectric contribution of $\epsilon_0 \mathbf{E}$ is negligible). In the experimental setup, the measurement is generally conducted with the external voltage applied to the electrodes varied linearly with time, and the displacement current is measured (differentiating $\mathbf{D} = \epsilon_0 \mathbf{E} + \mathbf{P}$ with respect to time gives the displacement current density $\mathbf{J}_D = \epsilon_0 \frac{\partial \mathbf{E}}{\partial t} + \frac{\partial \mathbf{P}}{\partial t}$). The experimental data measured thus already corresponds to the first derivative of the

APPENDIX I

hysteresis loop. Also to be noted; in most ferroelectric measurements of thin films, there is no contribution from the substrate due to the presence of electrodes, which are generally placed directly above and below the probed sample.

The displacement current recorded for lead zirconate titanate is presented in Figure Appendix 5(b) (symbols). A slight asymmetry in the loop was recorded, which is attributed to a parasitic effect originating from the experimental setup, not from the sample. Integration of the measured displacement current gives the hysteresis loop, which is shown in Figure Appendix 5 (a) (symbols). As shown in Figure Appendix 5 (b), also in the case of ferroelectric measurements, a Voigt function could be used to fit with the experimental data with a good accuracy. Like it was the case for magnetic materials, the method yields very good results, demonstrating once more the validity and versatility of a Voigt distribution as fitting function.

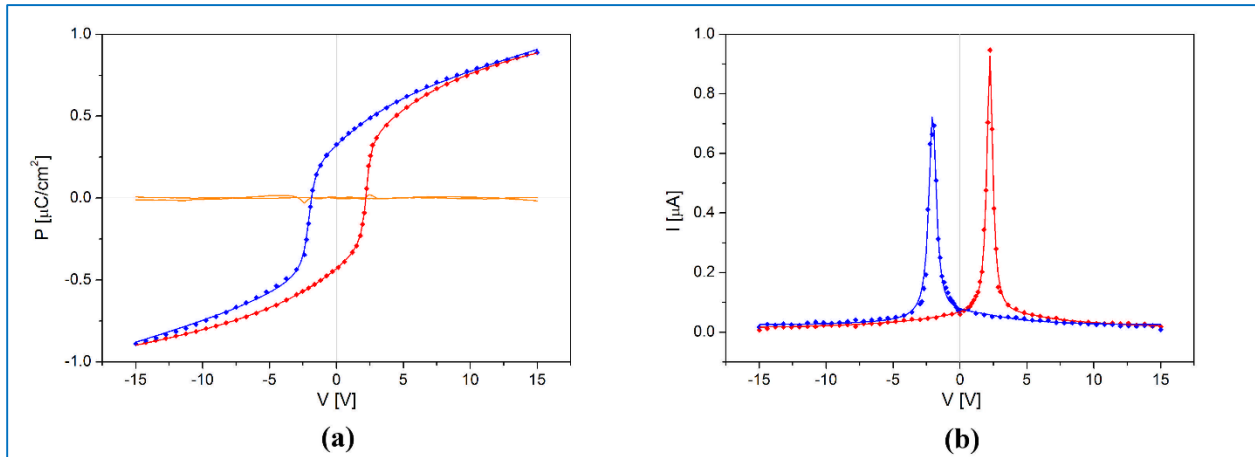


Figure Appendix 5: As was demonstrated for magnetic hysteresis loop, the D-D-SI yields good fitting also for ferroelectrics, as shown by the measured (a) (dots) and reconstructed (blue and red line) hysteresis loops of lead zirconate titanate, along with the error given by the fit (orange lines), and (b) for the plot of the 1st derivative which corresponds to the displacement current (I) of the measured loop of PZT (dots) and the Voigt fitting function (lines).

While in the case of PZT, the current loop shows the typical peak associated to the change of polarization in ferroelectric materials, we have observed that in the case of thin films of BFCO and TTB the loops are highly affected by leakage currents. Even if the origin of such currents may be different^{158,159}, their contribution to the loop can be well fitted with a high order polynomial series.

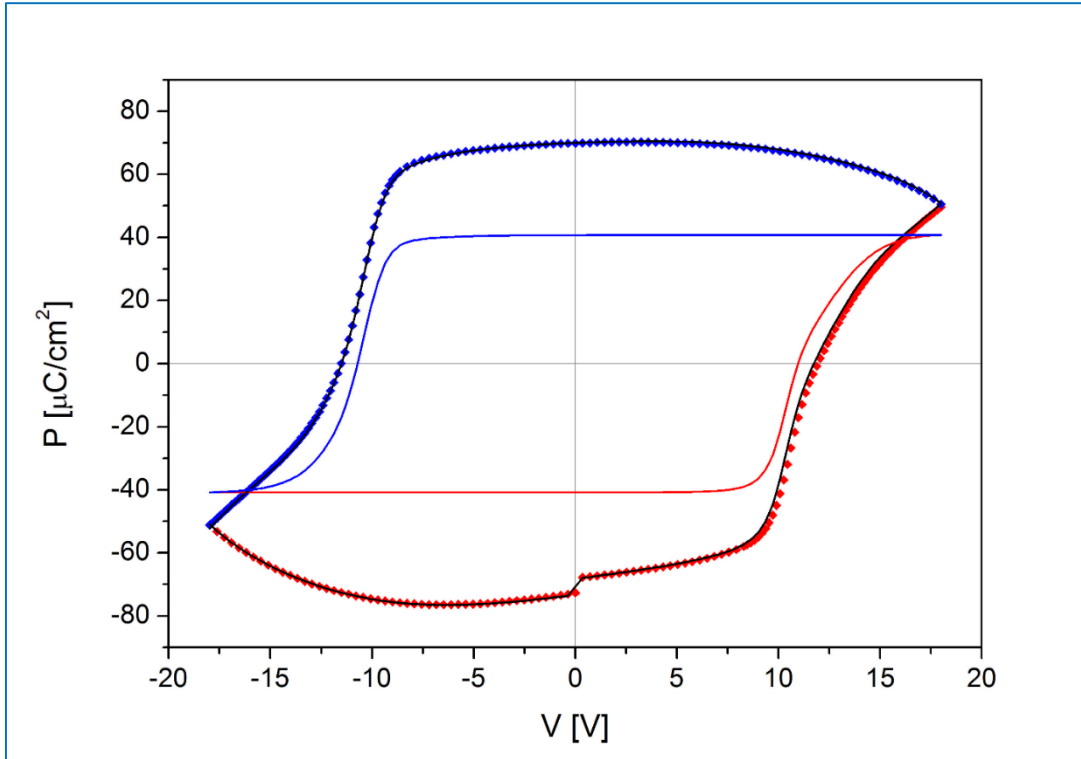


Figure Appendix 6: Fitting and further reconstruction allows to eliminate the contribution of leakage currents to ferroelectric loops, as shown in the plot of the measured ferroelectric loop of an epitaxial BFCO thin film (dots), along with the total fit (black lines), displaying the sole contribution of the ferroelectric material (blue and red line). The shift at 0 Voltage for the experimental upward curve is an instrumental artifact coming from the junction of the first and last measured point.

As it can be seen in Figure Appendix 6, the polarization loop for an epitaxial BFCO thin film is indeed affected by the contribution of leakage currents. The presence of leakage currents results in loops with rounded end and gives the impression that the polarization at saturation is reduced at high voltages, which is not the case in reality. It is a rather straightforward operation to subtract the contribution of the leakage current directly from the polarization hysteresis loop in order to obtain a constant value at saturation, as was done when the data shown in Figure Appendix 6 were first presented¹⁶⁰. However, such method is less reliable than the D-D-SI technique and often does not lead to complete removal of the leakage contributions.

In Figure Appendix 7, the measured switching current in the case of the multiferroic BFCO epitaxial thin film is shown. Fitting the contribution of leakage currents with a polynomial series allows its complete removal, which permits to obtain uniquely the contribution of the ferroelectric material (as shown in Figure Appendix 6), and to find the correct values for the polarization at saturation P_S , the remanent polarization P_R at zero applied field, and the coercive field E_C of the BFCO epitaxial film. Moreover, a detailed analysis of the switching currents (often overlooked) allowed us to note how two Voigt functions were required to properly fit the data, revealing the presence of two different peaks (most probably two phases) having different values of coercivity. Interestingly, in the case of the BFCO epitaxial film, structural analysis did

APPENDIX I

not reveal the presence of this second phase, in contrast to the case of the ϵ -Fe₂O₃ epitaxial films. However, due to the high asymmetry in the two current curves (visible by the much more pronounced shoulder for the positive current peak), it is rather difficult to separate and reconstruct satisfactorily the hysteretic contribution of each separate phase. In particular, we noticed how both the amplitude and the FWHM of the peaks are different for the upward and the downward current curve. On the other hand, the position of each peak and the total area underneath the curves are consistent, which is the reason why, once we sum the integrals belonging to each peak, we are able to reconstruct the total hysteresis loop satisfactorily.

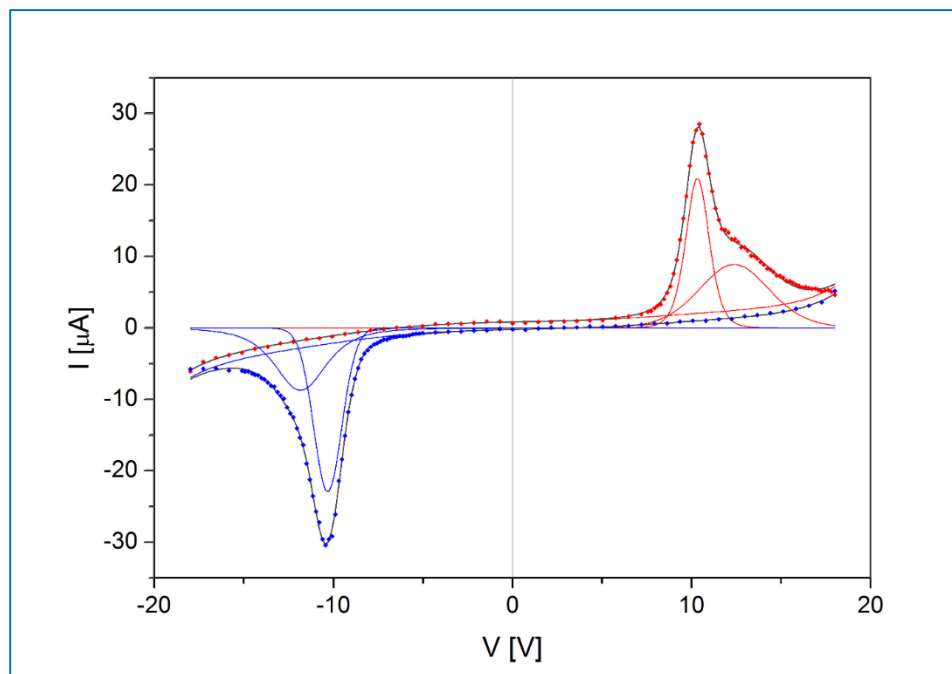


Figure Appendix 7: The current plot of an epitaxial thin film of BFCO (dots), gives evidence of the strong influence of the leakage currents, along with presence of two different coercivities. However, it is still possible to achieve a satisfactory fit of the measured signal (lines).

To the best knowledge of my supervisor and myself, such a second phase has not been detected before in this compound, and such a finding is worth further investigation since it may be a hint for the presence of several ‘phases’ of BFCO with different cationic ordering¹⁶¹. This further proves how a detailed analysis of hysteresis loop may lead to new and groundbreaking discoveries in the world of multifunctional complex oxides. However, since this is not the main topic of this paper, this interesting phenomenon will not be further discussed here.

The effect of leakage currents is even more critical for the hysteresis loop that was recorded for a low quality TTB film of composition Ba₂EuFeNb₄O₁₅, where there is actually no ferroelectric contribution at all. In that case, the loop measured is simply an artifact mostly due to leakage currents. It has to be noted that TTB ceramics of Ba₂EuFeNb₄O₁₅, as well as TTB thin films of the same composition and better quality

APPENDIX I

do exhibit clear ferroelectric properties, as should be the case, due to their polar crystal structure. The case of this specific TTB thin film is similar to what has been already highlighted in the famous paper ‘ferroelectrics go banana’¹⁵², namely a misinterpretation that unfortunately plague many reports on ferroelectric materials, presenting hysteresis loops claimed to be ferroelectric, which are actually artifacts generated by the presence of phenomena not related to the inversion of polarization. As shown in Figure Appendix 8, while the P vs E graph may be similar to a polarization loop, with the possibility to assign values for polarization at saturation, remanence, and coercive field (Figure Appendix 8(a)), the current loop, i.e. the derivative of the hysteresis loop, does not show any indication of the typical peaks associated to polarization switching in ferroelectric materials (peaks that should correspond to inflexion points in the hysteresis loop), the absence thereof obviously preventing any fit using a Voigt distribution, confirming the non-ferroelectric nature of this specific film (Figure Appendix 8(b)).

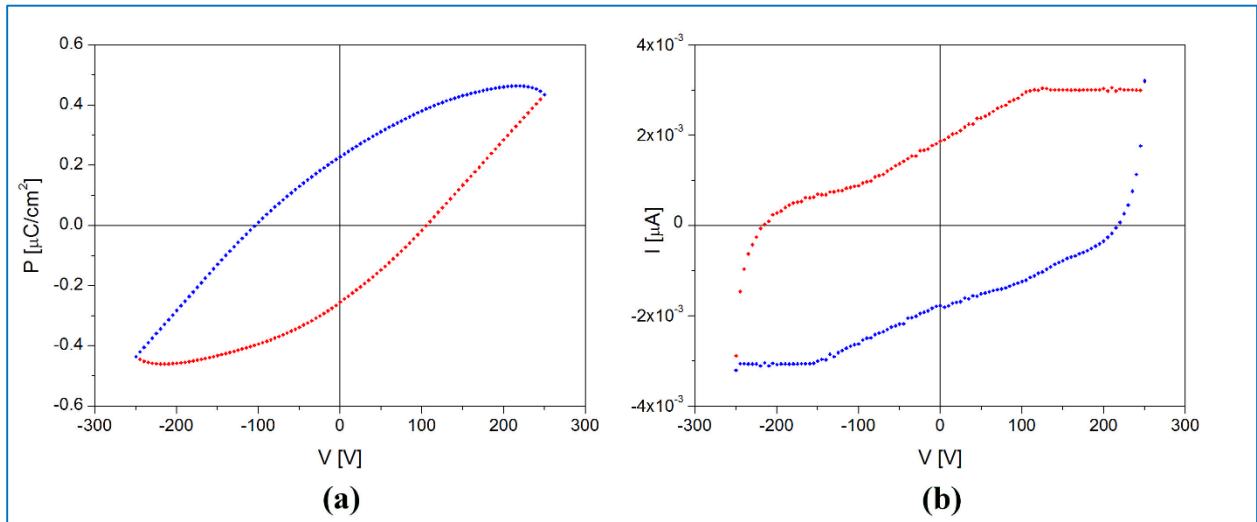


Figure Appendix 8: Hysteresis loop (a) and current loop (b) of a TTB film, used to highlight how loops resembling ferroelectric loops may be generated by spurious effects. The 1st derivatives have no visible feature that can be fitted with a peak-shaped function, revealing the non-hysteretic, therefore the non-ferroelectric, nature of our thin film.

I.3 Conclusions

An easy but powerful and useful method, D-D-SI, has been suggested to analyze hysteresis loops through first derivative of the measured loops, fitting the derivative with one more Voigt functions and a polynomial series, and finally by integrating the sole fitting function(s), which best represents the intrinsic hysteretic contribution of the ferroic material investigated. The D-D-SI proves to be of great interest given how easily and systematically it allows analyzing complex loops of multiphase ferromagnetic materials, such as epsilon ferrite thin films, as well as hysteresis loops of ferroelectric materials where there is a dominant contribution of leakage currents. The presented method allows to reliably extract the parameters intrinsic to the studied material (values of magnetization/polarization at saturation as well as remanence and coercive fields) with a good precision. Furthermore, such an analysis allowed us to reveal the possible presence of two phases in BFCO epitaxial films, which was not detected by structural characterization, such as X-ray diffractometry. Finally, we could not emphasize enough the usefulness of the D-D-SI technique for the analysis of ferroelectric loops, the ability of separating each contribution being of foremost importance, since it permits to easily recognize fictitious loops, which may help avoiding misinterpretation of results in future publications and related embarrassing consequences.